Development of a primary standard for absorbed dose to water from alpha-emitting radionuclides

By

Ahtesham Ullah Khan

A dissertation submitted in partial fulfillment of
the requirements for the degree of

Doctor of Philosophy
(Medical Physics)

at the
University of Wisconsin – Madison
2023

Date of final oral examination: April 14, 2023

This dissertation is approved by the following members of the Final Oral Committee:

Larry A. DeWerd, Professor, Medical Physics
Wesley S. Culberson, Associate Professor CHS, Medical Physics
Bryan P. Bednarz, Associate Professor, Medical Physics
Jonathan W. Engle, Associate Professor, Medical Physics
Douglass L. Henderson, Professor, Engineering Physics

"Scientific thought and it's creation is the common and shared heritage of humankind"

Dr. Abdus Salam

Abstract

Targeted radionuclide therapy (TRT) and brachytherapy with alpha particles has gained significant clinical relevance recently. Absorbed dose traceability to a standard is currently lacking in the dosimetry chain. The short range of alpha particles in water of <100 μm complicates the absorbed dose measurements in the form of significant attenuation and perturbation effects. The purpose of this work was to develop and validate absorbed dose to water standards for alpha-emitting radionuclides. Dosimetric formalisms to measure surface absorbed dose to water per radioactivity using windowless cylindrical parallel-plate extrapolation chambers (ECs) were introduced.

Monte Carlo (MC) investigations were launched to probe the alpha transport mechanism using a Fano cavity test. Optimal electromagnetic transport parameters were extracted from this study. The assumptions of the cavity theories were evaluated and the impact of source parameters on absorbed dose was studied. Following the construction of the apparatus, a thin film ^{210}Po source was employed with a radioactivity of 1.253 μCi for evaluation. A parallel-plate EC with a 4.00 mm collector diameter composed of D400 polystyrene-equivalent material was utilized as a standard. Addtionally, a printed circuit board (PCB) with a segmented guard was constructed to align the detector and the source plates using a differential capacitance technique. The PCB EC aimed to enhance the repeatability of the ionization current measurements. EC-based and MC-based correction factors were calculated for a planar circular ^{210}Po alpha emitter. Lateral and rotational alignment between the EC and the source was performed using translational and rotational shifts applied to the source using a hexapod motion stage. The initial air gap was determined using a contactless capacitance method. Ionization charge was collected as a function of applied voltage, varied between 1-200 V for a 0.3 mm air gap, to calculate the recombination correction. The polarity correction was measured by reversing the polarity

of the applied bias. Multiple measurement trials were performed to measure ionization current at air gaps in the 0.3-0.525 mm range. The proposed dosimetric formalisms were employed to calculate the surface absorbed dose to water from a point-like ^{210}Po source.

Negligible self-attenuation was found for the ^{210}Po source and the radius of the source was measured to be 1.60 mm. Lateral and rotational offsets of up to 0.20 mm and 1.50 deg were measured, respectively, when aligning the EC parallel to the source with their centers coincident with each other. The recombination and polarity correction factors were measured to be <0.50% when a 150 V/mm electric field strength was applied. The MC-calculated and measured absorbed dose to air agreed within 2.05% and 4.50% for the D400 and the PCB IC, respectively. Using the extrapolation method, the surface absorbed dose to water for the ^{210}Po was measured to be 2.8913×10^{-6} Gy/s/Bq and 2.304×10^{-6} Gy/s/Bq with a combined uncertainty of 3.74% and 3.55% for the D400 and the PCB IC, respectively. Large uncertainties, above 7% at k=1, were reported for the absorbed dose calculated using the cylindrical shell dosimetric formalism. Therefore, the extrapolation method was preferred to measure the surface absorbed dose to water.

This work demonstrated the ability of two windowless parallel-plate ECs as absorbed dose standards for alpha-emitting radionuclides.

Acknowledgements

I would like to thank my advisor Dr. Larry DeWerd for his mentorship and guidance throughout my time at the UW-Madison. His support and advice made this doctoral work possible. I wish to also thank Dr. Wesley Culberson for his insightful questions and suggestions that improved the quality of this work. I am thankful for my committee members Dr. Bryan Bednarz, Dr. Jonathan Engle, and Dr. Douglass Henderson for their contributions to this thesis work. A special thanks to all the staff members at the UWMRRC who actively made suggestions that improved this work. Specifically, I thank Keith Kunugi, Jeff Radtke, Benjamin Palmer, Jennifer Hull, Clifford Hammer, and Wendy Kennan for their assistance. Keith Kunugi was especially helpful and supervised this project from the very beginning. Jeff Radtke was the mastermind behind the PCB ion chamber and helped in many ways throughout this work. Benjamin Palmer and Jennifer Hull actively contributed to this work by advising on all constructional aspects of this work. Clifford Hammer advised on the radiochromic film portion of this study. Wendy Kennan fully supervised and assisted with the conception of the UWMRRC alpha lab. She also helped drafting the radiation safety protocols and ensured the safety of all workers. I also thank Leif Lervik for fabricating all the parts for this work. Thank you to the team at Eckert & Ziegler for making a custom Polonium source for this work. Brian Hooten from Standard Imaging helped with the modification of the extrapolation chambers.

I am extremely grateful for my parents and siblings who supported me in every way possible. This journey would have been cut short without their encouragement and love. I cannot thank my wife Willa Mihalyi-Koch enough who has supported and helped me with everything. She has been my rock and mentor since day 1 of my graduate school journey. Many thanks to my mentors Eric Simiele and Autumn Walter who took me under their wing and supported me all this time. I am also thankful to my peers especially Reed Kolany, Nicholas Nelson, and Andrew Bertinetti. Their advice has been insightful over the past few years. I am grateful for my time spent with them and all the things they have taught me.

Contents

Abstract **ii**

Acknowledgements **iv**

Contents **iv**

List of Figures **viii**

List of Tables **xv**

1 Introduction **1**
1.1 Introduction and Outline 1
1.1.1 Overview 1
1.1.2 Description of upcoming chapters 2

2 Background and motivation **5**
2.1 Introduction 5
2.1.1 Targeted radionuclide therapy (TRT) 6
2.1.2 Clinical work 10
2.1.3 Alpha particle decay and interactions with matter 13
2.1.3.1 Alpha decay 13
2.1.3.2 Alpha interactions with matter 15
2.2 Dosimetry in TRT 18
2.2.1 Overview 18
2.2.2 Internal dosimetry 19
2.2.3 Microdosimetry 25
2.3 The need for a primary standard for absorbed dose 28
2.3.1 Motivation 28
2.3.2 Ionization chamber as a primary standard 30
2.3.3 Dosimetric formalism for the cylindrical shell method 37
2.3.4 Dosimetric formalism for the extrapolation method 42

3 A Monte Carlo investigation of particle transport, cavity theory, and source specification for alpha particles 45
3.1 Alpha particle Monte Carlo transport . . . 45
3.1.1 Introduction and motivation . . . 45
3.1.2 GEANT4 alpha transport . . . 46
3.1.3 GEANT4 decay library . . . 61
3.2 Cavity theory . . . 66
3.2.1 Introduction and motivation . . . 66
3.2.2 Bragg-Gray cavity . . . 68
3.2.3 Spencer-Attix cavity . . . 71
3.2.4 Comparison of stopping power ratios . . . 78
3.3 Source and substrate specifications . . . 80
3.3.1 Introduction and motivation . . . 80
3.3.2 Source diameter . . . 81
3.3.3 Self-absorption and filtration . . . 84
3.3.4 Entrance window . . . 87

4 Construction and evaluation of a D400 planar windowless extrapolation chamber as a primary standard for absorbed dose 89
4.1 Construction of the apparatus . . . 89
4.1.1 D400 extrapolation chamber . . . 97
4.1.2 COMSOL electric field lines simulations . . . 101
4.1.3 Capacitance and parallelism measurements . . . 104
4.1.3.1 Parallel alignment between the detector and the source . 104
4.1.3.2 Capacitance measurements . . . 105
Dummy source measurements: . . . 106
Radioactive source measurements: . . . 109
4.1.4 Eckert & Ziegler ^{210}Po source . . . 110
4.2 Monte Carlo correction factors for ^{210}Po . . . 119
4.2.1 k_{point} . . . 120
4.2.2 Correction factors for the cylindrical shell method . . . 121
4.2.2.1 $k_{backscatter}$ . . . 122
4.2.2.2 $k_{inv}k_{cav}$ . . . 123
4.2.2.3 Air to water absorbed dose conversion . . . 126
4.2.3 Correction factors for the extrapolation method . . . 129
4.2.3.1 $k_{backscatter}$ . . . 129
4.2.3.2 k_{div} . . . 130
4.3 Measurement of absorbed dose from a ^{210}Po source . . . 132
4.3.1 Recombination correction . . . 134
4.3.2 Ionization current measurements . . . 136
4.3.3 Comparison of measured and MC absorbed dose to cavity . . . 140

4.3.3.1 Uncertainty budget 141
4.3.4 Absorbed dose measurements using the cylindrical shell method . 143
4.3.4.1 Uncertainty budget 144
4.3.5 Surface absorbed dose measurements using the extrapolation method 146
4.3.5.1 Uncertainty budget 147

5 Construction and evaluation of a printed circuit board (PCB) planar windowless extrapolation chamber as a primary standard for absorbed dose 149
5.1 Detector construction and characterization 149
5.1.1 PCB detector subassembly 151
5.1.2 COMSOL electric field lines simulations 155
5.1.3 Capacitance and parallelism measurements 157
5.1.3.1 Parallel alignment between the detector and the source . 157
5.1.3.2 Capacitance measurements 162
5.2 Monte Carlo correction factors for ^{210}Po 166
5.2.1 k_{point} 167
5.2.2 Correction factors for the cylindrical shell method 167
5.2.2.1 $k_{backscatter}$ 168
5.2.2.2 $k_{inv}k_{cav}$ 170
5.2.3 Correction factors for the extrapolation method 171
5.2.3.1 $k_{backscatter}$ 171
5.2.3.2 k_{div} 173
5.3 Measurement of absorbed dose from a ^{210}Po source 175
5.3.1 Ionization current measurements 175
5.3.2 Comparison of measured and MC absorbed dose to cavity 178
5.3.2.1 Uncertainty budget 180
5.3.3 Absorbed dose measurements using the cylindrical shell method . 181
5.3.3.1 Uncertainty budget 183
5.3.4 Absorbed dose measurements using the extrapolation method . . 184
5.3.4.1 Uncertainty budget 185

6 Conclusions and future work 187
6.1 Main conclusions 187
6.1.1 Monte Carlo investigation of alpha particle transport 187
6.1.2 Construction and evaluation of a D400 planar windowless extrapolation chamber 188
6.1.3 Construction and evaluation of a printed circuit board (PCB) extrapolation chamber 189
6.2 Future work 190

Bibliography **192**

List of Figures

2.1 Differences between EBRT and TRT are shown [1]. 6
2.2 A typical structure of a radiopharmaceutical [2] 7
2.3 Radioimmunotherapy process is illustrated [3]. 8
2.4 The effectiveness of alpha-emitters and beta-emitters is compared [1]. . . 9
2.5 ^{68}Ga-PSMA-11 PET scans are shown for a patient with metastatic prostate cancer [4]. 11
2.6 NaF PET scans are shown for a patient with osteosarcoma [5]. 12
2.7 A ^{149}Tb-DOTANOC PET image is shown [6]. 13
2.8 The potential energy of the alpha particle as a function of it's distance from the center of the daughter nucleus [7]. 13
2.9 The stopping power of water and air is plotted as a function of alpha energy [8]. 16
2.10 The differential scattering cross-sectional area is illustrated (from MP 501 notes). 17
2.11 An example of a dose distribution calculated using OLINDA software. . . 21
2.12 A schematic of the geometry used in DPK calculation is shown [9] 22
2.13 A dosimetry framework for total absorbed dose and dose rate in a patient-specific manner previously proposed by Besemer et al. [10] 24
2.14 A schematic of a Rossi chamber is shown [11]. 26
2.15 A traceability flowchart is shown for absorbed dose to water (from MP 501 lectures). 28
2.16 The proposed workflow for TRT treatments establishes *ex vivo* absorbed dose traceability. 30
2.17 Sectional view of the PTW type 23392 extrapolation chamber used in the work of Billas et al. [12] The entrance window and collector/guard electrodes are denoted by numbers 7 and 6, respectively. 32
2.18 Top: Range of alpha particles in water and air as a function of energy. Bottom: The water to air ratio of mass collision stopping power as a function of energy. 33
2.19 The integral depth dose (IDD) curve of a 5 MeV alpha particle in air. . . 34
2.20 The absorbed dose per Bq calibration coefficient is shown for various radii of vials filled with homogeneous ^{210}Po solution emitting 5.3 MeV alphas. 35
2.21 A schematic of the extrapolation chamber apparatus is shown. 36

2.22 The measurable dosimetric quantity and the quantity of interest are shown. 37
2.23 The conversion of the measurable quantity to the quantity of interest is illustrated. The quantity I is defined to be the ionization current at the air gap l. 37
2.24 A series of Monte Carlo (MC)-based correction factors are shown that allow conversion of the measured quantities to the quantities of interest. 39
2.25 The fall-off in fluence due to the inverse-square effect and the finite radius of the detector is shown. R is the radius of the air cavity and l is the air gap between the collector and source. 40

3.1 Simulated geometry used to implement a Fano cavity test for alpha particles (not to scale) [13]. 49
3.2 The Q-values (top) and the associated computational times (bottom) for various alpha energies are shown using the default electromagnetic parameters. The horizontal lines correspond to the ±0.3% margin from unity and the error bars correspond to 2σ statistical uncertainty [13]. 51
3.3 a) The Q-values (top) and the associated computational times (bottom) for various *dRover* magnitudes are shown for a variety of *final range* values for the Urban MCS model using a 6 MeV alpha particle energy. The horizontal lines correspond to the ±0.3% margin from unity and the error bars correspond to 2σ statistical un- certainty. The error bars are smaller than the symbols [13]. 53
3.4 The Q-values (top) and the associated computational times (bottom) for various *dRover* magnitudes are shown for a variety of *final range* values for the Wentzel-VI MCS model using a 7 MeV alpha particle energy. The horizontal lines correspond to the ±0.3% margin from unity and the error bars correspond to 2σ statistical uncertainty. The error bars are smaller than the symbols [13]. 54
3.5 The Q-values (top) and the associated computational times (bottom) for various *stepMax* values are shown for a 6 MeV alpha energy using the Urban MCS model and a 7 MeV alpha energy using the Wentzel-VI model. The horizontal lines correspond to the ±0.3% margin from unity and the error bars correspond to 2σ statistical uncertainty. The error bars are smaller than the symbols and the lines connecting the data points are for visual purposes only [13]. 56
3.6 The Q-values (top) and the associated computational times (bottom) for various cavity densities are shown for a 6 MeV alpha energy using the Urban MCS model and a 7 MeV alpha energy using the Wentzel-VI model. The horizontal lines correspond to the ±0.3% margin from unity and the error bars correspond to 2σ statistical uncertainty [13]. 57
3.7 The Q-values for the Urban MCS (top) and the Wentzel-VI MCS (bottom) models for various alpha energies, dRover, and *final range* values. The horizontal lines correspond to the ±0.3% margin from unity and the error bars correspond to 2σ statistical uncertainty [13]. 58

3.8 The Q-values (top) and the associated computational times (bottom) for various alpha energies are shown using the recommended electromagnetic parameters. The horizontal lines correspond to the ±0.3% margin from unity and the error bars correspond to 2σ statistical uncertainty [13]. . . 59
3.9 Decay schemes for a few clinically-relevant, alpha-emitting radionuclides such as ^{212}Pb, ^{227}Th, ^{223}Ra, and ^{225}Ac [14]. The nuclear transitions that lead to zero alpha emissions or include beta emissions are represented by double arrow heads and are red in color [13]. 61
3.10 A simplified version of the source and detector geometry. 66
3.11 Track-length distribution of 5 MeV alpha particles in a cylindrical cavity of radius 2.019 mm and of thickness 300 μm. 67
3.12 A schematic of the simulation setup is shown. 68
3.13 The change in fluence with change in cylindrical cavity thickness for parallel alpha particle beams is shown. Fluence was normalized to the value at 1 μm cavity thickness. The error bars correspond to 1σ statistical uncertainty. 69
3.14 The change in absorbed dose with change in cylindrical cavity thickness for parallel alpha particle beams is shown. Absorbed dose was normalized to the value at 1 μm cavity thickness. The error bars correspond to 1σ statistical uncertainty. 70
3.15 The loss in energy due to high energy δ-rays is shown (from MP 501 notes). 71
3.16 The maximum energy transferred to the δ-rays along with their range in air as a function of the incoming alpha particle energy. 73
3.17 A schematic of the simulation setup is shown. The black arrows illustrate alpha particles and the red arrows correspond to delta electrons emitted by the primary particles. 73
3.18 The δ-ray energy spectrum inside the air cavity from a 5.3 MeV parallel alpha particle beam source. 74
3.19 The δ-ray energy spectrum inside the air cavity from a 5.0 MeV parallel electron beam source. 75
3.20 The δ-ray build-up effect is demonstrated by plotting the ratio of absorbed dose deposited by δ-rays to kinetic energy per unit mass transferred to δ-rays by primary alpha particles.The error bars correspond to 1σ statistical uncertainty. 76
3.21 The emission angular distribution, with respect to the direction of the parent alpha particle, of the δ-rays in a 100 μm thick cylindrical air cavity is shown. 76
3.22 Top: The IRCU report 49 stopping powers are shown for water and air. Bottom: The ICRU report 90 stopping powers, normalized to the ICRU report 49 stopping powers, for water and air. 79
3.23 The water to air stopping power ratios are shown for the ICRU report 49 and report 90. 80

3.24 The impact of source diameter on the absorbed dose to cavity using a uniformly emitting source. The absorbed dose values were normalized to the absorbed dose calculated for a point source. The error bars correspond to 1σ statistical uncertainty. 82
3.25 The impact of source internal diameter on the absorbed dose to cavity using a 100 μm-thick ring source. The absorbed dose values were normalized to the absorbed dose calculated for a point source. The error bars correspond to 1σ statistical uncertainty. 83
3.26 The differences between the impact of a ring source and a circular source on absorbed dose are shown. The absorbed dose values were normalized to the absorbed dose calculated for a point source. 83
3.27 The magnitude of self-filtration and attenuation is demonstrated by plotting absorbed dose against various source thicknesses. The absorbed dose values were normalized to the value for smallest source thickness i.e. 1 nm. The error bars correspond to 1σ statistical uncertainty. 85
3.28 The alpha energy spectra are shown for various source thicknesses using a 5 MeV monoenergetic alpha source. 86
3.29 The impact of the thickness of an aluminized Mylar entrance window on the absorbed dose to cavity. The absorbed dose values were normalized to the value at the smallest window thickness. The vertical line indicates the 5 μm thick Mylar film that is commercially available. The error bars correspond to 1σ statistical uncertainty. 88

4.1 An XZ view of the apparatus assembly is shown with the D400 detector mounted. 90
4.2 A YZ view of the apparatus assembly is shown with the D400 detector mounted. 91
4.3 The PI hexapod stage and controller are shown. 93
4.4 An example of the macro commands for the hexapod motion stage. . . . 93
4.5 The PI linear stage and controller are shown. 94
4.6 The aluminum shield surrounding the source subassembly is shown. . . . 95
4.7 SolidWorks schematics of the source subassembly are shown. 96
4.8 The constructed source subassembly is shown. 96
4.9 The constructed apparatus assembly is shown with the centering part in the detector slot. 97
4.10 The DC voltage generator and the multimeter used throughout this work. 98
4.11 The D400 EC used by Hansen et al. for ophthalmic applicator measurements [15]. 98
4.12 The modified D400 EC used in this work for alpha dosimetry. 99
4.13 The surface flatness map of the unmodified D400 EC (left) and the modified EC (right). 99
4.14 The backscatter from the D400 collector is shown for 5-9 MeV monoenergetic alpha beams. 100

4.15 The simulated D400 EC geometry in COMSOL Multiphysics ®. 102
4.16 Electric field lines simulated near the collector-guard insulator (CGI) using COMSOL Multiphysics ® for the D400 EC. 103
4.17 Illustration of parallel alignment between the detector and the source plates. 104
4.18 Determination of the absolute air gap and the cavity diameter using the capacitance method. Measurements with an arbitrary unknown initial air gap are shown. 108
4.19 Confirmation of the absolute air gap and the cavity diameter using the capacitance method. Measurements with a l_{offset} shift applied are shown. 108
4.20 The charge induced by the capacitance of the air cavity, Q_{dis}, differentiated from the ionization charge using a voltage increase method is demonstrated [16]. 110
4.21 The decay scheme of ^{210}Po is shown. 111
4.22 An image of the steel substrate is shown. 112
4.23 The interferometry results for a single silver-coated steel substrate are shown. 113
4.24 The MC estimated signal for the D400 EC using a 1 μCi ^{210}Po source. . . 115
4.25 Measured alpha spectrum of the ^{210}Po source using the ORTEC Alpha Aria spectrometer. 116
4.26 Lateral profiles showing the positional offset of the ^{210}Po radioactive source from the center of the substrate disk. 116
4.27 The impact of a lateral positional offset of the ^{210}Po source on absorbed dose. The horizontal line indicates a 1% deviation in absorbed dose from unity. 117
4.28 The normalized 2D profile of the ^{210}Po source displaying the azimuthal emission uniformity of the source. 117
4.29 The graphics rendering of the D400 EC in TOPAS MC code. The guard is represented by yellow color and the air cavity by purple. 119
4.30 The k_{point} correction factor as a function of air gap for a ^{210}Po point source. 121
4.31 The backscatter correction factor as a function of air gap for a ^{210}Po point source. 123
4.32 The absorbed dose to air as a function of radial distance for a point ^{210}Po source. The error bars correspond to 1σ uncertainty and are smaller than the marker. 125
4.33 The absorbed dose to cylindrical shells as a function of radial distance for a point ^{210}Po source. The error bars correspond to 1σ uncertainty and are smaller than the marker. 125
4.34 The $k_{inv}k_{cav}$ correction factor as a function of radial distance from a point ^{210}Po source. The error bars correspond to 1σ uncertainty and are smaller than the marker. 126
4.35 The $k_{inv}k_{cav}$ correction factor as a function of radial distance from a point ^{210}Po source. The error bars correspond to 1σ uncertainty. 127

4.36 The integral depth dose (IDD) of a 5.3 MeV alpha beam source in water (top) and air (bottom). 128
4.37 The backscatter correction factor as a function of air gap for a ^{10}Po point source. 130
4.38 Top: absorbed dose to cavity plotted as a function of air gap with a 3rd order polynomial fit. Bottom: the divergence correction factor for 300-525 μm air gaps. 132
4.39 Measured and fitted Jaffe plots to determine the recombination correction factor. 135
4.40 The stability of the D400 ionization current signal over time. 137
4.41 The measurement procedure for each trial. 137
4.42 Capacitance-based method to determine the initial air gap. 138
4.43 The ionization current, normalized by radioactivity, collected by the D400 EC at each air gap. 139
4.44 The measured and MC simulated absorbed dose to cavity as a function of air gaps in the 300-525 μm range. 140
4.45 Measured absorbed dose to air as a function of radial distance from a point ^{210}Po source using the cylindrical shell method. 143
4.46 Surface absorbed dose to water measured at each radial distance from a point ^{210}Po source using the cylindrical shell method. 144
4.47 Corrected ionization current at each air gap for the ^{210}Po source. 146

5.1 The first version of the PCB EC is shown. The center circle is the collecting electrode and the surrounding segmented ring is the guard. 150
5.2 Left: the final version of the PCB mounted on the cylindrical aluminum part is shown. Right: the back side of the mounting part is shown. 152
5.3 The interferometer results for the final version of the PCB mounted on the detector subassembly. 153
5.4 The backscatter due to the presence of the gold or copper collector. . . . 154
5.5 The schematic of the PCB EC simulated in COMSOL Multiphysics®. The black lines demonstrate the 2D slice profiles that were extracted from the 3D simulation results. 157
5.6 The electric field lines near the collector-guard insulator (CGI) for a 100 μm air gap. 158
5.7 The electric field lines near the segmented guard edges for a 100 μm air gap. 159
5.8 A schematic of the PCB segmented mode readout procedure is shown. . . 160
5.9 A picture of the capacitor to digital convertor (AD7746 Analog Devices) employed in this work. 160
5.10 The circuit used to measure differential capacitance across the opposing guards. 161
5.11 The aluminum case for the CDC board with the individual channels. . . 161
5.12 A screenshot of the CDC software displaying the minimization of the differential capacitance by rotating the source substrate. 162

5.13 Determination of the absolute air gap and the cavity diameter using the capacitance method. Measurements with an arbitrary unknown initial air gap are shown. 163
5.14 Confirmation of the absolute air gap and the cavity diameter using the capacitance method. Measurements with a l_{offset} shift applied are shown. 164
5.15 The graphics rendering of the PCB EC in TOPAS MC code. The left figure shows the XZ view of the PCB and the source substrate. The right figure shows the XY view of the PCB without the presence of the substrate. 166
5.16 The k_{point} correction factor as a function of air gap for a ^{210}Po point source. 168
5.17 The backscatter correction factor for the PCB EC with a point ^{210}Po source. 169
5.18 The $k_{inv}k_{cav}$ correction factor for the PCB EC with a point ^{210}Po source. 170
5.19 The k_{inv} correction (left), calculated using an analytical expression, and the k_{cav} correction factor (right) for the PCB EC with a point ^{210}Po source. 171
5.20 The backscatter correction factor for the PCB EC with a point ^{210}Po source. 172
5.21 Top: absorbed dose to cavity plotted as a function of air gap with a 3rd order polynomial fit. Bottom: the divergence correction factor for 300-525 μm air gaps. 173
5.22 The stability of the PCB ionization current signal over time. 176
5.23 The ionization current, normalized by radioactivity, collected by the PCB EC at each air gap. The radioactivity values were decay corrected. 177
5.24 The measured and MC simulated absorbed dose to cavity as a function of air gaps in the 300-525 μm range. 178
5.25 The measured PCB absorbed dose to cavity normalized by the measured D400 absorbed dose to cavity. 179
5.26 Measured absorbed dose to air as a function of radial distance from a point ^{210}Po source using the cylindrical shell method. 181
5.27 Surface absorbed dose to water measured at each radial distance from a point ^{210}Po source using the cylindrical shell method. 182
5.28 The PCB surface absorbed dose to water normalized by the D400 surface absorbed dose to water measured using the cylindrical shell method for a ^{210}Po source. 183
5.29 Corrected ionization current at each air gap for the ^{210}Po source. 185

List of Tables

2.1 Alpha-emitting radiopharmaceuticals currently in clinical trials or approved. 9

3.1 Electromagnetic transport parameters, based on the *EMStandardOpt*4 physics list, used by GEANT4 along with their default values. 48
3.2 Comparison of radioactive decay data between GEANT4, RADAR, and MIRD for ^{212}Pb. 63
3.3 Comparison of radioactive decay data between GEANT4, RADAR, and MIRD for ^{223}Ra. 63
3.4 Comparison of radioactive decay data between GEANT4, RADAR, and MIRD for ^{227}Th. Only the first decay transition was considered to avoid redundancy between the decay data for ^{227}Th and ^{223}Ra radionuclides. . 63
3.5 Comparison of radioactive decay data between GEANT4, RADAR, and MIRD for ^{225}Ac. 64
3.6 Correlation between the FWHM of the alpha peaks and source thickness due to energy straggling. 85

4.1 Relevant specifications for the miniature hexapod motion stage. 92
4.2 Relevant specifications for the linear motion stage. 94
4.3 Effective diameter of the air cavity determined from the capacitance measurements using a dummy source. 109
4.4 Uncertainty budget for the absorbed dose measurement, acquired with the D400 EC, at a 300 μm air gap. 141
4.5 Uncertainty budget for the absorbed dose measurement, acquired with the D400 EC, at a 500 μm air gap. 142
4.6 Uncertainty budget for the absorbed dose to air measurement, using the D400 EC, at a 312.5 μm radial distance from a point source. 145
4.7 Uncertainty budget for the surface absorbed dose to water measured using the D400 EC. 148

5.1 Effective diameter of the air cavity determined from the capacitance measurements using a dummy source. 165
5.2 Uncertainty budget for the absorbed dose measurement, acquired with the PCB EC, at a 300 μm air gap. 180

5.3 Uncertainty budget for the absorbed dose measurement, acquired with the PCB EC, at a 500 μm air gap. 180
5.4 Uncertainty budget for the absorbed dose to air measurement, using the PCB EC, at a 312.5 μm radial distance from a point source. 184
5.5 Uncertainty budget for the surface absorbed dose to water measured using the PCB EC. 186

Chapter 1

Introduction

1.1 Introduction and Outline

1.1.1 Overview

The goal of this work was to develop and evaluate a primary standard for absorbed dose to water from alpha-emitting radionuclides. For this purpose, a windowless parallel-plate extrapolation chamber (EC) was deemed suitable with a thin film source deposited on the surface of the source acting as an electrode. The quantity of interest in this work was surface absorbed dose to water and two independent dosimetric formalisms were introduced to realize this quantity. Before the construction and evaluation of the primary standard, a Monte Carlo investigation was launched to study the alpha particle transport capabilities of the Monte Carlo code used in this study. A Fano cavity test was implemented to explore the sensitivity of various electromagnetic parameters to the simulated absorbed dose. The cavity theory assumptions and conditions were tested using Monte Carlo methods and the impact of source characteristics, such as diameter

and thickness, on absorbed dose to cavity was studied. A comparison was performed to investigate the impact of an entrance window on the absorbed dose.

In addition to an already existing EC, a printed circuit board (PCB) was designed and constructed to rotationally align the source and detector using a differential capacitance method. The constructed primary standards were evaluated using a pure alpha emitter and the simulated absorbed dose to cavity was compared with the measured dose. Surface absorbed dose to water was calculated using the two dosimetric formalism for both detectors.

1.1.2 Description of upcoming chapters

Chapter 2 provides the relevant background and motivation for this work. The targeted radionuclide therapy (TRT) modality was introduced and the role of alpha particles in TRT was accentuated. The physics of alpha particle decay and it's interaction with matter was also described in this chapter. The current dosimetry methods were outlined and the need for a primary standard for absorbed dose was stressed. Two independent methods of determining the absorbed dose to water were introduced and explained.

A detailed Monte Carlo (MC) investigation was reported in chapter 3 exploring parameters that affect absorbed dose measurements. Alpha particle transport using the MC method was described and the electromagnetic parameters related to the ionization process and the multiple Coulomb scattering process were investigated. Using a Fano cavity test, optimal parameters were highlighted that led to most accurate simulation results. The decay library of the MC code was also benchmarked by comparing the emission energy and intensity with other nuclear decay databases. Both Bragg-Gray and Spencer-Attix cavity theories were introduced and the underlying assumptions commonly used for these theories were evaluated in the context of alpha particles. The source parameters

affecting the absorbed dose, such as source diameter and self-attenuation, were probed with the motivation of selecting the optimal parameters. The impact of a thin Mylar window on the absorbed dose was investigated in this chapter as well.

Chapter 4 describes the design process for the primary standard and the construction of the entire apparatus. The source and the D400 detector subassemblies are described along with the employed motion stages and the electronic equipment. A COMSOL study was performed to simulate the electric field lines inside the air cavity and to determine the sensitive volume of the cavity. The methods to rotationally align the D400 ion chamber and to determine the air gap between the detector and the source using a contactless capacitance method are also outlined in this chapter. A ^{210}Po source, used to evaluate the primary standard, is characterized. MC-based correction factors for the D400 ion chamber are shown in this chapter for both dosimetric formalisms. Finally, the measured absorbed dose is reported and compared with the MC data. Uncertainty analysis was performed for each reported absorbed dose.

Chapter 5 follows the same structure as chapter 4 but instead describes the design process behind the construction of the printed circuit board (PCB)-based EC. The segmented guard design were introduced and the differential capacitance method to rotationally align the detector with the source was described. COMSOL simulations were outlined to study the impact of the insulator gap on the electric field lines inside the air cavity and near the segmented guard edges. The capacitance method to measure the cavity diameter was outlined and measurements using a ^{210}Po source were described. Measured surface absorbed dose to water, in accordance with both dosimetric formalisms, was reported in this chapter for the PCB ion chamber. The results were compared with the D400 results introduced in chapter 4.

Chapter 6 provides main conclusions and proposes future work to extend the work performed in this dissertation. Alternative source configurations were proposed and future

measurements were described for relevant alpha sources.

Chapter 2

Background and motivation

2.1 Introduction

In this era, there are multiple treatment options available in cancer care. Four widely used types of treatments are: surgery, chemotherapy, radiation therapy, and immunotherapy. In radiation therapy, ionizing radiation is used to target cancer cells while minimizing any normal tissue toxicity. Three major forms of radiation therapy include external beam radiation therapy (EBRT), brachytherapy, and targeted radionuclide therapy (TRT) or molecular radiotherapy (MRT) [18]. Figure 2.1 shows the major difference between EBRT and TRT [1]. EBRT utilizes an exogenous beam source and delivers radiation to desired spatial coordinates by leveraging geometrical parameters such as the beam's angular incidence, couch movement, and collimation [19]. Contrarily, TRT is a form of systemic therapy in which the radioactive source is injected into the patient [20][21][22][23]. In brachytherapy, radioactive sources are also utilized, but these sources are sealed and are placed into a desired anatomy to deliver high radiation to the tumor site [24]. In this

chapter, the clinical applications of TRT are discussed along with the dosimetric methods employed to calculate radiation dose to patient.

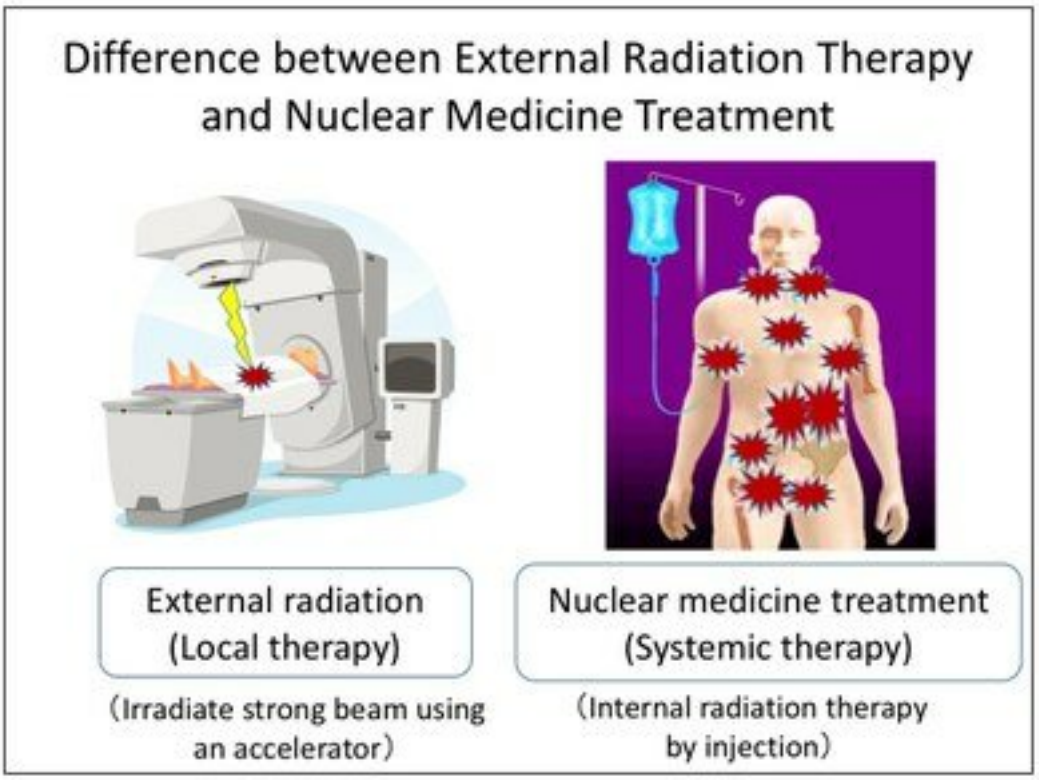

Figure 2.1: Differences between EBRT and TRT are shown [1].

2.1.1 Targeted radionuclide therapy (TRT)

Targeted radionuclide therapy (TRT) is a therapeutic technique which utilizes radiopharmaceuticals to target cancer cells. Radiopharmaceuticals, as shown in figure 2.2, are synthesized by attaching a radionuclide source to a cell-targeting molecule which biologically seeks and destroys cancer cells [25][26][27][28][29]. These drugs are unsealed radioactive sources which are injected directly into the patient's bloodstream [30][31]. The choice of the vector molecule as well as the radioactive source utilized in TRT highly depends on the clinical goal [3]. However, not all TRT drugs can be technically classified as "targeting". For example, NaF or $RaCl_2$ are salts with a high uptake in the skeleton,

however, both drugs lack a targeting molecule that binds to specific molecules [5][32]. In several cases, monoclonal antibodies are used as vector molecules in TRT. This is known as radioimmunotherapy. Radioimmunotherapy is an amalgamation of TRT and immunotherapy techniques where the labeled antibodies directly transport the radionuclide to the tumor by binding to cancer cells [3][33]. This is demonstrated in figure 2.3. For example, in the case of lymphoma, radiolabeled antigens attach to B cells in the body and deliver radiation [20]. The uptake of the radiopharmaceutical is non-uniform throughout the body and highly depends on the chemical and biological properties of the vector molecule utilized [34][35][36][37]. In a region of uptake, the radioactive source decays and emits energy in the form of ionizing radiation. The resulting ionizing radiation leads to single-strand or double-strand breaks of the DNA inside the cell nucleus. The goal of TRT is to simultaneously maximize cell-kills of cancer cells and minimize destruction of normal cells.

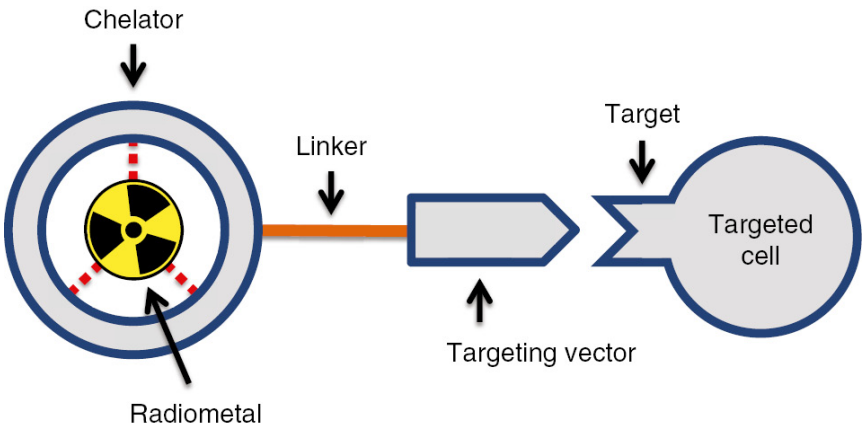

Figure 2.2: A typical structure of a radiopharmaceutical [2]

.

In the therapeutic realm, either alpha-emitters, beta-emitters, or Auger electron-emitters are employed. The choice of the type of radioactive source used depends on several parameters such as tumor biological expression and size, proximity of organs at risk (OAR) to the tumor, dose-limiting conditions, half-life, and energies of the particles emitted. Figure 2.4 illustrates the advantage of using an alpha-emitting radionuclide source over

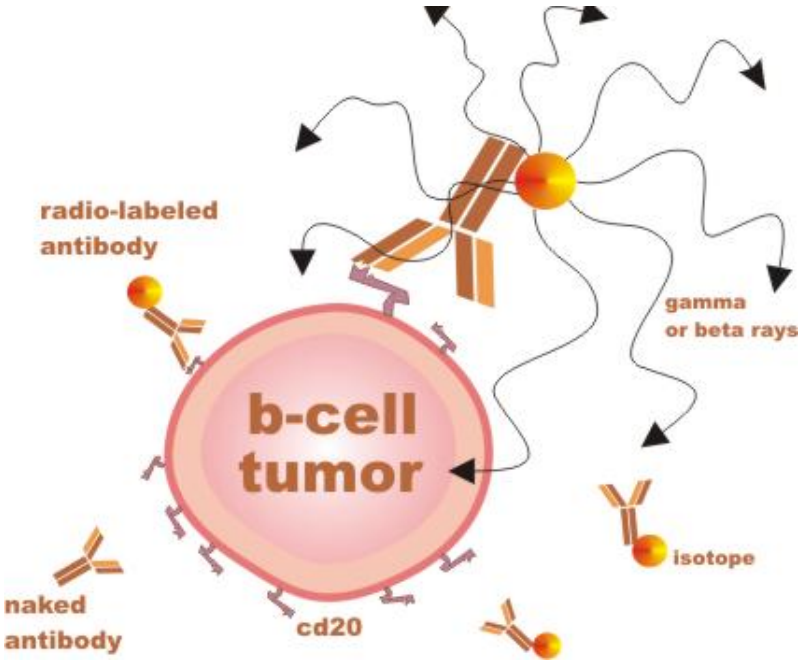

Figure 2.3: Radioimmunotherapy process is illustrated [3].

beta-emitting source. Beta particles tend to have a range of 50-2000 μm in tissue compared to the 40-100 μm tissue range of alpha particles. Therefore, alpha particles have a higher chance of minimizing radiation dose to normal cells. Alpha particles also tend to deposit higher energy along their pathways due to their higher linear energy transfer (LET) property which results in a larger number of double-stranded DNA breaks [38][39]. Thus, alpha particles have a larger relative biological effectiveness (RBE) than beta particles [40]. Due to these reasons, alpha particles are considered therapeutically superior. However, this is under the assumption that the radioactive source is precisely transported to the tumor site.

Seven most commonly used alpha-emitting radionuclides in TRT are ^{211}At, ^{213}Bi, ^{225}Ac, ^{223}Ra, ^{212}Pb, ^{149}Tb, and ^{227}Th [40]. Table 2.1 shows a list of commonly investigated alpha-emitting radiopharmaceuticals. It is important to note that $^{223}RaCl_2$ (Xofigo®) is the only FDA-approved alpha-emitting radiopharmaceutical and is used for treating

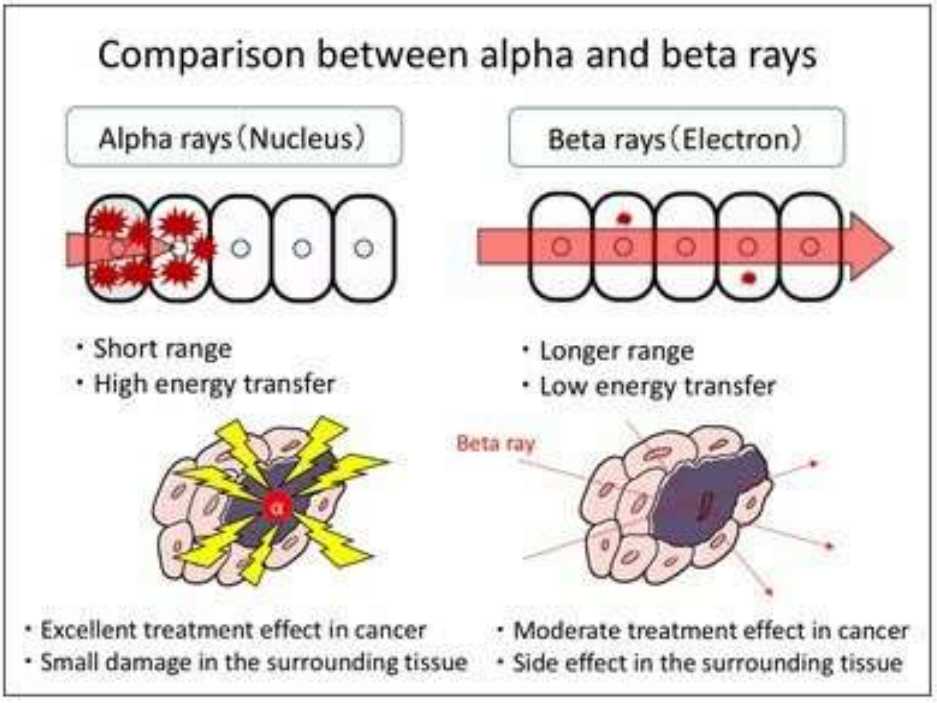

Figure 2.4: The effectiveness of alpha-emitters and beta-emitters is compared [1].

Table 2.1: Alpha-emitting radiopharmaceuticals currently in clinical trials or approved.

Radionuclide	Half-life	$\bar{E}_\alpha$ (MeV)	Radiopharmaceutical(s)	Company	Indication
^{211}At	7.2 h	5.87	-	-	-
^{213}Bi	45.6 min	5.84	-	-	-
^{225}Ac	10 d	5.75	^{225}Ac-aCD33, ^{225}Ac-FPX-01	Actinium Pharma, J&J/Fusion	Leukemia, NSCLC/Pancreatic Cancer
^{223}Ra	11.4 d	5.97	RaCl2	Xofigo, Bayer	Bone Mets
^{149}Tb	4.15 h	3.97	-	-	-
^{227}Th	18.7 h	5.9	^{227}Th-HER2-TTC, ^{227}Th-PSMA-TTC, ^{227}Th-MSLN-TTC, ^{227}Th-CD22-TTC	Bayer	Bone Mets, HER2 Tumors, Prostate, Mesothelin Tumors, Lymphoma
^{212}Pb	10.6 h	7.45	^{212}Pb-trastuzumab, ^{212}Pb-PRIT, ^{212}Pb-antisomatostatin, ^{212}Pb-aTEM1, ^{212}Pb-aCD37	Oranomed	HER2 Tumor, Somatostatin Tumors, TEM1, Leukemia

metastatic castration-resistant prostate cancer [41]. An optimal half-life is desired so that the source gets ample time to irradiate tumor cells while not occupying the patient's body for too long. An ideal radionuclide must have a half-life of several hours to days, adequate alpha particle range in tissue to create a sufficiently large cell-killing region, and an efficient and feasible manufacturing process [40].

2.1.2 Clinical work

There has been extensive work suggesting that TRT with alpha radionuclides, targeted alpha therapy (TAT), is clinically beneficial. Andersson et al. explored the efficacy of alpha-radioimmunotherapy both *in vitro* and *in vivo* using ovarian cancer cells OVCAR-3 and mice [42]. Monoclonal antibodies were labeled with ^{211}At and growth assay was used as an indicator of cell survival. Irradiation with the alpha radiopharmaceutical was found to be highly effective, relative to ^{60}Co irradiation, with no significant toxicities in both cell cultures and mice [42]. An additional experiment performed at Osaka university investigated the possibility of using sodium astatine (^{211}At) as a therapeutic drug for cancer. Mice that received grafts of thyroid cancer cells were used in this study, and it was shown that the mice treated with the radiopharmaceutical drug survived for almost three times as long as untreated mice [1].

Both ^{223}Ra and ^{225}Ac have been widely studied for castration-resistant metastatic prostate cancer [40]. Kratochwil et al. conducted the first clinical trial for human treatment of prostate cancer using ^{225}Ac radionuclide and prostate-specific membrane antigen (PSMA) as the radiopharmaceutical drug [4]. Positron emission tomography/computed tomography (PET/CT) scans were used to diagnose and assess the severity of the prostate cancer.

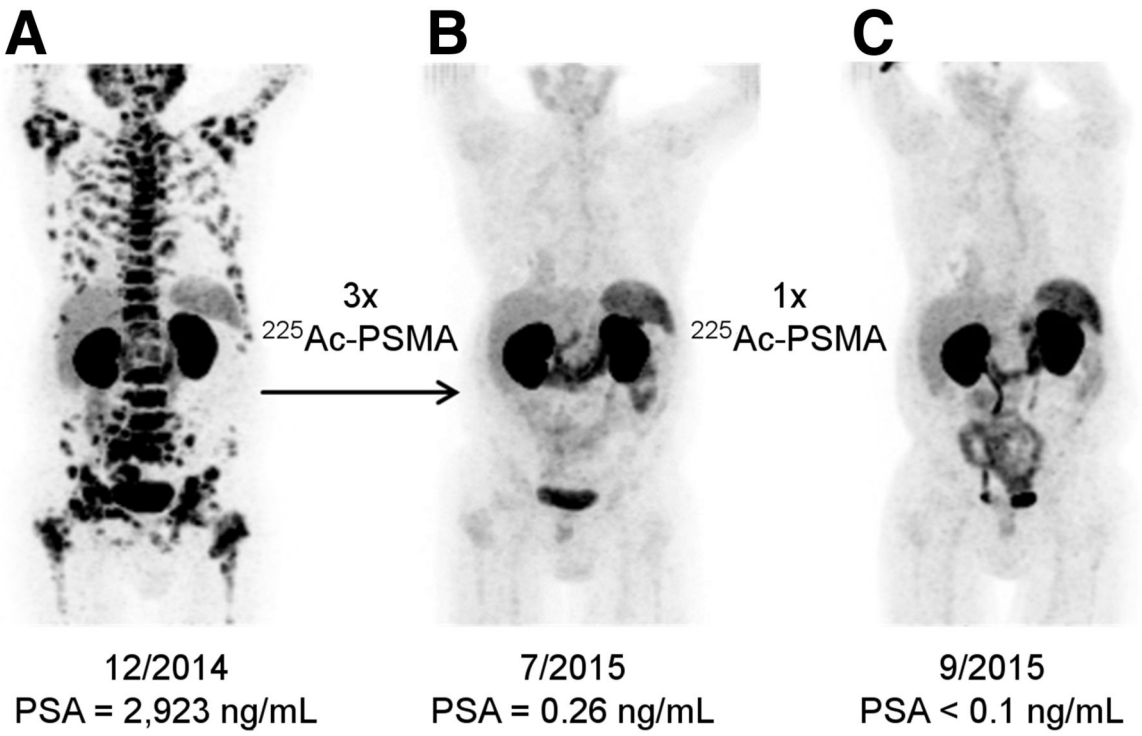

Figure 2.5: ^{68}Ga-PSMA-11 PET scans are shown for a patient with metastatic prostate cancer [4].

After several injections of the radiopharmaceutical, prostate-specific antigen (PSA) was found to decrease. Using ^{68}Ga-PSMA-11 PET/CT imaging, an improvement was found in patients treated with the TRT. Figure 2.5 shows the benefit of using ^{225}Ac-PSMA as a radiotherapeutic drug.

In a clinical trial led by Subbiah et al., bone-targeting radium 223 dichloride ($^{223}RaCl_2$) was used for the treatment of osteosarcoma [5]. Using dose-escalation method, several different concentrations of $^{223}RaCl_2$ (50, 75, and 100 kBq/kg) were injected into different patients and the uptake values extracted from NaF PET images were used as a biomarker for outcomes. Considering outcomes and hematological toxicity, 100 kBq/kg was recommended to be the phase II clinical trial dose [5]. Figure 2.6 shows the benefit of using $^{223}RaCl_2$ as a TAT drug for patients with osteosarcoma.

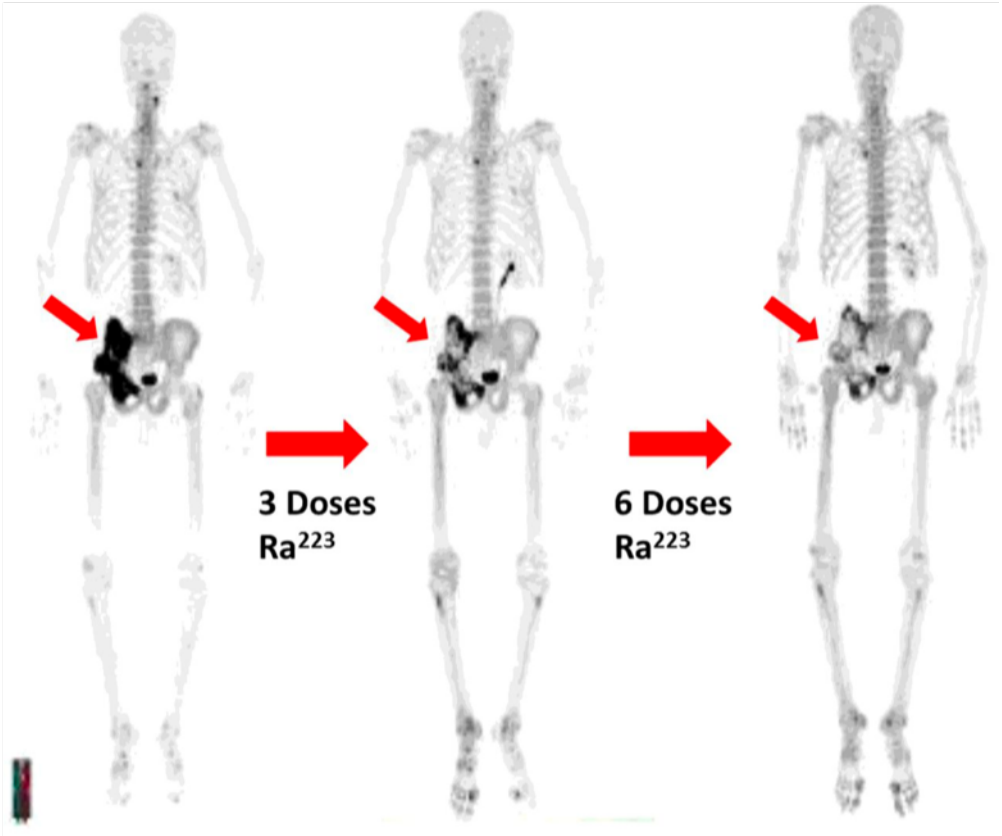

Figure 2.6: NaF PET scans are shown for a patient with osteosarcoma [5].

Initial clinical work has been performed with both ^{227}Th and ^{149}Tb, and first-in-human studies have been designed with these radionuclides [40][43]. Hagemann et al. used ^{227}Th and a mesothelin (MSLN)-targeted conjugate to target mesothelin-positive cancer cells in mice [44]. A significant survival benefit was found for mice treated with ^{227}Th radiopharmaceutical especially in a disseminated lung cancer model. Müller et al. utilized ^{149}Tb as a drug to target folate-receptor positive cancer cells in mice [6]. Complete remission or marked delay in tumor growth was found for mice treated with the TRT drug compared to the untreated mice. Furthermore, the work of Müller showed the ability of using ^{149}Tb as both a therapeutic and imaging radionuclide, a theranostic agent. Figure 2.7 shows a PET image acquired using ^{149}Tb-DOTANOC. Clinical trials using ^{212}Pb are also underway for HER2-expressing ovarian cancer treatments, therefore, a myriad of clinical studies are expected to follow these trials [43]

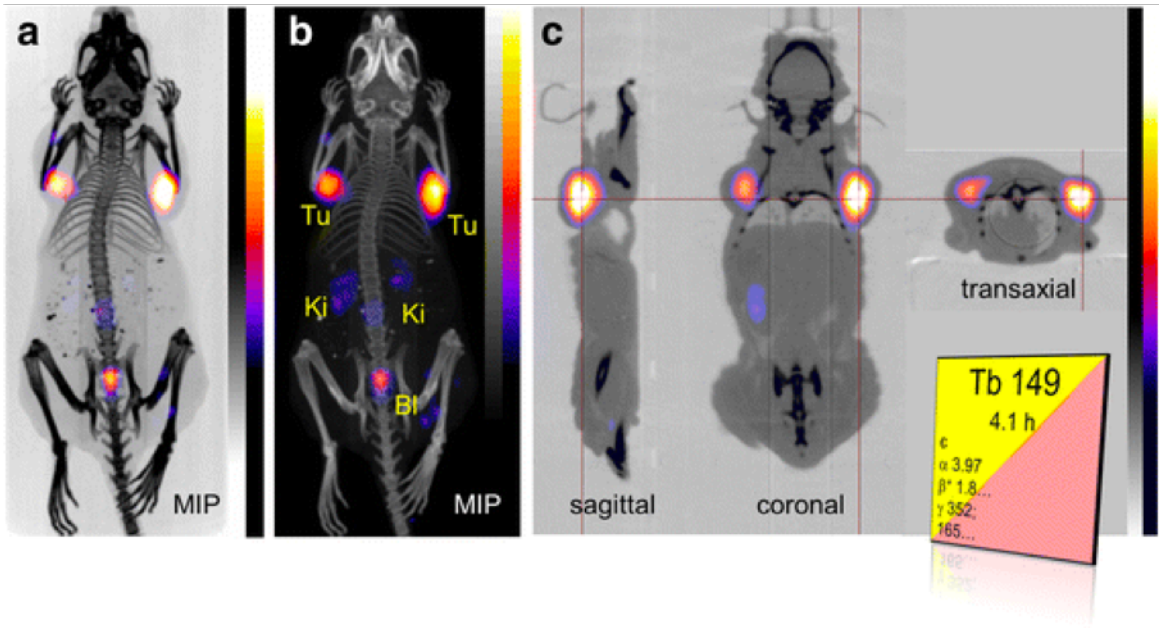

Figure 2.7: A ^{149}Tb-DOTANOC PET image is shown [6].

2.1.3 Alpha particle decay and interactions with matter

2.1.3.1 Alpha decay

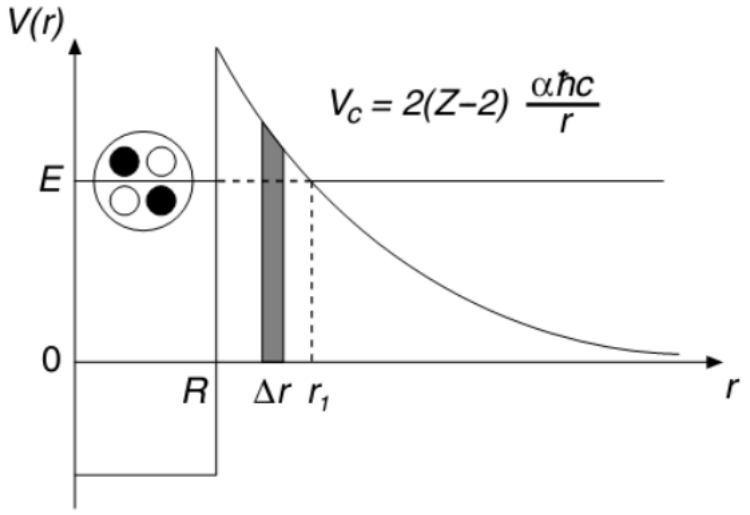

Figure 2.8: The potential energy of the alpha particle as a function of it's distance from the center of the daughter nucleus [7].

Alpha particle is a helium atom stripped of electrons with a mass number of 4 and an atomic number of 2. Alpha decay is a spontaneous process that typically occurs in heavy elements and can be denoted by:

$$ {}^{A}_{Z}X \rightarrow {}^{A-4}_{Z-2}X' + \alpha \tag{2.1} $$

where ${}^{A}_{Z}X$ is the parent atom and ${}^{A-4}_{Z-2}X'$ is the daughter atom, and α is the emitted alpha particle. Figure 2.8 shows the potential energy of the alpha particle based on it's separation from the daughter nucleus [7]. When the alpha particle is within the nucleus, the strong force attraction dominates creating a deep well of potential energy and a potential barrier. Since the strong nuclear force has a short range, it's impact is limited to when $r > R$ where R is the radius of the daughter nucleus. Outside the nucleus, the alpha particle experiences a Coulombic force that is proportional to $1/r^2$. Classical physics prohibits the alpha particles to escape the Coulombic barrier of 26 MeV; however, quantum mechanical tunneling yields a non-zero escape probability which allows the alpha particle to overcome the barrier.

Energy and momentum are conserved during alpha decay and can be written as:

Conservation of energy:

$$ m_X c^2 = m_{X'} c^2 + T_{X'} + m_\alpha c^2 + T_\alpha, \quad \text{where} \quad T_{X'} = \frac{1}{2} m_{X'} \nu_{X'}^2 \quad \text{and} \quad T_\alpha = \frac{1}{2} m_\alpha \nu_\alpha^2 \tag{2.2} $$

Conservation of momentum:

$$ m_\alpha \nu_\alpha = m_{X'} \nu_{X'} \tag{2.3} $$

where m_X is the mass of the parent nuclei, $m_{X'}$ is the mass of the daughter nuclei, m_α is the mass of the alpha particle, c is the speed of light, $T_{X'}$ is the kinetic energy of the daughter nuclei, T_α is the kinetic energy of the alpha particle, $\nu_{X'}$ is the velocity of the

daughter nuclei, and ν_α is the velocity of the alpha particles. The energy released during the alpha decay is shared between the alpha particle and the daughter nuclei and can be calculated by:

$$T_\alpha = \frac{m_{X'}}{m_{X'} + m_\alpha}\Big(T_\alpha + T_{X'}\Big) \quad \text{and} \quad T_{X'} = \frac{m_\alpha}{m_{X'} + m_\alpha}\Big(T_\alpha + T_{X'}\Big) \tag{2.4}$$

Since alpha particles tend to be significantly lighter than the daughter nuclei, majority of the released energy is converted into the kinetic energy of the alpha particle. The kinetic energy gained by the daughter nuclei is often sufficient to overcome the chemical bond between the radionuclide and the linked molecule leading to migration of the daughter from the parent molecule [45]. The migration of the daughter may pose problems such as inaccurate estimation of absorbed dose to tissue from any particles emitted by the daughter. However, the radiological range of the daughter nuclei is typically $< 1\mu m$ in tissue leading to local deposition of energy.

2.1.3.2 Alpha interactions with matter

Alpha particles interact with both the nucleus and the orbital electrons in a given media. The type of interactions can be classified as elastic versus inelastic depending on the conservation of the kinetic energy of the particles involved. The major cause of energy loss for alpha particles is Coulombic elastic collision losses that lead to dense ionization tracks in any media. Such interactions can involve either the nucleus or the orbital electrons with the electronic collisions being the dominant cause of energy loss. The collision losses in matter from charged particles is described by the collision stopping power and a simplified Bethe-Bloch formulation of this process is defined as:

$$S_{col} = 4\pi N_A r_e^2 m_e c^2 \frac{Z_2}{A_2}\frac{Z_1^2}{2\beta^2} ln \frac{2m_e c^2 \frac{\beta^2}{1-\beta^2}}{I} \tag{2.5}$$

where N_A is the Avogadro's number, r_e is the electronic radius, m_e is the electronic mass, Z_2 is the atomic number of the absorbing medium, A_2 is the mass number of the absorbing medium, Z_1 is the atomic number of the incoming particle, β is the relativistic velocity of the incoming particle, and I is the mean ionization energy of the medium. It is of note that the stopping powers are usually normalized by the physical density of the medium. Figure 2.9 shows the stopping power of water and air without a density normalization. It can be concluded that the energy loss in water is much greater when compared to air despite the $\frac{Z_2}{A_2}$ ratio being similar for the two materials. Therefore, the physical density of the material is a dominant parameter in terms of energy loss.

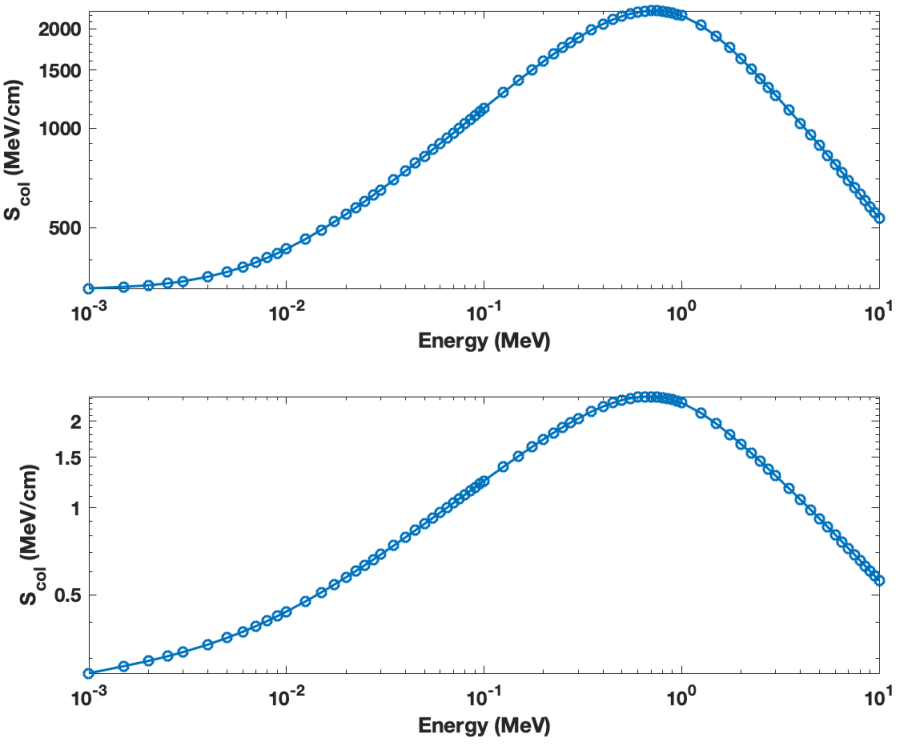

Figure 2.9: The stopping power of water and air is plotted as a function of alpha energy [8].

Another form of interaction of alpha particles with matter is Bremsstrahlung production through the radiative process. Unlike collision losses, the Bremsstrahlung process involves

interactions between the incoming alpha particles and the nucleus of the medium of interest. Similar to collision stopping power, the radiative energy losses from Bremsstrahlung production can be defined by the radiation stopping power. However, radiative losses in matter from heavy charged particles are often ignored due to the low radiation yield. The radiation power over a sphere is proportional to:

$$P_{rad} \propto \left(\frac{Z_1 Z_2}{m_1}\right)^2 \tag{2.6}$$

with m_1 being the mass of the incoming particle. It can be noted that the radiative losses will decrease as a function of $1/m_1^2$ and, therefore, heavy charged particles such as alpha particles will lead to a relatively small radiation cross-section. Similar to radiation yield, alpha particles also have a small cross-section for inelastic nuclear collisions, which lead to fragmentation of the absorber nucleus into smaller nuclei. Inelastic nuclear collisions are only significant near the end of the alpha particle track and must be considered when the alpha particle energy is < 1 MeV.

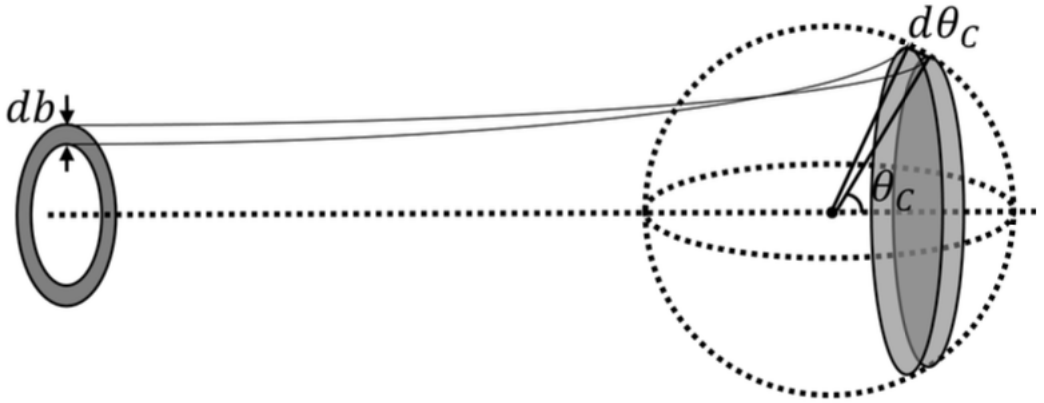

Figure 2.10: The differential scattering cross-sectional area is illustrated (from MP 501 notes).

Coulombic interactions of alpha particles lead to scattering in the absorbing media, which can deflect the direction of the alpha particles as they traverse matter. The scattering

cross-section is demonstrated by figure 2.10 and can be calculated as:

$$\frac{d\sigma}{d\Omega} = \left(\frac{Z_1 Z_2 e^2}{2\pi\epsilon_o \mu \nu_o^2}\right)^2 \frac{1}{16 sin^4(\frac{\theta_c}{2})} \tag{2.7}$$

where Ω is the differential solid-angle given by $d\Omega = 2\pi sin\theta_c d\theta_c$, ϵ_o is the vacuum permittivity, μ is the reduced mass of the incoming particle traveling with an initial velocity of ν_o in the center-of-mass frame, and θ_c is the scattering angle. The above equation is the Rutherford cross-section and is independent of the physical density of the medium of interest.

2.2 Dosimetry in TRT

2.2.1 Overview

During the initial clinical applications of TAT, dose escalation studies were used to estimate a suitable dose for maximum therapeutic gain. Clinical evidence of tumor remission and increased survival chance has been widely leveraged when prescribing a dose to a given patient [46]. The recommended "dose", units of Bq/kg, multiplied with the patient's body mass has previously been used to calculate the amount of activity to be injected into the patient's bloodstream [40]. The absorbed dose to organs can then be calculated using a pharmacokinetic model and the amount of uptake in a given compartment. It is important to realize that this requires an accurate knowledge of the activity distribution in the body as a function of time [47]. In the literature, the usage of absorbed dose to water/tissue has been greatly debated for TAT [48]. Instead, microdosimetry is recommended to calculate energy deposited in cells due to a wide variation of energy imparted in cells from alpha particle irradiation. Thus, both microdosimetric quantities

such as lineal energy or specific energy and absorbed dose have been utilized as energy deposition metrics in the literature.

2.2.2 Internal dosimetry

In both imaging and therapy disciplines, internal dosimetry is often used to estimate absorbed dose to organs by employing a tissue-compartment model and pharmacokinetic information. This is especially clinically significant in TRT where an estimate of the radiopharmaceutical uptake in tumor and other organs is required before a high dose is injected into patients. The major internal dosimetry formalism is referred to as medical internal radiation dose (MIRD) issued by committee of the society of nuclear medicine [47]. Once a known volume of activity is injected into a patient or a phantom, the absorbed dose rate at any given time, t, is given by:

$$\dot{D}(r_T, t) = \sum_{r_S} A(r_S, t) S(r_T \leftarrow r_S, t), \tag{2.8}$$

where A(r_s, t) is the time-dependent activity in the source tissue, r_S, and S($r_T \leftarrow r_S$, t) is the radionuclide-specific coefficient that provides the mean absorbed dose rate to target tissue, r_T, at time t due to per unit activity present in the source tissue [47]. The S-values are calculated using whole-body computational phantoms for a given age, sex, total body mass, and height. The MIRD S-value formalism assumes a uniform activity distribution in a given compartment/organ and neglects patient-specific dosimetry [47]. In the case where the source organ and the target organ are different, the absorbed dose to target is referred to as "cross-talk". Otherwise, the absorbed dose to target is referred to as "self-dose". If a total absorbed dose to target organs over a time period, T_D, is

desired, equation 2.8 can be written as:

$$D(r_T, T_D) = \sum_{r_S} \int_0^{T_D} A(r_S, t) S(r_T \leftarrow r_S, t) dt. \tag{2.9}$$

The quantity S, also referred to as S-value, can be further broken down into several sub-quantities:

$$S(r_T \leftarrow r_S, t) = \frac{1}{M(r_T, t)} \sum_i E_i Y_i \phi(r_T \leftarrow r_S, E_i, t) \tag{2.10}$$

where M(r_T, t) is the time-dependent mass of the target organ, E_i is the mean energy of the ith nuclear transition, Y_i is the number of ith nuclear transitions per nuclear transformation, and $\phi(r_T \leftarrow r_S, E_i, t)$ is the absorbed fraction which gives the fraction of radiation energy E_i emitted within the source tissue at time t that is absorbed in the target tissue [47]. A weighting factor is used to accurately assess the biological outcomes due to irradiation to account for the different LET of different particle types. This is defined as equivalent dose and can be calculated by:

$$H(r_T, T_D) = \sum_R w_R D_R(r_T, T_D) \tag{2.11}$$

where w_R is the radiation weighting factor for the radiation type R [47]. ICRP recommended weighting factors are 1.0 for photons, electrons, positrons, and β particles, and 20 for α particles [49]. Thus, irradiation with alpha particles tends to create more biological damage than other particles. Several commercial dosimetry software utilize the MIRD formalism and aim to calculate absorbed dose to tissue. MIRDOSE3 and OLINDA/EXM are examples of such software [40].

The time-dependent activity in every compartment can be obtained by several different

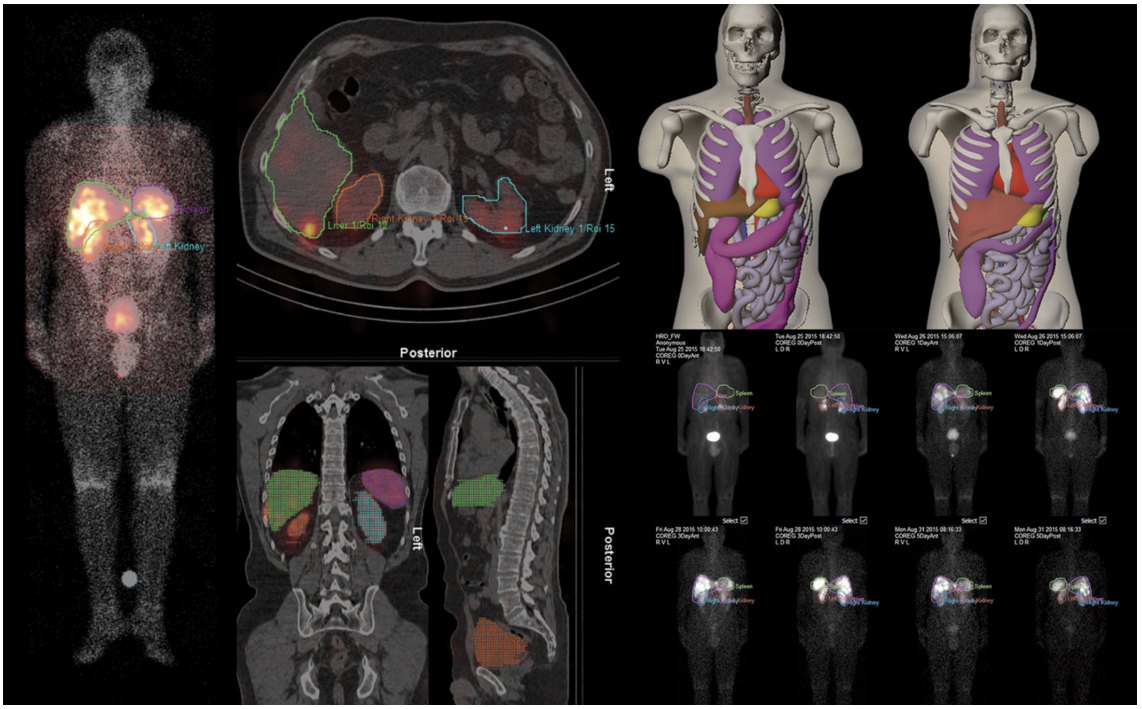

Figure 2.11: An example of a dose distribution calculated using OLINDA software.

methods. A pharmacokinetic model can be employed and solved using a set of first-order coupled differential equations for each compartment. Alternatively, quantitative imaging such as single photon emission computed tomography (SPECT) or PET can be used to determine the 3D activity distribution inside the body at a given time. A typical workflow for patient-specific TAT dosimetry includes measurement of radioactivity in the solution using a dose calibrator, injection into the patient's bloodstream, multiple time point *in vivo* activity determination using SPECT, fusion of the 3D time-integrated activity map with the patient's CT scan, and calculation of absorbed dose in a patient-specific voxelized geometry using computational methods such as dose point kernels or Monte Carlo simulations [50][51][52]. Using a voxelized geometry, absorbed dose to voxels can be calculated using the equations given above. In the described workflow, multiple time point imaging poses the most significant clinical burden due to limited imaging scanner time [53].

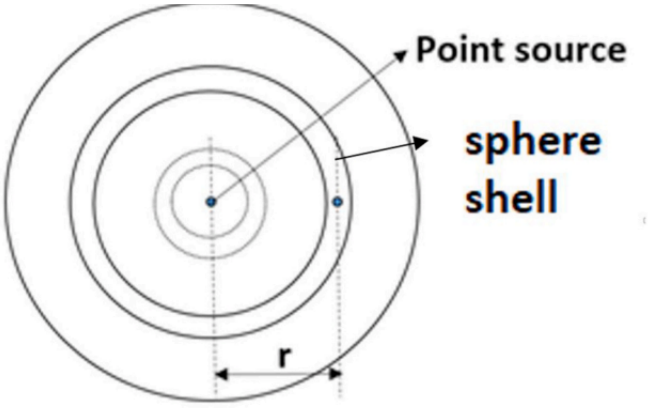

Figure 2.12: A schematic of the geometry used in DPK calculation is shown [9]

Conversion of patient-specific time-integrated activity distribution to absorbed dose distribution can be performed using either dose point kernels (DPK) or full MC simulations. Utilization of DPK to perform patient-specific dosimetry allows for reasonable computational cost [54]. Time-integrated activity distribution in a patient can be convolved with the precomputed radionuclide-specific DPK to acquire dose distributions in a voxelized geometry. Figure 2.12 shows a voxelized spherical geometry widely used in DPK generation [9]. Absorbed dose to medium is scored, using either analytical methods or MC methods, in spherical shell at various radial distances from a point source. The source atoms or molecules distributed inside a patient can be individually represented by point sources emanating radiation isotropically, which is the underlying assumption of using a point source. DPKs generated for various radionuclides in a homogeneous water phantom using MC methods were previously compiled by Graves et al., including several alpha-emitters [55]. Since tissue heterogeneity was not addressed in the work, Tiwari et al. investigated the impact of tissue types on DPKs for beta-emitting radionuclides and found that tissue-specific density-based scaling is sufficient for accurate dosimetry [56]. However, a comparison between the scaled DPK and full MC simulation has yet to be performed to fully assess the accuracy of the scaling method. Due to their limited range in tissue, alpha particles have been neglected from most DPK studies and local energy

deposition is considered because of the large voxel size utilized in DPK-based dosimetry [55]. However, alpha DPKs can be utilized similarly to beta or gamma DPKs. In our previous work, the impact of the density-based scaling on DPKs was evaluated using the GEANT4 MC code [57]. A 5% accuracy was noted if a density-based scaling is performed, except near the Bragg peak regions.

A full MC simulation using patient-specific time-integrated activity distribution and CT scans leads to the most accurate way of performing personalized dosimetry. Using the CT image, a correlation can be establish to convert the Hounsfield Units (HU) to material composition and mass density required by the MC codes [58]. With the use of nuclear decay data, radiation emission from radionuclides can be fully transported throughout the patient and absorbed dose can be tallied in a voxelized geometry [59] [60] [61]. However, these simulations require significant computational resources. Otherwise, the run time can be up to several days for a single patient. A MC conversion of activity to absorbed dose fully considers tissue heterogeneity and has been previously proposed by numerous studies [62] [10] [63] [64] [65] [66]. Both general-purpose MC codes, such as GEANT4 and MCNP, and dedicated commercial codes have been successfully developed to perform patient-specific internal dosimetry. Figure 2.13 shows a full workflow of one such tool i.e. RAPID [10]. It's worth noting that the dosimetric validation of these MC-based software is often performed computationally.

It is noteworthy that the uncertainties involved in the absorbed dose calculation can be easily over 15 % using the methods described above [67]. Finocchiaro et al. previously demonstrated that the uncertainty in the absorbed dose is inversely proportional to the tumor size [67]. The total uncertainty was found to be dominated by the tumor delineation and limited spatial resolution of the imaging systems.

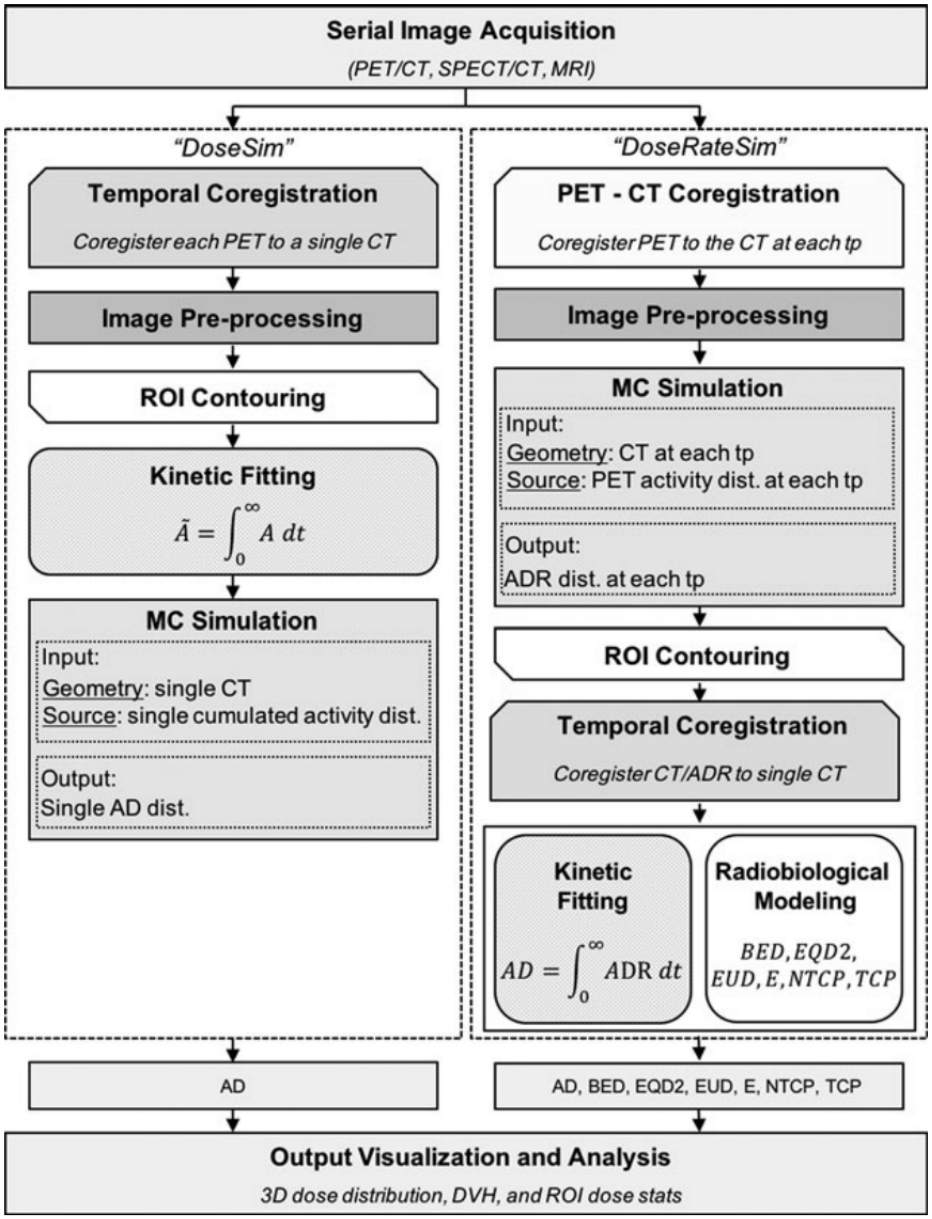

Figure 2.13: A dosimetry framework for total absorbed dose and dose rate in a patient-specific manner previously proposed by Besemer et al. [10]

2.2.3 Microdosimetry

The concept of absorbed dose is confined to a large number of low-LET charged particles depositing energy in a finite volume. Whereas, due to a very short range of alpha particles, the distance traversed by an alpha particle is on the order of micrometers. Alpha particles are considered to have a high LET compared to beta or gamma radiation. Therefore, statistical variations and the path taken by the alpha particle in the cell becomes critical. Due to the stochastic nature of this problem, microdosimetrical methods are employed to calculate energy deposited in a small target such as a human cell [46]. Herald H. Rossi studied microdosimetry and published the first framework describing microdosimetry calculations [11].

In order to classify charged particles based on the amount of energy deposited "locally", the quantity LET was defined as:

$$LET = \frac{dE_L}{dl}, \tag{2.12}$$

where dE_L is the average energy locally imparted to the medium by a charged particle of a specific energy in traversing a distance of dl [11]. The local aspect of LET manifests in the form of an energy cut-off above which the losses are no longer considered local.

In lieu of absorbed dose, term specific energy is used which is defined as:

$$z = \frac{\epsilon}{m} \tag{2.13}$$

where ϵ is the energy deposited in a material with mass m [48]. To calculate the amount of energy deposited in a site of mass m, a probability distribution of z, defined as f(z), is

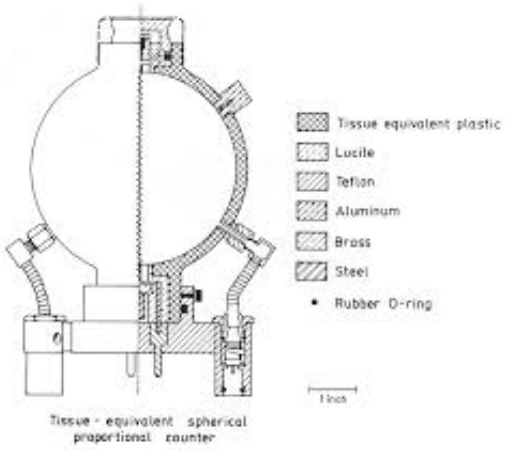

Figure 2.14: A schematic of a Rossi chamber is shown [11].

required. However, this task poses many challenges due to the limitation of the apparatus at hand. Instead, a single-hit distribution, $f_1(z)$, is measured by using a Rossi chamber [11]. A Rossi chamber is a tissue-equivalent proportional counter that derives single-hit specific energy distribution by measuring pulse height spectra in the chamber. However, this apparatus can only be utilized for a target with a spherical geometry. Figure 2.14 shows a schematic of a Rossi chamber. Assuming the number of energy deposition events is randomly distributed, its distribution can be estimated by a Poisson distribution. Therefore, the distribution of number of absorption events, n, at dose D can be given by:

$$f(n) = e^{-D/\bar{z}_F} \sum_n \frac{(-D/\bar{z}_F)^n}{n!}, \tag{2.14}$$

where $\bar{z}_F$ is the mean number of absorbed dose events given by the first moment of $f_1(z)$ probability distribution:

$$\bar{z}_F = \int_0^\infty z.f_1(z)dz \tag{2.15}$$

Under the assumption of Poisson statistics, the probability distribution f(z) can then be calculated by:

$$f(z) = \sum_n f(n) f_n(z) = e^{-D/\bar{z}_F} \sum_n \frac{(-D/\bar{z}_F)^n}{n!} f_n(z) \tag{2.16}$$

Since z is a stochastic quantity with a probability distribution, $f_n(z)$ can be given by:

$$f_n(z) = \int_0^z f_{n-1}(s) f_1(z-s) ds \tag{2.17}$$

The above equation describes a convolution operation of $f_1(z)$ by itself [48]. This comes from the law of total probability. Therefore, an iterative convolution can be used to calculate the specific energy distribution f(z) for multiple-hit events. This provides a path to calculate energy imparted in a small spherical target by a radioactive particle.

Analytical methods or Monte Carlo (MC) methods can be used to simulate microdosimetric quantities [40] [68] [69]. Bertolet et al. utilized MC methods to simulate direct damage to different DNA structures using monoenergetic alpha particles [39]. The TOPAS-nBio MC code used by Bertolet et al. is a GEANT4-DNA based code and simulates track structures at a micro and nano scale along with first physicochemical and chemical reactions [70]. In their work, a strong linear correlation was found between the total number of DNA strand breaks per track and fluence-averaged lineal and specific energy. Addionally, the yield of double-strand breaks linearly correlated with dose-averaged lineal and specific energy. While the work of Bertolet et al. establishes a microdosimetric formalism for standard sub-cellular volumes, a study by De Cunha et al. seeked to perform patient-specific 2D microdosimetry for gamma-emitting radionuclides [71]. The fundamental concept behind this study can be applied to alpha-emitting radionuclides.

2.3 The need for a primary standard for absorbed dose

2.3.1 Motivation

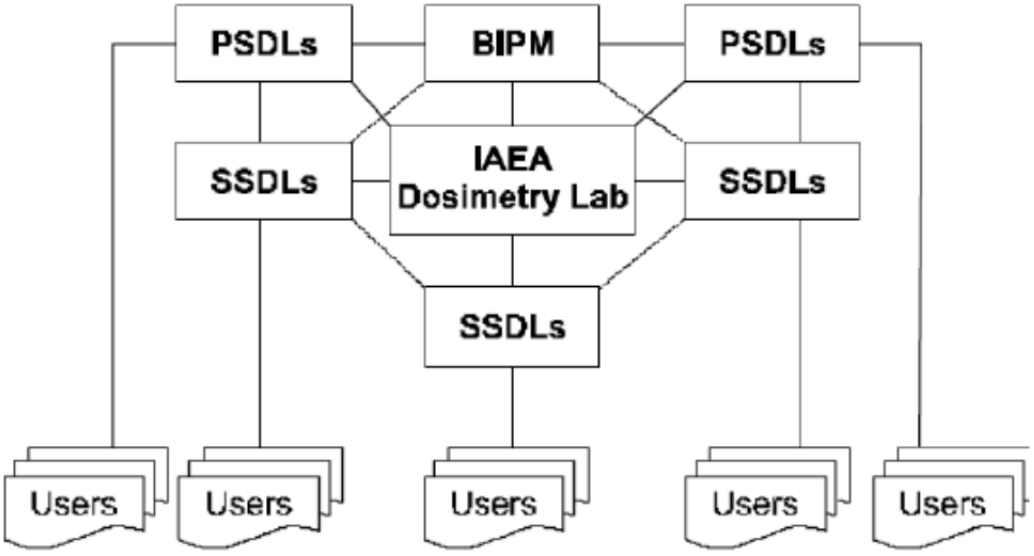

Figure 2.15: A traceability flowchart is shown for absorbed dose to water (from MP 501 lectures).

The usage of traceable quantities is crucial in radiation oncology [72]. It is pertinent that the fundamental quantities such as absorbed dose or air kerma are standardized in order to directly compare clinical treatment outcomes between different institutions or other entities. Furthermore, without traceability, any correlation found between the quantity of interest such as absorbed dose and clinical outcome metrics such as tumor control probability would be meaningless. Figure 2.15 shows an example of a traceability chain for absorbed dose to water. Therefore, the absorbed dose to water delivered to any patient is directly traceable to primary and secondary labs. In order to establish a traceability chain, a primary standard is required that can directly determine the quantity of interest without requiring a calibration. Once the quantity of interest has been

realized, the measurement can be transferred to secondary standard labs via a transfer standard. Finally, the secondary labs can calibrate the end user's equipment and determine a traceable calibration coefficient. Alternatively, the primary standard lab can directly calibrate the end user's equipment. In the united states, the National Institute of Standards and Technology (NIST) is considered a primary standards lab; whereas, the University of Wisconsin Accredited Dosimetry Calibration Laboratory (UWADCL) is an example of a secondary standards lab.

Traceability for TRT treatments currently only exists for radioactivity [73]. A liquid scintillation counter (LSC) is used as a primary standard by NIST to realize radioactivity [74]. The unit of becquerel is then transferred to the secondary standards lab and the clinics using either a dose calibrator or a scintillator detector. However, one simply cannot correlate the TRT treatment outcomes with the unit of becquerel. Radioactivity units contain no information regarding the energy deposited in and near the tumor volume, which is a more accurate predictor of treatment success. It can be argued that knowing the radioactivity distribution of the radiopharmaceutical inside the patient's body can be converted to absorbed dose using the methods described in 2.2.2, but such a calculation of absorbed dose is only indirectly traceable. Any contaminant activity in the TRT radiopharmaceutical can further exacerbate any link between absorbed dose and activity. Furthermore, the conversion of radioactivity to absorbed dose is a highly non-standard process since a myriad of algorithms and software exist to perform such a conversion. Most of these software are not experimentally validated and are highly dependent on the transport parameters used computationally. MC methods are generally considered to be most accurate when calculating absorbed dose from radioactivity; however, the underlying transport algorithms and cross-section databases vary greatly between codes. The variability in MC transport physics can weaken the link between absorbed dose and activity and necessitates a direct measurement of absorbed dose. Additionally, absorbed

dose calculation using MC relies on nuclear decay databases, adding another source of variability in the calculation process.

Figure 2.16: The proposed workflow for TRT treatments establishes *ex vivo* absorbed dose traceability.

A non-invasive measurement of absorbed dose after the injection of the radionuclide inside the patient's body, i.e. *in vivo* measurements, is extremely challenging. Therefore, a traceability to absorbed dose can be established using external dosimetry methods. By realizing the absorbed dose to water from alpha emitters using a primary standard, a calibration coefficient in the units of Gy/s/Bq can be established for each radiopharmaceutical. Whether such a calibration needs to be performed for each TRT treatment remains to be resolved; therefore, an investigation is required to study the variation in the calibration coefficient for different radiopharmaceuticals, radionuclides, and even batch of a given radiopharmaceutical. Additionally, any commercial and non-commercial softwares attempting to convert radioactivity to absorbed dose can be experimentally validated using the primary standard. This method is not limited to TAT treatments only and can be applied towards all TRT treatments. It also allows for a standardization in the field of TRT in terms of absorbed dose calculation.

2.3.2 Ionization chamber as a primary standard

A calorimeter, Fricke ferrous, or an ionization chamber can be considered suitable candidates for a primary standard for absorbed dose to water from unsealed radionuclides. Calorimeters are difficult to manufacture and require heat defect corrections that are little understood for high LET particles [75]. Fricke ferrous dosimeters are chemical in nature

and require extensive preparations before use. They are also sensitive to chemical impurities and to the readout procedure used [76]. Ionization chambers (ICs), on the other hand, are well-studied and widely used in radiation metrology. ICs with known volumes already serve as primary standards for low and medium energy x-ray beams as well as for beta particles [16] [77] [78] [79] [80]. ICs directly measure the radiation exposure, X, generated by a radiation source:

$$X = \frac{Q}{m} \tag{2.18}$$

where Q is the charge liberated in the sensitive volume of the IC with a mass m. The radiation exposure can then be converted to kinetic energy released per unit mass (KERMA), and consequently to absorbed dose to medium using a suitable cavity theory:

$$D_{medium} \overset{\text{under cavity theory conditions}}{\approx} X\left(\frac{W}{e}\right)_{det}\left(\frac{S_{col}}{\rho}\right)_{det}^{medium} \tag{2.19}$$

where D_{med} is absorbed dose to medium, $\frac{W}{e}$ is the average energy required to generate an ion electron pair in the detector's sensitive volume's material, and $\left(\frac{S_{col}}{\rho}\right)_{det}^{medium}$ are the mean mass collision stopping power ratio of medium of interest's material to detector's sensitive volume's material [81] [82]. In order for an ionization chamber to behave as a primary standard, the mass of the sensitive volume must be known accurately. Otherwise, ICs can be calibrated and used as transfer standards. Sealed ICs may leak over time so vented ICs are considered suitable for absolute dosimetry if the volume of the sensitive region is well-known. Air-filled ion chambers are desirable due to the low density of air that leads to minimal charged particle fluence perturbation. Any changes in the mass of the air due to non-standard temperature and pressure can be corrected using the ideal gas law. While there are many types of ICs available, most of them have an entrance window or walls that the radiation must pass through before reaching the sensitive volume. The presence of an entrance window or wall poses a major limitation for absorbed dose

measurement due to the perturbation of the fluence and violation of the ideal cavity theory conditions. Therefore, a thin-window or windowless IC is desired as a primary standard. Extrapolation chambers (ECs) are parallel-plate ionization chambers with a variable plate separation and are appropriate for surface absorbed dose measurements [83]. Measurements taken with different electrode separation, therefore different mass, are used to calculate the absorbed dose rate at a region of interest.

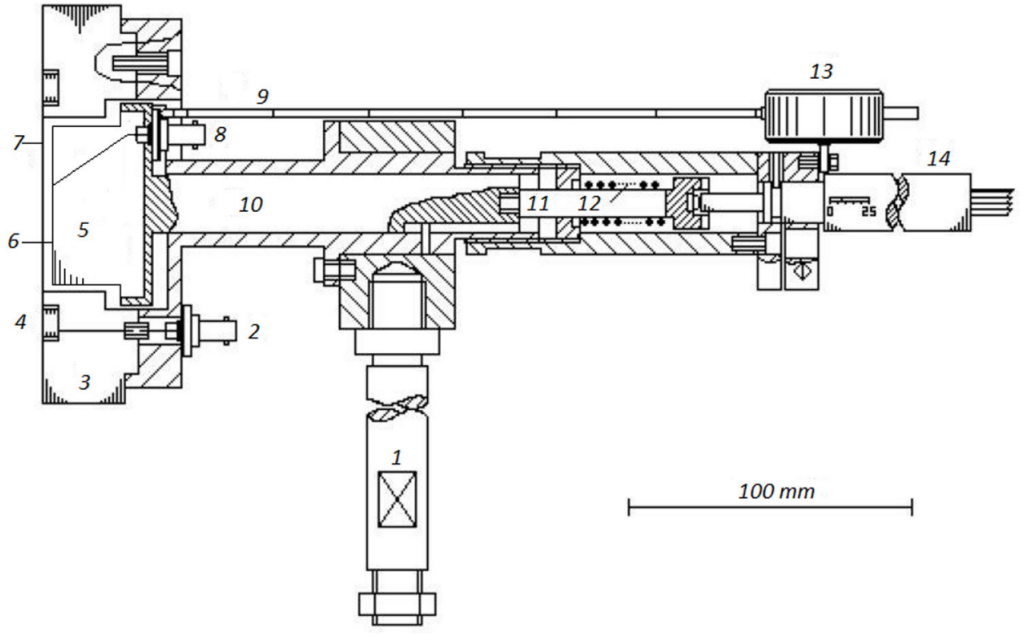

Figure 2.17: Sectional view of the PTW type 23392 extrapolation chamber used in the work of Billas et al. [12] The entrance window and collector/guard electrodes are denoted by numbers 7 and 6, respectively.

Billas et al. at the National Physics Laboratory (NPL) first proposed the use of a thin window extrapolation chamber to measure absorbed dose from unsealed radionuclides [12]. Figure 2.17 shows the EC used in their work. The quantity of interest for their work was absorbed dose at the center of ^{90}YCl, a beta-emitting radionuclide solution. Although the work of Billas et al. was the first study proposing a primary standard for absorbed dose from unsealed radionuclides, there were several limitations observed in their study such as the inclusion of energy released via Bremsstrahlung in the absorbed dose which

would otherwise be carried away and deposited non-locally and Monte Carlo correction factors with magnitudes up to 260%. Nonetheless, for the first time, a primary standard for absorbed dose to water from unsealed beta emitting radionuclide was developed. No study currently exists proposing a primary standard for absorbed dose from alpha sources.

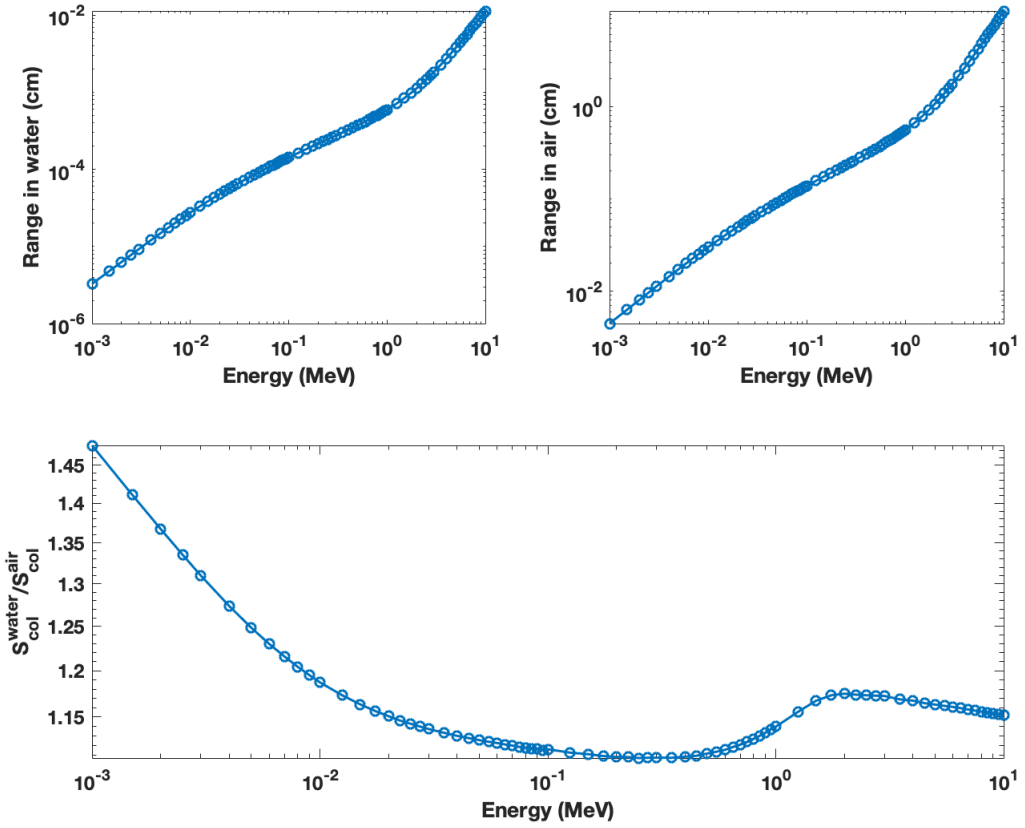

Figure 2.18: Top: Range of alpha particles in water and air as a function of energy. Bottom: The water to air ratio of mass collision stopping power as a function of energy.

The energy range of alpha particles used in TAT is 5-9 MeV, which corresponds to a range of 40-70 μm and 3.6-10.8 cm in water and air, respectively. Figure 2.18 shows the range, calculated with a continuous-slowing-down-approximation (CSDA), and the mass stopping power ratio of water to air for alpha particles in both water and air as a function of energy [8]. The low density of air allows for much longer track-length of alpha particles in the detector, relative to water, which makes in-air exposure a suitable

measurable quantity. Figure 2.19 demonstrates a typical integral depth dose (IDD) curve for alpha particles. The IDD curve for heavy charged particles can be decomposed into several regions. The build-up region allows establishment of delta-ray equilibrium until the absorbed dose is relatively constant, which is referred to as the plateau region. As charged particles lose energy, the stopping power increases leading to increase in absorbed dose with the increase in depth. Near the end of their respective range, the stopping power of charged particles increases drastically leading to a Bragg peak. Distally to the Bragg peak, a fragmentation tail is observed due to energy deposited by secondary charged particles emitted via nuclear interactions with the media. The plateau region is well-suited for reference dosimetry due to delta-ray equilibrium and smaller dose gradients. In external beam proton and heavy ion therapy, absolute dosimetry is performed in this region using ionization chambers [84].

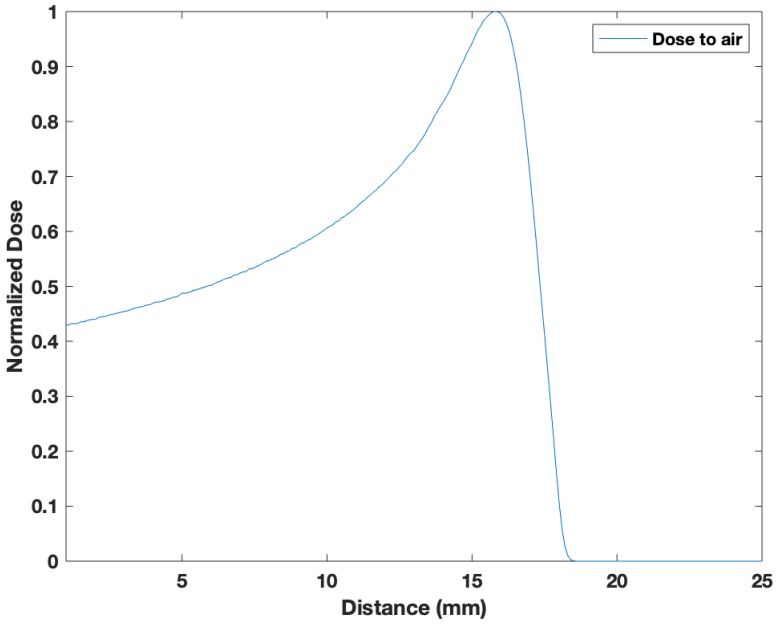

Figure 2.19: The integral depth dose (IDD) curve of a 5 MeV alpha particle in air.

A volumetric source is undesirable due to significant self-absorption and attenuation of alpha particles before they escape the boundaries of the source. Figure 2.20 quantifies

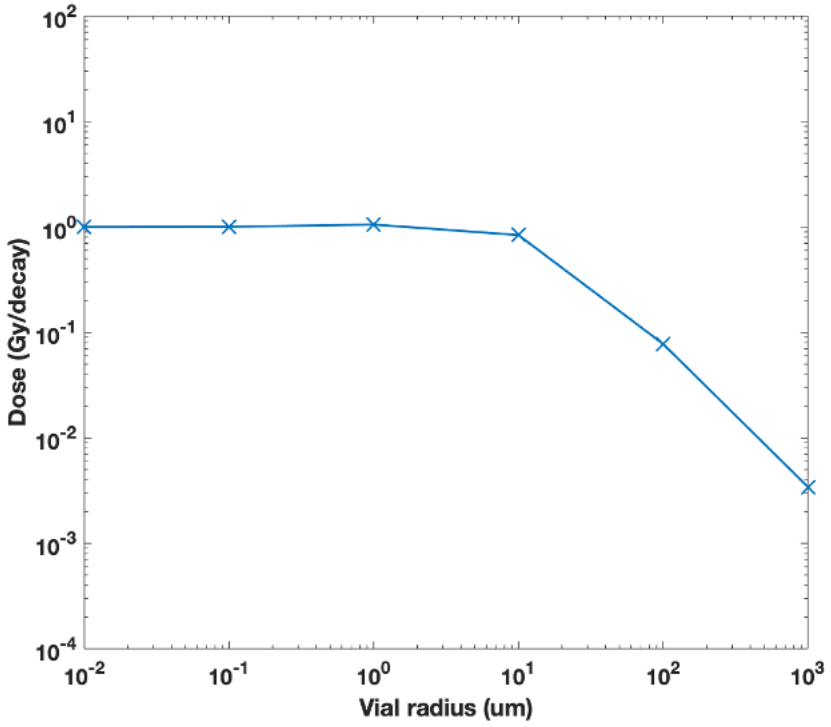

Figure 2.20: The absorbed dose per Bq calibration coefficient is shown for various radii of vials filled with homogeneous ^{210}Po solution emitting 5.3 MeV alphas.

the underestimation of absorbed dose per Bq calibration coefficient using Monte Carlo calculations. A cylindrical homogeneous ^{210}Po volumetric source was simulated of 1 cm length and variable radius and absorbed dose was scored in a cylindrical shell surrounding the source. For a vial with 1 mm radius, the absorbed dose per unit activity was calculated to be only 0.3 % of the absorbed dose per unit activity when the radius was 0.1 μm. Therefore, a point source was considered to desirable for absorbed dose measurements. Ideally, measurement of absorbed dose from a point-like source would be performed due to it's similarity with dose calculation methods such as dose point kernels, however, fabrication of such a source is prohibitively challenging. Instead, a thin-film circular source can be fabricated and used in lieu of a point source, and a Monte Carlo correction factor can be applied to correct for the finite radius and thickness of the source.

Figure 2.21 illustrates the cylindrical geometrical setup chosen in this work for the primary

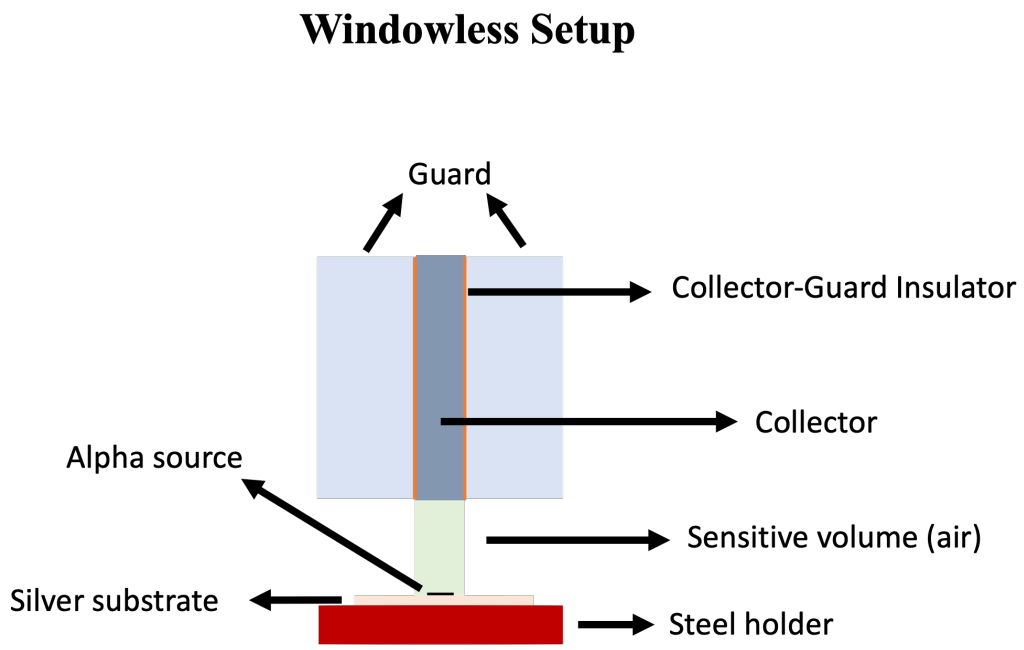

Figure 2.21: A schematic of the extrapolation chamber apparatus is shown.

standard of absorbed dose from alpha-emitting radionuclides. A windowless extrapolation chamber was proposed since any detector with an entrance window can significantly attenuate the incoming alpha particles [85]. By employing a thin film alpha source on a metal substrate, an air cavity can be created by applying an electric field across the two electrode surfaces. By varying the air gap between the two electrodes, absorbed dose to air can be measured at an arbitrary radial distance from the source. Most clinically-relevant TAT sources, such as ^{223}Ra or ^{225}Ac, emit mixed charged particles such as alphas and betas. In order to evaluate the proposed extrapolation chamber in the context of alpha dosimetry, a pure alpha emitter is required to fully characterize the dosimetric properties of the extrapolation chamber. Therefore, a ^{210}Po source was considered suitable for initial characterization of the apparatus since it emits 5.3 MeV alpha particles with an intensity of 100%.

2.3.3 Dosimetric formalism for the cylindrical shell method

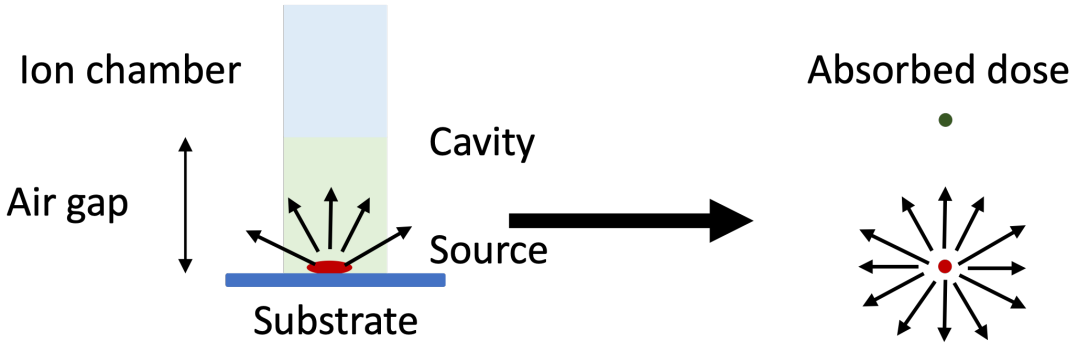

Figure 2.22: The measurable dosimetric quantity and the quantity of interest are shown.

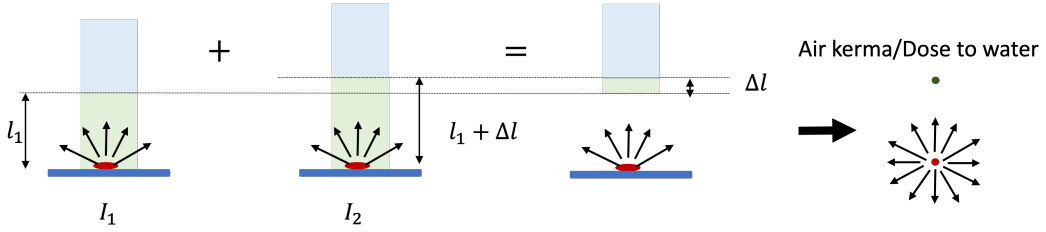

Figure 2.23: The conversion of the measurable quantity to the quantity of interest is illustrated. The quantity I is defined to be the ionization current at the air gap l.

In-air exposure, and therefore absorbed dose to air, can be measured using equation 2.18 by measuring the ionization current at a known air gap. However, the absorbed dose at an arbitrary radial distance from the source is the quantity of interest in this work, as shown in figure 2.22. By varying the air gap between the source electrode and the collecting electrode, the change in energy deposited can be measured as a consequence of change in the mass of the air cavity. Therefore, as shown in figure 2.23, absorbed dose to air in a cylindrical shell can be measured by measuring the change in ionization current due to the change in air gap from l to $l + \Delta l$. Consequently, a series of Monte Carlo-based correction factor can be applied to calculate absorbed dose to air/water. It is noteworthy that the dosimetric formalism described in this section was derived as a part of this dissertation. The detectors used in this work had variable plate separations but weren't used as extrapolation chambers for this formalism since the absorbed dose

measured using the two air gap method at each l distance from the source was considered to be unique. The absorbed dose to air at a point some arbitrary distance, l, away from the source can be calculated by:

$$\dot{D}_{air}(l) = \frac{1}{A_o}\left(\frac{\partial E}{\partial m}\right)\Pi_{i=0}^{n} k_i = \frac{1}{A_o}\frac{\left(\frac{\bar{W}}{e}\right)_{air}}{\rho_o A_{eff}}\frac{\Delta I}{\Delta l}\left(k_{pol}k_{recom}k_{TP}k_{elec}\right)\left(k_{point}k_{backscatter}k_{inv}k_{cav}\right) \tag{2.20}$$

where A_o is the activity of the radionuclide of interest, E is the energy deposited in the cavity, m is the mass of the cavity, $\left(\frac{\bar{W}}{e}\right)_{air}$ is the mean energy required to liberate an ion pair in dry air, ρ_o is the physical density of air at standard temperature and pressure, A_{eff} is the effective cross-sectional area of the cylindrical air cavity, I is the ionization current, l is the air gap between the collector and source surfaces, k_i is the ith correction factor. The first series of the correction factors in equation 2.20 are related to ion chambers in general. k_{pol} is the polarity correction that corrects for the differences in the signal due to the polarity of the applied voltage, k_{recom} is the recombination correction that accounts for the signal lost due to the recombination of the liberated electrons with ions in the cavity, k_{TP} is the temperature and pressure correction factor that accounts for the difference in the mass of the cavity due to non-standard temperature and pressure of the air, and k_{elec} is the electrometer correction factor that converts the displayed current value to a traceable current value. The second set of correction factors are specifically-related to dosimetry of unsealed radionuclides where k_{point} corrects for the finite 2D activity distribution of the thin-film source to allow measurement from a point-like source, $k_{backscatter}$ accounts for the difference in backscatter between the medium surrounding the air-cavity and air, k_{inv} corrects for the off-axis fluence fall-off due to the divergence of the particle field, and k_{cav} accounts for the fluence perturbation due to the finite size of the cavity. In this work, the

k_{inv} and k_{cav} correction factors are combined together to ease the calculation process. It is of note that the self-absorption of the source is considered negligible in this formalism.

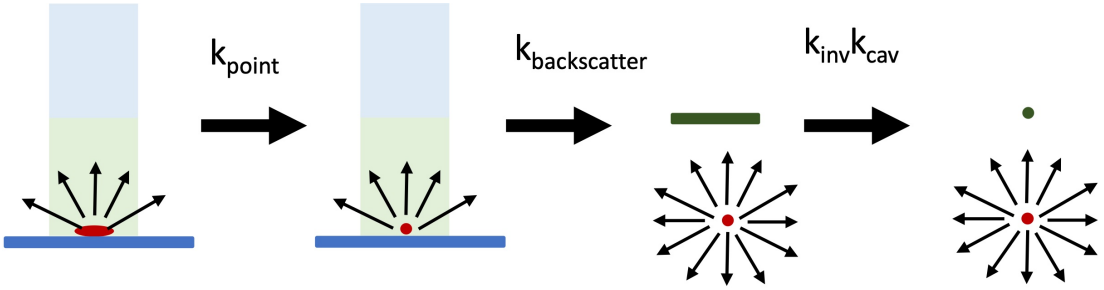

Figure 2.24: A series of Monte Carlo (MC)-based correction factors are shown that allow conversion of the measured quantities to the quantities of interest.

Since fabrication of a point source is challenging, a thin-film planar source of negligible self-absorption was proposed to be employed in this work. A MC correction factor that accounts for the finite spatial emission distribution of the source can be calculation by:

$$k_{point} = \frac{D_{cavity,point}}{D_{cavity,planar2D}} \tag{2.21}$$

where $D_{cavity,point}$ is the absorbed dose to the air cavity and $D_{cavity,planar2D}$ is the absorbed dose to the same cavity using the real 2D emission profile of the source. While simulating a point source using MC simulations is trivial, a custom source must be implemented to simulate the 2D spatial distribution of a given radionuclide. For such a task, unlaminated radiochromic films can be utilized as previously proposed by Lee et al. [86]. Relative cross-sectional fluence distribution can be measured using unlaminated EBT3 films and the fluence map can be simulated using MC.

The presence of the detector and the substrate on both flat ends of the cylindrical air cavity induces different backscatter conditions than in free air. Therefore, a correction

factor can be calculated to account for these different scatter conditions:

$$k_{backscatter} = \frac{D_{cavity,point,air}}{D_{cavity,point,det,substrate}} \tag{2.22}$$

where $D_{cavity,point,air}$ is the absorbed dose to cavity from a point source without the presence of the substrate or the detector and $D_{cavity,point,det,substrate}$ is the absorbed dose to air from a point source to the same cylindrical cavity with the presence of the substrate and the detector. In order to minimize the backscatter correction factor, the detector and the substrate must be constructed from air-equivalent materials. Air-equivalent conductive plastics can be used as electrodes for this purpose. Since alpha particles are considered heavy charged particles, their path in matter is relatively unobstructed as they traverse along a direction. Therefore, the backscatter correction is expected to be smaller for alpha particles than for betas.

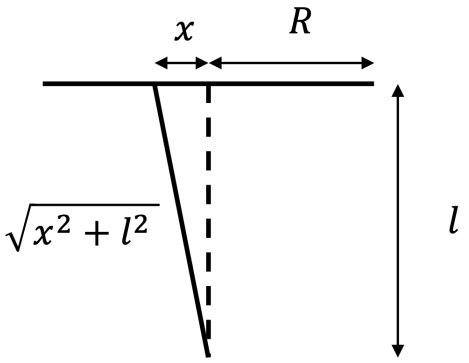

Figure 2.25: The fall-off in fluence due to the inverse-square effect and the finite radius of the detector is shown. R is the radius of the air cavity and l is the air gap between the collector and source.

Figure 2.25 illustrates the off-axis drop in fluence in a cylindrical air cavity with a finite radius. The analytical form of the inverse-square correction factor can be given by:

$$k_{inv} = \frac{2\pi \int_0^R x dx}{2\pi \int_0^R x \frac{l^2}{l^2+x^2} dx} = \frac{R^2}{l^2 ln(l^2 + x^2)|_0^R} \tag{2.23}$$

where R is the radius of the air cavity and l is the air gap between the collector and source. The above equation doesn't perfectly describe the fluence drop off from an alpha source due to the change in the direction of the alpha particles following scatter events and disregards the delta-rays that might lead to a deviation of the fluence fall-off from an inverse-square function. Additionally, the alpha particles that traverse a longer distance in the cavity lose more energy before reaching the cavity compared to the particles that travel closer to the central axis. This effect is accounted in the k_{cav} correction factor. Thus, the k_{inv} correction factor is coupled with the k_{cav} correction factor and can be calculated by:

$$k_{inv}k_{cav} = \frac{D_{cube}}{D_{cyl,point,air}} \tag{2.24}$$

where D_{cube} is the absorbed dose to air from a point source scored in a infinitesimally-small cube made of air without the presence of the detector and the substrate and $D_{cyl,point,air}$ is the absorbed dose to air to a cylindrical shell of Δl thickness $l_1 + \frac{\Delta l}{2}$ away from a point source without the presence of the substrate or the detector. A small cube length when scoring D_{cube} is desired to better approximate point dose; however, such a cube requires a large number of MC histories which can require significant computational time. In this work, the definition of a infinitesimally-small cube is defined such that the length of the cube is at least a factor of 10 smaller than the radial distance from the source. This definition was motivated by previous works in brachytherapy that use a 1 mm TLD cube at 1 cm radial distance from the source to measure or calculate absorbed dose [87] [88].

The described dosimetric formalism in equation 2.20 realizes absorbed dose to air from a point-like radionuclide. However, absorbed dose to water is a more relevant quantity in dosimetry due to water's similarity to tissue. Therefore, the calculated absorbed dose to

air, $\dot{D}_{air}$, can be converted to absorbed dose to water by:

$$\dot{D}_{water} = \dot{D}_{air}\left(\frac{S_{col}}{\rho}\right)_{air}^{water} k_{atten,scatter} k_{inv} \tag{2.25}$$

where $\left(\frac{S_{col}}{\rho}\right)_{air}^{water}$ is the water to air mass collision stopping power ratio averaged over the charged particle fluence spectrum, $k_{atten,scatter}$ is the difference in attenuation and scatter of the alpha particles in water and air, and k_{inv} is the inverse-square fall-off in absorbed dose in the case the absorbed dose to water is determined at a different radial distance than the radial distance of absorbed dose to air.

With the dosimetric framework described in this subsection, absorbed dose to water from unsealed alpha-emitting radionuclides can be measured using variable air gap parallel-plate extrapolation chambers. The magnitude of the correction factors is dependent on the material and geometry of the detector and substrate utilized as well as on the emission profile of the radionuclide of interest.

2.3.4 Dosimetric formalism for the extrapolation method

An alternative quantity of interest is the surface absorbed dose to water, which can be measured by operating the ion chambers as extrapolation chambers. Using this method, the ionization current versus air gap curve is extrapolated to zero air gap and the surface absorbed dose is determined. Unlike the cylindrical shell method described in the previous section, the extrapolation method determines surface absorbed dose instead of measuring absorbed dose as a function of radial distance from the source. The surface absorbed dose rate to water can be given by:

$$\dot{D}_{water}(l) = \frac{1}{A_o}\left(\frac{\partial E}{\partial m}\right)\Pi_{i=0}^{n} k_i = \frac{1}{A_o}\frac{\left(\frac{\bar{W}}{e}\right)_{air}\left(\frac{S_{col}}{\rho}\right)_{air}^{water}}{\rho_o A_{eff}}\left(\frac{\Delta I}{\Delta l}\right)_{l\to 0}\left(k_{pol}k_{recom}k_{TP}k_{elec}\right)\left(k_{point}k_{backscatter}k_{div}\right) \tag{2.26}$$

where the quantities in equation 2.26 remain the same as equation 2.20. The MC-calculated correction factors differ between the two dosimetric formalisms except the k_{point} correction. The $k_{backscatter}$ correction exists since the materials of the source substrate and the detector differs from water. Therefore, the backscatter correction is calculated by:

$$k_{backscatter}(l) = \frac{D_{cavity,point,water}(l)}{D_{cavity,point,det,substrate}(l)} \tag{2.27}$$

where $D_{cavity,point,water}$ is the absorbed dose to cavity from a point source with the substrate and the detector composed of water and $D_{cavity,point,det,substrate}$ is the absorbed dose to air from a point source to the same cylindrical cavity with the nominal materials of the substrate and the detector. Therefore, water-equivalent materials for the source substrate and the detector are desired.

As the air gap between the source and the detector increases, the side-loss of alpha particle fluence also increases leading to a sharp decrease in absorbed dose as a function of air gap. To determine the surface absorbed dose, this loss must be accounted for using a MC-calculated divergence correction factor given by:

$$k_{div} = \frac{D_{cavity,point,water}(l \to 0)}{D_{cavity,point,water}(l)} \tag{2.28}$$

where $D_{cavity,point,water}(l \to 0)$ is the absorbed dose to cavity from a point source with the substrate and the detector composed of water extrapolated to a zero air gap. The

extrapolated absorbed dose can be determined by fitting the absorbed dose versus air gap curve and calculating the intercept.

Chapter 3

A Monte Carlo investigation of particle transport, cavity theory, and source specification for alpha particles

3.1 Alpha particle Monte Carlo transport

3.1.1 Introduction and motivation

The dosimetric formalisms described in sections 2.3.3 and 2.3.4 requires the usage of several Monte Carlo (MC)-based correction factors. It is pertinent that an accurate MC code is employed to ensure maximum accuracy of the proposed primary standard. The

two main component that dictate the accuracy of any MC calculations include cross-section data and transport algorithm. The former is typically extracted from standardized databases such as NIST XCOM or ASTAR [89][8]. The accuracy of the transport algorithm varies greatly between the codes and needs rigorous evaluation. Among the common general-purpose MC codes, GEometry ANd Tracking 4 (GEANT4) has been the most popular code for alpha particle dosimetry due to its adaptability [51][90][52][91]. While the Monte Carlo N-Particle (MCNP) transport code is capable of transporting alpha particles, the export restrictions placed on this code and the previously observed discrepancies for the micron-sized geometries have prevented a wider adoption of MCNP for TAT dosimetry [92]. Therefore, GEANT4 was selected for all MC simulations in this work. Prior to usage of this code to calculate correction factors, the alpha transport mechanism must be understood and tested under stringent conditions. Since the electromagnetic interactions dominate all interaction types for alpha particles, the following sections will solely focus on these interaction types. In addition to the transport algorithm, the radioactive decay library must be evaluated and compared with other standardized databases. The fluence of the emitted particles depends on the accuracy of the decay database and can influence the calculated correction factors.

3.1.2 GEANT4 alpha transport

Each alpha interaction type described in section 2.1.3.2 is modeled separately in GEANT4 as a G4 class using object-oriented programming. The electromagnetic (EM) processes are divided into the G4VEnergyLossProcess class and the G4VMultipleScattering class, which simulates the energy loss and Coulomb scattering in a given media, respectively. While transporting the alpha particles through matter, continuous energy loss is challenging to model due to the energy dependence of the cross-sections. Therefore, small steps are taken in order to consider the change in cross-sections as energy is lost. Ideally,

infitessimally-small step sizes would be taken to mimic the real world conditions but this requires too much computational power and is infeasible. In GEANT4, the energy loss process limits the maximum step size using the following equation:

$$\Delta S_{lim} = \alpha_R R + \rho_R(1 - \alpha_R)(2 - \frac{2\rho_R}{R}) \tag{3.1}$$

where α_R is the *dRover* parameter, R is the range of the particle in a given medium, and ρ_R is the *final range* parameter. At the end of a given step, both scattering and energy loss is considered and the energy/momentum of the particle is adjusted accordingly. Compared to light-charged particles such as electrons, alpha particles are subjected to significantly less Coulomb scattering due to their larger mass. GEANT4 combines multiple Coulomb scattering (MCS) events in a single step and applies lateral displacement and other corrections at the end of each step. While the single scattering model is considered the most accurate, the utilization of this model is limited due to its low computational efficiency. Handled by the electromagnetic physics list, the condensed history technique increases the computational efficiency of the transport algorithm. The two major multiple scattering models used by GEANT4 for heavy charged particles are Urban and Wentzel-VI models with the Urban model being the default for alpha particles and the Wentzel-VI model being the default for protons [93]. The Wentzel-VI model employs a hybrid technique by utilizing MCS for events with scattering angles less than 0.2 radians and using a single scattering model for scattering events that result in larger deflections. The electromagnetic transport parameters that control the step length and step limitations are described in Table 3.1 along with their default values based on the EMStandardOpt4 physics list. The EMStandardOpt4 physics list was chosen to be the default due to its high accuracy and computational efficiency [94]. A careful selection of the electromagnetic physics parameters is especially significant for alpha particles due to their dense

ionization tracks and short ranges in most materials, which can require step lengths on the nanoscale.

Table 3.1: Electromagnetic transport parameters, based on the *EMStandardOpt*4 physics list, used by GEANT4 along with their default values.

Parameter	Process	Description	Default value
MCS model	MCS	MCS model	G4UrbanMCSModel
MCS range factor (f_r)	MCS	Limits the maximum step size for a newly generated particle or when the particle enters a new volume using the relation $stepMax = f_r.max\{r, \lambda_1\}$, where λ_1 is the first transport mean free path and r is the range of the particle	0.2
MCS step limitation	MCS	The type of step limitation used	UseMinimal
Geometry factor (f_g)	MCS	Controls the maximum step size when the particle enters a new volume using the relation $stepMax = d/f_g$ where d is the distance to the closest boundary in the direction of the particle and $stepMax$ is the maximum step size	2.5
linLossLimit	Ionization	Limits the energy loss of the particle along the step using a single-point integration using the constraint $\frac{stepsize}{range} < linLossLimit$	0.02
integral	Ionization	Corrects the interaction cross-sections for variation in energy along the particle step	true
dRover	Ionization	Prevents drastic changes in the stopping power of the particle using the constraint $\frac{step}{range} < dRover$ to limit the particle step size	0.1
final range	Ionization	When the particle range is below final range, completes the tracking in a single step	10 μm

A Fano cavity test can be employed to investigate the accuracy of the electromagnetic transport algorithm of any MC code [95]. Fano's theorem states "that the fluence of particles, emitted uniformly per unit mass, is constant throughout an infinite medium of uniform composition but varying density". Therefore, by simulating the Fano conditions,

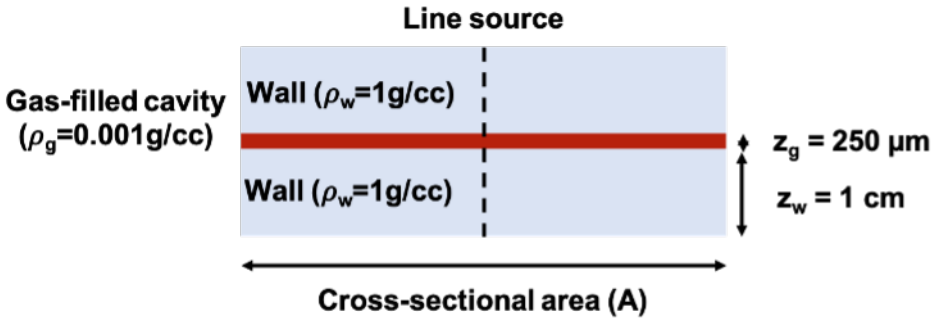

Figure 3.1: Simulated geometry used to implement a Fano cavity test for alpha particles (not to scale) [13].

an evaluation of the EM physics can be performed in the case where the result is known *a priori*. With the theory in place, the implementation of the Fano cavity test can take various forms [96] [97] [98]. An agreement between the calculated and theoretical results displays the accuracy of the transport algorithm. The latest versions of the GEANT4 MC code contain a built-in Fano cavity test, $fanoCavity2$, which was initially proposed by Sempau and Andreo [97]. In this investigation, the source code of the fanoCavity2 was modified to implement a Fano cavity test for alpha particles. According to Sempau and Andreo, simulating a source with uniform intensity per unit mass, I, creates charged particle equilibrium conditions in the geometry, regardless of the particle type simulated. While their work evaluated the electron transport algorithm, the Fano theorem must hold even when alphas are utilized. Therefore, a monoenergetic line source was simulated and charged particle equilibrium was ensured by sampling the source intensity proportional to the local density of the material. Figure 3.1 shows the simulation geometry, which consists of a 0.25 mm thick cylindrical cavity sandwiched between two 1 cm thick cylindrical walls, all made of the same material composition as water. The 1 cm wall thickness was selected to ensure that the wall thickness was greater than the range of the highest energy alpha particle used in water i.e. 95 μm for 9 MeV. The density of the cavity was set to 0.001 g/cc, unless stated otherwise, while the wall density was assigned to 1 g/cc creating a sharp density gradient between the two geometries. The physics list was modified to

only include electromagnetic interactions and the secondary production thresholds were set to 10 km to avoid inclusion of any secondary charged particles. Under Fano's theorem, the absorbed dose must the be same everywhere in the given geometry assuming charged particle equilibrium conditions [95]. Using the described setup, the theoretical expected result can be correlated with the calculated result via a unitless quantity, Q, which can be defined as:

$$Q = \frac{D}{IE_o} \quad \text{with} \quad I = \frac{N}{A(2\rho_{wall}t_{wall} + \rho_{gas}t_{gas})} \tag{3.2}$$

where D is the absorbed dose to cavity, I is the source intensity per unit mass, N is the number of particle histories, A is the cross-sectional area of the cavity, ρ is the density, t is the thickness of the cylinder, and E_o is the simulated alpha-particle energy. Since $D = \Delta E/m$, the above equation can be rewritten as:

$$Q = \frac{\Delta E}{NE_o}\left(1 + \frac{2\rho_{wall}t_{wall}}{\rho_{gas}t_{gas}}\right) \tag{3.3}$$

where ΔE is the energy absorbed in the cavity [97]. An accurate implementation of the transport algorithm must result in the Q-value being unity. If deviations from unity are found, the transport parameters must be altered until a good agreement is reached between the theoretical and calculated results. Alpha particles with energies in the 5–9 MeV range were simulated and the Q-value was calculated for both the Urban and the Wentzel-VI MCS models. Two million original particle histories were run to achieve statistical uncertainty of $< 0.1\%$. The *dRover* and *final range* parameters were varied from 0.001 to 1 and 0.1–20 μm, respectively for the results with the largest discrepancies obtained for both MCS models. The effect of the maximum step value and cavity mass density on the Q-value was also investigated for both MCS models.

Figure 3.2 shows the Q-values for a range of alpha energies using the default parameters shown in Table 3.1. The Wentzel-VI MCS model outperformed the Urban MCS model

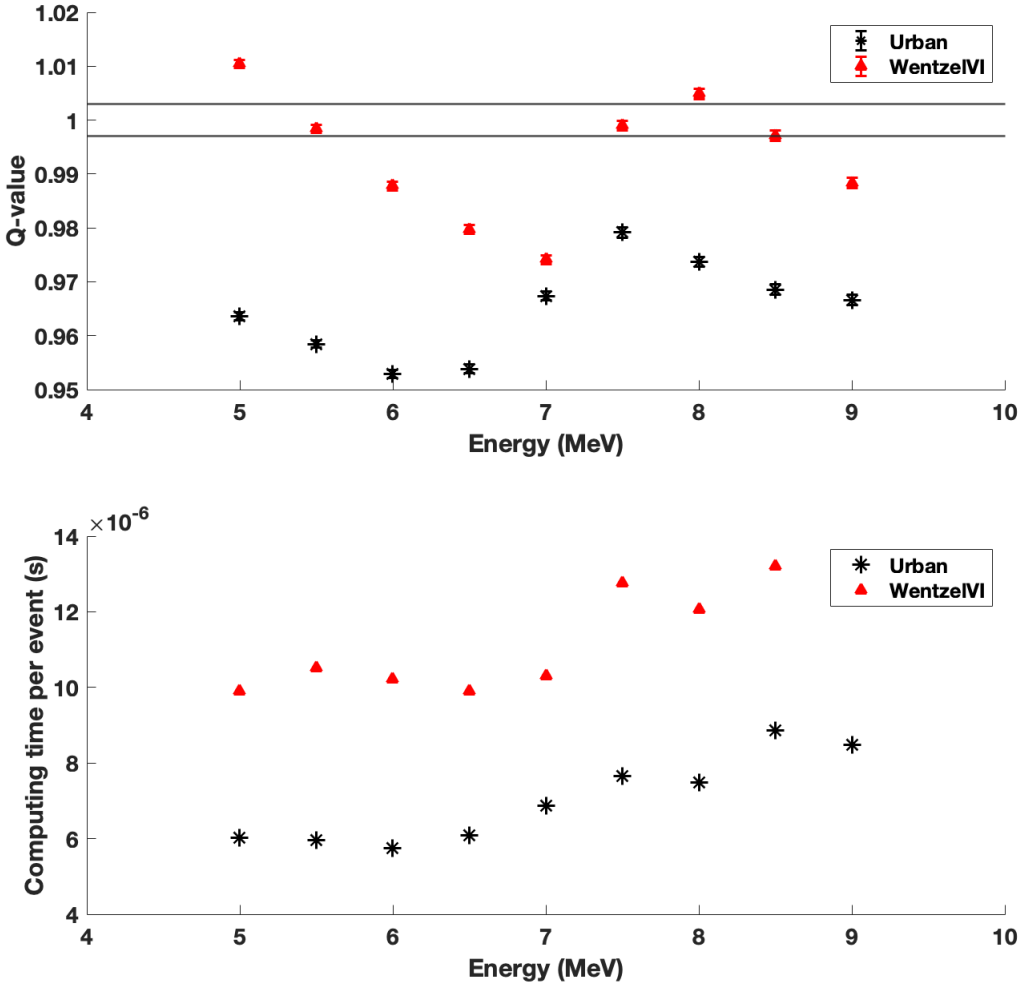

Figure 3.2: The Q-values (top) and the associated computational times (bottom) for various alpha energies are shown using the default electromagnetic parameters. The horizontal lines correspond to the $\pm 0.3\%$ margin from unity and the error bars correspond to 2σ statistical uncertainty [13].

for the investigated energy range. The superior performance of the Wentzel-VI model can be partially attributed to its utilization of a single scattering algorithm for events that lead to larger scattering angles. A similar result was found by Makarova et al. when comparing the Urban and Wentzel-VI MCS models for proton beams [99]. Out of the nine alpha energies simulated, only three Q-values passed the Fano cavity test within $< 0.3\%$. Additionally, all three passed results utilized the Wentzel-VI MCS model. Deviations

from unity of up to 4.7% and 2.6% were found for the Urban and Wentzel-VI MCS models, respectively. The 6 MeV and 7 MeV alpha energies were identified to have the largest disagreement for the Urban and Wentzel-VI MCS models, respectively. On average, the Urban and the Wentzel-VI MCS models passed the Fano cavity test within 3.5% and 1.0% using the default parameters. Thus, the default parameters were deemed unsuitable when an accuracy of $< 1\%$ is desired. Greater accuracy for GEANT4 has been reported in the literature for other charged particles such as electrons and protons [100] [101] [102]. Therefore, optimal parameters must be determined by varying the parameters that control the step size and step limitations. Since the majority of the physics events belonged to the ionization class, the ionization parameters such as *dRover* and *final range* were altered and the change in Q-values was studied. Due to its utilization of a single Coulomb scattering technique for large scattering angles, the simulations using the Wentzel-VI MCS model were observed to take 60% longer, on average, than the Urban model. The increase in computational time was found to be compensated by the increase in accuracy offered by the Wentzel-VI MCS model.

For the 6 MeV alpha energy and the Urban MCS model, the Q-values for the 0.001–1 *dRover* range are shown in figure 3.3 for 0.1–20 μm *final range* values. Figure 3.4 shows the Q-values for the 0.001–1 *dRover* and 0.1–20 μm *final range* magnitudes using a 7 MeV alpha energy and the Wentzel-VI MCS model. The agreement between the theoretical and calculated results was observed to be greater for the smaller *final range* values and the Q-values were found to be more sensitive to the *final range* parameter relative to the *dRover* parameter for both MCS models. Better agreement with theory was observed for the Wentzel-VI model compared to the Urban model using the 10 μm and 20 μm *final range* values. Below 0.1 *dRover* magnitude, the Q-value was found to be relatively insensitive to the *dRover* parameter, especially for the smaller *final range* values. Sterpin et al. showed the agreement between the theoretical and computed response for a proton beam to be

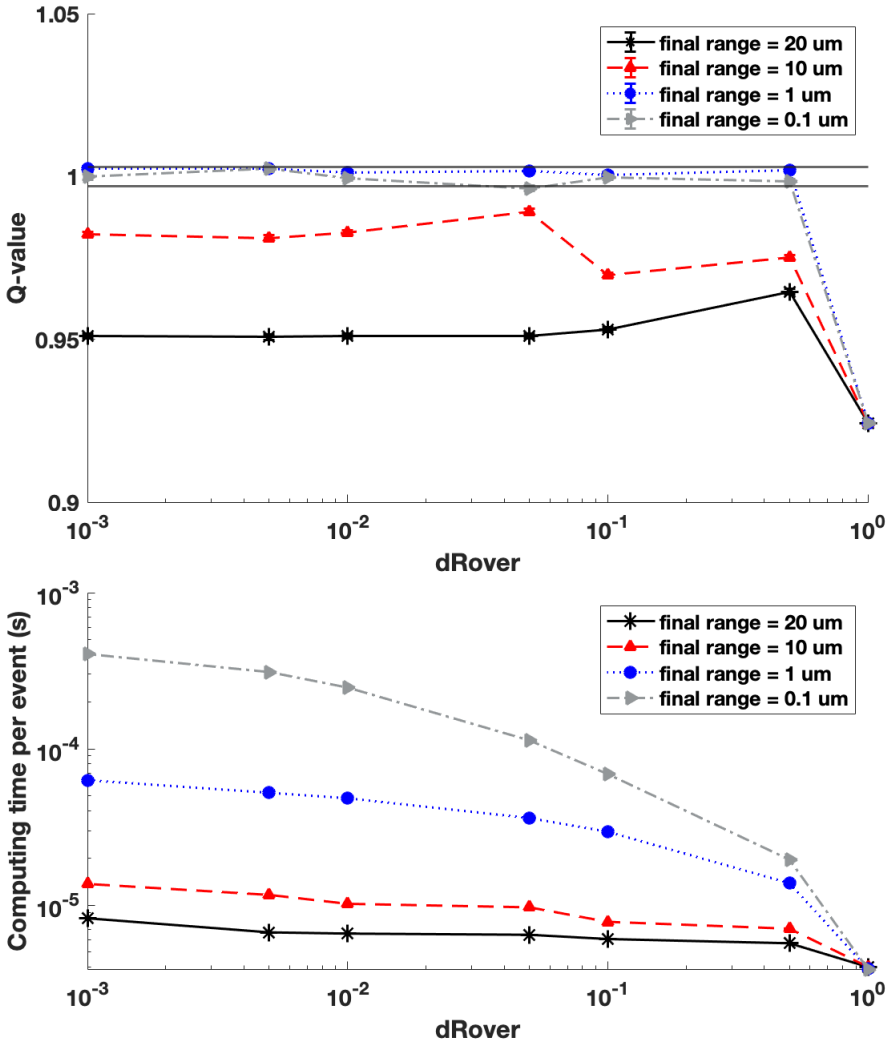

Figure 3.3: a) The Q-values (top) and the associated computational times (bottom) for various *dRover* magnitudes are shown for a variety of *final range* values for the Urban MCS model using a 6 MeV alpha particle energy. The horizontal lines correspond to the $\pm 0.3\%$ margin from unity and the error bars correspond to 2σ statistical un- certainty. The error bars are smaller than the symbols [13].

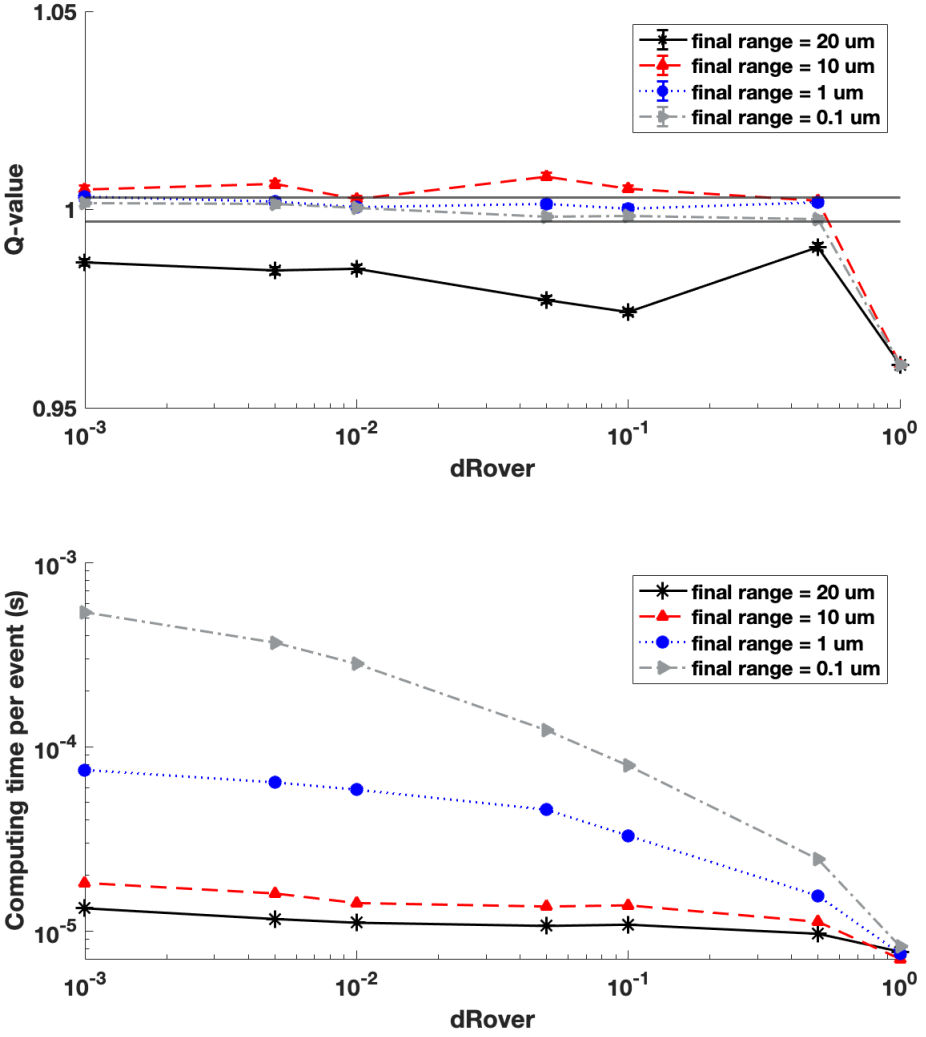

Figure 3.4: The Q-values (top) and the associated computational times (bottom) for various *dRover* magnitudes are shown for a variety of *final range* values for the Wentzel-VI MCS model using a 7 MeV alpha particle energy. The horizontal lines correspond to the $\pm 0.3\%$ margin from unity and the error bars correspond to 2σ statistical uncertainty. The error bars are smaller than the symbols [13].

relatively insensitive to the *dRover* and *final range* parameters, which is contradictory to what was observed in this study for alpha particles [98]. In contrast, Simiele and DeWerd found the Q-value to be much more sensitive to the *dRover* parameter, relative to the *final range* parameter, for electrons under the influence of a magnetic field [103]. Arce et al. subjected various GEANT4 electromagnetic physics lists to a Fano cavity test using electrons and found an agreement with theory within $< 0.5\%$ for the $EmStandardOpt4$ physics list and the Wentzel-VI MCS model [100]. Deviations from theory of up to 6.5% were noted in their work for other physics lists, which decreased to $< 1\%$ when the parameter $dRoverRange$ was decreased to 0.01. While *dRover* prevents large changes in the stopping power, $dRoverRange$ limits the maximum step size of the particles based on their range. However, a direct comparison between this work and the previous studies is not possible due to the different physical properties of the investigated charged particles and their energies. Both MCS models passed the Fano cavity test to within 0.3% when *final range* of $\leq 1\mu m$ and *dRover* of ≤ 0.1 were used. As demonstrated by figures 3.3 and 3.4, the computational time increased with decreasing *dRover* and *final range* values for both MCS models. The computational time was found to be more sensitive to *dRover* for smaller *final range* magnitudes. Based on the Q-values and the computational times, a *dRover* of 0.1 and a *final range* of 1 μm is recommended regardless of the MCS utilized.

The effect of maximum step size on the Q-values for both MCS models is shown in figure 3.5. The Q-values were found to converge to within 0.3% of unity at a larger maximum step size for the Wentzel-VI MCS model compared to the Urban model. Below a 1 μm maximum step size, both MCS passed the Fano cavity test within 0.3%. However, the increase in accuracy with the decrease in maximum step size comes with an exponential increase in computational time. Therefore, a maximum step size of 1 μm is recommended for both MCS models. While a large sensitivity of Q-values to maximum step size was reported in this study, Sterpin et al. showed a relatively insensitive relationship between

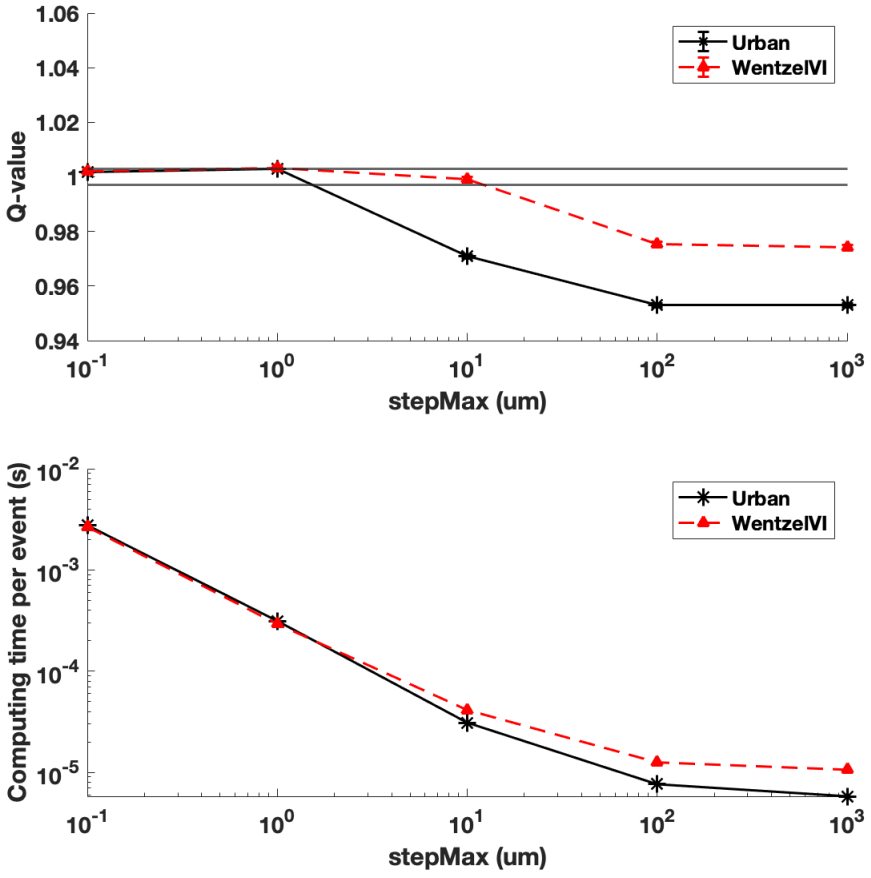

Figure 3.5: The Q-values (top) and the associated computational times (bottom) for various *stepMax* values are shown for a 6 MeV alpha energy using the Urban MCS model and a 7 MeV alpha energy using the Wentzel-VI model. The horizontal lines correspond to the ±0.3% margin from unity and the error bars correspond to 2σ statistical uncertainty. The error bars are smaller than the symbols and the lines connecting the data points are for visual purposes only [13].

the Q-value and the maximum step size parameter for protons [98]. Figure 3.6 shows the Q-values for a range of cavity mass densities for the Urban and the Wentzel-VI MCS models. A larger mass density gradient between the walls and the cavity was found to result in larger deviations between the theoretical and calculated results. Below 0.1 g/cc of cavity density, both MCS models failed the Fano cavity test to within 0.3%. Therefore, special considerations need to be taken when strong mass density gradients are present in the simulation geometry. Therefore, this study demonstrates that the default GEANT4

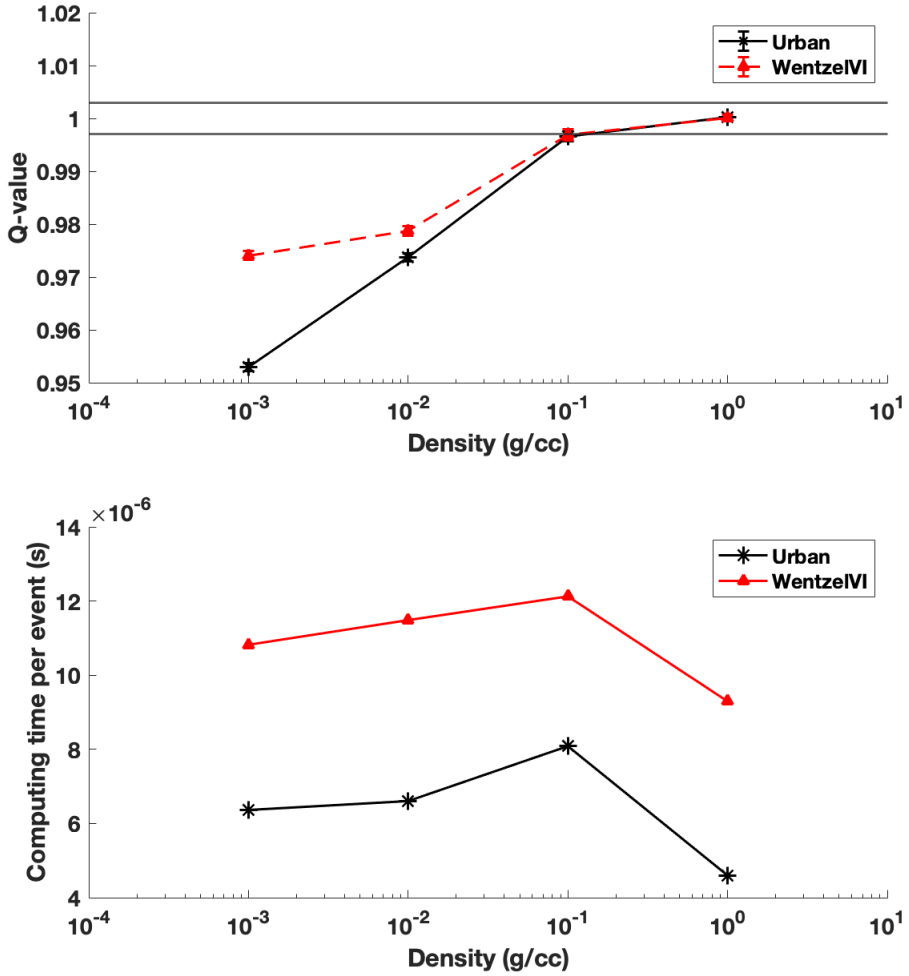

Figure 3.6: The Q-values (top) and the associated computational times (bottom) for various cavity densities are shown for a 6 MeV alpha energy using the Urban MCS model and a 7 MeV alpha energy using the Wentzel-VI model. The horizontal lines correspond to the $\pm 0.3\%$ margin from unity and the error bars correspond to 2σ statistical uncertainty [13].

transport parameters are appropriate for internal dosimetry for patient geometries with relatively homogeneous densities above 0.1 g/cc.

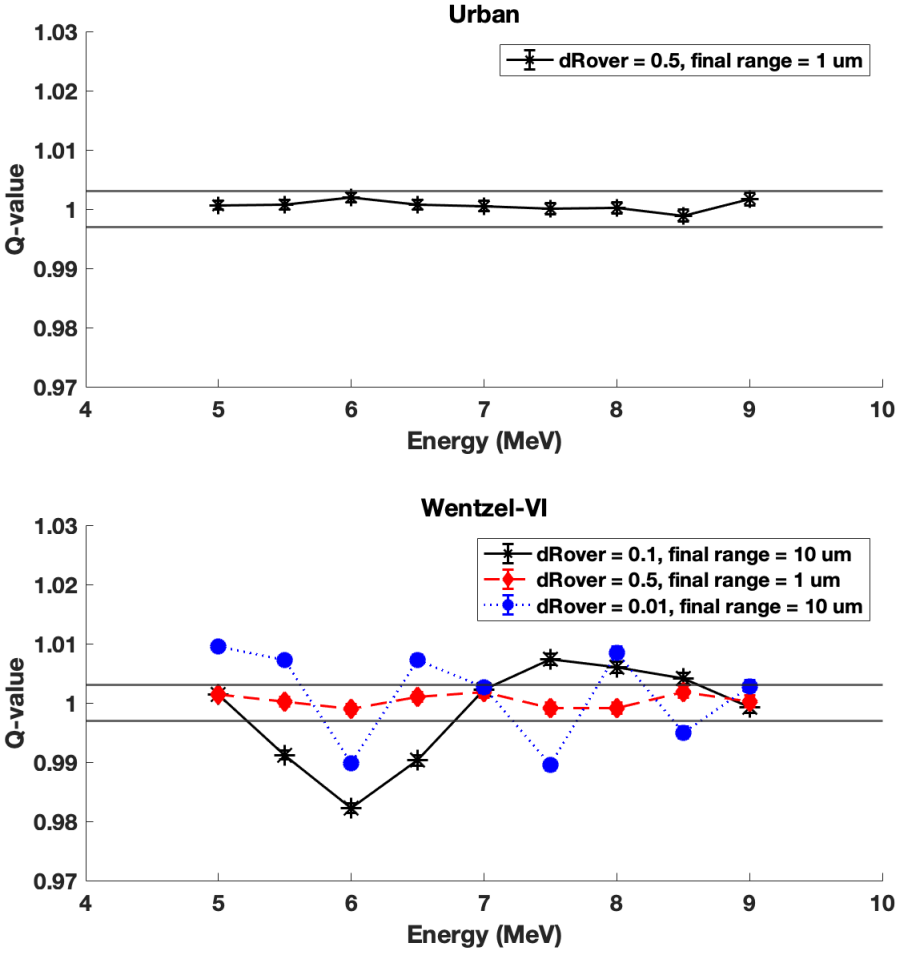

Figure 3.7: The Q-values for the Urban MCS (top) and the Wentzel-VI MCS (bottom) models for various alpha energies, dRover, and *final range* values. The horizontal lines correspond to the ±0.3% margin from unity and the error bars correspond to 2σ statistical uncertainty [13].

While figures 3.3 and 3.4 show results for single alpha energy, various combinations of *dRover* and *final range* values were simulated for all alpha energies in the 5–9 MeV range in pursuit of parameters that lead to the highest accuracy and computational efficiency. As shown in figure 3.3, a *final range* value of 10 μm is suboptimal for the Urban model considering the Q-value being in the 0.92–0.99 range. For the Wentzel-VI model and a

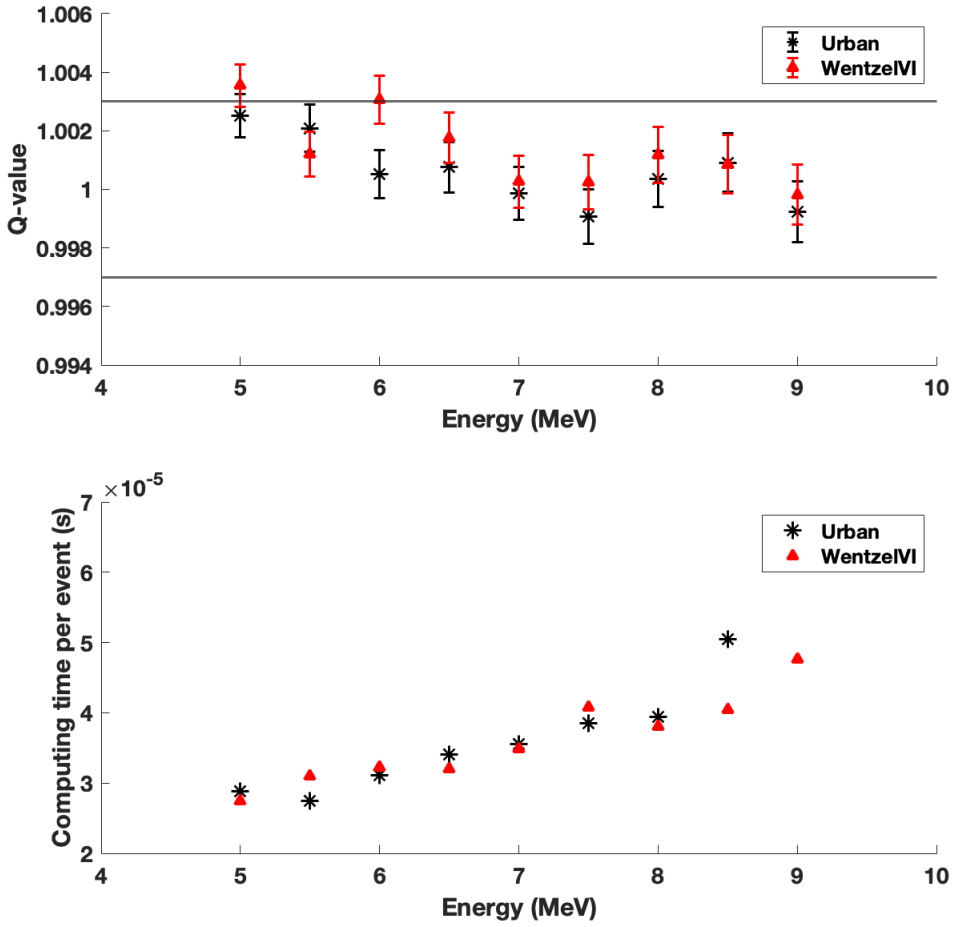

Figure 3.8: The Q-values (top) and the associated computational times (bottom) for various alpha energies are shown using the recommended electromagnetic parameters. The horizontal lines correspond to the ±0.3% margin from unity and the error bars correspond to 2σ statistical uncertainty [13].

final range value of 10 μm, the only *dRover* values that led to Q-values within 0.3% of unity were observed to be 0.5 and 0.01. According to the data shown in figure 3.7, a *final range* value of 10 μm was deemed unsuitable for the Wentzel-VI model considering that deviations of up to 1.8% from unity were found with these parameters in the 5–9 MeV alpha energy range. Therefore, a maximum *final range* of 1 μm must be used if an accuracy of $< 0.3\%$ is desired. With this *final range* value, a maximum *dRover* value of 0.5 can be used for both MCS models, as demonstrated by 3.7. However, considering the

default GEANT4 *dRover* value being 0.1, a conservative selection of optimal parameters would include a *final range* value of 1 μm and a *dRover* value of 0.1. The default values of other electromagnetic parameters, including maximum step size, were found to be sufficient if the recommended *dRover* and *final range* magnitudes are utilized. With these optimal parameters, the Fano cavity test was found to pass within 0.3% for both MCS models for the investigated alpha energy range of 5–9 MeV, as shown in figure 3.8. On average, the Urban MCS model was found to agree better with the theory with a mean deviation of 0.10% compared to the Wentzel-VI model for which a mean deviation of 0.14% was found. The simulation times for the Urban model were also observed to be similar to the times for the Wentzel-VI model. Therefore, with the optimal parameters recommended in this investigation, either Urban or Wentzel-VI MCS models can be utilized without a loss in accuracy or computational efficiency.

3.1.3 GEANT4 decay library

In addition to an accurate transport algorithm, the MC code used for dosimetry purposes must also utilize accurate and standardized radioactive decay data. GEANT4 contains an internal decay database for a large number of radionuclides which samples emission data obtained from the National Nuclear Decay Center (NNDC) in the form of Evaluated Nuclear Structure Data Files (ENSDF) [104]. In an initial comparison of the GEANT4 emission intensities and the ENSDF intensity data, a discrepancy in the alpha intensities of $2.47\% \pm 2.26\%$ was found [104]. Various compiled decay databases can be utilized for TAT dosimetry including Medical Internal Radiation Dose (MIRD) and Radiation Dose Assessment Resource (RADAR) [14][105]. A comparison of the alpha energies and intensities between the GEANT4 internal dataset, RADAR decay data, and MIRD decay data can be performed to investigate any possible deviations for various alpha-emitting radionuclides.

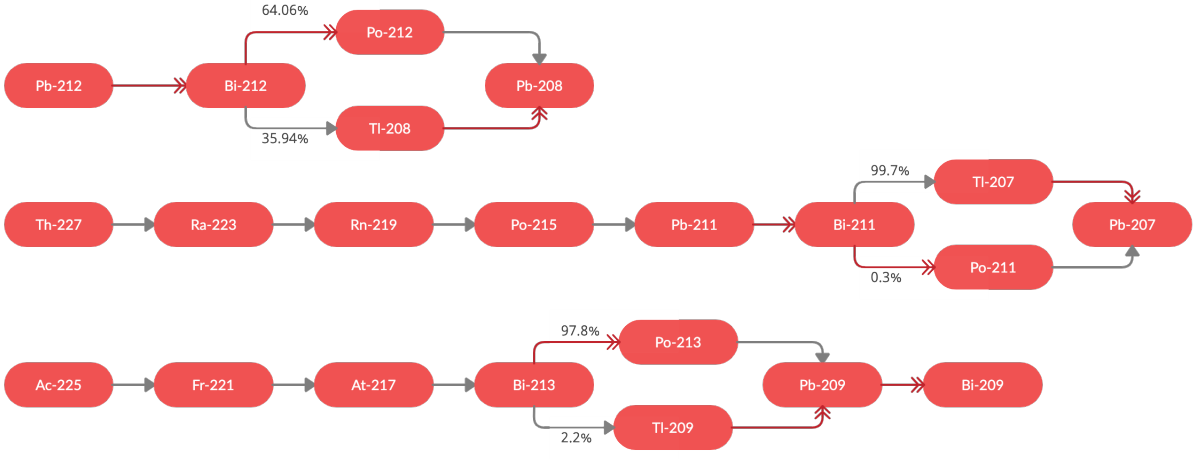

Figure 3.9: Decay schemes for a few clinically-relevant, alpha-emitting radionuclides such as ^{212}Pb, ^{227}Th, ^{223}Ra, and ^{225}Ac [14]. The nuclear transitions that lead to zero alpha emissions or include beta emissions are represented by double arrow heads and are red in color [13].

In this study, only alpha emissions were considered and decay data was extracted from the RADAR and MIRD databases for ^{223}Ra, ^{225}Ac, ^{227}Th, and ^{212}Pb alpha-emitting radionuclides and their progenies [14]. The decay schemes for these radionuclides are shown in figure 3.9. The GEANT4 decay data was extracted by simulating a point source in a vacuum and scoring the energy spectrum over a sphere with a 1 μm radius. While all decays were simulated, a particle filter was implemented to only extract information related to alpha particle emission. The *G4RadioActiveDecay* physics list was turned on and the source was initialized by providing the atomic number and the atomic mass of the radionuclide. Throughout these simulations, the production threshold for secondary particles was set to 10 km. For each alpha peak, the absolute difference in energy and intensity was quantified between the GEANT4, RADAR, and MIRD decay data. Average Absolute Difference (AAD) and Maximum Absolute Difference (MAD) in energy and intensity were reported for each decay transition:

$$AAD = \frac{1}{N}\Sigma_i^N|x_i - x_{GEANT}| \quad \text{and} \quad MAD = max|x_i - x_{GEANT}| \tag{3.4}$$

where N is the number of alpha peaks, x_i is the ith peak energy or intensity for RADAR/MIRD data, and x_{GEANT} is the ith peak energy or intensity for GEANT4 data. Furthermore, the total energy emitted via the alpha channel was also calculated for each radionuclide:

$$E_{released} = \Sigma E_i I_i \tag{3.5}$$

where E_i is the alpha peak energy and I_i is the intensity of the peak. Using these metrics, the GEANT4 radioactive decay data was compared against the RADAR and MIRD data.

Tables 3.2-3.5 show a comparison of alpha peak energies and intensities between GEANT4, RADAR, and MIRD databases for ^{212}Pb, ^{227}Th, ^{223}Ra, and ^{225}Ac radionuclides using AAD and MAD comparison metrics for a given decay transition. Total alpha energy

Table 3.2: Comparison of radioactive decay data between GEANT4, RADAR, and MIRD for ^{212}Pb.

Transition	GEANT $E_{released}$ (MeV)	RADAR AAD Energy (keV)	RADAR MAD Energy (keV)	RADAR AAD Intensity (%)	RADAR MAD Intensity (%)	RADAR Norm. $E_{released}$	MIRD AAD Energy (keV)	MIRD MAD Energy (keV)	MIRD AAD Intensity (%)	MIRD MAD Intensity (%)	MIRD Norm. $E_{released}$
^{212}Bi→ ^{212}Po & ^{208}Tl	2.17	0.06 ± 0.03	0.10	0.02 ± 0.01	0.03	1.00	0.05 ± 0.00	0.05	0.01 ± 0.01	0.02	1.00
^{212}Po→ ^{208}Pb	8.78	0.04 ± 0.00	0.04	0.00 ± 0.00	0.00	1.00	0.05 ± 0.00	0.05	0.00 ± 0.00	0.05	1.00

Table 3.3: Comparison of radioactive decay data between GEANT4, RADAR, and MIRD for ^{223}Ra.

Transition	GEANT $E_{released}$ (MeV)	RADAR AAD Energy (keV)	RADAR MAD Energy (keV)	RADAR AAD Intensity (%)	RADAR MAD Intensity (%)	RADAR Norm. $E_{released}$	MIRD AAD Energy (keV)	MIRD MAD Energy (keV)	MIRD AAD Intensity (%)	MIRD MAD Intensity (%)	MIRD Norm. $E_{released}$
^{223}Ra→ ^{219}Rn	5.66	0.06 ± 0.04	0.12	0.41 ± 0.89	3.43	1.02	0.10 ± 0.05	0.15	0.56 ± 0.80	2.43	1.00
^{219}Rn→ ^{215}Po	6.75	0.03 ±0.01	0.05	0.12 ± 0.15	0.37	1.00	0.05 ± 0.00	0.05	0.18 ± 0.20	0.37	1.00
^{215}Po→ ^{211}Pb	7.38	0.06 ± 0.02	0.07	0.04 ± 0.03	0.06	1.00	0.15 ± 0.10	0.25	0.02 ± 0.02	0.04	1.00
^{211}Bi→ ^{207}Tl & ^{211}Po	6.54	0.06 ± 0.02	0.07	0.01 ± 0.001	0.01	1.00	0.05 ± 0.00	0.05	0.04 ± 0.05	0.10	1.00
^{211}Po→ ^{207}Pb	7.44	0.05 ± 0.06	0.12	0.02 ± 0.02	0.04	0.99	0.08 ± 0.06	0.15	0.02 ± 0.01	0.03	1.00

Table 3.4: Comparison of radioactive decay data between GEANT4, RADAR, and MIRD for ^{227}Th. Only the first decay transition was considered to avoid redundancy between the decay data for ^{227}Th and ^{223}Ra radionuclides.

Transition	GEANT $E_{released}$ (MeV)	RADAR AAD Energy (keV)	RADAR MAD Energy (keV)	RADAR AAD Intensity (%)	RADAR MAD Intensity (%)	RADAR Norm. $E_{released}$	MIRD AAD Energy (keV)	MIRD MAD Energy (keV)	MIRD AAD Intensity (%)	MIRD MAD Intensity (%)	MIRD Norm. $E_{released}$
^{227}Th→ ^{223}Ra	5.88	0.05 ± 0.03	0.13	0.02 ± 0.03	0.13	1.00	0.09 ± 0.05	0.15	0.01 ± 0.02	0.06	1.00

released was reported for GEANT4, whereas the GEANT-normalized total alpha energy released was reported for RADAR and MIRD. Nuclear transitions with no alpha emissions were ignored and not included in this study. However, several of the evaluated radionuclides emit other particle types such as betas, auger electrons, gamma rays, and x-rays that can significantly contribute to the total energy emission and should be accounted for when simulating these sources. Since ^{227}Th decay to ^{223}Ra and the radium decay chain was analyzed separately, only the first transition was reported for ^{227}Th. For a single

Table 3.5: Comparison of radioactive decay data between GEANT4, RADAR, and MIRD for ^{225}Ac.

Transition	GEANT $E_{released}$ (MeV)	RADAR AAD Energy (keV)	RADAR MAD Energy (keV)	RADAR AAD Intensity (%)	RADAR MAD Intensity (%)	RADAR Norm. $E_{released}$	MIRD AAD Energy (keV)	MIRD MAD Energy (keV)	MIRD AAD Intensity (%)	MIRD MAD Intensity (%)	MIRD Norm. $E_{released}$
^{225}Ac→ ^{221}Fr	5.78	0.10 ± 0.05	0.15	0.07 ± 0.30	1.35	0.99	0.10 ± 0.07	0.25	0.12 ± 0.37	1.35	0.98
^{221}Fr→ ^{217}At	6.30	0.09 ± 0.07	0.24	0.10 ± 0.30	0.80	1.01	0.07 ± 0.04	0.15	0.11 ± 0.24	0.60	1.01
^{217}At→ ^{213}Bi	7.07	0.29 ± 0.10	0.35	0.02 ± 0.02	0.04	1.00	0.25 ± 0.00	0.25	0.05 ± 0.08	0.13	1.00
^{213}Bi→ ^{213}Po & ^{209}Tl	0.12	0.20 ± 0.20	0.35	0.02 ± 0.00	0.03	0.98	0.55 ± 0.00	0.55	0.00 ± 0.00	0.01	1.00
^{213}Po→ ^{209}Pb	8.38	0.04 ± 0.00	0.04	0.00 ± 0.00	0.00	1.01	0.10 ± 0.07	0.15	0.00 ± 0.00	0.00	1.00

nuclear disintegration, a total energy emission of 10.96 MeV was found through the alpha channel for ^{212}Pb using GEANT4. Total alpha energy emission for ^{212}Pb using GEANT4, RADAR, and MIRD databases were found to agree within 0.2% of each other. Additionally, an agreement of < 0.1 keV and $< 0.1\%$ was found between the three databases for alpha energies and intensities, respectively. For ^{223}Ra, a total alpha emission energy of 33.79 MeV per decay was found, which was much larger than ^{212}Pb. The agreement between GEANT4 and MIRD for total alpha energy emission was found to be within 0.2%; whereas, a difference of 2% was found between GEANT4 and RADAR. This discrepancy was found to be due to the ^{223}Ra→^{219}Rn nuclear transition for the 5.72 MeV alpha peak, where a large absolute difference between the GEANT4 and RADAR alpha intensity was observed. Besides this anomaly, an agreement of < 0.3 keV and $< 0.4\%$ was found between GEANT4, RADAR, and MIRD data for alpha energies and intensities, respectively. A total energy emission through alpha particles for ^{227}Th was calculated to be 39.67 MeV considering all nuclear transitions and progenies including the ^{223}Ra decay chain. For the ^{227}Th→^{223}Ra transition, all three decay databases agreed with each other to within 0.3%, 0.2 keV, and 0.15% for the total alpha energy released, alpha peak energies, and intensities, respectively. An agreement of <0.6 keV and <1.4% was found for the alpha energies and intensities, respectively, for ^{225}Ac using the GEANT4, RADAR, and MIRD decay

data. Such a large absolute difference in intensity was attributed to the 5.37 MeV alpha peak for the ^{225}Ac→^{221}Fr transition, for which the MIRD and RADAR data agreed to within 0.1% while the GEANT4 overestimated the alpha intensity by 1.4%. Furthermore, GEANT4 was found to overestimate the total energy released through alpha emission by 2.1% for the ^{213}Bi→^{213}Po & ^{209}Tl nuclear transition. MIRD decay data was observed to underestimate the total alpha energy released for the ^{225}Ac→^{221}Fr transition by 1.9%; whereas the GEANT4 and RADAR data agreed to within 0.2%. Besides the reported discrepancies, an agreement within 0.5% was found between GEANT4, RADAR, and MIRD for the total alpha energy emission. Overall, good agreement was found between the three databases for all investigated alpha- emitting radionuclides. Such an outcome was hypothesized since all three decay datasets originate from the NNDC data library. Due to the large amount processing involved in converting the NNDC dataset into a specific format, small deviations between the decay data can be expected, as concluded in this work. Furthermore, any updates in the NNDC data over a given time period can contribute to additional discrepancies between the three datasets.

A comparison between the GEANT4 alpha spectrum and the ENSDF data for various alpha-emitting radionuclides was previously performed by Hauf et al. [104]. Deviations in alpha intensities of up to 2.47% were reported by Hauf et al., while a comparison of alpha peak energies was not performed. This work demonstrated that the GEANT4 alpha peak energies were within 0.6 keV of each other for the GEANT4 internal decay database, RADAR decay data, and MIRD decay data; however, differences of up to 1.4% were shown in the peak intensities. Overall, the GEANT4 internal decay database was found to agree within 2% with the RADAR and MIRD databases. Therefore, the GEANT4 internal alpha spectra can be utilized for TAT dosimetry.

3.2 Cavity theory

3.2.1 Introduction and motivation

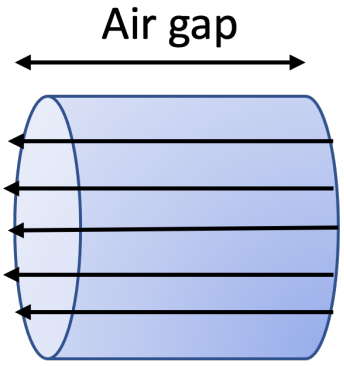

Figure 3.10: A simplified version of the source and detector geometry.

The quantity directly measured by any ionization chamber is radiation exposure. Exposure can be converted to absorbed dose by applying a suitable cavity theory. Multiple cavity theories exist for this purpose and each theory is unique and has its own set of assumptions and limitations. In order for the proposed primary standard to measure absorbed dose, a suitable cavity theory must be selected. As shown previously in section 2.3.3, the measurable quantity is illustrated in figure 2.23. By changing the air gap by Δl, absorbed dose to a cylindrical shell is measured using a two air-gap method. It is noteworthy that there is a wide track-length distribution inside the air cavity due to the finite radius of the collector. Additionally, as the air-gap increases, the side loss of fluence increases due to the diverging fluence. Therefore, the limitations and assumptions of the cavity theories are challenging to deconvolve from the above stated effects in the geometry shown in figure 2.23 i.e. a 2D source approximating a point source emitting particles from the flat source of the cylindrical air cavity. This section simplifies this problem by assuming a parallel beam source of monoenergetic alpha particles incident on the flat surface of the cylindrical air cavity as shown in figure 3.10. With this simplification, any

track-length changes inside the cavity only arise from the Rutherford scattering instead of the geometry of the setup and the side losses become negligible. Therefore, the results presented in this section must be carefully translated to the actual geometry of the setup.

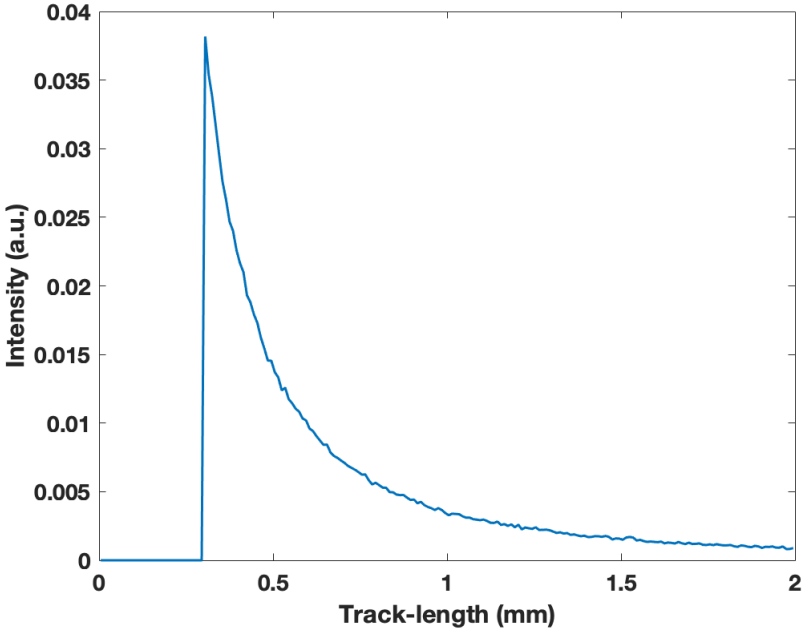

Figure 3.11: Track-length distribution of 5 MeV alpha particles in a cylindrical cavity of radius 2.019 mm and of thickness 300 μm.

The detector construction and dimensions will be discussed in the following chapters. However, it is of note that the cavity radius is approximately 2.019 mm in this work. Figure 3.11 shows the track-length distribution, calculated using the GEANT4 Monte Carlo (MC) code, inside a cylindrical cavity being irradiated with a point source of 5 MeV alphas placed at the center of the flat surface of the cavity. The dimension of the cavity were chosen to be 2.019 mm radius and 300 μm thickness. It is evident from the figure that the alpha particles traverse a wide range of distances inside the cavity before reaching the detector.

3.2.2 Bragg-Gray cavity

The Bragg-Gray (BG) cavity theory applies to small cavities that don't perturb the fluence of the charged particles traversing the cavity [81]. Therefore, the absorbed dose deposited inside the cavity must be from the charged particles crossing it. Typically, this condition is fulfilled if the size of the cavity is smaller than the range of the charged particles. If BG conditions are fulfilled, the absorbed dose is calculated by:

$$\frac{D_{med}}{D_{det}} = \frac{\int_0^{E_{max}} \Phi_E \left(\frac{S_{col}(E)}{\rho}\right)_{med} dE}{\int_0^{E_{max}} \Phi_E \left(\frac{S_{col}(E)}{\rho}\right)_{det} dE} \tag{3.6}$$

where D_{med} is the absorbed dose to the medium of interest, D_{det} is the absorbed dose to the detector, E is the energy of the charged particle, Φ_E is the fluence at a given energy, and $\left(\frac{S_{col}(E)}{\rho}\right)$ is the mass collision stopping power at the same energy. The BG conditions were evaluated using the geometry shown in figure 3.10. Since there is no divergence, the absorbed dose to air must be constant under BG conditions regardless of the simulated air gap. Any perturbation in the fluence must be due to the elastic Coulomb scattering effect and may change the direction of the alpha particle leading to an increase in fluence when compared to a cavity of negligible thickness.

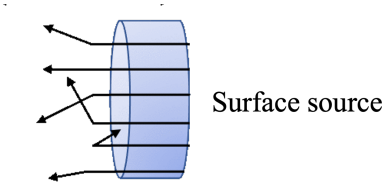

Figure 3.12: A schematic of the simulation setup is shown.

The GEANT4 MC code was used with the optimal physics parameters determined in section 3.1.2. Monoenergetic parallel alpha particles, as shown in figure 3.12, were simulated in the 5-9 MeV energy range. A cavity radius of 2 mm was selected arbitrarily and the production thresholds for all particles were set to 10 km. Production thresholds in

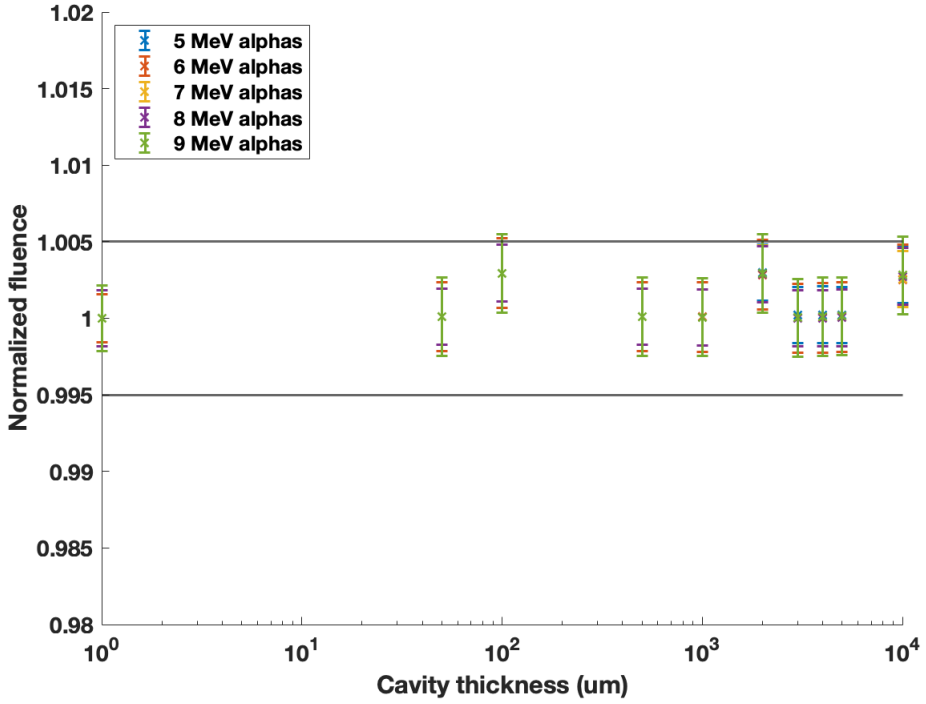

Figure 3.13: The change in fluence with change in cylindrical cavity thickness for parallel alpha particle beams is shown. Fluence was normalized to the value at 1 μm cavity thickness. The error bars correspond to 1σ statistical uncertainty.

GEANT4 are entered in the form of a distance that determines the range of the given secondary particle in the medium of origin above which the secondary particles are explicitly tracked. Setting the production thresholds to 10 km ensures that no δ-rays are generated inside the geometry. According to the results shown in figure 3.13, a perturbation correction factor is not required for cylindrical air cavities when the maximum track-length is < 1 cm in the sensitive volume. The normalized fluence was within 0.5% of each other regardless of the cavity thickness. Since heavy charged particles have a less tortuous path in any media, relative to light charged particles, a negligible fluence perturbation was hypothesized. For the same geometrical setup, the absorbed dose to air is shown in figure 3.14 as a function of cavity thickness. Unlike fluence, a significant increase in absorbed dose was observed with the increase in cavity thickness. Such a trend can be explained by the increasing stopping power of the alpha particles as they traverse the air

cavity and lose energy. This trend is more significant for lower energy alphas. Due to the $1/\beta^2$ dependence in equation 2.5, the increase in absorbed dose is nonlinear with the decrease in energy. This poses a dosimetric challenge when the energy of the incoming alpha particle at the surface of a cylindrical shell, shown in figure 2.23, is varying as a function of off-axis distance due to the wide track-length distribution. Thus, the energy deposited in the cylindrical shell will be varying depending on the off-axis distance. This effect induces a non-linear relationship between the ionization current and the change in air gap.

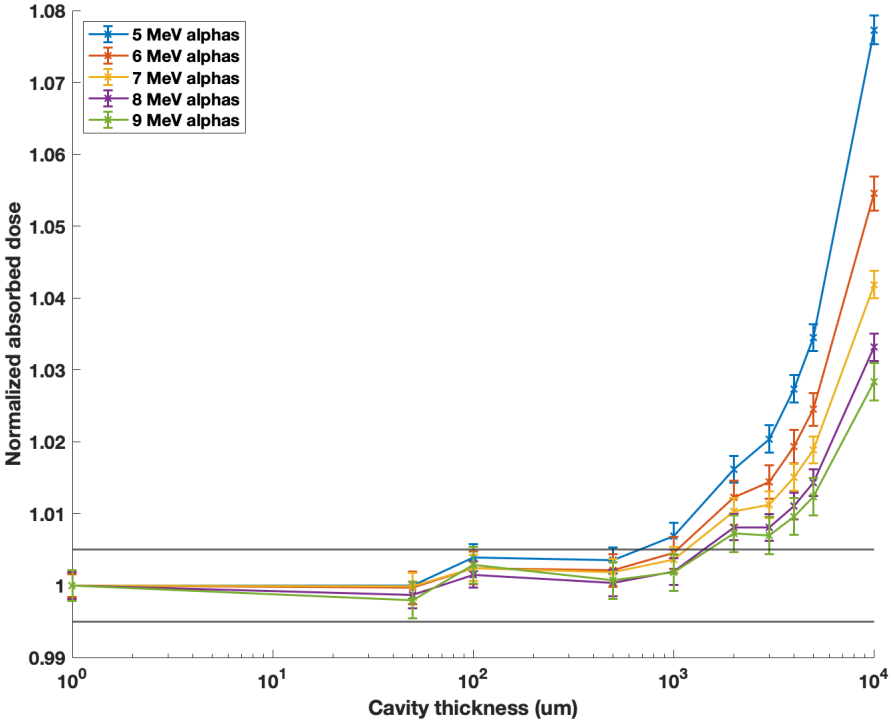

Figure 3.14: The change in absorbed dose with change in cylindrical cavity thickness for parallel alpha particle beams is shown. Absorbed dose was normalized to the value at 1 μm cavity thickness. The error bars correspond to 1σ statistical uncertainty.

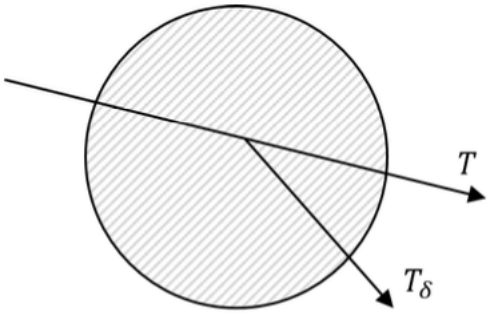

Figure 3.15: The loss in energy due to high energy δ-rays is shown (from MP 501 notes).

3.2.3 Spencer-Attix cavity

Following the introduction of the BG theory, several research groups noticed that the BG cavity theory collapsed when medium was composed of high Z materials such as lead [106]. This was later explained by Spencer and Attix that Bragg and Gray neglected the presence of δ-rays and didn't include the secondary charged-particle fluence in the BG theory [107]. As demonstrated in figure 3.15, secondary electrons (or δ-rays) generated by the primary particles might have sufficient energy to escape the cavity. If the loss of the energy carried away by the high energy δ-ray from the cavity is not replenished by another δ-ray entering the cavity, δ-ray equilbrium doesn't hold. Spencer-Attix (SA) cavity theory addresses two major problems with the BG cavity theory. The inclusion of secondary charged-particle fluence in the stopping power ratio calculation is formulated in SA cavity theory. Additionally, Spencer and Attix introduced an energy cut-off, Δ, for secondary particles that cannot cross the cavity. By doing so, the secondary charged particle spectrum can be divided into two groups: crosser particles that successfully traverse the cavity without any perturbation and absorber particles that may stop in the cavity and violate the BG condition. According to SA cavity theory and under δ-ray

equilibrium condition:

$$\frac{D_{med}}{D_{det}} = \frac{\int_{\Delta}^{E_{max}} \Phi_E^{total} \left(\frac{L_\Delta(E)}{\rho}\right)_{med} dE + \Phi_E^{total} \left(\frac{S_{col}(E)}{\rho}\right)_{med} \Delta}{\int_{\Delta}^{E_{max}} \Phi_E^{total} \left(\frac{L_\Delta(E)}{\rho}\right)_{det} dE + \Phi_E^{total} \left(\frac{S_{col}(E)}{\rho}\right)_{det} \Delta} \tag{3.7}$$

where L_Δ is the restricted stopping power and Δ is the energy cut-off. The choice of Δ is usually selected based on the detector size.

The maximum energy of the δ-rays, E_δ^{max}, when $m >> m_e$, where m is the mass of the primary particle and m_e is the mass of an electron, can be calculated by:

$$E_\delta^{max} = 2 m_e \nu_o^2 \tag{3.8}$$

where ν_o is the velocity of the primary particle. For an electron traveling with a relativistic velocity, the maximum energy of the δ-rays can be given by:

$$E_\delta^{max} = 2 m_e c^2 \beta^2 \gamma^2 \Big[2 + 2\gamma \Big] \tag{3.9}$$

where β is the relativistic velocity normalized by speed of light of the incoming electrons, and γ is the Lorentz factor [108]. In the case of 5-9 MeV alpha particles, the E_δ^{max} for δ-rays is shown in figure 3.16, using the equation 3.8, as well as their corresponding range in air. As seen in the figure, the E_δ^{max} has a linear relationship with the alpha energy due to ν^2 being proportional to the kinetic energy. It is of note that the alpha particles in the TAT energy range have non-relativistic velocities since their rest mass energy is 3727.379 MeV. The range of these δ-rays in air can be up to 0.9 mm depending on the energy of the alpha particle. Therefore, using a cylindrical air cavity of thicknesses < 1 mm as the l_1, as shown in figure 2.23, may not be sufficient to achieve δ-ray equilibrium in the cylindrical shell denoted by the Δl thickness.

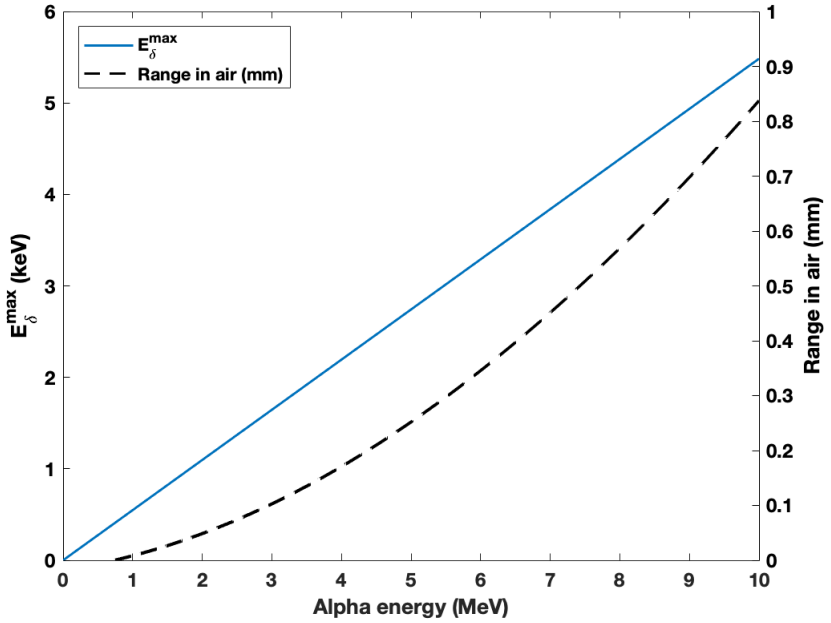

Figure 3.16: The maximum energy transferred to the δ-rays along with their range in air as a function of the incoming alpha particle energy.

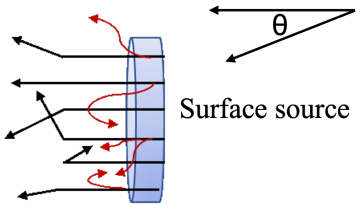

Figure 3.17: A schematic of the simulation setup is shown. The black arrows illustrate alpha particles and the red arrows correspond to delta electrons emitted by the primary particles.

A MC investigation was performed using a simplified geometry shown in figure 3.10. The GEANT4 MC code was used with the optimal physics parameters determined in section 3.1.2. Monoenergetic parallel alpha particles, as shown in figure 3.17, were simulated in the 5-9 MeV energy range. A cavity radius of 2 mm was selected arbitrarily and the production thresholds for all particles were set to <0.1 mm. This geometrical setup was identical to the one described in section 3.2.2 except that the δ-rays were simulated and tracked explicitly everywhere in the geometry. The δ-ray build-up and equilibrium was quantified by scoring the ratio of absorbed dose to air deposited by δ-rays to kinetic energy

per unit mass transferred to δ-rays by primary alpha particles. This ratio is analogous to Dose/KERMA ratio often used for photon beams to study charged particle equilibrium (CPE). The angular and spectral distribution of the δ-rays was also tallied.

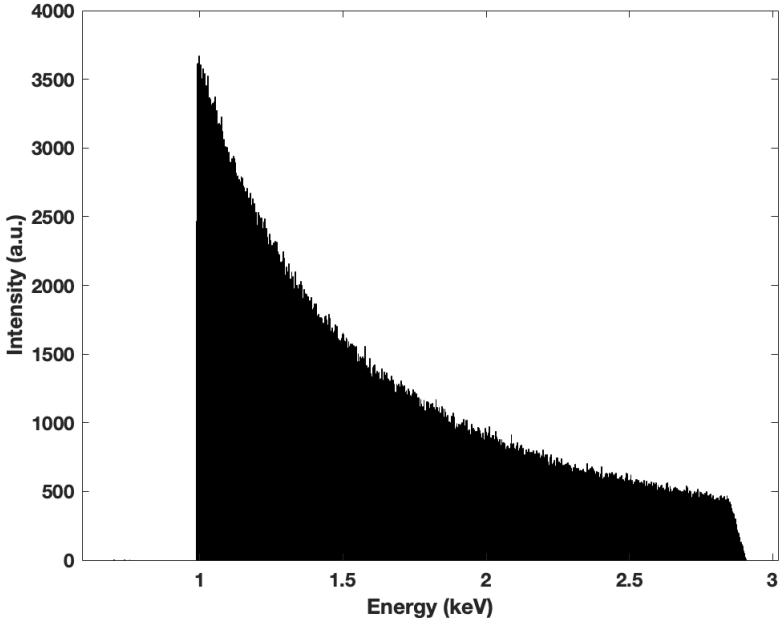

Figure 3.18: The δ-ray energy spectrum inside the air cavity from a 5.3 MeV parallel alpha particle beam source.

Figure 3.18 shows an in-air δ-ray energy spectrum from a 5.3 MeV alpha source. The E_{δ}^{max} value calculated by GEANT4 was found identical to the analytical equation written above. A broad energy distribution was observed for the δ-rays, which can be partially attributed to the spectral broadening of electrons as they traverse matter and lose energy to the surrounding medium. The δ-ray intensity was noted to be higher for smaller energies. The average δ-ray energy was calculated to be 1.61 keV. The sharp edge on the left side of the δ-ray energy spectrum is due to the production threshold parameter that halts tracking of any secondary particles with range below the specified value. In an attempt to compare the alpha particles to betas, an in-air δ-ray energy spectrum from a 5.0 MeV electron source is shown in figure 3.19. The average energy for δ-rays was

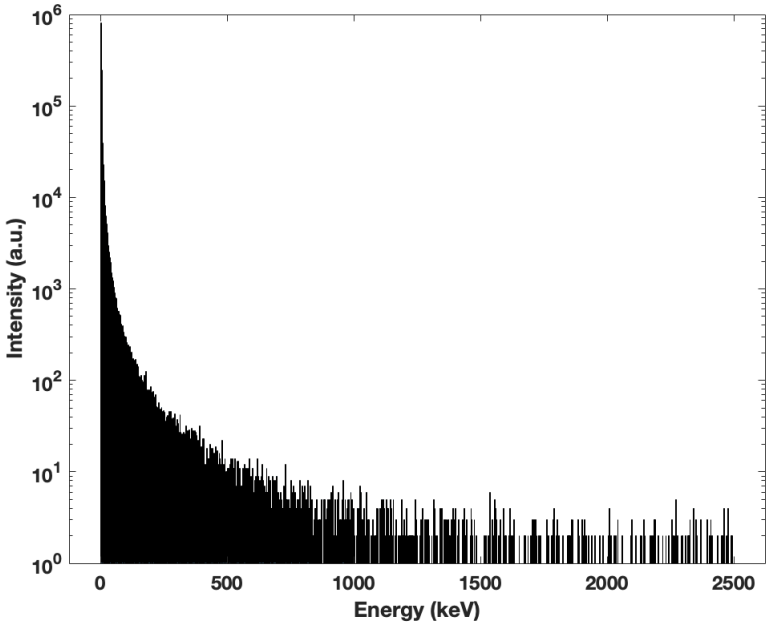

Figure 3.19: The δ-ray energy spectrum inside the air cavity from a 5.0 MeV parallel electron beam source.

calculated to be 7.37 keV, which is much greater than the maximum energy of the δ-rays liberated by alpha particles in the TAT energy range.

The build-up effect in the cylindrical air cavity is shown in figure 3.20. As the cavity thickness increases, the energy carried by high energy δ-rays outside the cavity decreases and an equilbrium is reached. The build-up region was found to be larger for higher energy alpha particles since the energy of the δ-rays, and hence the range, is directly proportional to the kinetic energy of the alpha particles. It was found that the equilibrium is achieved past the range of the δ-ray with the maximum energy, which was hypothesized in figure 3.16. The presence of the build-up region can be attributed to the forwardly-peaked δ-rays, as illustrated in figure 3.21. If the angular distribution of the emitted δ-rays was isotropic, the energy carried away from the cavity would have been replenished by the energy carried inside the cavity. It was found that the δ-rays from higher alpha energy particles was relatively more forwardly-peaked than the lower energy particles.

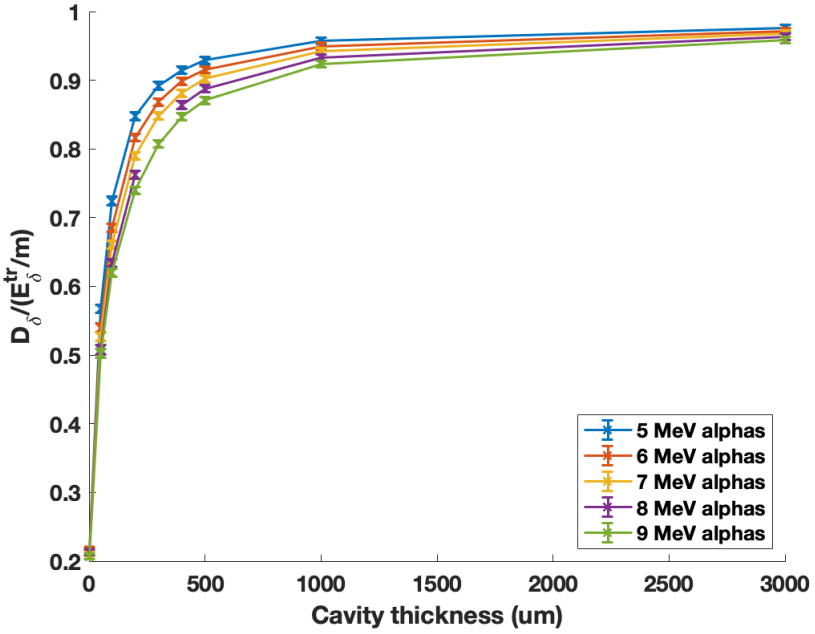

Figure 3.20: The δ-ray build-up effect is demonstrated by plotting the ratio of absorbed dose deposited by δ-rays to kinetic energy per unit mass transferred to δ-rays by primary alpha particles.The error bars correspond to 1σ statistical uncertainty.

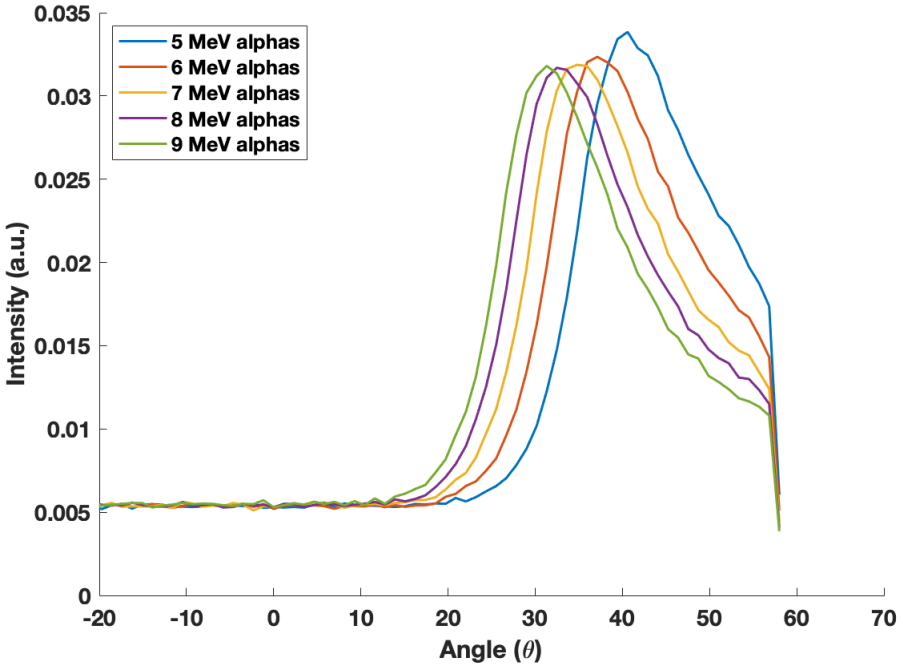

Figure 3.21: The emission angular distribution, with respect to the direction of the parent alpha particle, of the δ-rays in a 100 μm thick cylindrical air cavity is shown.

The average emission angle was calculated to be in the 17-21° range. The build-up region due to high $\delta - rays$ has been previously shown in proton therapy and is analogous to the build-up region found in the megavoltage photon beams [109]. Although the forwardly-peaked electrons emitted in megavoltage photon beams are due to the Compton scattering, whereas the electrons emitted in TAT are due to hard collisions of alphas with the medium, the fundamental concept behind the escape of the δ-rays remains the same. It is noteworthy that the build-up region due to δ-rays is much smaller in water since the range of a 6 keV electron is <1 μm in water.

Although a build-up effect was observed with a parallel alpha beam source, the δ-rays in the measured geometry, shown in figure 2.23, traverse a much longer distance than the air gap (l). Due to the diverging source, the δ-rays traveling along an oblique angle, relative to the central axis, reach an equilbirum before reaching the detector. On the other hand, any δ-rays that traverse along the central axis only reach equilibrium if the air gap is greater than the range of the δ-rays. Thus, this effect induces a non-linear relationship between the ionization current and the air gap.

3.2.4 Comparison of stopping power ratios

Over the past few decades, there have been many updates to the Bethe-Bloch stopping power shown in equation 2.5. The updated stopping power equation can be given by:

$$\frac{dT}{dx} = 2\pi r_e^2 mc^2 n_{el} \frac{z^2}{\beta^2}\left[ln\left(\frac{2mc^2\beta^2\gamma^2 T_{max}}{I^2}\right) - 2\beta^2 - \delta - \frac{2C_e}{Z} + S + F\right] \tag{3.10}$$

where r_e is the classical electron radius, m is the mass of an electron, c is the speed of light, n_{el} is the electron density in the absorber medium, I is the mean ionization energy, Z is the atomic number of the absorber, z is the atomic number of the incoming particle, γ is the Lorentz factor, β is the relativistic velocity normalized by speed of light, T is the kinetic energy of the incoming particle, δ is the density-effect function, C_e is the shell correction function, S is the spin term, and F is a combination of high order corrections [110] [111] [108]. The International Commission on Radiation Units and Measurements (ICRU) has previously reported stopping power tables considering the published Bethe-Bloch corrections. In chronological order, the two reports that are relevant for alpha particles are report 49 and report 90 [112] [113]. The GEANT4 MC version used in this work utilizes the ICRU 49 stopping power by default and can be adapted to use the latest ICRU 90 stopping power tables. Before making such a change, the differences between the two stopping power tables for water and air need to be evaluated.

Figure 3.22 shows the ICRU report 49 stopping powers for water and air and compares them to the ICRU 90 data. The air stopping power data for both reports were within 0.1% of each other. However, the report 90 water stopping power was observed to be 1.5% lower relative to report 49 data especially in the 2-10 MeV alpha energy range. This difference can be partially attributed to the different mean ionization energies for water used by the two reports. The report 90 used an I of 78 eV, whereas the report

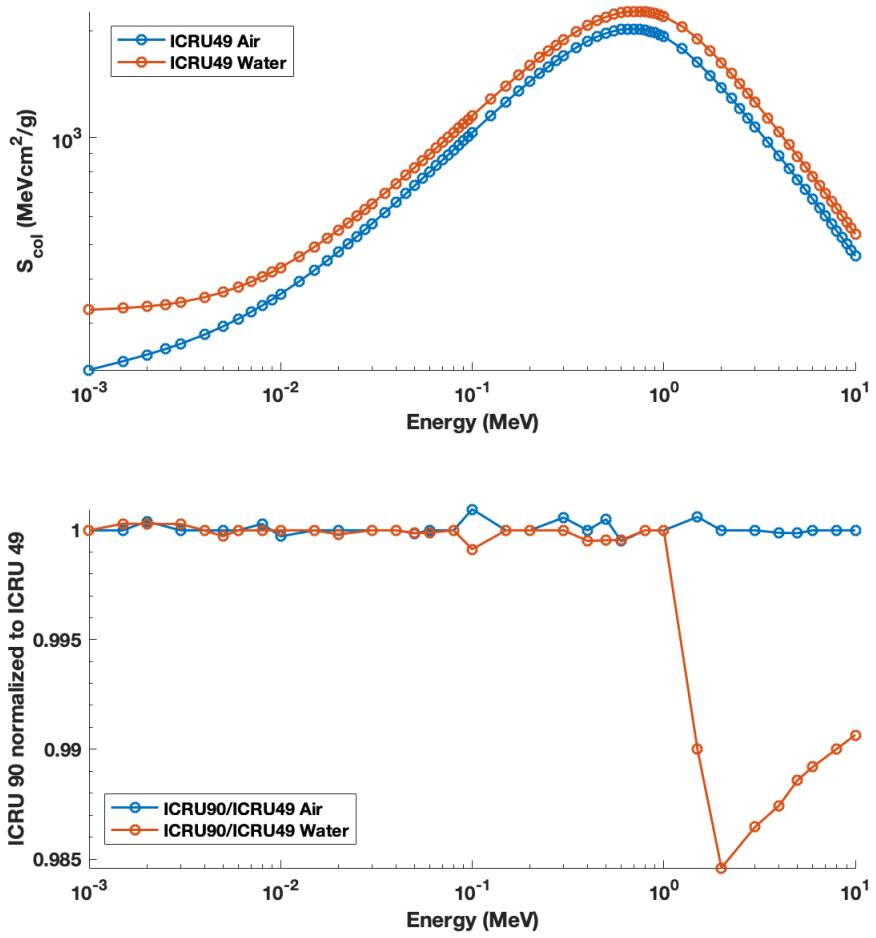

Figure 3.22: Top: The IRCU report 49 stopping powers are shown for water and air. Bottom: The ICRU report 90 stopping powers, normalized to the ICRU report 49 stopping powers, for water and air.

49 uses an I value of 75 eV [112] [113]. The difference in the water stopping power data manifests in the water to air stopping power ratio curves, as shown in figure 3.23.

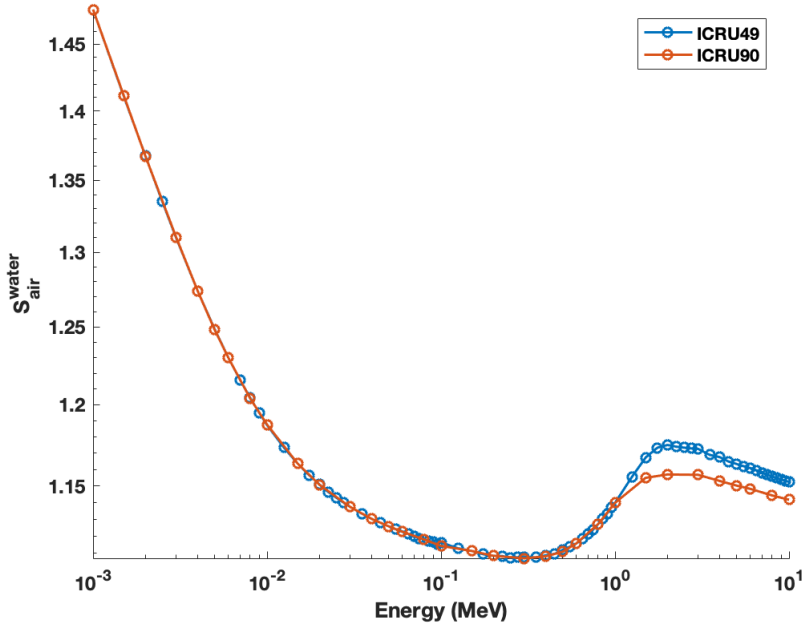

Figure 3.23: The water to air stopping power ratios are shown for the ICRU report 49 and report 90.

3.3 Source and substrate specifications

3.3.1 Introduction and motivation

In this work, the quantity of interest is absorbed dose from point-like alpha-emitting radionuclides. However, such sources are rarely fabricated and can only be approximated in the best case scenario. Any encapsulation used on alpha sources can completely absorb the emitted alpha particles or greatly attenuate the source depending on the material and thickness of the encapsulation. Further, the finite thickness of the source itself can filter the alphas to great extent. The effect of self-absorption, presence of an entrance window for an ion chamber, and finite diameter of the source must be investigated using the measurable geometry shown in figure 2.23. It is noteworthy that this section only studies alpha particles, whereas clinical alpha-emitting radionuclides may have beta and gamma emissions in addition to alphas.

3.3.2 Source diameter

Changing the source diameter has an impact on the track-length distribution of alpha particles inside the air cavity and, therefore, influences the absorbed dose. A MC investigation was performed using the GEANT4 code with the optimal physics parameters determined in section 3.1.2. Monoenergetic isotropically-emitting alpha particles were simulated in the 5-9 MeV energy range. A cylindrical cavity diameter of 4 mm and thickness of 100 μm was selected arbitrarily and the production thresholds for all particles were set to <0.1 mm. Circular sources of varying radii were simulated at the flat surface of the cylindrical air cavity and the impact of source diameter on absorbed dose was studied. As demonstrated in figure 3.24, the absorbed dose to air decreases with increasing source diameter. The absorbed dose to cavity was found to gradually decrease with increasing source diameter until the source diameter exceeded the cavity diameter. The change in absorbed dose with source diameter was found to be independent of the alpha energy simulated. When source diameter > cavity diameter, a sharp fall-off in the absorbed dose was observed with increasing cavity diameter, which is due to the loss of fluence in the cavity once particles start originating outside the surface of the sensitive volume. Therefore, a source diameter < 4 mm is desired to minimize the magnitude of the correction factor when the quantity of interest is absorbed dose to water from a point source.

Employing a uniformly-emitting source was considered appropriate for an initial characterization of the source dimensions. However, most actual alpha sources exhibit a strong "coffee-ring" effect due to the radially-outwards flow of the fluid during evaporation. Therefore, it is pertinent that the impact on absorbed dose from ring-like sources must be investigated. MC simulations were repeated using the geometry above except substituting uniformly-emitting circular source to ring sources with a 100 μm thick annuli

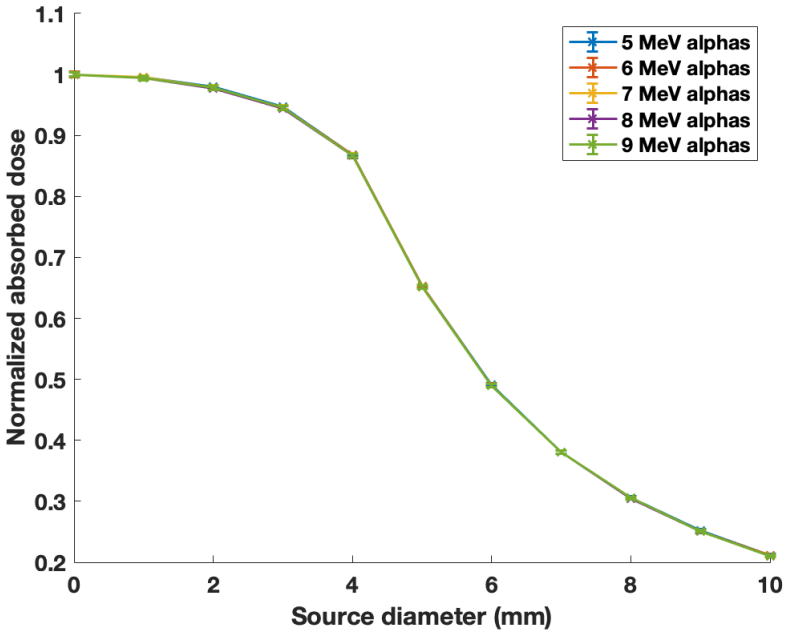

Figure 3.24: The impact of source diameter on the absorbed dose to cavity using a uniformly emitting source. The absorbed dose values were normalized to the absorbed dose calculated for a point source. The error bars correspond to 1σ statistical uncertainty.

and varying internal diameter. Figure 3.25 shows the effect of various internal diameters of a ring source on absorbed dose to air. The absorbed dose versus source's inner diameter curve was found to resemble the circular source curve shown in figure 3.24. As sharp decrease in absorbed dose was noted when the inner diameter of the ring source exceed the cavity diameter due to the loss of fluence from the air cavity. The impact on absorbed dose to cavity from both a ring source and a circular source was compared in figure 3.26. With an increase in source diameter or source's inner diameter, the absorbed dose decreased in both cases with a much sharper decrease for the ring source. For a circular source, increasing the source diameter increases the probability of an alpha particle originating outside the air cavity, which leads to a reduction in absorbed dose when compared to a point source. Even when the source diameter exceeds the cavity diameter, the probability of an alpha particle originating on the surface of the cavity remains non-zero. Contrarily, when the inner diameter of a ring source exceeds the cavity

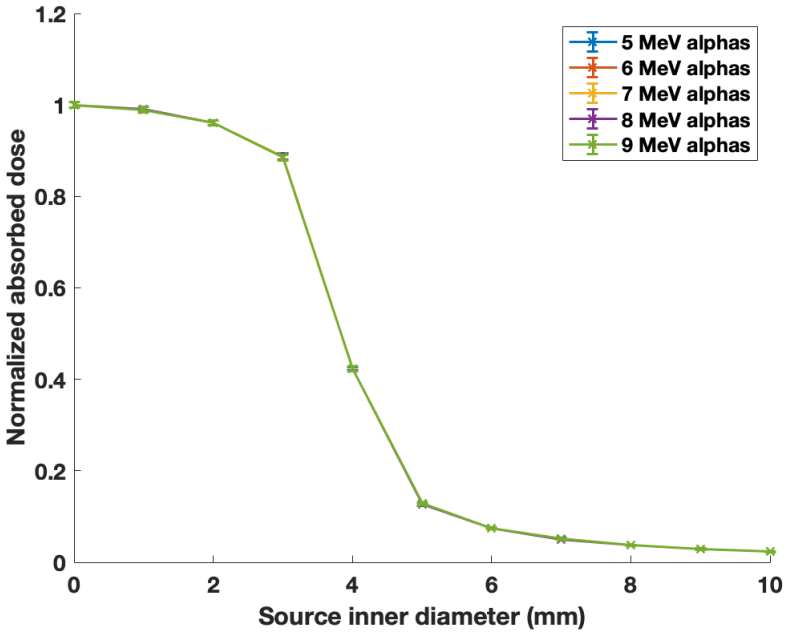

Figure 3.25: The impact of source internal diameter on the absorbed dose to cavity using a 100 μm-thick ring source. The absorbed dose values were normalized to the absorbed dose calculated for a point source. The error bars correspond to 1σ statistical uncertainty.

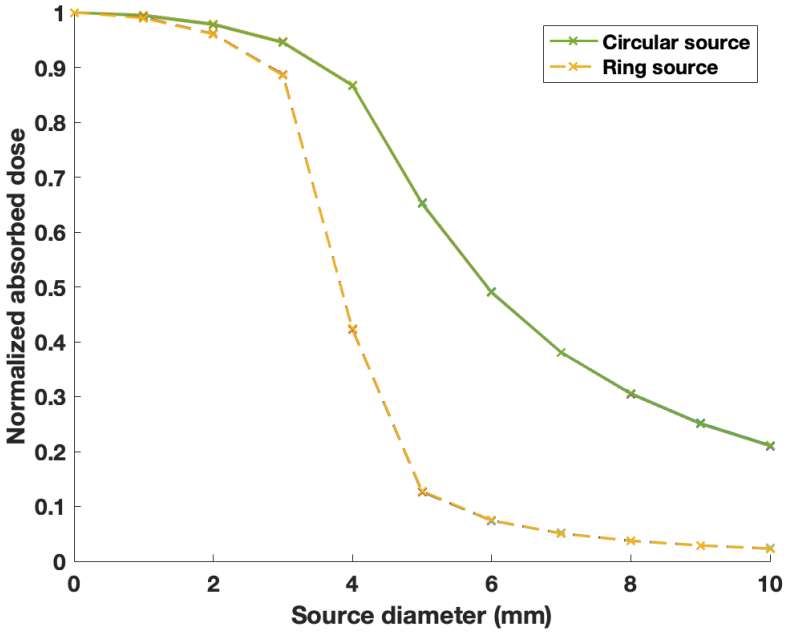

Figure 3.26: The differences between the impact of a ring source and a circular source on absorbed dose are shown. The absorbed dose values were normalized to the absorbed dose calculated for a point source.

diameter, all alpha particles originate outside the air cavity leading to a drastic reduction in fluence inside the cavity. It can be concluded from this work that the correction factor accounting for the finite size of the source, k_{point}, remains small when the source outer diameter is smaller than the air cavity diameter. Sources with larger spatial distribution must be avoided especially when ring-like sources are involved.

3.3.3 Self-absorption and filtration

All alpha sources have some magnitude of self-absorption and filtration that can degrade the energy of the emitted alpha particles. At extreme cases, a significant number of alpha particles are absorbed and never escape the boundaries of the source. The extent of the self-absorption is predominantly determined by the thickness and the density of the source. A MC investigation was performed using the GEANT4 code with the optimal physics parameters determined in section 3.1.2. Monoenergetic isotropically-emitting alpha particles were simulated in the 5-9 MeV energy range. A cylindrical cavity diameter of 4 mm and thickness of 100 μm was selected arbitrarily and the production thresholds for all particles were set to <0.1 mm. A uniformly emitting disk source of 3 mm diameter and varying thickness was simulated at the flat surface of the cylindrical air cavity and the impact of source thickness on absorbed dose was studied. The simulated source consisted of polonium dioxide with a 8.9 g/cc mass density. The high atomic number, atomic mass, and density of polonium serves as a good approximation of the radionuclides used in TAT. Ideally, the magnitude of self-filtration should be determined using the exact material composition and density of the radionuclide being investigated. Using polonium as an approximation, the impact of source thickness on absorbed dose is shown in figure 3.27. A self-attenuation of $< 2\%$ was found for source thickness below 500 nm for all alpha particle energies; whereas, a significant attenuation was found for sources with thickness > 1 μm. The self-filtration effect is greater for lower energy alpha particles especially

when the source thickness was greater than $> 1\ \mu m$. To avoid correction factors $> 5\%$, source thickness < 500 nm is desired.

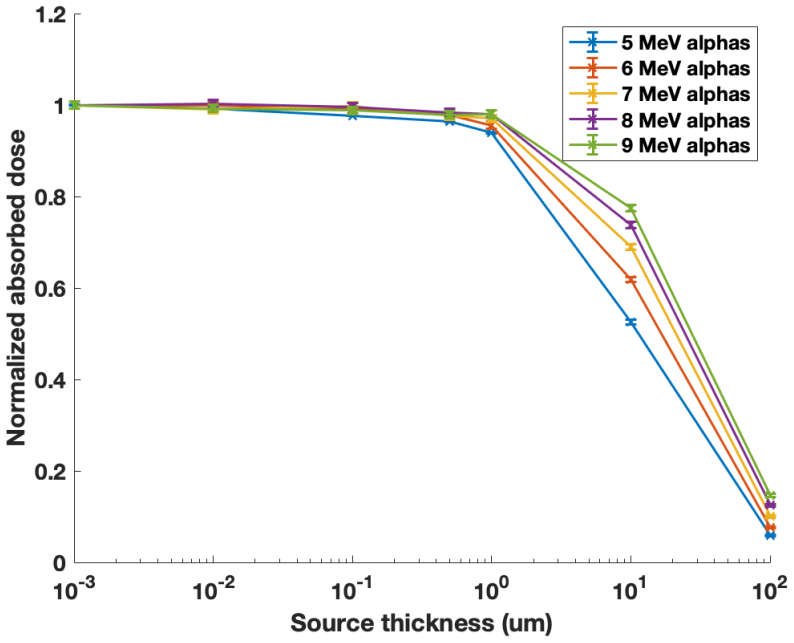

Figure 3.27: The magnitude of self-filtration and attenuation is demonstrated by plotting absorbed dose against various source thicknesses. The absorbed dose values were normalized to the value for smallest source thickness i.e. 1 nm. The error bars correspond to 1σ statistical uncertainty.

Table 3.6: Correlation between the FWHM of the alpha peaks and source thickness due to energy straggling.

Source thickness (μm)	FWHM (keV)
0.001	3
0.01	8
0.1	38
1	358
10	3520

Self-filtration in an alpha source is closely related to the source thickness and can be indirectly quantified using the full width at half maximum (FWHM) value of a given alpha peak using alpha spectroscopy [114]. To authors' knowledge, there is a paucity of literature establishing a correlation between the source thickness and the FWHM of the

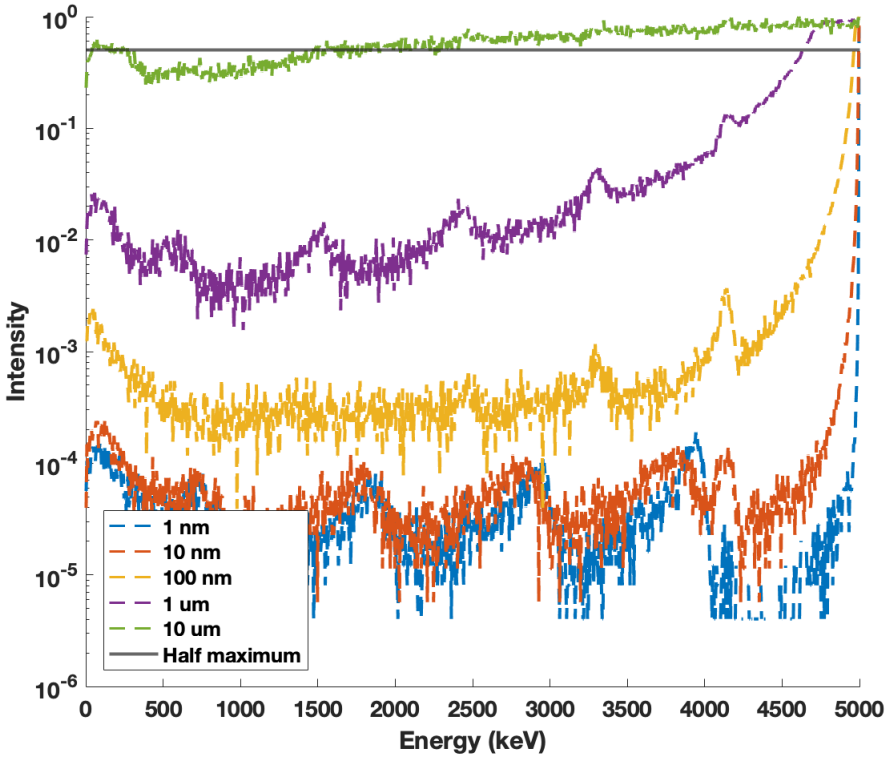

Figure 3.28: The alpha energy spectra are shown for various source thicknesses using a 5 MeV monoenergetic alpha source.

alpha peaks measured using spectroscopy. Therefore, the change in the alpha spectrum with increase in source thickness at the surface of the source was investigated using MC simulations. The simulation geometry was the same as the one described above except that a phase space file was scored at the surface of the source and the source was simulated to be a 5 MeV monoenergetic source with the source material being polonium dioxide. The energy distribution was extracted from the phase space file and binned into 5 keV energy bins. Figure 3.28 shows the 5 MeV alpha energy spectra for various polonium source thicknesses in an attempt to correlate the FWHM of the alpha peak with physical thickness of the source. The intensity was normalized to the maximum value for all thicknesses. The energy straggling effect increases with increasing source thickness leading to a broadening of the alpha peak. For larger thicknesses, the alpha peak gets

significantly degraded and eventually becomes indistinguishable. The FWHM values for various source thicknesses are compiled in table 3.6. Based on the displayed data, any source with a FWHM < 40 keV will lead to a negligible self-filtration and can be simulated as a planar 2D source instead of a volumetric source. Therefore, the upper limit on the FWHM of alpha peaks was set to 40 keV throughout this work and any source with a wider peak must employ a correction factor accounting for the reduction in absorbed dose due to self-filtration. The thickness estimate made in this work is a conservative one considering the measured energy resolution of the alpha peak will be lower than the actual resolution due to the imperfection of the spectroscopy equipment. The results from this study provide good approximation of the self-filtration and attenuation alpha particles undergo before escaping the source boundaries.

Based on the results discussed in this section, a thin-film source with thickness < 500 nm and diameter < 4 mm is desired. The desired source specifications compete with each other since a smaller source diameter often leads to a thicker source to retain the same radioactivity magnitude.

3.3.4 Entrance window

The usage of an entrance window or a wall for ionization chambers is common in radiation dosimetry. However, the presence of an entrance window may deteriorate the absorbed dose measurements and must be avoided. Therefore, this work resorts to using only windowless extrapolation chambers. The possibility of contaminating the collecting electrode with radioactivity and the difficulty in achieving a good alignment between the substrate and the electrode surfaces was hypothesized to be challenging when using windowless chambers. Therefore, the inclusion of an aluminized Mylar as entrance window was put forth as an alternative if the problems described above become too dominating. A MC

investigation was performed to study the impact of an entrance window on absorbed dose to cavity using the GEANT4 MC code and a cylindrical air cavity of 4 mm diameter and 100 μm thickness. With the presence of a Mylar entrance window, the change in absorbed dose to cavity with various window thicknesses is shown in figure 3.29. The distance from cavity entrance to source's surface was kept constant at 100 μm to avoid excessive side-loss of particles. Due to the increase in stopping power with decreasing alpha energy, absorbed dose was found to increase for window thicknesses below 5 μm as alpha particle energy decreased with attenuation. For window thickness > 5 μm, a sharp decrease in absorbed dose was observed due to the complete absorbance of particles in the entrance window. As an alternative to a windowless geometrical setup, an entrance window with thickness ≤ 5 μm may be utilized, along with a correction factor.

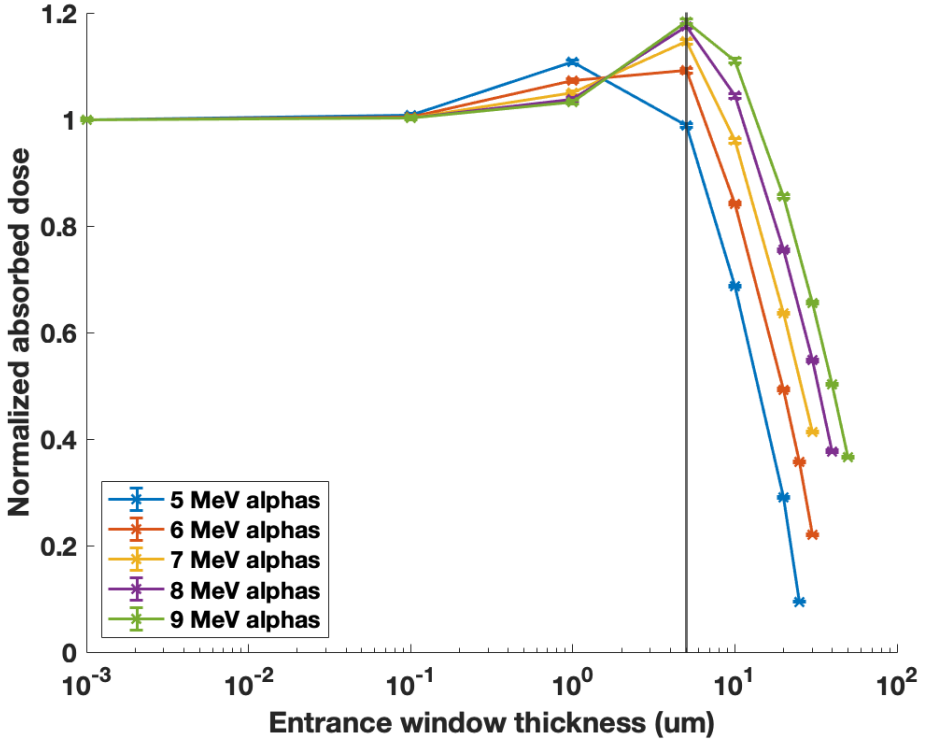

Figure 3.29: The impact of the thickness of an aluminized Mylar entrance window on the absorbed dose to cavity. The absorbed dose values were normalized to the value at the smallest window thickness. The vertical line indicates the 5 μm thick Mylar film that is commercially available. The error bars correspond to 1σ statistical uncertainty.

Chapter 4

Construction and evaluation of a D400 planar windowless extrapolation chamber as a primary standard for absorbed dose

4.1 Construction of the apparatus

To measure absorbed dose to air, several ionization current readings are required at various different air gaps between the source and the detector planes. Additionally, the change in mass of the cylindrical cavity must be accurately and precisely known, which requires high precision motion stages. It is crucial that the detector and source are aligned parallel to each other. Any tilts in the geometry can lead to an inaccurate assessment of the mass of the air cavity. The air gaps for these measurements can be as low as 100 μm. With such a small distance between the detector and the source surfaces, it

is important to evaluate the flatness of the surfaces to determine the smallest air gap possible for measurements. Any surfaces with large camber/bowing will limit small air gaps. Further, it is important to ensure that the detector and the source are not in contact with each other to prevent contamination of the detector with radioactive sources.

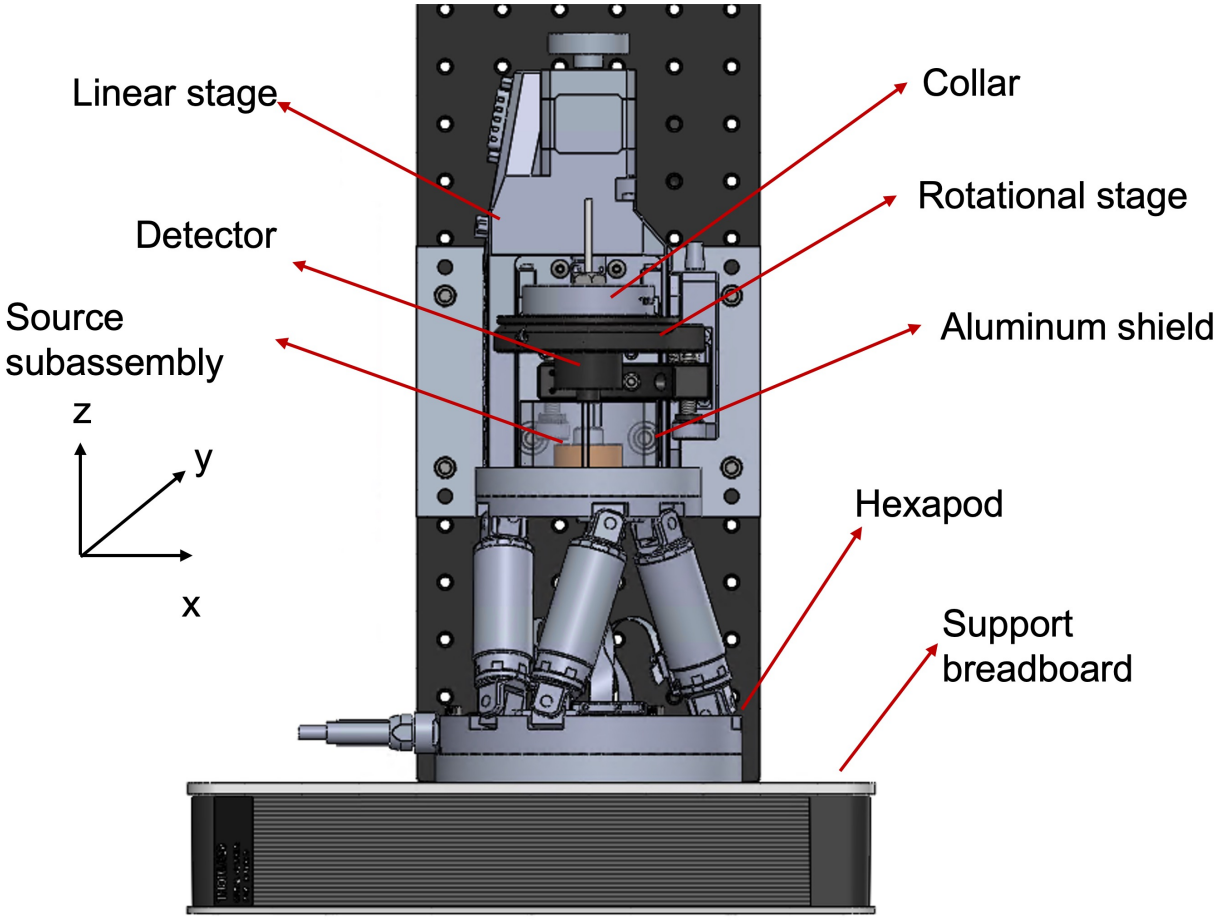

Figure 4.1: An XZ view of the apparatus assembly is shown with the D400 detector mounted.

Figures 4.1 and 4.2 show SolidWorks design of the apparatus assembly. The individual parts are labeled in figure 4.1. Throughout this work, the coordinate system shown in figure 4.1 will be used. The detector and the source are supported by two breadboards placed orthogonal to each other using 90 ° aluminum brackets. The source subassembly was mounted on a miniature hexapod stage (PI H-811.I2) that is capable of both translation and rotational motion in all three axes. The translational motion allows variation

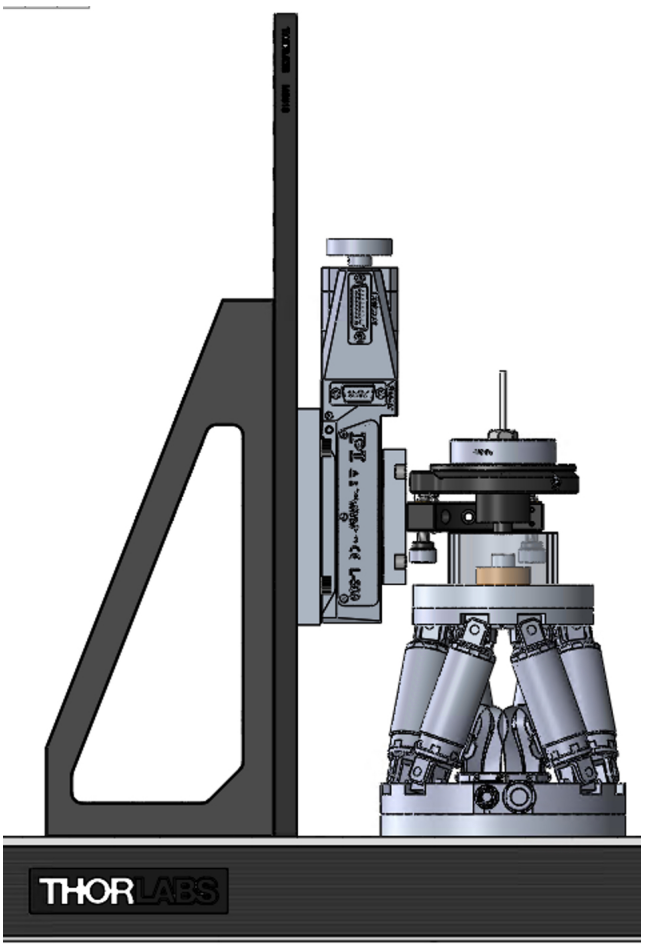

Figure 4.2: A YZ view of the apparatus assembly is shown with the D400 detector mounted.

of the air gap and the rotational motion allows establishment of parallelism between the detector and source planes. The travel range, minimum incremental motion, and repeatability of the hexapod stage are compiled in table 4.1. The excellent repeatability ($< 1\mu m$) and small incremental motion ($< 1\mu m$) for the hexapod stage allows for a highly precise alignment of the detector and source with respect to each other. Additionally, the change in air gaps on the order of 1-10 μm are possible with the current assembly. The hexapod also allows rotation about an arbitrary pivot point and can manipulate the coordinate system based on rotational or translational shifts. Figure 4.3 shows the hexapod stage

along with the controller (PI C-887) that is used to drive the motion stage. The hexapod stage can be driven using a set of macro commands that can be provided to the PI hexapod software. Macro commands can be utilized for basic stepping motion, scanning along arbitrary axes, or to create a custom coordinate system.

Table 4.1: Relevant specifications for the miniature hexapod motion stage.

Motion	Value
Travel range in X, Y (mm)	$\pm$17, $\pm$16
Travel range in Z (mm)	$\pm$6.5
Travel range in θ_X, θ_Y (deg)	$\pm$10, $\pm$10
Travel range in θ_Z (deg)	$\pm$21
Minimum incremental motion X, Y (μm)	0.2
Minimum incremental motion Z (μm)	0.08
Minimum incremental motion θ_X, θ_Y (urad)	2.5
Minimum incremental motion θ_Z (urad)	5
Repeatability X, Y (μm)	$\pm$0.15
Repeatability Z (μm)	$\pm$0.06
Repeatability θ_X, θ_Y (urad)	$\pm$2
Repeatability θ_Z (urad)	$\pm$3

Since the travel range along the z-axis of the hexapod is only 6.5 mm, a linear stage (PI L-509) was mounted on a breadboard that is capable of 52 mm travel. Table 4.2 shows the appropriate specifications for the linear motion stage. The linear stage is driven by a controller (PI Hydra controller), as shown in figure 4.5. Similar to the hexapod stage, the linear stage can be driven using a set of macro commands similar to the ones shown in figure 4.4. A rotational stage (Thor labs KS2RS) with a 2" diameter was mounted on top of the linear stage to allow rotational freedom about the z-axis. An optical collar with a radial step of 0.1 " was screwed onto the rotational stage to allow placement of different detectors or parts. With the use of the linear and rotational stages, the detector subassembly can be translated or rotated about the z-axis.

The source subassembly was placed on top of the hexapod stage with an aluminum shield placed around the source to reduce electronic noise and provide shielding from the

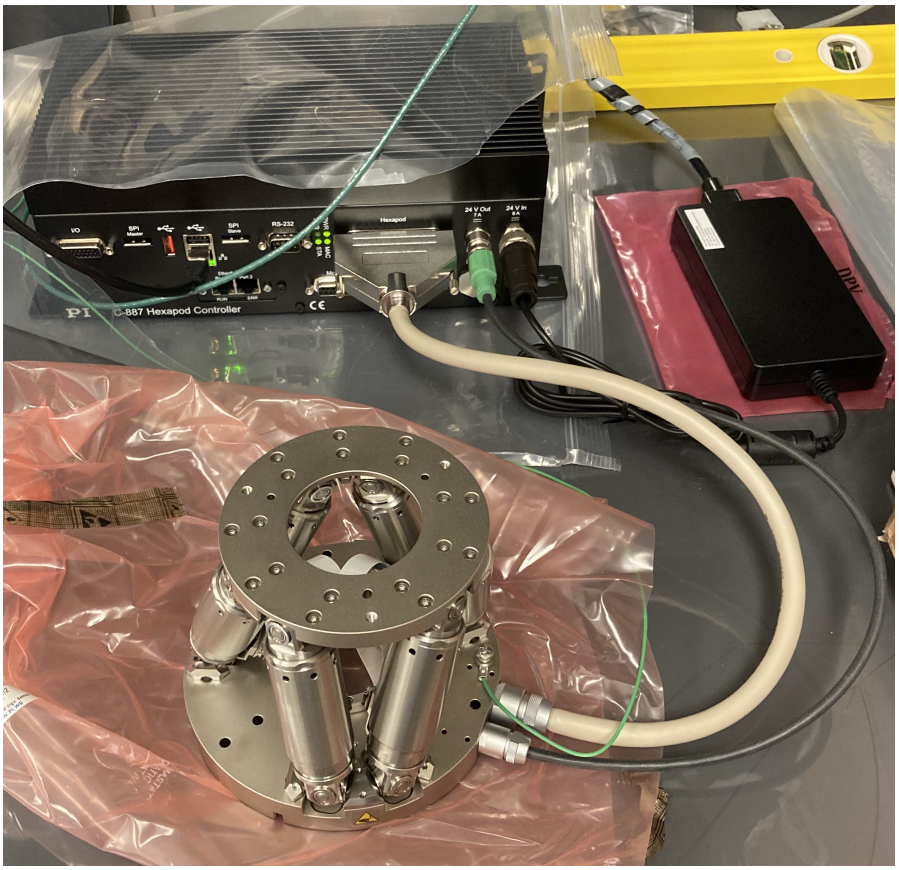

Figure 4.3: The PI hexapod stage and controller are shown.

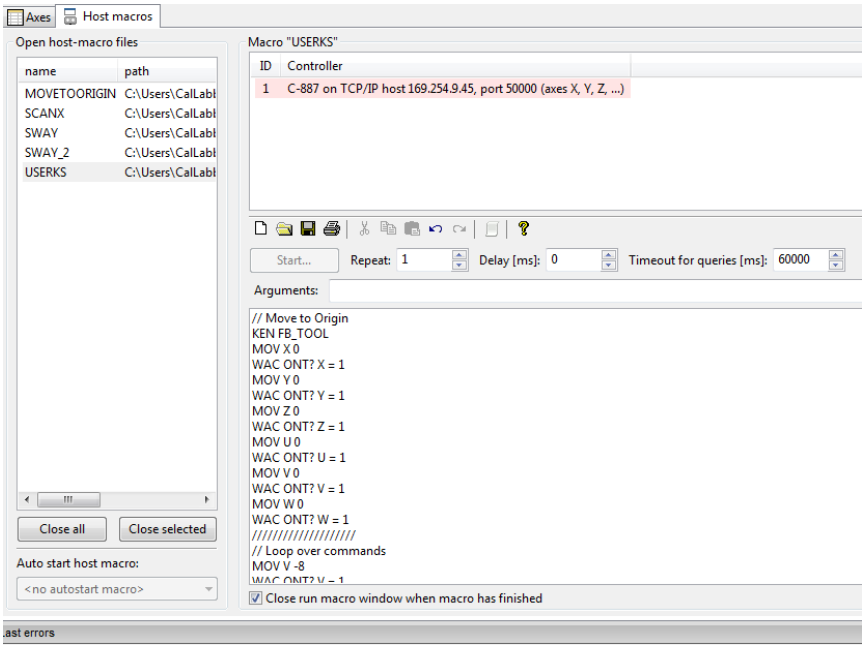

Figure 4.4: An example of the macro commands for the hexapod motion stage.

Table 4.2: Relevant specifications for the linear motion stage.

Motion	Value
Travel range in Z (mm)	52
Minimum incremental motion Z (μm)	0.5
Repeatability Z (μm)	± 0.2

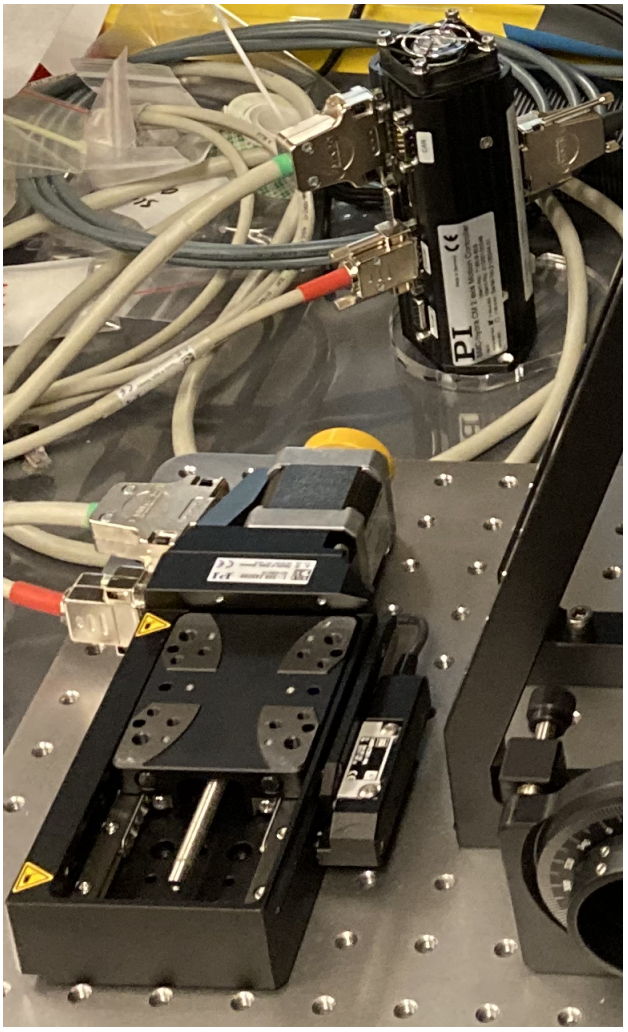

Figure 4.5: The PI linear stage and controller are shown.

radiation sources. Figure 4.6 shows the two halves of the aluminum shield that can be combined to form a cylindrical ring placed around the source. The shield was placed in a well created in the mating plate between the hexapod stage and the source subassembly. The well was machined to match the outer diameter of the shield. Schematics of the source subassembly are shown in figure 4.7. A polycarbonate-based holder and a cover were designed to hold the aluminum source holder and to contain the source for transportation purposes. The cover can be guided onto the plastic holder using dowel pins. The source itself was placed onto an aluminum part that contains a hole in the middle for a long metal screw. The aluminum part also has three other holes placed 120 ° apart to allow placement of neodymium magnets inside them. The neodymium magnets hold the source substrate in its place. The function of the screw in the middle is to provide electrical connectivity to the source substrate as well as to push the source substrate out for safe manipulation of the source. Figure 4.8 shows the constructed source assembly without the source substrate placed on the aluminum holder.

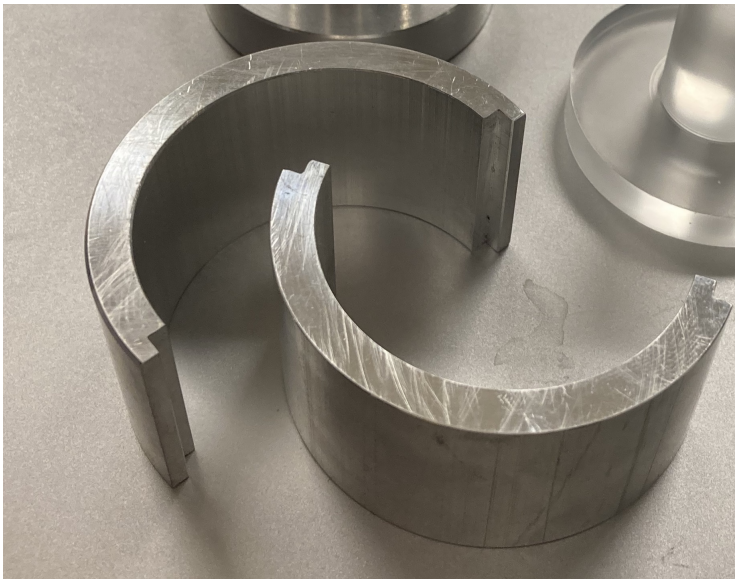

Figure 4.6: The aluminum shield surrounding the source subassembly is shown.

In order to align the z-axis of the source and detector subassemblies, a cylindrical centering part was constructed with an inner diameter equal to the outer diameter of the

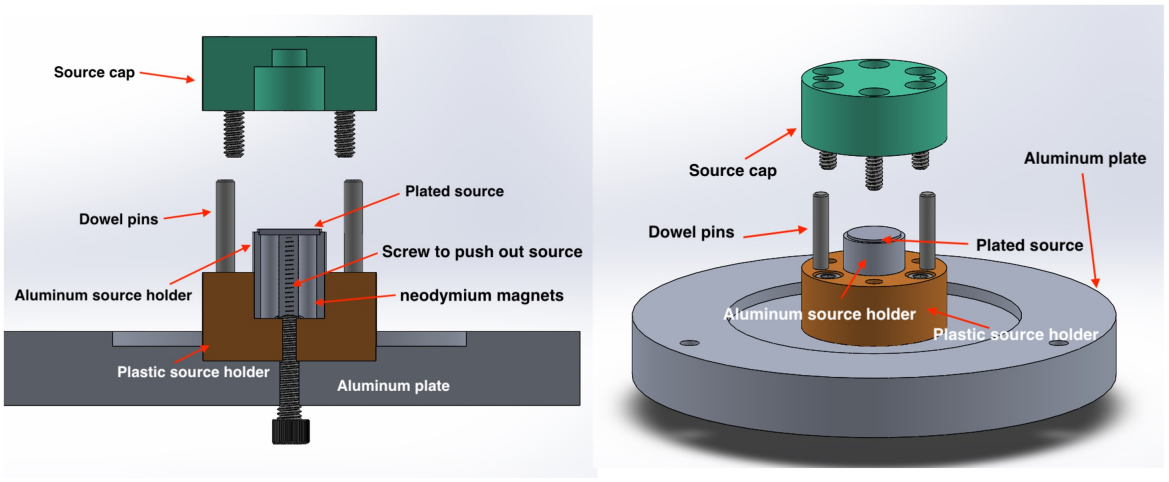

Figure 4.7: SolidWorks schematics of the source subassembly are shown.

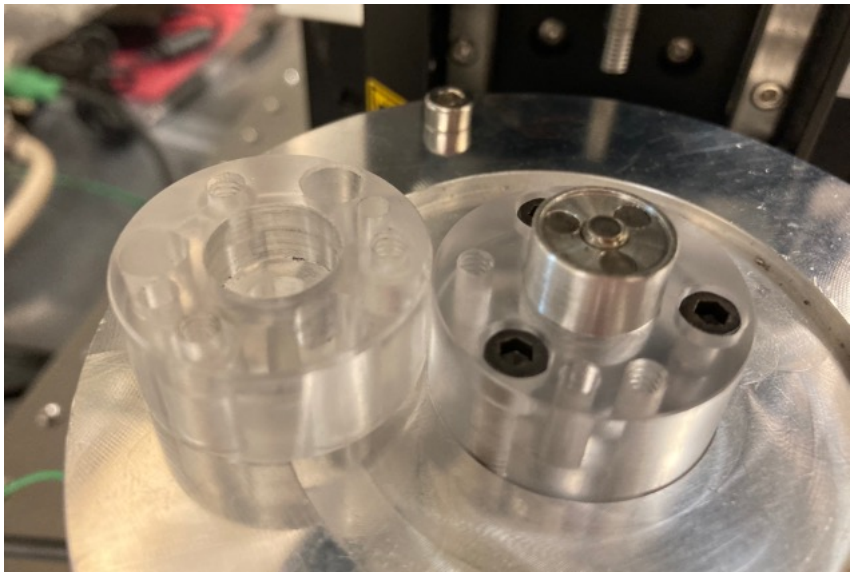

Figure 4.8: The constructed source subassembly is shown.

aluminum source holder shown in figure 4.8 with an added margin of 0.1 mm. Figure 4.9 shows the constructed apparatus with the centering part aligning the detector and source subassemblies. The electrical bias to the source substrate was provided using a DC voltage generator (Fluke 343A). The applied bias was measured and confirmed using a multimeter (HP 34401A). The voltage generator and the multimeter are shown in figure 4.10.

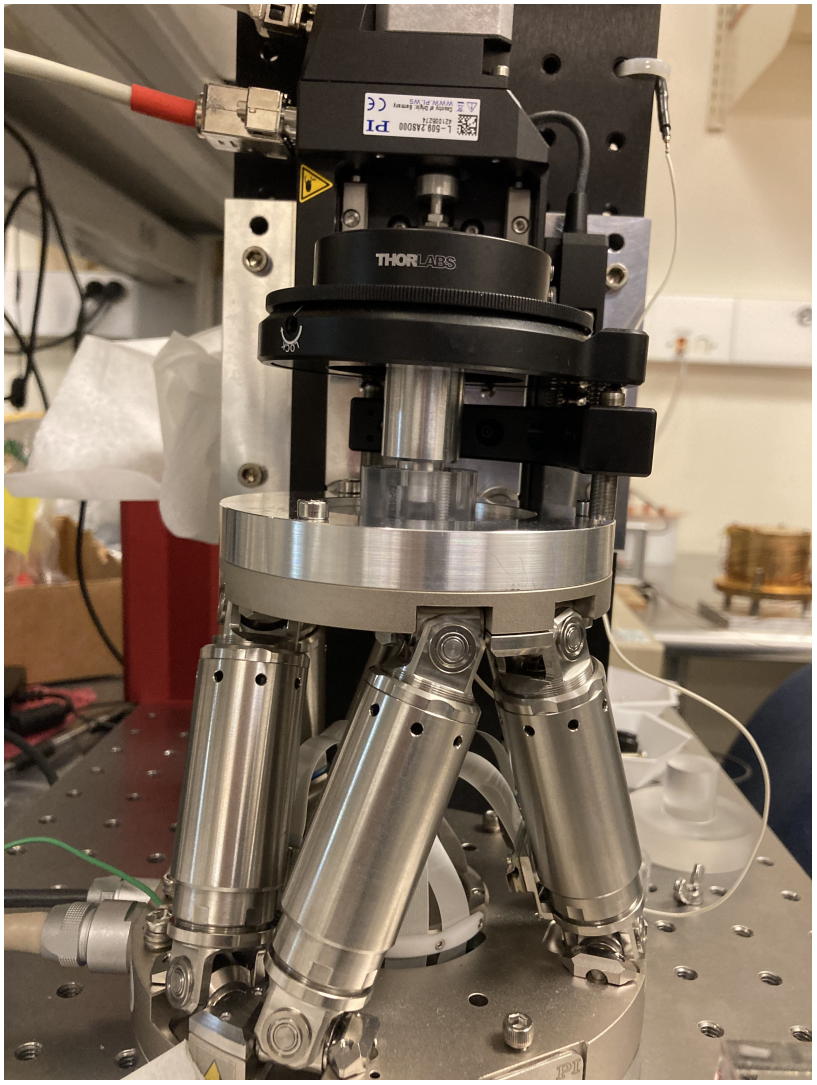

Figure 4.9: The constructed apparatus assembly is shown with the centering part in the detector slot.

4.1.1 D400 extrapolation chamber

The D400 extrapolation chamber (EC), shown in figure 4.11, was previously used by Hansen et al. for measurement of surface absorbed dose to water from ophthalmic applicators [77] [115] [15]. Figure 4.12 shows the modified D400 EC for alpha dosimetry. The collector and the guard were made of D400 material, which is a conducting plastic equivalent to polystyrene in atomic composition and has a physical density of 1.16 g/cm^3. The collector nominal diameter of 4.00 mm remained the same between the two versions.

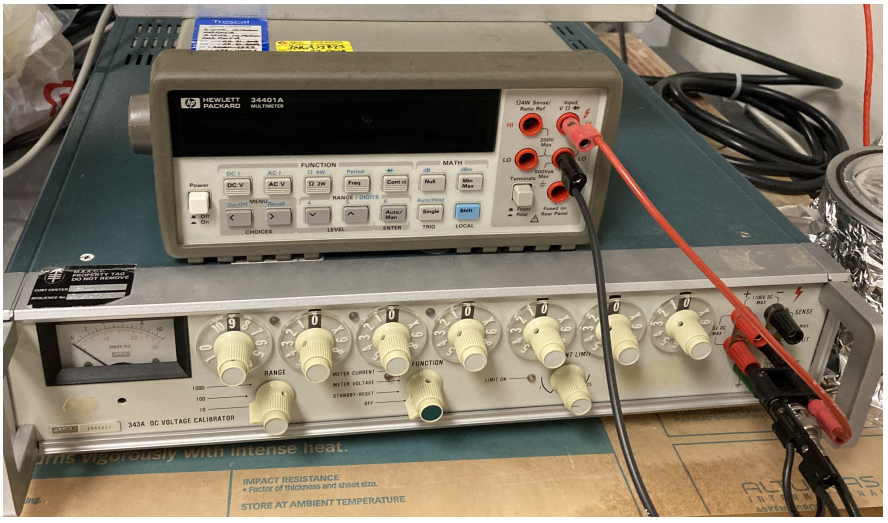

Figure 4.10: The DC voltage generator and the multimeter used throughout this work.

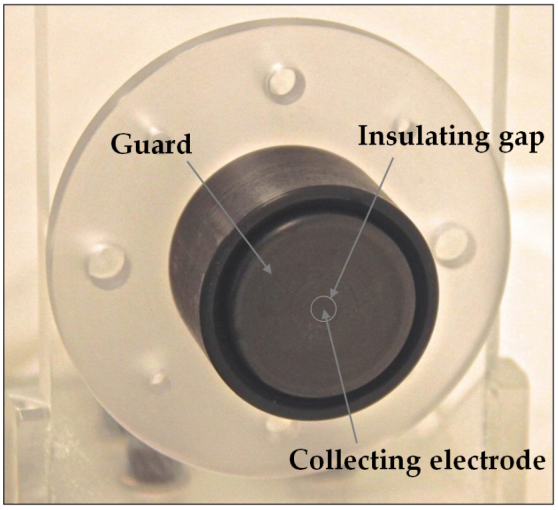

Figure 4.11: The D400 EC used by Hansen et al. for ophthalmic applicator measurements [15].

The two major changes to the EC were reduction of the guard's outer diameter from 30 mm to 10.16 mm and the replacement of the acrylic base plate with a cylindrical holder with a radial step to attach the detector onto to the rotational collar described in the previous section. The reduction of the guard's outer diameter allows construction of source substrates with smaller diameters. For the modified D400 EC, the depth of the collector and the guard was 14.1 mm.

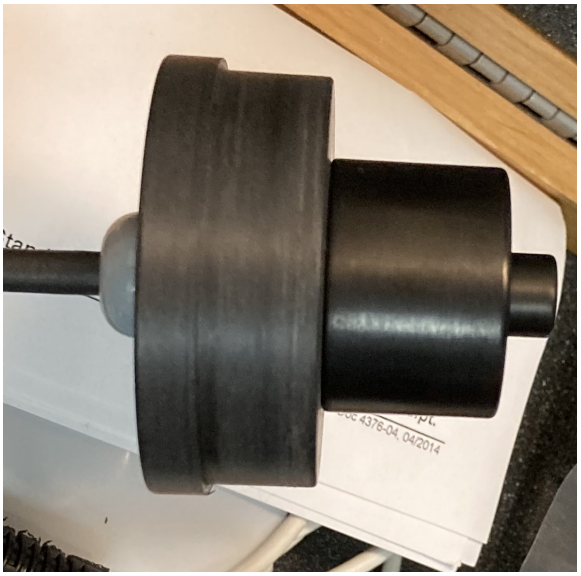

Figure 4.12: The modified D400 EC used in this work for alpha dosimetry.

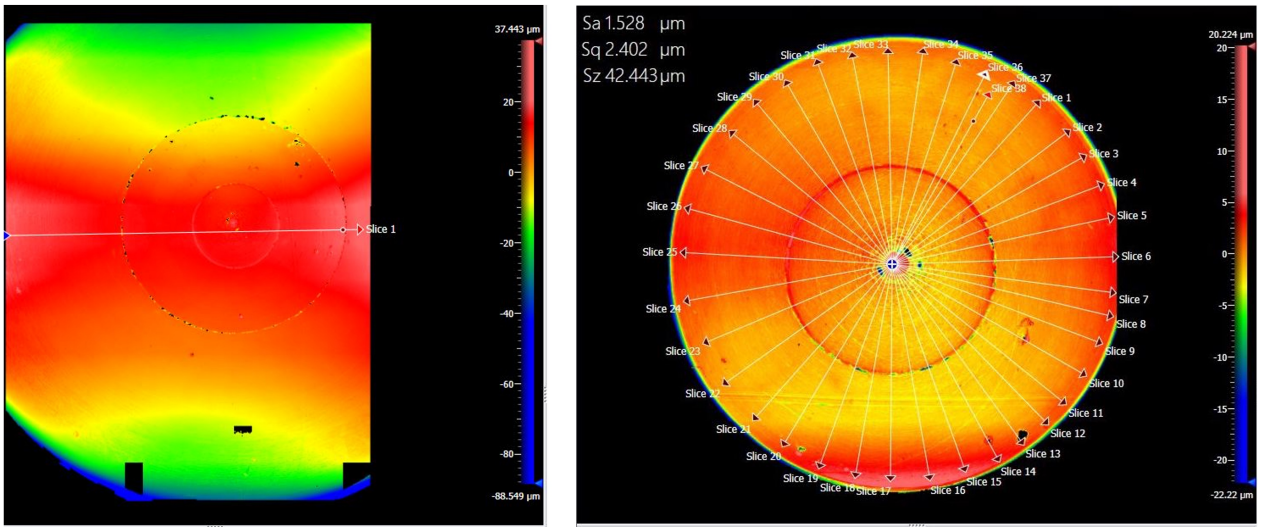

Figure 4.13: The surface flatness map of the unmodified D400 EC (left) and the modified EC (right).

The surface flatness of the D400 EC was evaluated using coherence scanning interferometry (Zygo NewView 9000) at the University of Wisconsin Centers for Nanoscale Technology (UWCNT). The interferometer utilized throughout this work was capable of a 150 μm vertical scan range with a spatial resolution of 1 nm. The largest field of view (FOV) available on the interferometer was 1.7x1.7 mm^2 with a lateral spatial resolution of 11 μm. Since the D400 EC had a cross-sectional diameter much greater than the FOV,

multiple scans were acquired using the interferometer and the Zygo software was used to patch the independent scans. It is of note that the individual patches overlapped by at least 10 % to allow a continuous flatness evaluation. Following the scans and patching, several 1D profiles were measured on the 2D surface flatness map to quantify the flatness. The two metrics of interest were root-mean-square (RMS) values and peak-to-valley (PV) values. The latter metric is a more strict evaluator of the surface flatness. Figure 4.13 shows the 2D surface flatness profiles of the unmodified and the modified D400 EC. The dark patches on the flatness profile of the unmodified EC correspond to regions with insufficient reflection of light. The poor flatness of the unmodified EC is evident from the figure with PV measured up to 60 μm. A concave bowing of the chamber was observed with magnitudes up to 50 μm. The reduction of the guard's outer diameter led to a flatness within 20 μm, as shown in figure 4.13. With this modification, much smaller air gaps between the source and the detector are possible.

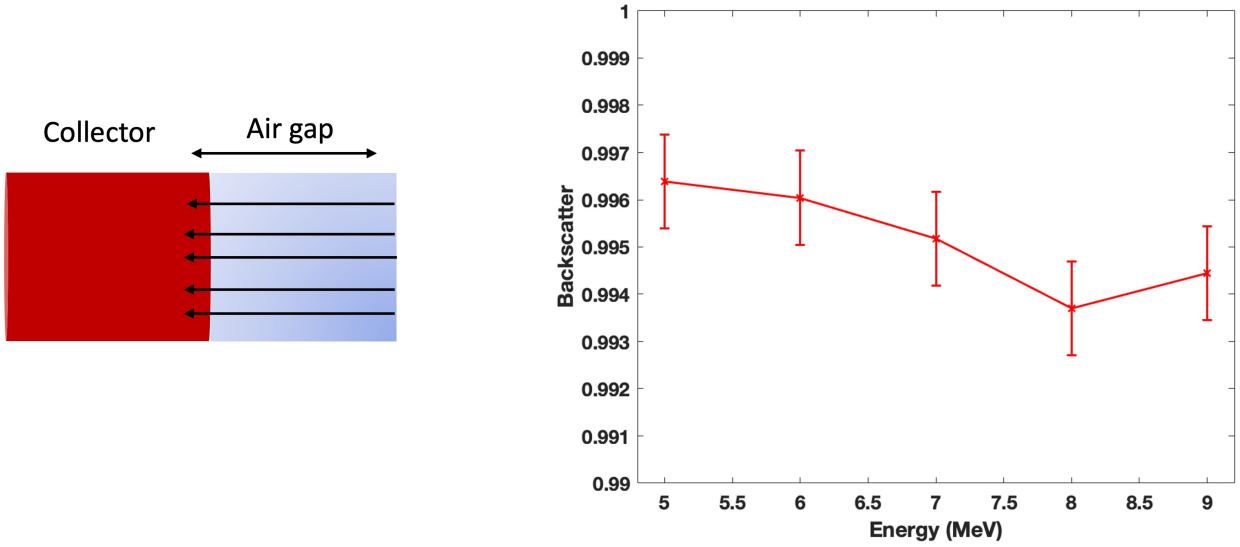

Figure 4.14: The backscatter from the D400 collector is shown for 5-9 MeV monoenergetic alpha beams.

The D400 material was selected for the EC since it is constructed of atoms with low atomic number leading to minimal backscatter of alpha particles traversing the cavity and hitting

the detector shown in figure 2.22. The magnitude of the backscatter was quantified using GEANT4 Monte Carlo (MC) simulations. A parallel monoenergetic alpha beam source was simulated on the flat surface of a cylindrical air cavity and absorbed dose to cavity was scored with and without the presence of a cylindrical collector placed distally to the air cavity, as demonstrated in figure 4.14. The optimal physics parameters determined in section 3.1.2 were utilized. The atomic de-excitation was turned on and the production threshold was set to 1 μm. The backscatter was calculated as:

$$\text{Backscatter} = \frac{D_{air}(\text{collector present})}{D_{air}(\text{collector absent})} \tag{4.1}$$

with D_{air} being the absorbed dose to air. Figure 4.14 shows the magnitude of the backscatter for a collector constructed of the D400 material. The backscatter from D400 was found to be smaller than the air since it is composed mostly of carbon (Z = 6) versus air where nitrogen (Z = 7) dominates the material composition. The relative D400 to air backscatter was found to be $< 0.6\%$ making D400 a suitable material for alpha dosimetry.

4.1.2 COMSOL electric field lines simulations

For ionization chambers, the air cavity is defined by the electric field, which collects the charged carriers as a signal. The active volume of the ion chamber can be sensitive to irregularly-shaped field lines or fringe fields. It is crucial that the volume of the active region of the ion chamber be well-known for absolute dosimetry. Although uniform electric field lines are expected inside the collector area, the electric field near the edges must be investigated to ensure that the active volume is well-defined. Additionally, the presence of a guard minimizes fringe fields and discards charged carriers that originate outside the sensitive volume. The electric field line simulations were performed to evaluate the magnitude of the electric field distortion in the vicinity of the insulating gap separating the

collector and the guard. The field lines terminating at the collecting electrode contribute to signal and were of interest for this work.

The COMSOL Multiphysics® software was utilized for this purpose. A finite element analysis was performed using COMSOL to solve coupled systems of partial differential equations describing electrostatic systems. A 2D radially-symmetric geometrical model was simulated for the D400 EC and the source substrate. The dimensions of the detector and the substrate were extracted from the manufacturer-provided drawings. As mentioned previously, the collector and the guard of the D400 EC are constructed of D400 conducting plastic. The collector-guard insulator was constructed using Parylene and the source substrate was simulated to be pure silver. The source substrate was applied with a constant static electric potential such that the electric field strength inside the air gap remained 100 V/mm. The parylene insulator was allowed to float. An air gap of 100 μm between the EC and the source substrate was simulated. The D400 and source substrate materials were simulated as conductors. The parylene material was given a density of 1.272 g/cm^3, relative permittivity of 2.88, and conductivity of 8.62E-16 S/m [15]. A physical density of 1.197 kg/m^3, relative permittivity of 1.0, and electric conductivity of 5.0E-015 S/m were assigned to air. A triangular "extra-fine" mesh was created with sides $< 5\mu m$ for high-resolution electric field simulations. A streamline plot was used to visualize the electric field lines in the geometry.

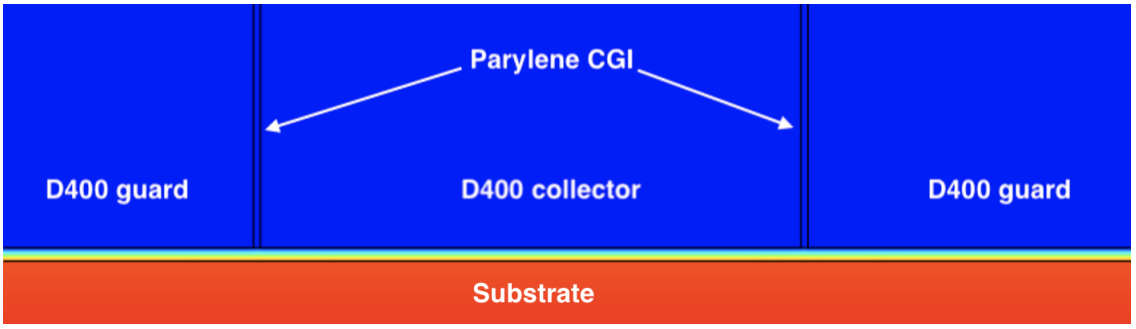

Figure 4.15: The simulated D400 EC geometry in COMSOL Multiphysics ®.

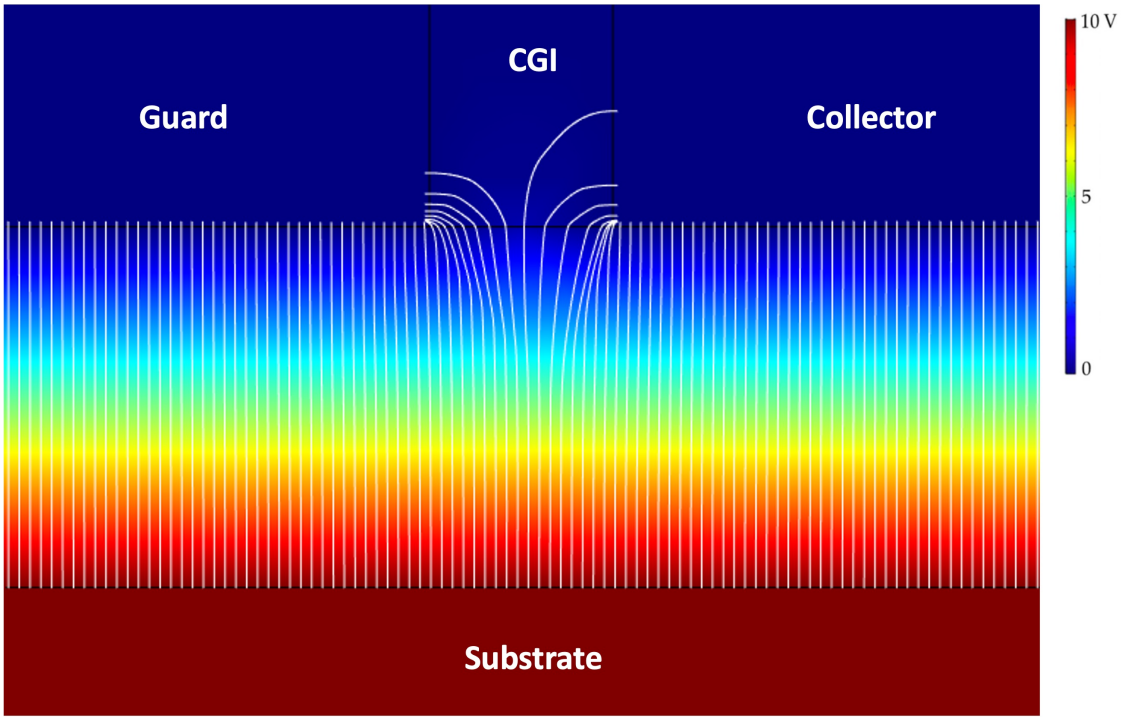

Figure 4.16: Electric field lines simulated near the collector-guard insulator (CGI) using COMSOL Multiphysics ® for the D400 EC.

Figure 4.15 shows the simulated 2D EC geometry in COMSOL with a 100 μm air gap between the source substrate and the detector. The electric field lines of interest near the collector-guard insulator (CGI) region are shown in figure 4.16. The field lines were observed to be parallel and uniform inside the geometry except inside the CGI region. The field diverges where the adjacent field lines terminate at the collector and the guard. The coordinates of the diverging field line were noted and found to be exactly halfway between the collector and the guard's radius. Therefore, the radius of the active volume was calculated to be

$$r_{\text{cavity}} = 0.5(r_{\text{collector}} + r_{\text{guard inner}}) \tag{4.2}$$

where $r_{\text{collector}}$ is the radius of the collector and $r_{\text{guard inner}}$ is the inner radius of the guard. This result agrees with previous works evaluating the radius of the air cavity for parallel-plate ionization chambers [116].

4.1.3 Capacitance and parallelism measurements

4.1.3.1 Parallel alignment between the detector and the source

With the detector and the source planes facing each other, a parallel alignment between them is needed to ensure accurate assessment of the cavity volume. The air gaps between the two plates can be as low as 60 μm and therefore cannot be aligned with a high precision using most mechanical methods. Additionally, any contact between the source and the detector can contaminate the detector and may lead to inaccurate measurement of absorbed dose. Hence, a partially non-contact method was devised to align the two plates parallel to each other.

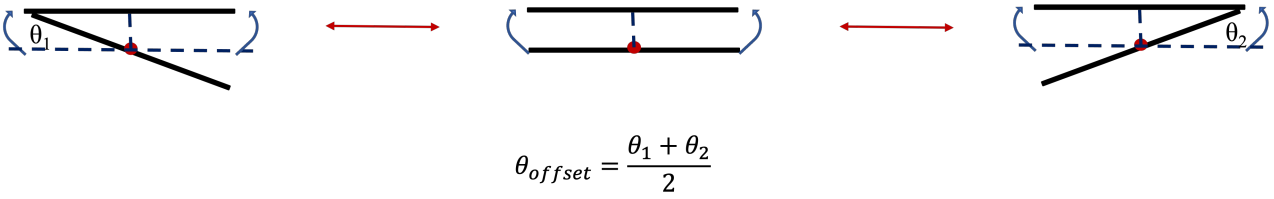

Figure 4.17: Illustration of parallel alignment between the detector and the source plates.

Figure 4.17 shows a simple method to align two plates in a parallel configuration. By rotating one of the plates about it's center and measuring the angle at which the edges of the plates are in contact with each other, any tilts can be detected and corrected for. This method operates under the assumption that the two plates are perfectly flat. Since the source subassembly was placed on a hexapod stage, the source substrate can be rotated about both x and y axes with respect to its center point. If the source substrate and the detector share the same central axis, the diameter of the source substrate must be greater than the collector diameter and the air gap small enough to ensure that there is no contact between the source substrate and the collecting electrode. While rotating the source substrate, the edge of the substrate makes contact with the guard ring instead of the collector due to the dimensions of the two planes. This contact prevents contamination

and allows measurement of the tilt angles based on the electric conductivity between the two plates.

A custom connector was fabricated to read the signal from the guard ring instead of the collecting electrode. By connecting the guard electrode and the source substrate to an ohmmeter, the resistivity between the two conductors was measured. A decrease in resistivity, resembling a step function, was indicative of a contact between two electrodes. Once the source cylinder and the D400 EC were aligned using the centering part shown in figure 4.9, the source substrate was rotated about its center in 0.1 deg increments. The air gap between the two plates was kept within 1 mm. Any sharp decrease in the resistivity was observed after each rotational increment on the ohmmeter. Once a contact between the two electrodes was noted, the angle of the tilt was noted and the experiment was repeated along the negative rotational direction. If the two plates are parallel, the tilt in the negative, θ_1, must be equal to the tilt in the positive direction, θ_2. Otherwise, the rotational offset can be calculated using the equation given in figure 4.17. Tilts along both x and y axes were noted using the method described above. Following this experiment, appropriate rotational offsets were applied to the hexapod coordinate system so that any translational motion, such as change in air gaps, maintains the parallel configuration between the source and the detector planes.

4.1.3.2 Capacitance measurements

Once the detector and the source planes were aligned in a parallel configuration, the absolute air gap between the two plates must be known. Additionally, any remaining tilts in the geometry may lead to a deviation between the nominal cavity cross-sectional area and the actual cross-sectional area. Thus, capacitance measurements were acquired to determine the absolute air gap as well as the effective diameter of the air cavity. Assuming the detector and the source plates act as a parallel-plate capacitor, any change

in the applied potential leads to a flow of electric charge, Q, across the air gap that can be given by

$$Q = C_o \Delta V \tag{4.3}$$

where C_o is the capacitance and ΔV is the change in electric potential between the two plates. The capacitance of an ideal parallel-plate capacitor can be calculating by

$$C_o = \frac{\epsilon_r \epsilon_o A_{eff}}{l_o} \tag{4.4}$$

where ϵ_r is the dielectric constant of air with a value of 1.000537, ϵ_o is the permittivity of vacuum with a magnitude of 8.8542E-12 F/m, A_{eff} is the effective cross-sectional area of the cavity, and l_o is the air gap between the two plates. Since the initial air gap is unknown, the offset between the actual, l_o, and the assumed air gap, $l_{assumed}$, can be calculated by

$$l_{offset} = l_{assumed} - l_o \ . \tag{4.5}$$

Equations 4.4 and 4.5 can be combined to yield

$$l_{assumed} = \frac{\epsilon_r \epsilon_o A_{eff}}{C} + l_{offset} \ \ . \tag{4.6}$$

The capacitance between the source and the detector can be measured using equation 4.3 at various air gaps. By plotting a curve of $1/C$ versus $l_{assumed}$, the absolute effective area of the cavity and the offset between the actual and the assumed air gap can be measured.

Dummy source measurements: Several experiments were carried out in an attempt to measure the effective area of the cavity to corroborate the results reported in section 4.1.2. A dummy source substrate was used in this experiment without any radioactivity

present. The dimensions and the material composition of the substrate were kept identical to the radioactive sources utilized throughout this work. A DC voltage was applied using the generator shown in figure 4.10. After centering the detector and the source cylinders, an arbitrary unknown air gap was chosen and assumed to be zero. A ΔV of 90 V bias was applied for each air gap. The induced charge was collected using a MAX 4000 electrometer (Standard Imaging) in the threshold mode. The threshold mode automatically triggers the electrometer on and off based on the starting and stopping threshold limits, which were set to 0.02 pA and 0.01 pA, respectively. The air gap was increased five times with 50 μm increments and charge was collected at each interval. Using equation 4.6, the offset in the air gap and the diameter of the air cavity was calculated. Following this experiment, the offset in the air gap was applied as a translational shift using the hexapod stage and the measurements were repeated with the known air gaps ranging from 200 μm to 400 μm in 50 μm increments. Figure 4.18 shows the results from a single trial plotting $1/C$ against $l_{assumed}$. The initial air gap was assumed to be zero, therefore, l_{offset} was calculated to be the y-intercept of the curve. Figure 4.19 shows the capacitance measurements following the determination and application of the l_{offset} shift.

Four trials were conducted to measure the diameter of the air cavity and to assess the variation in the measurements. During each trial, the source and detector assemblies were centered and aligned parallel to each other using the hexapod motion stage before acquiring capacitance measurements. Since capacitance measurements were acquired both before and after the determination of the l_{offset} shift, each trial yielded two measurements of the A_{eff}. Table 4.3 shows the results from the capacitance measurements using the dummy source. A variation of 1% was determined in the cavity diameter based on the multiple trial results. These results agree well with the work of Hansen in terms of both the average diameter and the percent standard deviation [15]. The nominal diameter of the cavity was calculated to be 4.03 mm, which is only 20 μm greater than the measured

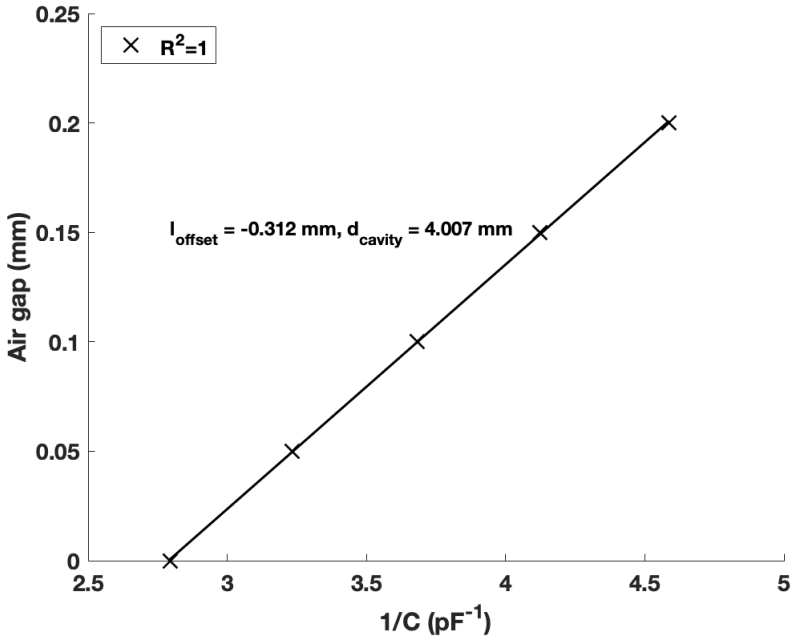

Figure 4.18: Determination of the absolute air gap and the cavity diameter using the capacitance method. Measurements with an arbitrary unknown initial air gap are shown.

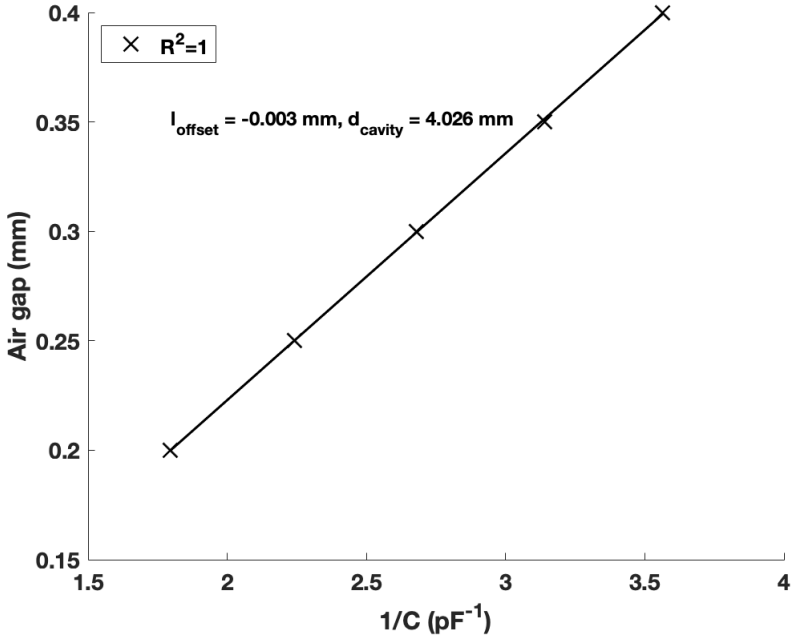

Figure 4.19: Confirmation of the absolute air gap and the cavity diameter using the capacitance method. Measurements with a l_{offset} shift applied are shown.

average diameter. Any tilts in the detector or the source also lead to a reduction of the cavity diameter. Therefore, a 20 μm difference between the nominal and measured diameters was considered to be minimal.

Table 4.3: Effective diameter of the air cavity determined from the capacitance measurements using a dummy source.

Trial	Cavity diameter (mm)
1	4.01/3.97
2	4.04/3.96
3	4.09/4.00
4	4.01/4.03
Avg.	4.01±1.00%

Radioactive source measurements: Equation 4.3 can be used to measure capacitance when the collected charge is induced due to the energy stored in the electric field lines. However, this case is only applicable to a dummy substrate without any radioactivity present. With the presence of a radionuclide, the measured electric charge is a combination of ionization current and current induced due to the capacitance of the air cavity. In order to deconvolve these two effects, a voltage increase method was utilized as previously proposed by Selbach et al. [16]. Figure 4.20 illustrates this method by plotting charge collection time against collected charge. Multiple 30 s charge readings were initially collected at a voltage V_1 and defined to be Q_o. The Q_Δ was measured by initializing a 30 s charge reading and increasing the voltage by ΔV. The amount of time between the charge initialization and the voltage increase was defined to be Δt. After measuring Q_Δ, Q_f was measured as a 30 s charge reading at a bias of $V_1 + \Delta V$. By keeping Δt close to zero, the charge induced by the capacitance of the air cavity can be given by

$$Q_\Delta = \frac{\Delta t}{30s} Q_o + \left(1 - \frac{\Delta t}{30s}\right) Q_f + Q_{dis} \approx Q_f + Q_{dis} \quad . \tag{4.7}$$

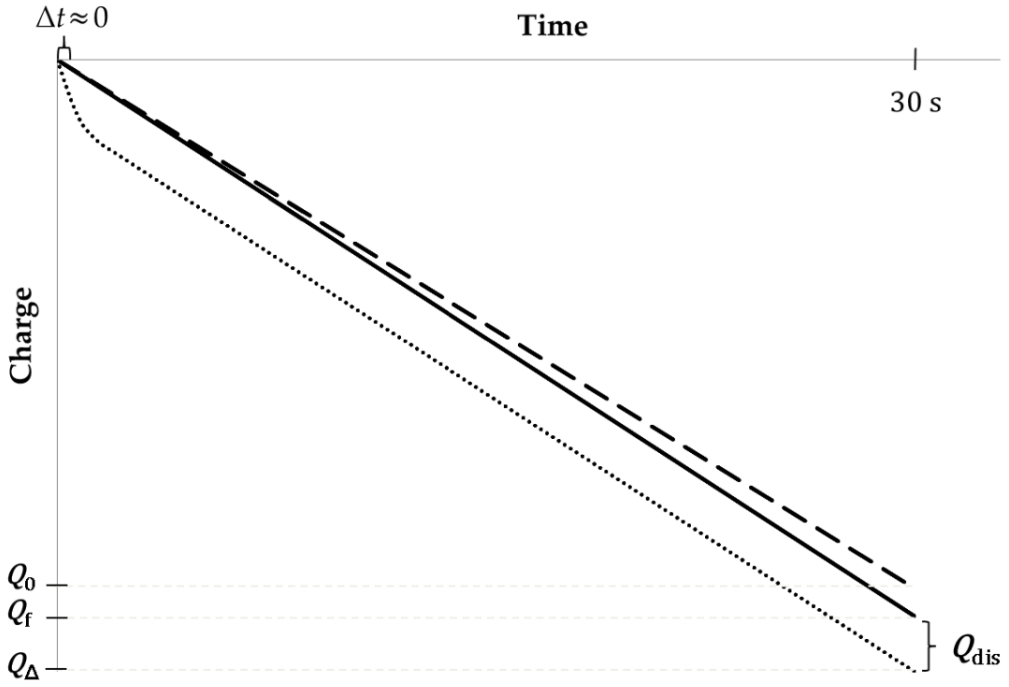

Figure 4.20: The charge induced by the capacitance of the air cavity, Q_{dis}, differentiated from the ionization charge using a voltage increase method is demonstrated [16].

Following the measurements described above, the capacitance can be calculated using equation 4.3. This method was employed to measure the initial air gap with the radioactive source in place. Due to the windowless setup, the capacitance method provides a contactless way to measure the absolute air gap.

4.1.4 Eckert & Ziegler ^{210}Po source

The constructed primary standard of absorbed dose was evaluated using a pure alpha-emitter i.e. ^{210}Po. Figure 4.21 shows the decay scheme of ^{210}Po. A 5.305 MeV alpha is emitted with an intensity of ∼100% for each nuclear disintegration. The ^{206}Pb daughter is a stable atom but can be charged and may deposit energy inside the air cavity before losing its kinetic energy. The average energy of the recoiled daughter can be calculated

by:

$$E_{Pb-206} = \frac{m_\alpha}{m_\alpha + m_{Pb-206}}\left[m_{Po-210} - m_{Pb-206} - m_\alpha\right]c^2 = 103\ keV \tag{4.8}$$

where m is the mass and c is the speed of light. The recoiled daughter ions inside the air cavity have a short range ($< 50\mu m$) and do not affect the change in ionization current measurements acquired at larger air gaps.

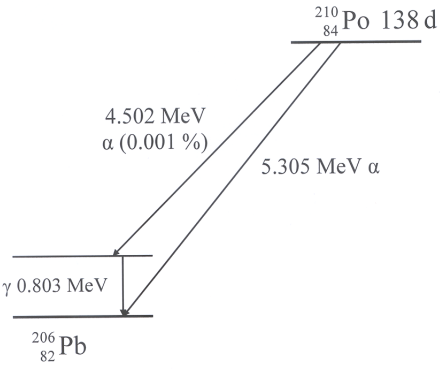

Figure 4.21: The decay scheme of ^{210}Po is shown.

In this work, a custom ^{210}Po source was requested from Eckert & Ziegler (E&Z) based on the ideal source specifications determined in section 3.3. The source had a FWHM of $<$ 40 keV and a diameter of <3 mm. Alpha spectroscopy measurements were performed by E&Z to determine a NIST-traceable activity to within 1% uncertainty at k = 1.

The source substrates were fabricated in-house and shipped to E&Z for chemical plating of ^{210}Po. The dimension and material composition of the substrates were selected based on the the E&Z plating cell requirements. The plating cell required a silver cylindrical substrate with a 11.1 mm diameter and 1 mm thickness. Constructing a silver substrate can lead to poor surface flatness due to the high malleability of silver. Therefore, silver-coated steel substrates were employed in this work. A dozen stock steel disks with 12.7 mm diameter and 1 mm thickness were initially selected. The diameter was reduced to 11.1 mm, adhering to the plating cell requirements, and the edges were chamfered to

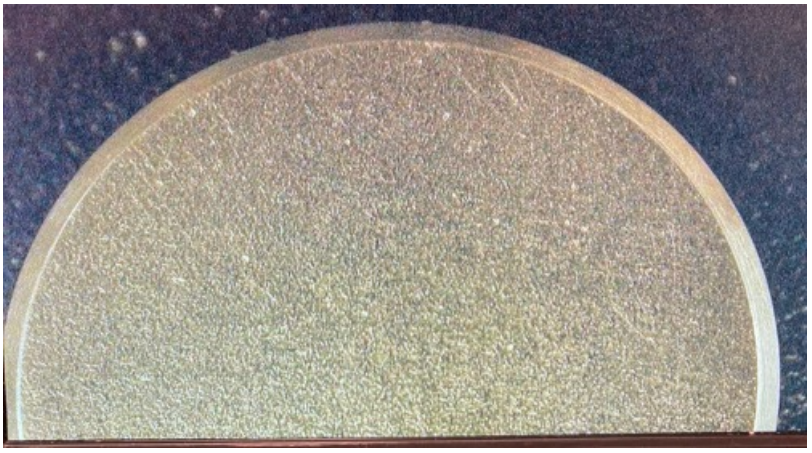

Figure 4.22: An image of the steel substrate is shown.

eliminate sharp corners and, therefore, non-uniform electric field lines. The fabricated steel disks were chemically plated with a 40 μm silver layer by Chem Processing Inc. (Rockford, IL). The variation in the thicknesses of the substrates was measured to be < 20 μm using a micrometer. The silver-plated steel substrates were then evaluated under an interferometer for surface flatness assessment. The interferometer settings discussed in section 4.1.1 were used for this purpose. Figure 4.23 shows a 2D surface flatness profile for a single substrate. The radial profiles at various polar angles show a flatness of < 10 μm for the given substrate. The surface flatness for all substrates was found to be < 20 μm.

The ionization current signal in the air cavity is directly proportional to the radioactivity of the ^{210}Po. For measurement of absorbed dose, a high signal-to-noise ratio (SNR) is required to minimize Type A uncertainty [117]. The signal for the D400 EC can be estimated using Monte Carlo (MC) methods. The magnitude of the ^{210}Po radioactivity required to generate a high SNR was determined using GEANT4 MC code. The D400 extrapolation chamber (EC) was modeled according to the drawings provided by the manufacturer. A silver-coated steel substrate was modeled using the dimensions provided in this section. The diameter of the air cavity was modeled based on the COMSOL and the capacitance measurements. A planar uniform circular ^{210}Po source of 3 mm diameter

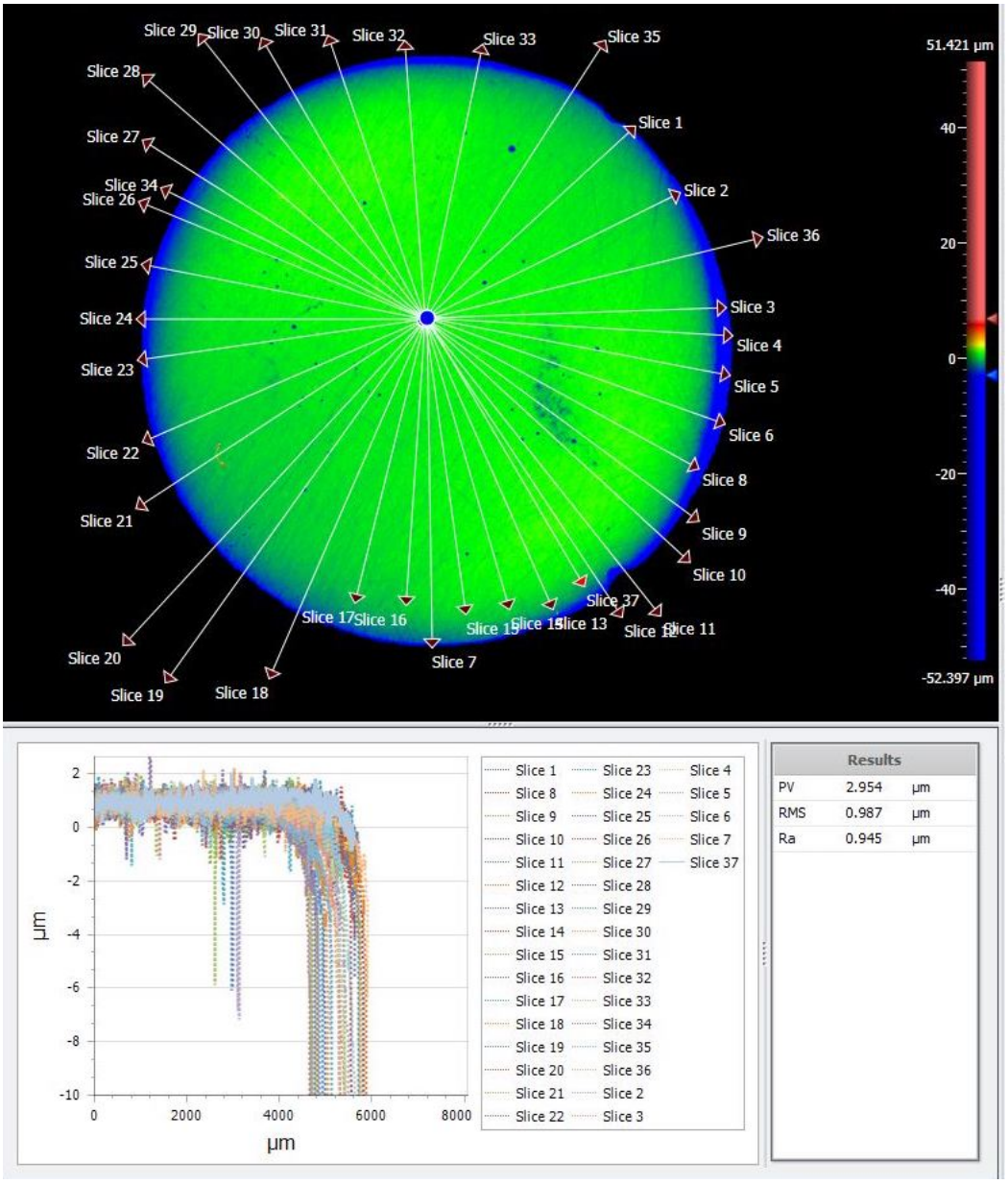

Figure 4.23: The interferometry results for a single silver-coated steel substrate are shown.

was simulated on the surface of the substrate. The *G4RadioActiveDecay* library was used for the nuclear decay data. It is of note that a single MC history corresponds to 1 Bq of activity. The absorbed dose to air cavity was scored at various air gaps and the ionization current, I, was calculated by:

$$I = A_o \frac{D \rho_o A_{eff} l}{(\frac{\bar{W}}{e})_{air}} \tag{4.9}$$

where A_o is the radioactivity of the ^{210}Po source, D is the scored absorbed dose per Bq, ρ_o is the density of air at standard temperature and pressure, A_{eff} is the effective area of the air cavity, l is the air gap between the source and detector, and $(\frac{\bar{W}}{e})_{air}$ is the average energy required to produce an ion pair in dry air by alpha particles with a value of 34.96 J/C [118][119].

Figure 4.24 shows the approximated signal for a 1 μCi ^{210}Po source. For air gaps of 300-700 μm, a change in air gap, Δl, of 25 μm leads to a mean net ionization current of 0.25 pA. With an estimated noise for the D400 EC of 0.01 pA, the SNR was expected to be ~ 25. As the l_1 air gap increases, the net ionization current due to a Δl of 25 μm decreases from 0.3 pA to 0.23 pA. The decrease in net ionization current can be attributed to the increase in side-loses of charged particles. The non-linearity in the ionization current versus air gap curve, shown in figure 4.24, arises from the effects discussed in section 2.3.3. Based on these results, a 1 μCi ^{210}Po source was deemed strong enough for this work. The change in air gap, Δl, must be chosen carefully as smaller values will lead to small net ionization currents and hence small SNR.

Following the shipment of the ^{210}Po source, the radioactivity was measured by E&Z to be 1.253 μCi on 10/15/2022 at 2:00 pm CT. The FWHM of the ^{210}Po peak was measured to be <30 keV by E&Z. Alpha spectroscopy measurements were repeated using the in-house spectrometer to assess the self-absorption of the source. The source disk was

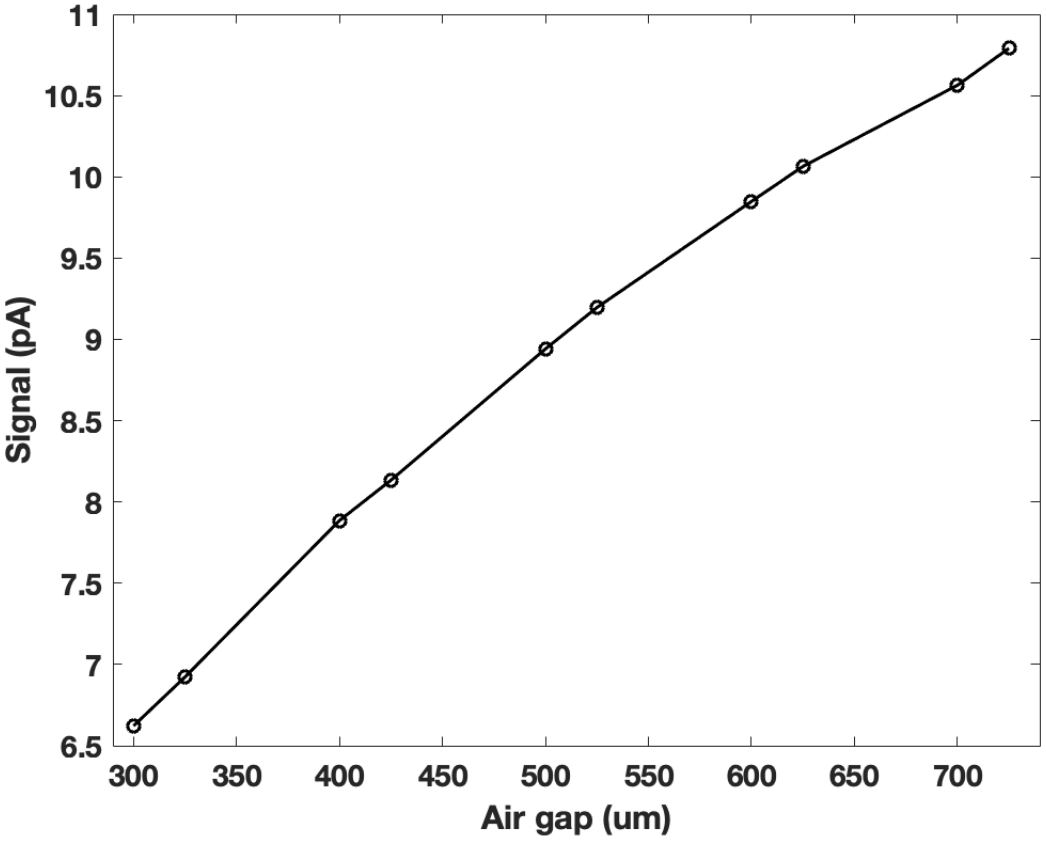

Figure 4.24: The MC estimated signal for the D400 EC using a 1 μCi ^{210}Po source.

placed in a plastic holder used for transportation and the alpha spectrum was measured with a source-to-detector distance (SDD) of 18 mm. Figure 4.25 displays the normalized alpha spectrum with the associated FWHM of the 5.3 MeV alpha peak. Based on this measurement and simulations discussed in subsection 3.3.3, a negligible self-absorption and attenuation can be safely assumed.

The primary standard in this work was designed so that the long axes of the source and detector cylinders coincide. However, a lateral positional offset can be expected between the source and substrate centers. Therefore, unlaminated EBT3 film measurements were acquired to evaluate the offset of the source with the center of the source substrate. The results from the same measurement were also used to determine the uniformity of

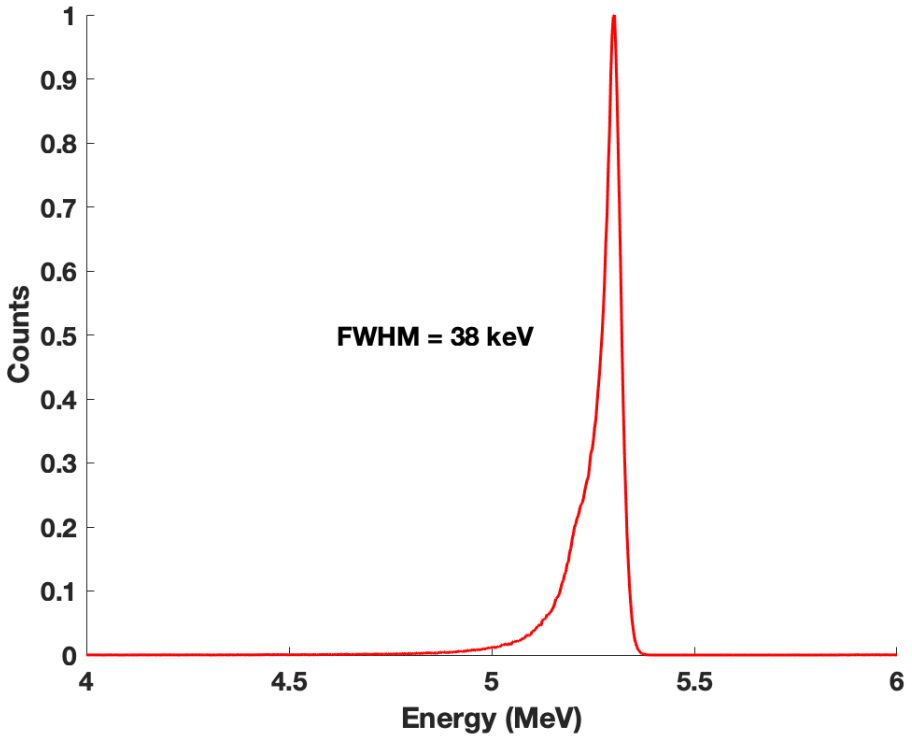

Figure 4.25: Measured alpha spectrum of the ^{210}Po source using the ORTEC Alpha Aria spectrometer.

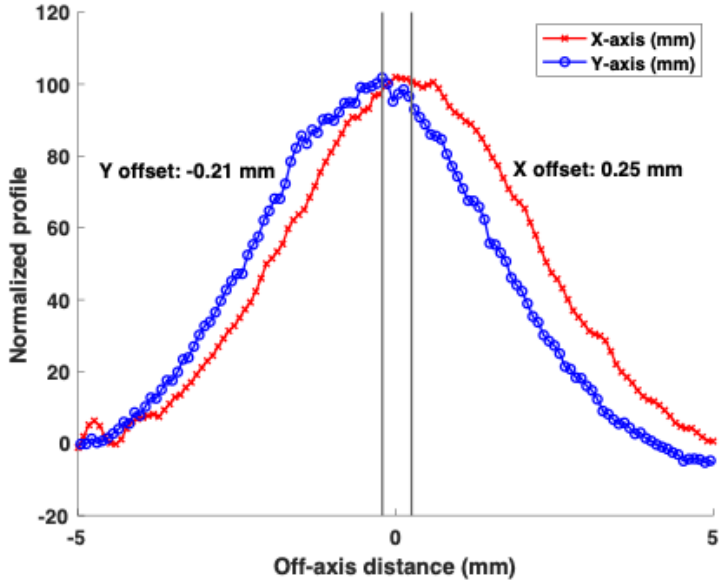

Figure 4.26: Lateral profiles showing the positional offset of the ^{210}Po radioactive source from the center of the substrate disk.

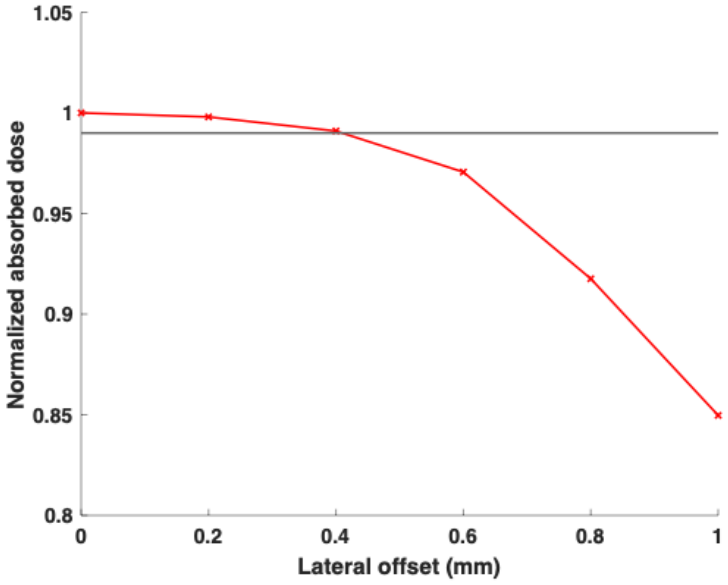

Figure 4.27: The impact of a lateral positional offset of the ^{210}Po source on absorbed dose. The horizontal line indicates a 1% deviation in absorbed dose from unity.

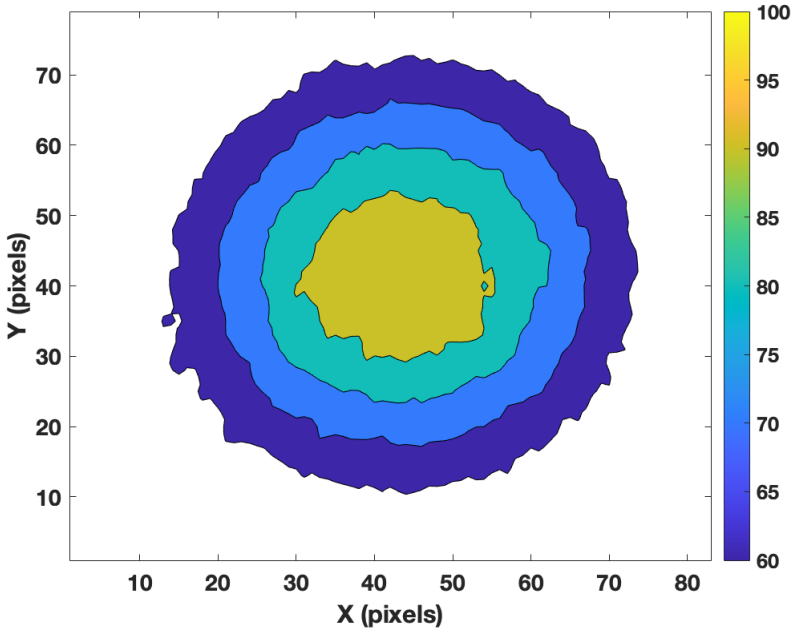

Figure 4.28: The normalized 2D profile of the ^{210}Po source displaying the azimuthal emission uniformity of the source.

the source. A circular 0.8" film piece was laser cut and mounted on a plastic cylinder designed to fit in place of the detectors. By aligning the centers of the plastic mount and the source, a film measurement was acquired and the offset of the source from the center of the substrate disk was calculated in both lateral directions. Figure 4.26 shows the calculated offsets in both lateral directions. The source was found to be centered within 0.25 mm of the center of the substrate disk. A MC investigation was launched to determine the impact of the positional offset of the source on the measured absorbed dose to cavity. With the air gap of 300 μm, the absorbed dose was scored as a function of lateral shift introduced intentionally to the source. The absorbed dose, normalized to the zero offset dose, as a function of lateral offset is shown in figure 4.27. The results conclude that the absorbed dose is relatively insensitive to lateral offsets <0.4 mm with a deviation of <1%. Nevertheless, positional offsets should be taken into account during measurements by aligning the source center with the center of the detector. Figure 4.28 shows the uniformity and the azimuthal anisotropy of the source. The source was found to be uniform with a minimal anisotropy based on the unlaminated EBT3 film measurement.

4.2 Monte Carlo correction factors for ^{210}Po

Employing a windowless extrapolation chamber (EC) relies on a series of Monte Carlo (MC) correction factors described in sections 2.3.3 and 2.3.4. The MC correction factors account for the geometrical mismatch between the measurable quantity and the quantity of interest, as demonstrated in figure 2.24. The TOPAS MC code was utilized for correction factor calculations. The TOol for PArticle Simulation (TOPAS) MC code is a GEANT4 wrapper developed for heavy charged particle simulations [120]. In this work, a modular physics list was used consisting of *G4RadioactiveDecay*, *G4Decay*, *G4HadronElasticPhysicsHP*, *G4HadronPhysicsQGSP_BIC_HP*, *G4IonElasticPhysics*, *G4IonQMDPhysics*, and *G4StoppingPhysics*. A modified *G4EMStandardOpt4* physics list was used for electromagnetic physics. The electromagnetic parameters for electrons were unchanged since the *G4EMStandardOpt4* physics list is considered to be highly accurate for light charged particle transport [93][100]. For alpha particles, the optimal electromagnetic physics parameters determined in section 3.1.2 were utilized.

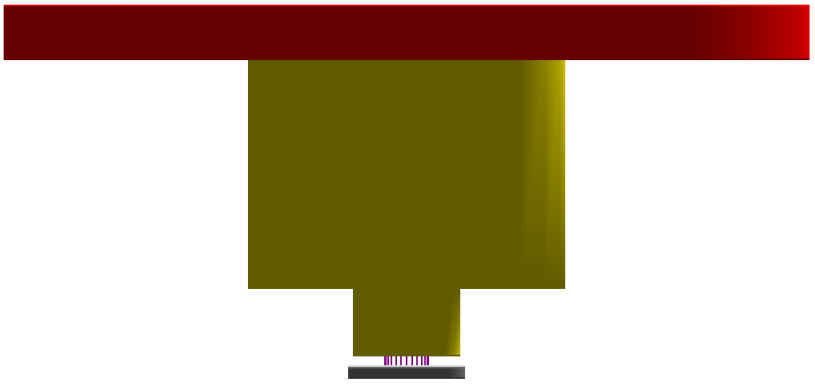

Figure 4.29: The graphics rendering of the D400 EC in TOPAS MC code. The guard is represented by yellow color and the air cavity by purple.

The D400 EC was simulated according to the drawings provided by the manufacturer and is shown in figure 4.29. The dimensions of the air cavity were selected based on

the COMSOL simulations and the capacitance results. The substrate was simulated as a steel disk with a silver layer on the surface. The atomic composition of the D400 material is equivalent to polystyrene. The physical density and mean excitation energy of the D400 material was set to 1.16 g/cm^3 and 68.7 eV, respectively. The GEANT4 internal materials $G4\_AIR$ and $G4\_WATER$ were selected to represent air and water. The mean excitation energies of air and water were 85.7 eV and 78 eV, respectively.

4.2.1 $\mathbf{k}_{point}$

The k_{point} correction factor accounts for the finite radius of the source and aims to determine absorbed dose from a point source. This correction can be calculated by:

$$k_{point} = \frac{D_{cavity,point}}{D_{cavity,planar2D}} \tag{4.10}$$

where $D_{cavity,point}$ is the absorbed dose to the air cavity from a point source and $D_{cavity,planar2D}$ is the absorbed dose to the same cavity using the real 2D emission profile of the source. Based on the unlaminated film results shown in figure 4.28, the ^{210}Po source was modeled as a circular planar source with uniform emission profile. The diameter of the source was measured using an image of a ruler placed next to the source and using unlaminated EBT3 films (see figure 4.28). Several line profiles, passing through the center of the circle, were drawn and the average diameter was calculated to be 3.2 mm. The k_{point} correction was calculated independently for air gap ranging from 300-525 μm. The atomic de-excitation was turned on and the production thresholds were set to 1 μm for these simulations.

Figure 4.30 shows the k_{point} correction factor as a function of air gap. The correction was calculated to be in the 7-9.5% range and observed to be increasing with the air gap. As previously demonstrated in figure 3.24, the absorbed dose to cavity decreases as the

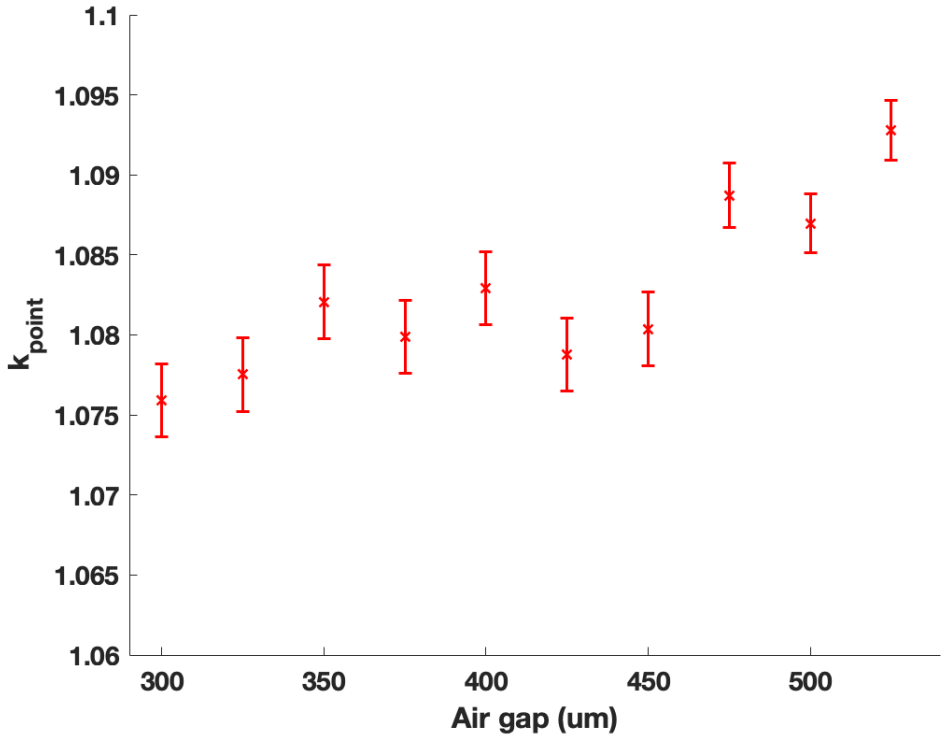

Figure 4.30: The k_{point} correction factor as a function of air gap for a ^{210}Po point source.

air gap increases, which leads to a k_{point} correction greater than unity. The mean track-length of the emitted alpha particles increases with decreasing source diameter leading to an increase in energy deposited in the cavity. Additionally, the k_{point} correction was found to be dependent on the air gap.

4.2.2 Correction factors for the cylindrical shell method

The MC-calculated correction factors for the dosimetric formalism described in section 2.3.3 are calculated and reported in this section.

4.2.2.1 $\mathbf{k}_{backscatter}$

The backscatter correction factor, $k_{backscatter}$, accounts for the differences in scatter conditions between the measurement setup and the quantity of interest. Specifically, the $k_{backscatter}$ corrects for the presence of the D400 detector and the source substrate. The magnitude of the correction depends on the differences in the energy being deposited inside the air cavity due to the detector and substrate versus free air. The $k_{backscatter}$ correction can be calculated by:

$$k_{backscatter} = \frac{D_{cavity,point,air}}{D_{cavity,point,det,substrate}} \tag{4.11}$$

where $D_{cavity,point,air}$ is the absorbed dose to cavity from a point ^{210}Po source without the presence of the substrate or the detector and $D_{cavity,point,det,substrate}$ is the absorbed dose to air from a point source to the same cylindrical cavity with the presence of the substrate and the detector. The backscatter correction was calculated as a function of air gap between the source and the detector. Therefore, the $k_{backscatter}$ correction must be applied to the measured ionization current at each air gap.

Air gaps of 300-525 μm with increments of 25 μm were simulated independently. The production thresholds were set to 1 μm and the atomic de-excitation parameter was turned on. Figure 4.31 shows the results for the ^{210}Po source. A mean correction of 7.5% was found with a maximum correction of 8.28%. The backscatter correction was observed to have a dependence on the air gap with the magnitude of the correction decreasing with increasing air gaps. It can be concluded that the backscatter correction was dominated by the presence of the source substrate since the D400 EC was found to have a backscatter magnitude of $< 1\%$, relative to air, as demonstrated in figure 4.14. The backscatter correction for alpha particles was found to be larger in this work when

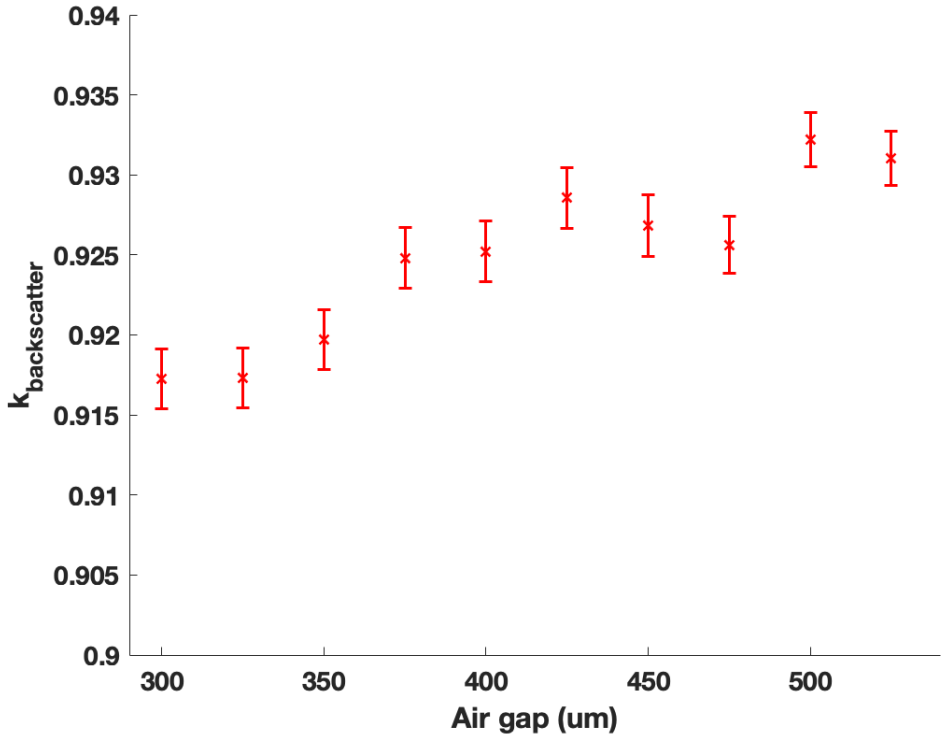

Figure 4.31: The backscatter correction factor as a function of air gap for a ^{210}Po point source.

compared to Hansen et al. for beta particles [77]. The backscatter effect in this work was caused by the presence of both the detector and the source substrate, whereas, only the detector backscatter was considered in Hansen's work due to the applicator being present during the irradiation [15].

4.2.2.2 $\mathbf{k}_{inv}\mathbf{k}_{cav}$

The absorbed dose to a cylindrical shell with a thickness of Δl and radial distance of $l_1+\frac{\Delta l}{2}$ from the source can be measured after applying the k_{point} and $k_{backscatter}$ correction factors to the net ionization current. The diameter of the cylindrical shell is equal to the diameter of the air cavity subtended by the D400 EC. Therefore, the measured absorbed dose must

be converted from a cylindrical shell to a infinitesimally-small cube by:

$$k_{inv}k_{cav} = \frac{D_{cube}}{D_{cyl,point,air}} \tag{4.12}$$

where D_{cube} is the absorbed dose to air from a point source scored in a infinitesimally-small cube made of air without the presence of the detector and the substrate and $D_{cyl,point,air}$ is the absorbed dose to air to a cylindrical shell of Δl thickness $l_1 + \frac{\Delta l}{2}$ away from a point source without the presence of the substrate or the detector. In this work, the $k_{inv}k_{cav}$ correction was defined such as the radial distance of the cube is equal to $l_1 + \frac{\Delta l}{2}$ distance of the cylindrical shell. Hence, the off-axis drop in fluence must be accounted for.

A point ^{210}Po source was simulated in TOPAS MC code. These simulations were run in sequential mode, with 500 concurrent independent simulation jobs (500 cores), on the University of Wisconsin-Madison Center of High Throughput Computing (CHTC) cluster. The total run time was 4-5 hours for these simulations. The D_{cube} was calculated in an array of 10x10x10 μm^3 air cubes placed at radial distances of 5-995 μm away from the source. The production thresholds for all particles were set to 3 μm. The $D_{cyl,point,air}$ was calculated in an array of cylindrical shells with diameters and thicknesses of 4.012 mm and 25 μm, respectively, placed at distances of 12.5-987.5 μm from the source.

Figures 4.32 and 4.33 show the simulation results for the D_{cube} and $D_{cyl,point,air}$ quantities. Due to the $1/r^2$ radial fall-off, the D_{cube} was found to have a much steeper dose distribution than the $D_{cyl,point,air}$. Additionally, the magnitude of the absorbed dose to air was observed to be much higher for D_{cube}. Based on these results, the $k_{inv}k_{cav}$ correction was calculated using equation 4.12 and is shown in figure 4.34. The dominating contribution to the $k_{inv}k_{cav}$ correction belongs to the k_{inv} part since the off-axis reduction in fluence was found to be much greater than the cavity perturbation. Assuming alpha particles have straight trajectories, the k_{inv} correction can be approximated by equation 2.23.

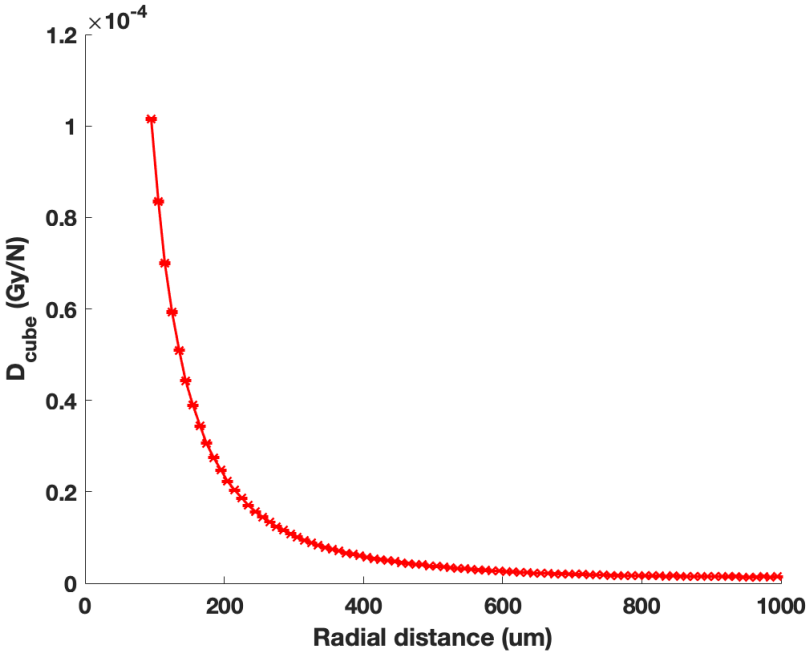

Figure 4.32: The absorbed dose to air as a function of radial distance for a point ^{210}Po source. The error bars correspond to 1σ uncertainty and are smaller than the marker.

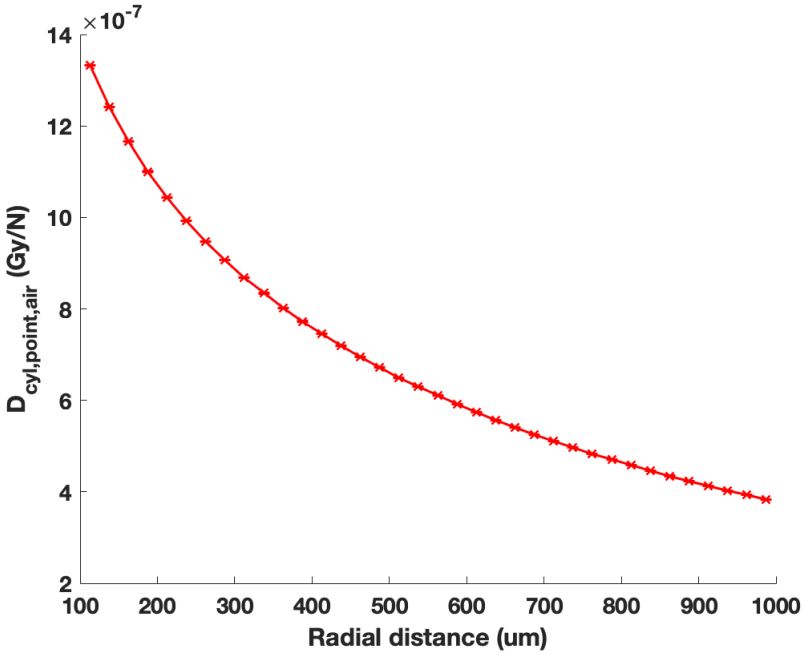

Figure 4.33: The absorbed dose to cylindrical shells as a function of radial distance for a point ^{210}Po source. The error bars correspond to 1σ uncertainty and are smaller than the marker.

Figure 4.35 shows the k_{inv} correction factor using the defined analytical expression and the corresponding k_{cav} correction. As hypothesized, the differences in the absorbed dose to cylindrical shells and absorbed dose to cubes originate from the off-axis reduction in fluence. The k_{cav} correction was found to be $< 1\%$ at all investigated radial distances.

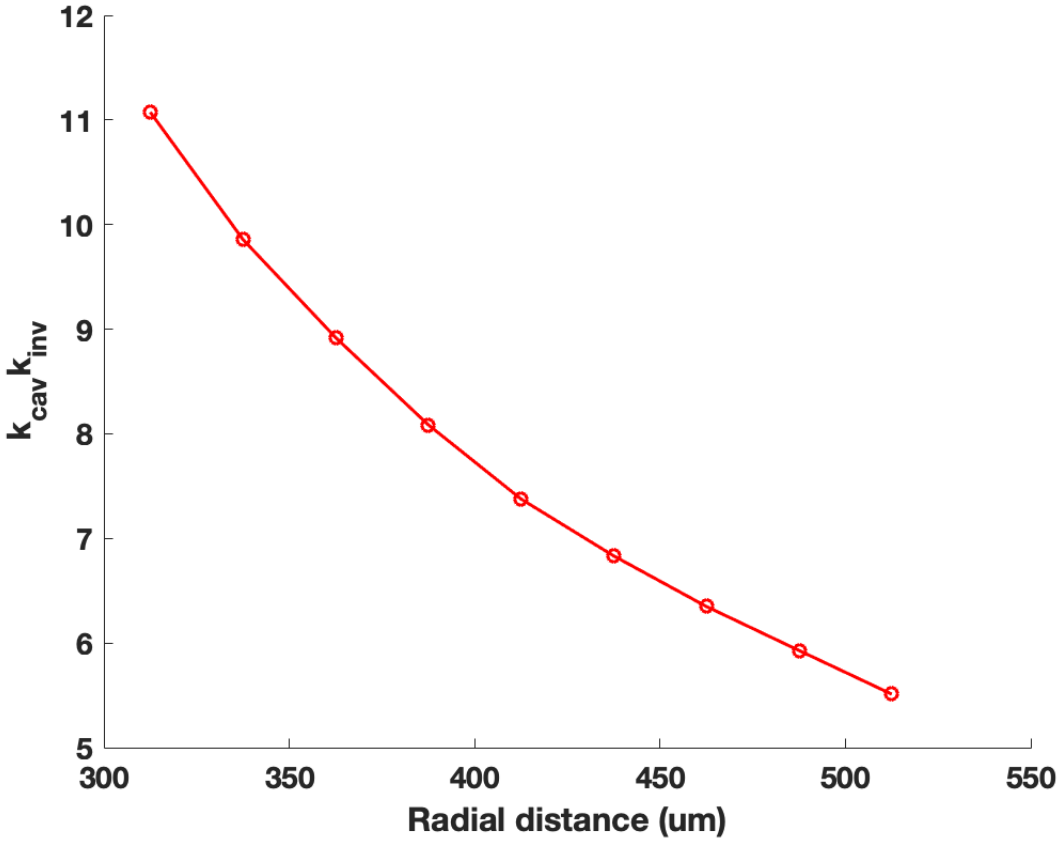

Figure 4.34: The $k_{inv}k_{cav}$ correction factor as a function of radial distance from a point ^{210}Po source. The error bars correspond to 1σ uncertainty and are smaller than the marker.

4.2.2.3 Air to water absorbed dose conversion

The measured absorbed dose to air can be converted to absorbed dose to water by applying the appropriate stopping power ratio and a scatter/attenuation correction. In this work, a single MC based correction factor was utilized for such a conversion and can be given

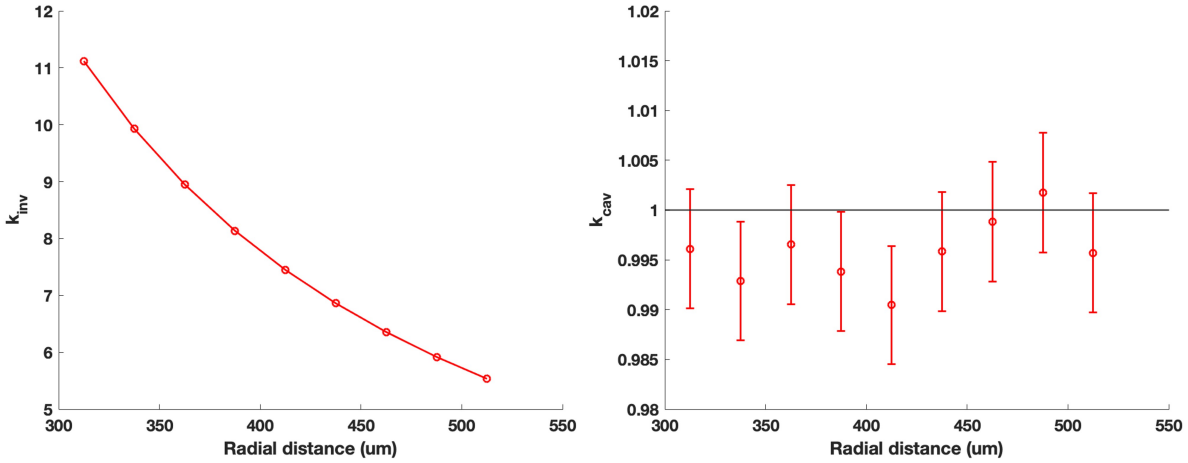

Figure 4.35: The $k_{inv}k_{cav}$ correction factor as a function of radial distance from a point ^{210}Po source. The error bars correspond to 1σ uncertainty.

by:

$$D_{water}(r_{water}) = D_{air}(r_{air})k_{water}\frac{r_{air}^2}{r_{water}^2} \tag{4.13}$$

where $D_{air}(r_{air})$ is the absorbed dose to air at a radial distance of r_{air} from a point source and $D_{water}(r_{water})$ is the absorbed dose to water at a radial distance of r_{water}. The final term in the equation accounts for the inverse-square fall-off. Energy loss of charged particles is proportional to ρ, where ρ is the physical density of the absorbing material. After the application of water-to-air stopping power ratios, the primary cause of energy loss differences in the two materials is due to the physical density differences. Therefore, attenuation of alpha particles at a radial distance of r in air is equivalent to attenuation at a radial distance of $\sim 0.001r$ in water. This assumption is valid if the inverse-square fluence drop-off is considered. As shown in figure 4.36, the plateau region of alpha particles in air extends up to 1-5 mm depth in air and up to 5 μm depth in water. Since radial distances of 300-525 μm in air were utilized in this work, absorbed dose to water at 1 μm distance from a point source was considered to be the quantity of interest.

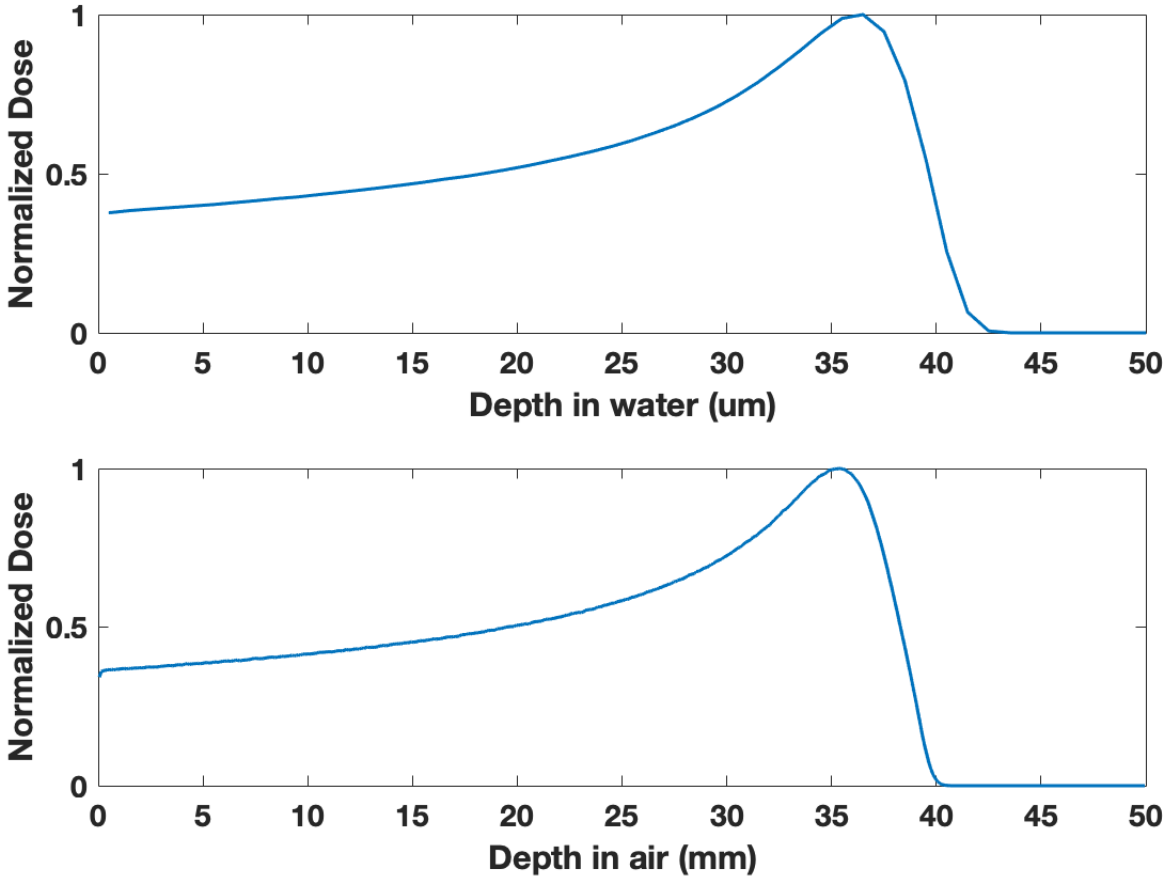

Figure 4.36: The integral depth dose (IDD) of a 5.3 MeV alpha beam source in water (top) and air (bottom).

The air to water absorbed dose correction was calculated by simulating absorbed dose to a 0.2 μm thick spherical water shell with a 1 μm radial distance from a point source in a water phantom. The k_{water} conversion factor was calculated using equation 4.13 with r_{water} and r_{air} of 1 μm and 312.5 μm, respectively. The magnitude of the correction factor was calculated to be 1.165±0.006. Since TOPAS employed the ICRU-49 stopping power tables, the stopping power ratio of water-to-air for 5.3 MeV alpha particles was determined to be 1.1624. Hence, the correction for scatter and attenuation differences between the water and air were $< 0.5\%$. It can be concluded that by measuring absorbed dose to air at 300 μm radial distance in air can be converted to absorbed dose to water at

1 μm radial distance in water by application of an inverse-square correction and water-to-air stopping power ratio.

4.2.3 Correction factors for the extrapolation method

The MC-calculated correction factors for the extrapolation method dosimetric formalism described in section 2.3.4 were calculated and reported in this section. Both dosimetric formalism introduced in this work share a common k_{point} correction factor.

4.2.3.1 $k_{backscatter}$

Since the quantity of interest for this formalism is absorbed dose to water, the backscatter correction accounts for the differences in the scatter conditions between the nominal source substrate and detector materials and water. The backscatter correction can be calculated by:

$$k_{backscatter}(l) = \frac{D_{cavity,point,water}(l)}{D_{cavity,point,det,substrate}(l)} \tag{4.14}$$

where $D_{cavity,point,water}$ is the absorbed dose to cavity from a point source with the substrate and the detector composed of water and $D_{cavity,point,det,substrate}$ is the absorbed dose to air from a point source to the same cylindrical cavity with the nominal materials of the substrate and the detector. The backscatter correction must be calculated independently for each air gap using MC simulations. Air gaps of 300-525 μm were simulated with production thresholds set to 1 μm and atomic de-excitation turned on.

The results for the backscatter correction are shown in figure 4.37. The mean backscatter correction was calculated to be 5.6% with a range of 2.83%. Similar to the backscatter correction reported in figure 4.31 for the cylindrical shell formalism, the correction factor was found to be dependent on the air gap. However, there was a $\sim$ 3.0% difference

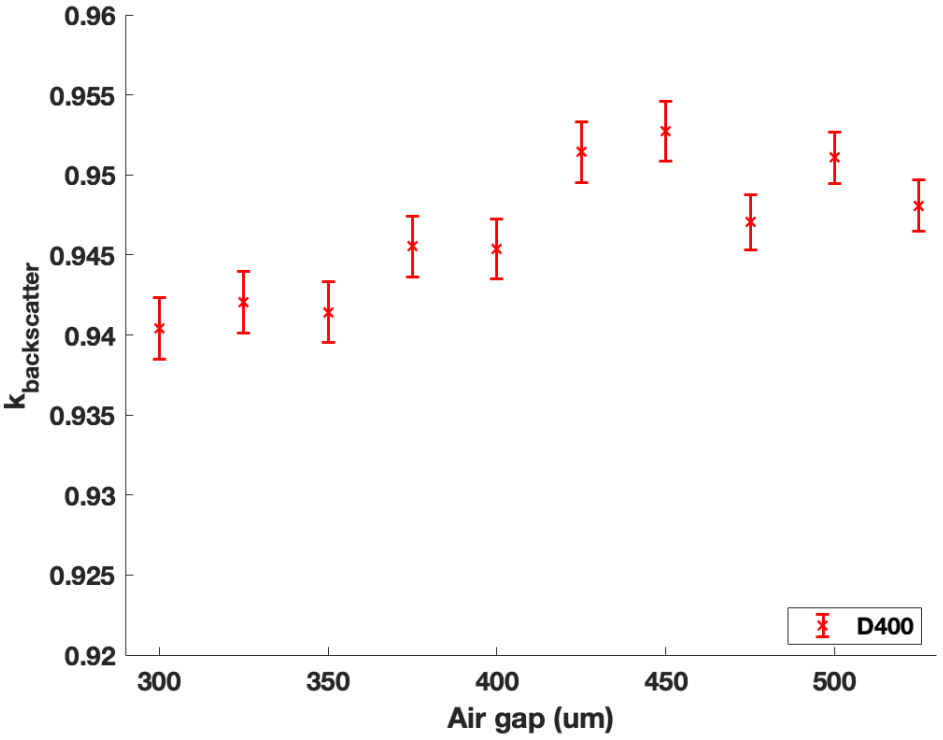

Figure 4.37: The backscatter correction factor as a function of air gap for a ^{10}Po point source.

between the two corrections. The backscatter correction when the source substrate and detector was composed of air was greater than water due to its higher effective atomic number and presence of relatively heavier elements in the material composition.

4.2.3.2 k_{div}

The divergence correction is the largest correction factor for this formalism. The k_{div} is dependent on the air gap and typically increases with increasing air gaps. Therefore, measurements with small air gaps are desired to reduce the magnitude of the divergence correction factor. The k_{div} is given by:

$$k_{div} = \frac{D_{cavity,point,water}(l \to 0)}{D_{cavity,point,water}(l)} \tag{4.15}$$

where $D_{cavity,point,water}$ is the absorbed dose to cavity from a point source with the substrate and the detector composed of water and $(l \rightarrow 0)$ refers to this curve extrapolated to a zero air gap. Absorbed dose to cavity was scored for air gaps ranging from 50-525 μm with production thresholds set to 1 μm and atomic de-excitation turned on. Absorbed dose at air gaps $< 300\mu m$ were also simulated to accurately extrapolate the curve to a zero air gap. A 3rd order polynomial function was used to fit the dose versus air gap curve and the intercept was taken as the $D_{cavity,point,water}(l \rightarrow 0)$ value. The divergence correction was then computed for air gaps in the 300-525 μm range.

The MC-calculated absorbed dose versus air gap curve with the fitted function are shown in figure 4.38. The divergence correction is also plotted as a function of air gap. As hypothesized, the divergence correction was found to be the largest correction factor for the extrapolation method. The associated uncertainty in the polynomial fit was calculated to be 1.70% with an R^2 of 0.997. Since the absorbed dose has a non-linear relationship with the air gap, the extrapolated absorbed dose was found to be dependent on the fitting parameters leading to a relatively higher uncertainty. A linear relationship, with R^2 of 0.999, was observed between the k_{div} and the air gap. The magnitude of the correction ranged from 93% to 239% within the simulated range of air gaps.

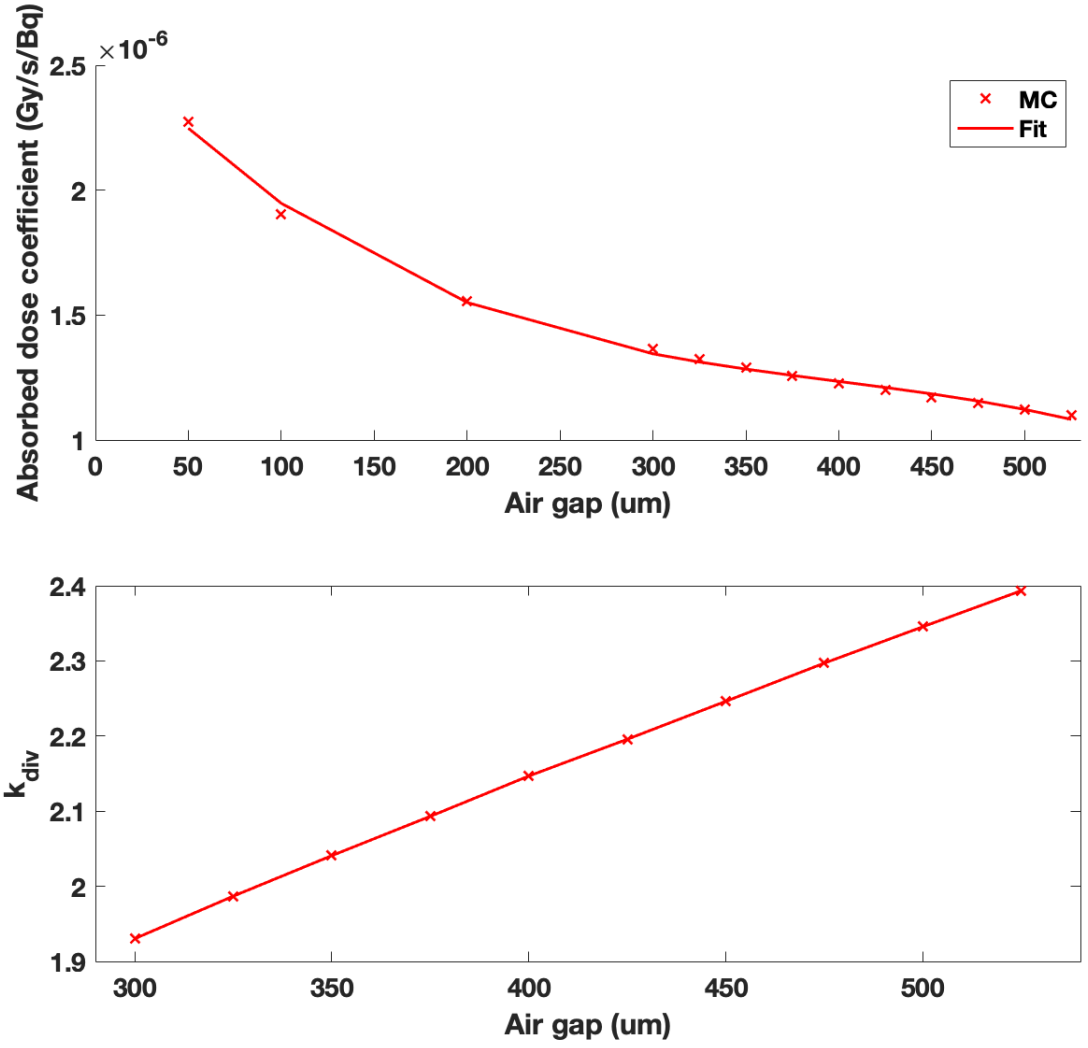

Figure 4.38: Top: absorbed dose to cavity plotted as a function of air gap with a 3rd order polynomial fit. Bottom: the divergence correction factor for 300-525 μm air gaps.

4.3 Measurement of absorbed dose from a ^{210}Po source

The constructed primary standard was evaluated using a ^{210}Po source described in section 4.1.4. The measurements consisted of ionization current readings at various air gaps with an electrical bias applied to the source substrate. The measured absorbed dose to air cavity was directly compared with MC-calculated dose. Using the formalism provided in equation 2.20 and the Monte Carlo (MC)-based correction factors calculated in section

4.2, the absorbed dose to air was measured and then converted to absorbed dose to water at 1 μm radial distance from a point source. The surface absorbed dose to water was also determined using the formalism provided in equation 2.26 and correction factors calculated in section 4.2. The $\left(\frac{\bar{W}}{e}\right)_{air}$ constant was taken from the literature to be 34.96 J/C with a total uncertainty of 0.2% [118][119]. Additionally, no energy dependence was found previously in the $\left(\frac{\bar{W}}{e}\right)_{air}$ values for alpha particles in the 3-14 MeV energy range [121].

The ionization chamber (IC)-specific correction factors were calculated individually and applied to the measured ionization current. The temperature and pressure correction, k_{TP} was calculated by:

$$k_{TP} = \frac{273.2 + T}{273.2 + 22} \times \frac{101.33}{P} \tag{4.16}$$

where T is the temperature in degrees Celsius and P is the pressure in kPa of the air. The k_{elec} correction factor was based on an electrometer-specific calibration provided by the University of Wisconsin Accredited Calibration Lab (UWADCL). The k_{pol} correction factor accounted for the polarity effect of the applied voltage and was calculated by:

$$k_{pol} = \left| \frac{M^+ - M^-}{2M^-} \right| \tag{4.17}$$

where M^+ is the positive charge collected by the detector and M^- is the negative charge. The polarity correction was calculated for each air gap. The k_{recom} correction accounts for the signal lost due to the recombination of the liberated electrons with ions in the air cavity. It is pertinent that an appropriate voltage is applied to minimize recombination effects. However, application of large voltages can lead to charge multiplication effects, which must be avoided for these measurements.

4.3.1 Recombination correction

In order to determine the optimal voltage and to investigate the recombination effects in the air cavity, experimental methods were considered. The recombination correction can be calculated by:

$$k_{recom} = k_{initial} k_{general} k_{diffusion} \tag{4.18}$$

where $k_{initial}$ is the initial recombination, $k_{general}$ is the general recombination, and $k_{diffusion}$ is the correction for loss of signal due to charges diffusing against the applied electric field. The diffusion component of the recombination correction is considered negligible when compared to the initial and general recombination. The recombination correction, k, is calculated as the inverse of the collection efficiency f. The initial recombination occurs when the liberated electron and positive ion from the same ionization event combine together to neutralize the charge. The general recombination occurs when an electron and a positive ion from different ionization events combine with each other. Typically, initial recombination is dependent on the ionization density, or the linear energy transfer (LET), of the particles traversing the cavity and general recombination is proportional to the dose rate of the radiation source. It is worth noting that the initial and the diffusion recombination collection efficiencies are proportional to the applied voltage V, and the general recombination efficiency is proportional to V^2.

For photon and electron beams, the recombination correction is usually determined by plotting $1/V^2$ against $1/Q$, where V is the applied voltage and Q is the collected charge. The saturation charge, Q_{sat}, is calculated as the inverse of the y-intercept. The total recombination correction is determined by $\frac{Q_{sat}}{Q}$. This method assumes that the initial and diffusion recombination effects are minimal and the total recombination is proportional to V^2. Previously, this assumption has been proven to be untrue for heavy charged particles due to their high LET and high initial recombination contribution [122] [123] [124] [125].

Therefore, the recombination correction must be modeled by considering the dependence of charge on both V and V^2:

$$\frac{1}{Q} = \left(\frac{1}{Q_{sat}} + \frac{\alpha}{V} + \frac{\beta}{V^2}\right) e^{-\gamma V} \tag{4.19}$$

where α, β, and γ are fitting parameters [126]. The exponential term dictates the collected charge in the multiplication region.

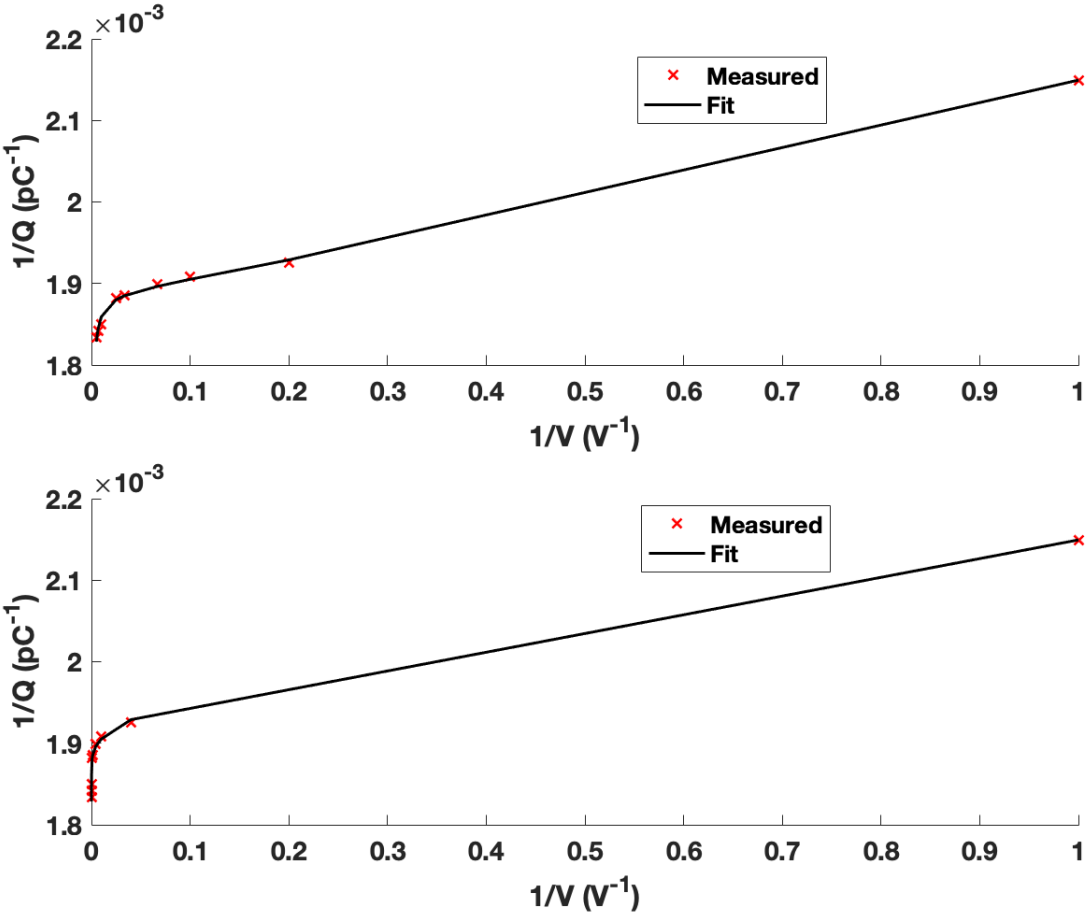

Figure 4.39: Measured and fitted Jaffe plots to determine the recombination correction factor.

The total recombination correction can be measured by acquiring charge readings at various electric potentials. The measured data can be fitted to equation 4.19 and the

saturation charge can be determined. In this work, a least square optimization tool was used in MATLAB to fit the measured data. Measurements were acquired at a 300 μm air gap with electric potential ranging from 1-200 V. Figure 4.39 shows an example of the measured and fitted data where 1/Q is plotted as a function of both 1/V and $1/V^2$. For this example, the fitting parameters Q_{sat}, α, β, and γ were calculated to be 529.94 pC, 2.06×10^{-4} V/pC, 5.68×10^{-5} V^2/pC, and 1.59×10^{-4} V^{-1}, respectively. Therefore, the recombination correction was determined to be $< 0.5\%$ for an electric field strength of 150 V/mm.

4.3.2 Ionization current measurements

Before the measurements were acquired, the stability of the signal was investigated by acquiring ionization current measurements at an arbitrary air gap for a long period of time. The current was measured using a MAX4000 electrometer (Standard Imaging, Middleton, WI) at a rate of 1 Hz for 30 minutes. The current was observed to be fluctuating within 0.22% of the mean value, as shown in figure 4.40. The mean period of the oscillation was found to be 28 seconds. Therefore, all charge readings must be taken for a longer time period than that.

Multiple trials were launched to determine the D400 ionization current due to the ^{210}Po source. Independent measurements were acquired for each trial and the entire measurement process was repeated from the beginning. Figure 4.41 illustrate the steps taken to acquire the ionization current for each trial. With the ^{210}Po source mounted on the source subassembly, the D400 EC was lowered using the linear motion stage to an air gap < 1 mm. The source was then biased with an electric potential of -40 V and lateral scans were acquired using the hexapod motion stage with 0.1 mm steps. At each dwell position, a single 45 s charge reading was taken using a MAX4000 electrometer. The position

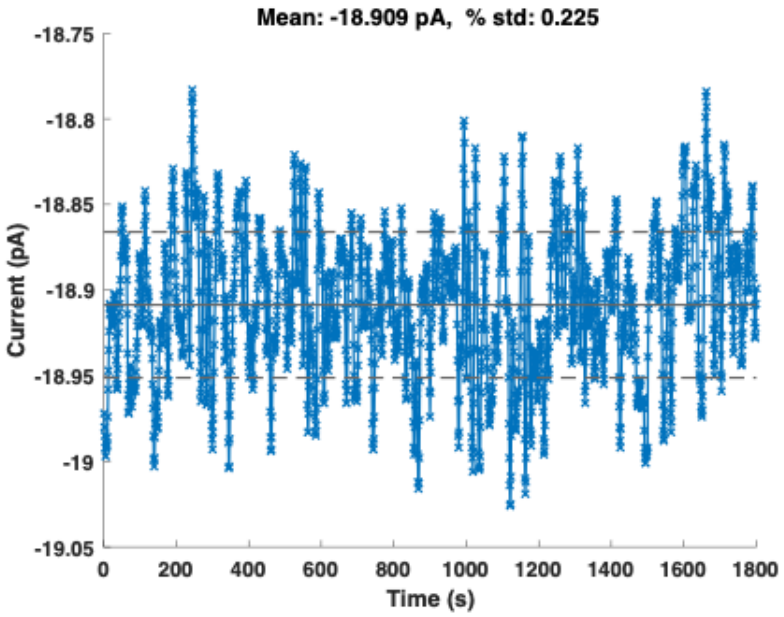

Figure 4.40: The stability of the D400 ionization current signal over time.

Figure 4.41: The measurement procedure for each trial.

with the maximum signal was selected for all consequent measurements. Following the lateral alignment, the rotational alignment is performed for the D400 EC based on the methodology described in section 4.1.3.1. It is noteworthy that any lateral offsets were considered when selecting the pivot point of the rotation.

Once the lateral and rotational alignment has been performed, the initial air gap between the source and the D400 EC is determined using the capacitance method described in section 4.1.3.2. A voltage change from -10 V to -100 V is applied and a 30 s charge reading is collected. Following this measurement, a 30 s charge reading is collected at the -100 V bias to distinguish the charge due to the capacitance and charge due to ionization. These measurements are acquired at least three times at four separate air gaps with increments

of 50 μm. The equations 4.7 and 4.6 are then used to determine the initial air gap. An example of a capacitance measurement from one of the measurement trial is shown in figure 4.42.

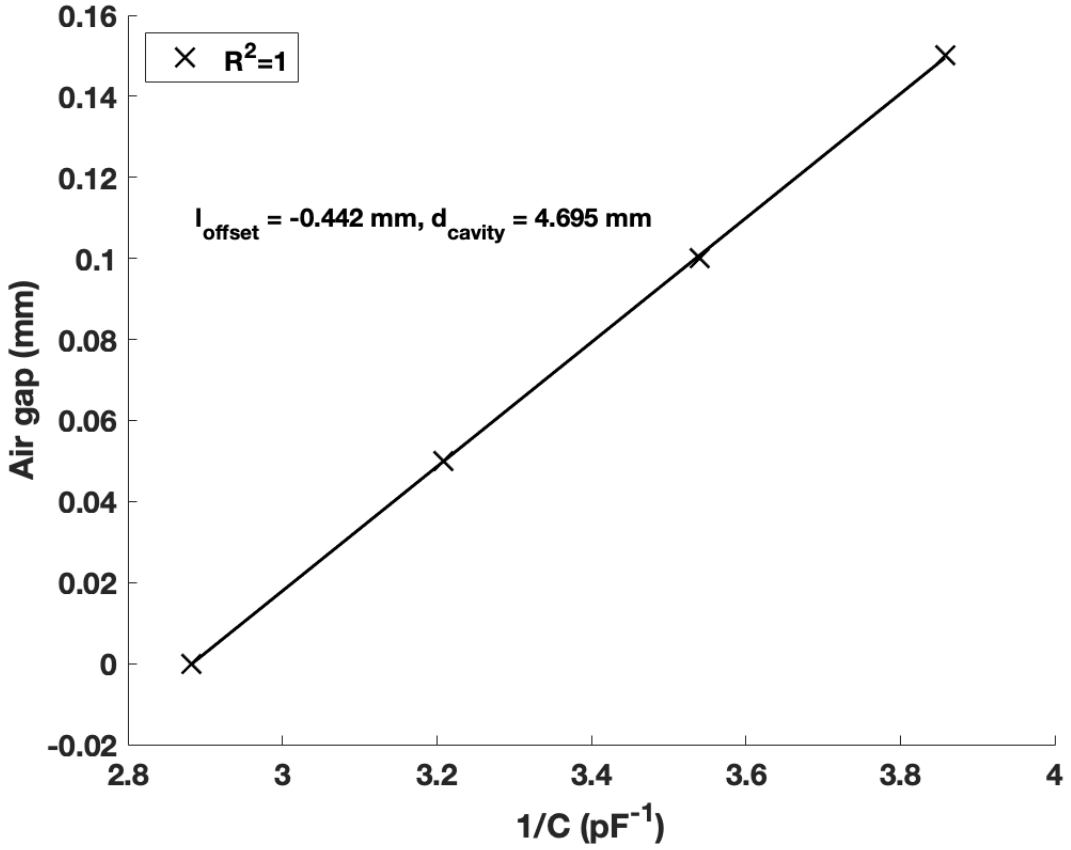

Figure 4.42: Capacitance-based method to determine the initial air gap.

The recombination correction was measured based on the method described in section 4.3.1 for each measurement trial. Three 60 s charge readings were acquired at each applied voltage with the air gap set to 300 μm. The recombination correction was calculated using the fitting function reported in equation 4.19 for the 150 V/mm electric field strength. Both positive and negative bias as applied and three 60 s charge readings were collected to calculate the polarity correction factor using equation 4.17. The temperature and pressure was noted to apply an air density correction to the ionization current readings. Three 60 s charge readings were collected at each air gap ranging from 300-525 μm

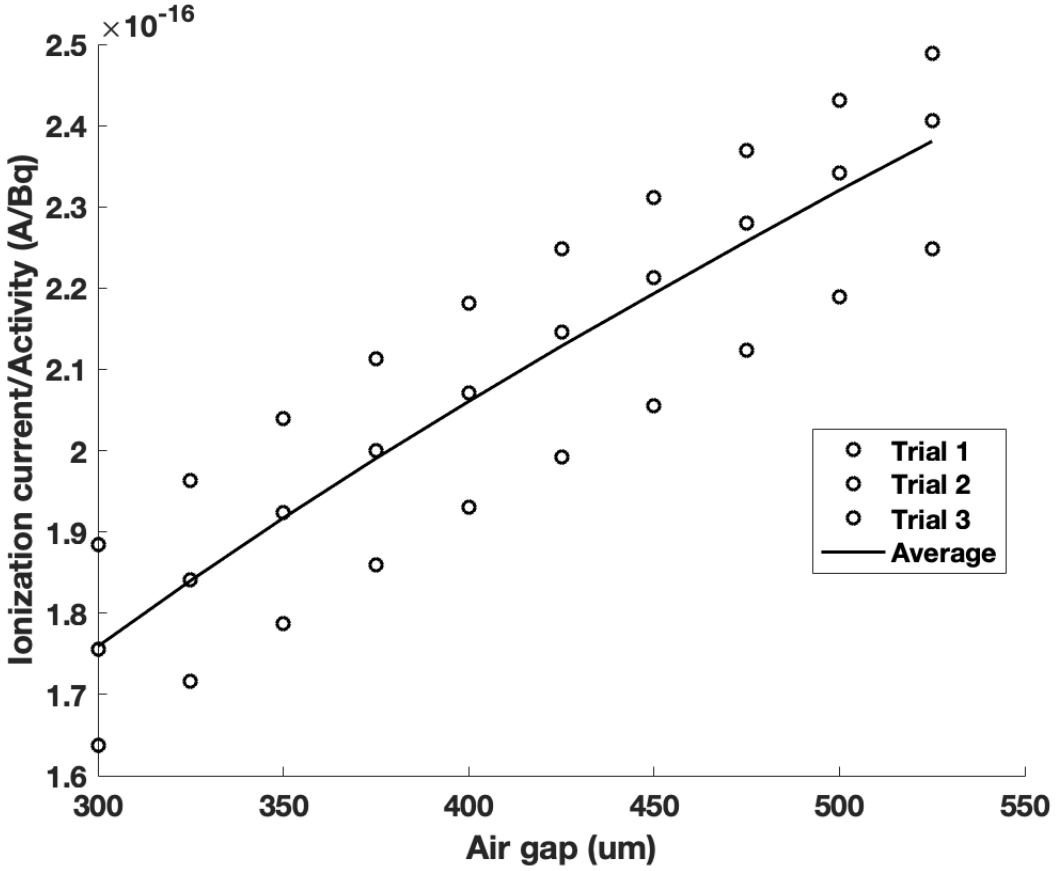

Figure 4.43: The ionization current, normalized by radioactivity, collected by the D400 EC at each air gap.

in 25 μm increments. The $k_{T,P}$, k_{pol}, k_{recomb}, and k_{elec} corrections were applied to the charge readings, which were then normalized by the decay-corrected radioactivity of ^{210}Po. Figure 4.43 displays the current readings for the three trials conducted in this study. Percent standard error in the range of 2.19-3.30% was found in the ionization current readings when results from all trials were considered.

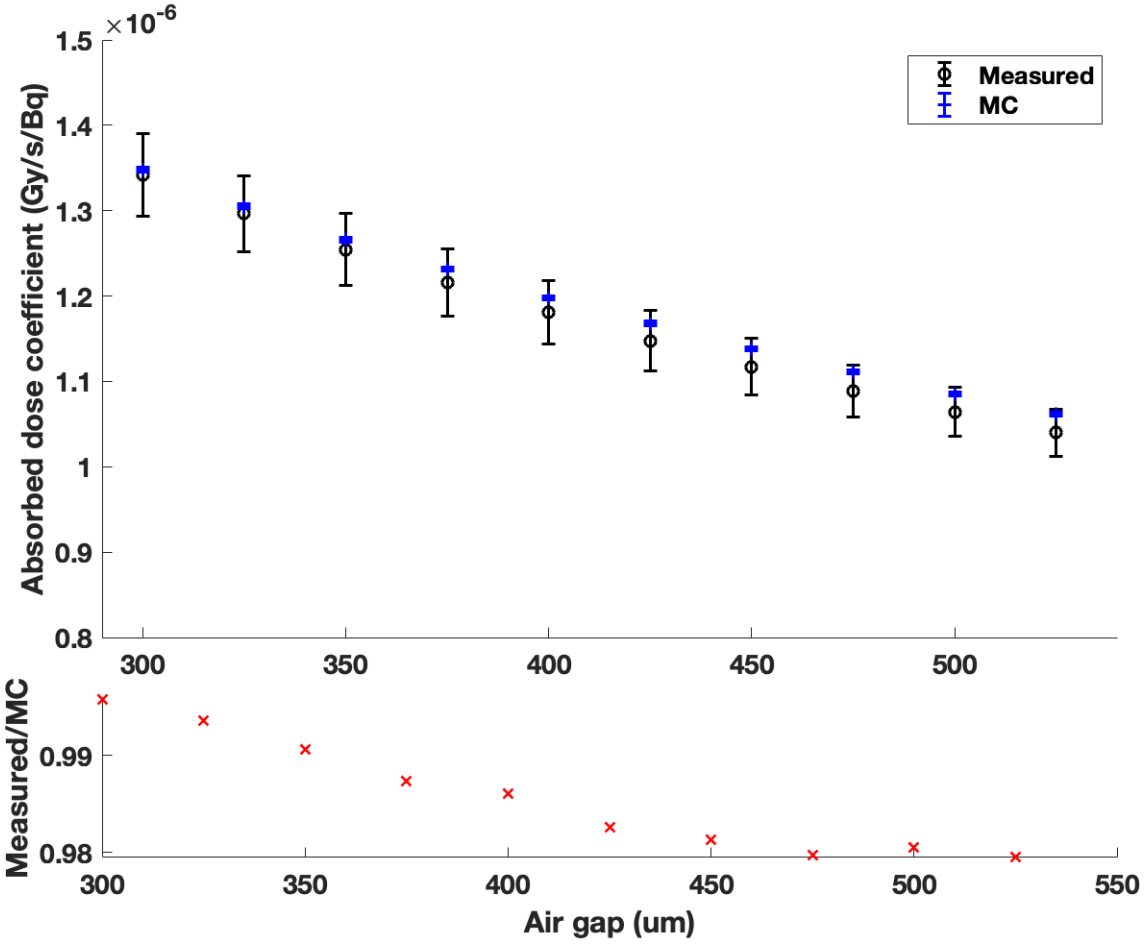

Figure 4.44: The measured and MC simulated absorbed dose to cavity as a function of air gaps in the 300-525 μm range.

4.3.3 Comparison of measured and MC absorbed dose to cavity

The accuracy of the MC-predicted absorbed dose to cavity, normalized by radioactivity, was assessed by comparing it with the measured absorbed dose. The measurement apparatus was simulated using parameters discussed in section 4.2 and the ^{210}Po source was modeled to match the measured source specifications. The measured absorbed dose to cavity was calculated by:

$$\dot{D}_{air}(l) = \frac{1}{A_o}\frac{\left(\frac{\bar{W}}{e}\right)_{air}}{\rho_o A_{eff}}\frac{I}{l}\left(k_{pol}k_{recom}k_{TP}k_{elec}\right) \tag{4.20}$$

where A_o is the activity of the ^{210}Po source, $\left(\frac{\bar{W}}{e}\right)_{air}$ is the mean energy required to liberate an ion pair in dry air, ρ_o is the physical density of air at standard temperature and pressure, A_{eff} is the effective cross-sectional area of the cylindrical air cavity, I is the ionization current, and l is the air gap between the collector and source surfaces. The last few terms, denoted by k, are the ion chamber-specific correction factors discussed in previous sections. Figure 4.44 compares the measured and MC-simulated absorbed dose to air cavity subtended by the D400 EC. Good agreement was found between the two curves with average and maximum deviations of 1.43% and 2.05%, respectively. These results demonstrate the ability of MC methods to accurately calculate absorbed dose for alpha-emitting radionuclides.

4.3.3.1 Uncertainty budget

Table 4.4: Uncertainty budget for the absorbed dose measurement, acquired with the D400 EC, at a 300 μm air gap.

Component of uncertainty	Type A (%)	Type B (%))
Net current	0.20	
Current repeatability	3.29	
Air density correction		0.10
Recombination correction		0.10
Average energy per ion pair		0.20
Air collection volume		1.00
Radioactivity		1.00
Combined uncertainty (k=1)	3.61	
Combined uncertainty (k=2)	7.22	

Tables 4.4 and 4.5 show the combined uncertainty in the measured absorbed dose to air cavity for the 300 μm and 500 μm air gaps. The random fluctuations in the signal,

Table 4.5: Uncertainty budget for the absorbed dose measurement, acquired with the D400 EC, at a 500 μm air gap.

Component of uncertainty	Type A (%)	Type B (%))
Net current	0.20	
Current repeatability	2.19	
Air density correction		0.10
Recombination correction		0.10
Average energy per ion pair		0.20
Air collection volume		1.00
Radioactivity		1.00
Combined uncertainty (k=1)	2.63	
Combined uncertainty (k=2)	5.26	

shown in figure 4.40, led to a 0.2% Type A uncertainty in the signal for a given trial. The current repeatability was calculated by computing the percent standard error in the current readings considering all measurement trials. This uncertainty component was the largest contributor to the total uncertainty and is attributed to the positional uncertainty in the air gap and uncertainty in the rotational alignment. Any uncertainty in the capacitance method to determine the initial air gap is also represented by the current repeatability component of the uncertainty. The ionization signal was observed to be highly sensitive to the positional offsets in the air gap. Based on the MC simulated absorbed dose, deviations of $\sim 20\mu m$ between the actual and measured air gap can lead to deviations $> 3\%$ in the absorbed dose. Any tilts in the geometry further add to the uncertainty. Additionally, the uncertainty in the current readings was noted to decrease with increasing air gap since the slope of the dose versus air gap curve decreases with increasing air gap. Therefore, current readings acquired at smaller air gaps were found to be more sensitive to positional offsets. The combined uncertainty at k=1 ranged between 2.63-3.61%.

4.3.4 Absorbed dose measurements using the cylindrical shell method

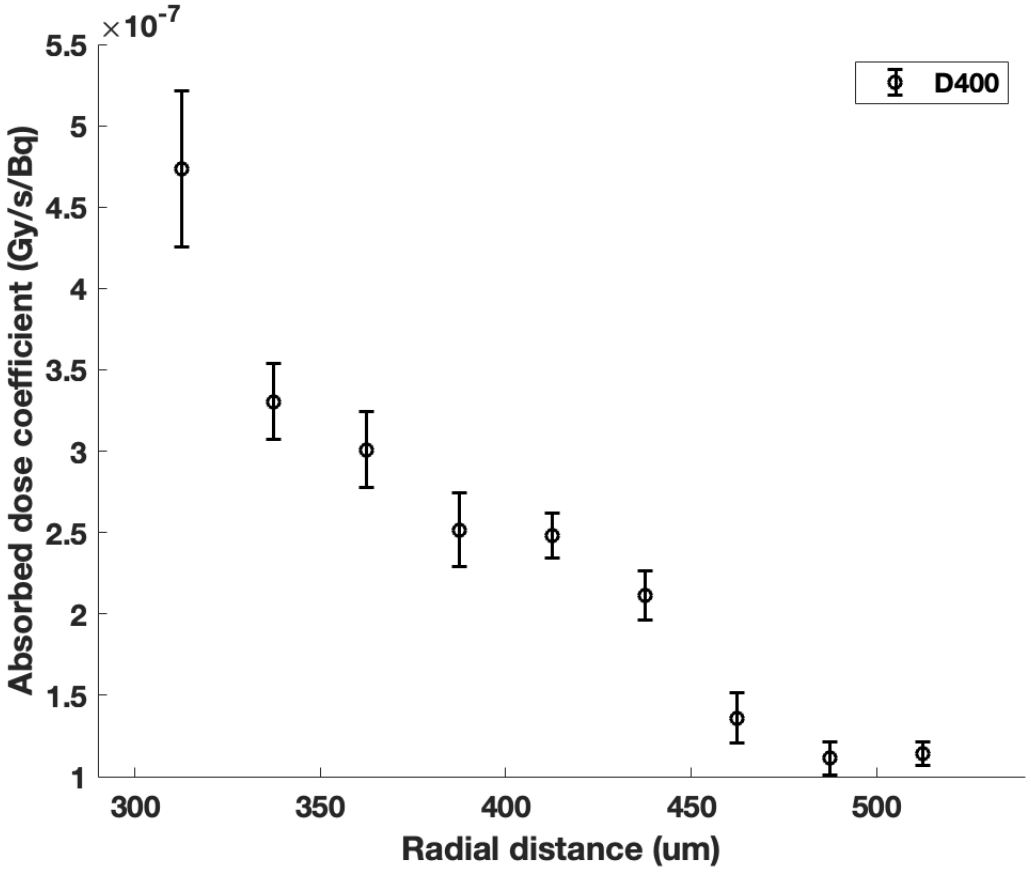

Figure 4.45: Measured absorbed dose to air as a function of radial distance from a point ^{210}Po source using the cylindrical shell method.

The quantity of interest proposed in the cylindrical shell dosimetric formalism measures absorbed dose to air as a function of radial distance from a point source, as discussed in section 2.3.3. Following this calculation, the absorbed dose to air is converted to surface absorbed dose to water using equation 4.13. Figure 4.45 shows the measured absorbed dose to air as a function of radial distance. This curve was calculated using equation 2.20. Due to the inverse square law, the absorbed dose was found to decrease as the radial distance increases. The converted surface absorbed dose to water at each radial distance is reported in figure 4.46. Ideally, the surface absorbed dose to water

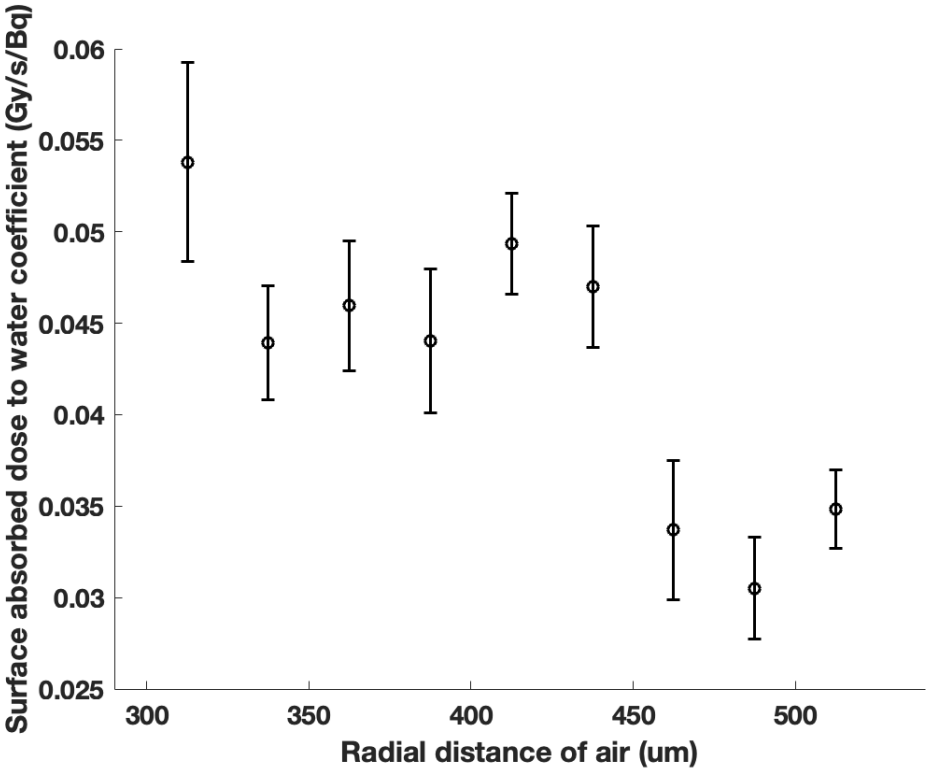

Figure 4.46: Surface absorbed dose to water measured at each radial distance from a point ^{210}Po source using the cylindrical shell method.

calculated using each independent absorbed dose to air would be equivalent. However, the induced uncertainty in the measurements lead to a large range of calculated dose to water. The mean surface dose to water was calculated to be 0.0426 Gy/s/Bq with a range of 0.0233 Gy/s. Therefore, the uncertainty in the absorbed dose values was found to be prohibitively large to yield a precise absorbed dose measurement.

4.3.4.1 Uncertainty budget

Table 4.6 compiles the combined uncertainty for absorbed dose to air at a 312.5 μm radial distance from a point ^{210}Po source. The largest component of uncertainty was the current repeatability uncertainty in the net ionization current readings calculated by the difference in the current readings at 300 μm and 325 μm air gaps. As discussed in section

Table 4.6: Uncertainty budget for the absorbed dose to air measurement, using the D400 EC, at a 312.5 μm radial distance from a point source.

Component of uncertainty	Type A (%)	Type B (%))
Net current	0.28	
Current repeatability	10.0	
Air density correction		0.10
Recombination correction		0.10
Average energy per ion pair		0.20
Air collection volume		1.00
Radioactivity		1.00
k_{point} correction		0.20
$k_{backscatter}$ correction		0.20
k_{cav} correction		0.20
Combined uncertainty (k=1)	10.11	
Combined uncertainty (k=2)	20.22	

4.3.3.1, the repeatability uncertainty in the ionization current at each air gap can be as large as 3.29 %. Therefore, the current difference method to measure absorbed dose to a cylindrical shell introduces uncertainty from current readings at two different air gaps, leading to a much larger overall uncertainty. Furthermore, the net current reading is much smaller than the individual current reading at each air gap lowering the SNR of the absorbed dose. Assuming the dose fall-off follows approximately the $1/r^2$ function, a 15 μm positional offset error at 0.3 mm radial distance from the source will lead to a 10% difference in the ionization current. Therefore, the uncertainty in the positional and rotational alignment of the air gap propagates at a much larger magnitude for this dosimetric formalism leading to combined uncertainties greater than 10%, regardless of the radial distance from the source. The high magnitude of the uncertainty was found to be reflected in the surface absorbed dose to water calculation shown in figure 4.46. Hence, the percent standard deviation in the surface absorbed dose to water was calculated to be 18.40%. It can be concluded that the cylindrical shell dosimetric formalism yields large uncertainties in the absorbed dose measurements.

4.3.5 Surface absorbed dose measurements using the extrapolation method

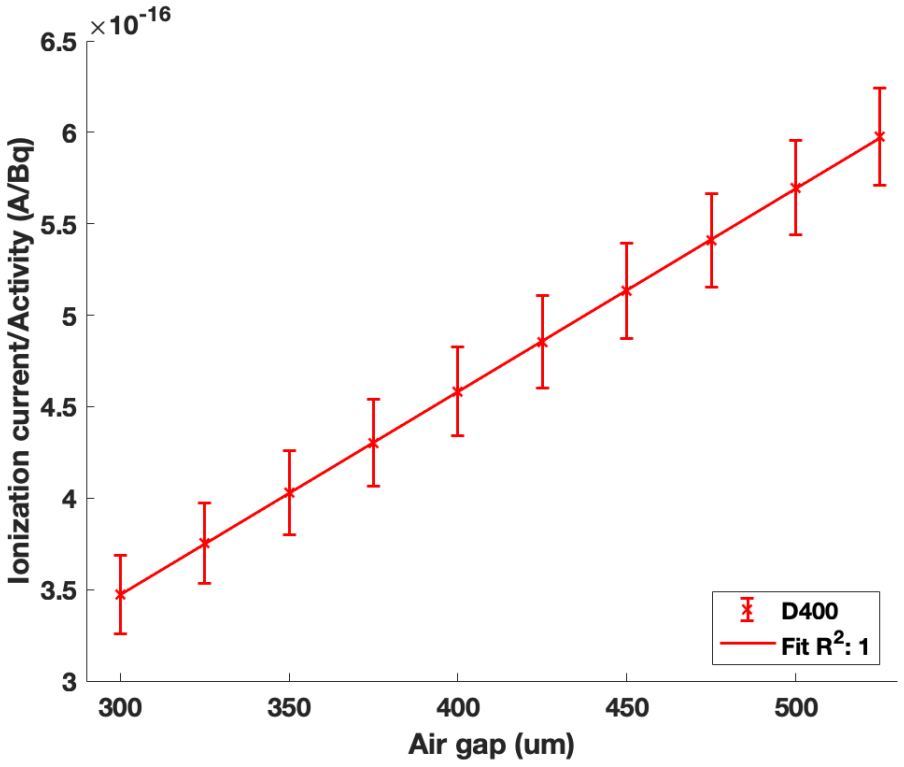

Figure 4.47: Corrected ionization current at each air gap for the ^{210}Po source.

The extrapolation method directly measures the absorbed dose to water by extrapolating the ionization curve to a zero air gap. This dosimetric formalism was previously described in section 2.3.4. The ionization current at each air gap corrected by the ion chamber-specific correction factors and MC-calculated correction factors is shown in figure 4.47. The current data were found to be linearly increasing with the air gap with an R^2 of 1.00. The mean slope of the curve, $(\frac{\Delta I}{\Delta l})_{l\to 0}$, was calculated to be 1.11×10^{-18} A/Bq/μm. Based on this calculation, the mean surface absorbed dose to water was measured to be 2.8913×10^{-06} Gy/s/Bq.

It is important to address the differences in the surface absorbed dose to water between the two dosimetric formalisms. The surface dose measured using the extrapolation method

was many times smaller than the surface dose measured using the cylindrical shell method. This difference arises due to the different definitions of surface absorbed dose. For the cylindrical shell formalism, the surface absorbed dose to water is defined by scoring absorbed dose to a spherical shell at 1 μm radial distance away from a point source. Therefore, this formalism accounts for the inverse-square fall off along both the lateral direction and the radial direction. The extrapolation formalism doesn't explicitly account for the inverse-square fall off and only considers the decrease in absorbed dose to cavity with the increasing air gap between the source and detector electrodes. Both formalisms measure absolute absorbed dose, albeit considering different geometries.

4.3.5.1 Uncertainty budget

Table 4.7 shows the combined uncertainty in the surface absorbed dose to water using the extrapolation dosimetric formalism. Besides the uncertainty in the stopping power ratio, the largest contributor to the total uncertainty was the current slope repeatability, calculated by considering the standard error in the slope of the corrected ionization current versus air gap curve. This uncertainty was observed to be relatively smaller than the repeatability uncertainty reported in previous section. This can be partially explained by the usage of a highly precise hexapod motion stage capable of relatively moving with a high repeatability. Therefore, despite having possible rotational and positional errors, the slope of the ionization versus air gap curve was found to be repeatable over multiple trials. The uncertainty in the divergence correction was the third largest contributor. This uncertainty was calculated by considering both the statistical uncertainty in the MC simulations and the polynomial fitting error when calculating the dose extrapolated to zero air gap. The surface absorbed dose to water uncertainty using the extrapolation method was found to be 3.74% at k=1.

Table 4.7: Uncertainty budget for the surface absorbed dose to water measured using the D400 EC.

Component of uncertainty	Type A (%)	Type B (%))
Net current	0.20	
Current slope repeatability	1.61	
Air density correction		0.10
Recombination correction		0.10
Average energy per ion pair		0.20
Air collection volume		1.00
Radioactivity		1.00
$(\frac{S_{col}}{\rho})$		2.45
k_{point} correction		0.20
$k_{backscatter}$ correction		0.20
k_{div} correction		1.79
Combined uncertainty (k=1)	3.74	
Combined uncertainty (k=2)	7.48	

Chapter 5

Construction and evaluation of a printed circuit board (PCB) planar windowless extrapolation chamber as a primary standard for absorbed dose

5.1 Detector construction and characterization

In addition to the D400 extrapolation chamber (EC), a printed circuit board (PCB) was constructed and utilized as an absolute dosimeter in this work. The motivation behind construction of such an EC was its ability to align in a more accurate parallel configuration with the source substrate than the D400 EC. Figure 5.1 shows the first version of the PCB EC. The PCB was constructed with a 35 μm copper layer on a FR-4

fiberglass material. The fiberglass provides a base support layer for the PCB and also act as an insulator between the conducting regions. The thickness of the fiberglass substrate was 2 mm. The clearance between the conducting regions was set to be 0.2 mm. The collecting electrode was constructed to be 4.00 mm in diameter, matching the collector dimensions of the D400 EC. The collector was surrounded by a guard ring with a 2.5 mm radial thickness and was segmented into quarters. Each segmented guard region was read out using the leads running towards each corner of the PCB. The bottom right corner of the PCB shown in figure 5.1 shows two leads, one for the collector and one for the bottom right guard. The segmented guard ring was surrounded by conducting material to form a square.

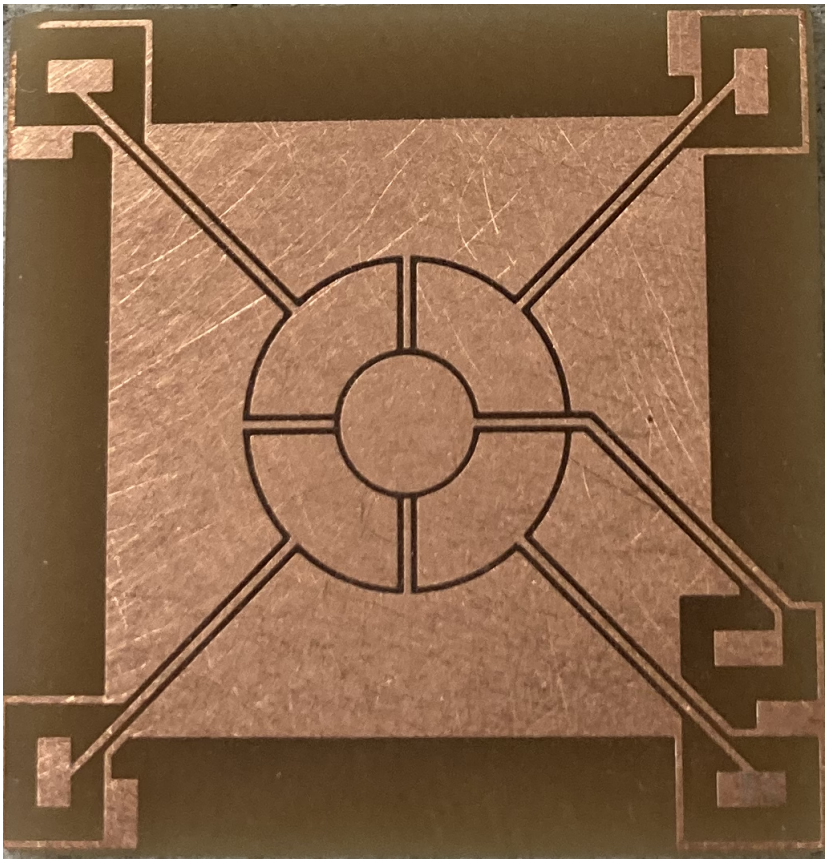

Figure 5.1: The first version of the PCB EC is shown. The center circle is the collecting electrode and the surrounding segmented ring is the guard.

The novelty of the PCB EC originates from its segmented guard design. Since capacitance between the guard ring and the source substrate is inversely proportional to the air gap between them, a parallel configuration between the detector and source would lead to an equivalent capacitance between the opposing segmented guards. Therefore, by measuring and minimizing the differential capacitance between the two sets of opposing guards, a parallel alignment can be achieved with great accuracy. This concept was borrowed from the field of micromechanics. An accurate parallel alignment between the detector and the source leads to a more accurate knowledge of the air cavity dimensions and the measured absorbed dose. However, the construction of the PCB with metallic conductors, instead of plastic-based conductors such as D400, leads to a larger backscatter correction factor.

5.1.1 PCB detector subassembly

The apparatus assembly described in section 4.1 was used with the PCB detector subassembly. The D400 EC was swapped out with the PCB subassembly described in this section. The source subassembly and the ancillary components were kept unchanged for measurements using the PCB EC. Following the construction of the first version of the PCB EC, the electronic noise level was measured by applying an electric potential of 30 V to the source substrate. The leakage current was measured to be < 10 fA using the MAX 4000 electrometer. Based on these results, the FR-4 fiberglass was deemed suitable as an insulator.

The final version of the PCB was constructed by Silver Circuits Inc. (Houston, TX) and is displayed in figure 5.2. The PCB had a gold finishing on top of the copper layer. The PCB was mounted on a cylindrical aluminum part with holes to accommodate the wires. The aluminum part was machined so that it can slide into the optical collar shown in figure 4.1. The PCB was held onto the mounting part using three plastic screws and

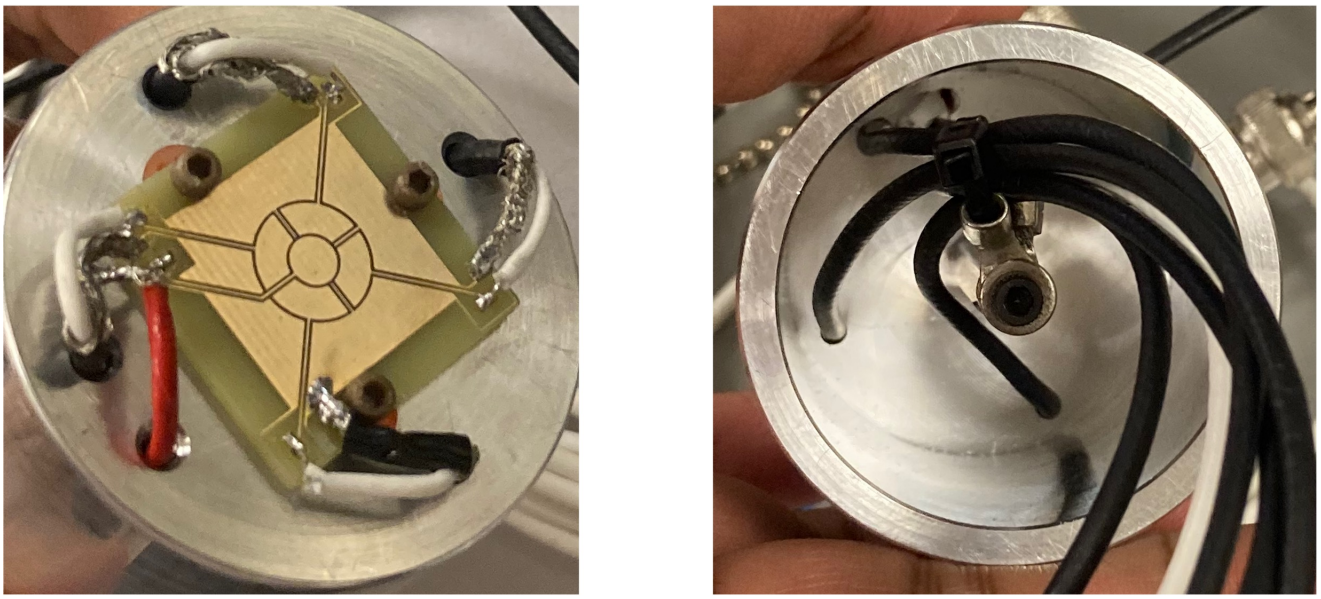

Figure 5.2: Left: the final version of the PCB mounted on the cylindrical aluminum part is shown. Right: the back side of the mounting part is shown.

polyamide washers. A hex standoff was screwed on the back side of the PCB mounting part to clamp down the wires. The electrical wires for each segmented guard were read out individually when measuring differential capacitance across the opposing guards. This was defined to be the "segmented mode." When measuring the ionization current due to the radioactive source, the individual segmented guard channels were combined to form a single guard ring. This was labeled to be the "combined mode." The electrical signal was read out using coaxial cables.

Following the construction of the PCB, soldering of the wires, and mounting on the aluminum part, the surface flatness was evaluated using the Zygo NewView 9000 interferometer. The parameters described in section 4.1.1 were utilized for these measurements. Figure 5.3 shows the 2D flatness profile of the PCB. Several radial profiles were plotted at various polar angles as shown on the bottom of the figure. The dips in the profile correspond to the 0.2 mm clearance gaps separating the conductors. Since the diameter of the source substrate was 5.55 mm in radius, the region of interest for this work was the central circular area within this radial distance. The upper left and lower right corners of

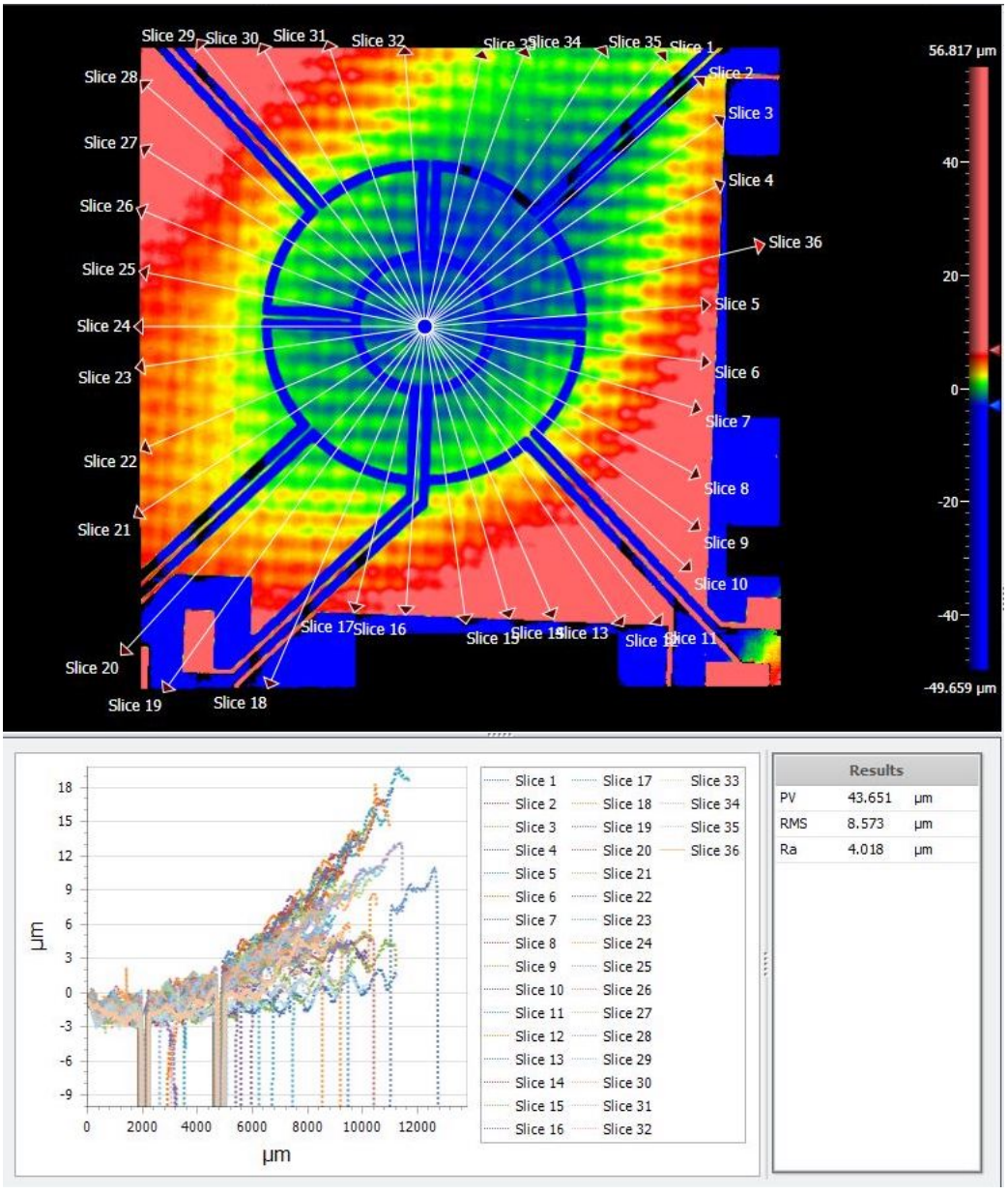

Figure 5.3: The interferometer results for the final version of the PCB mounted on the detector subassembly.

the PCB were observed to bow out with a magnitude of up to 18 μm. Within the central collector and guard region, the flatness was within 10 μm. Therefore, small air gaps can be permitted between the PCB and the source substrate.

Since the PCB was constructed with high atomic number metallic materials, the backscatter was quantified using a similar approach first introduced in section 4.1.1. Monte Carlo simulations (MC) were performed using the GEANT4 code and parallel monoenergetic alpha beam sources simulated on the flat surface of a cylindrical air cavity. The absorbed dose to cavity was scored with and without the presence of the gold cylindrical collector placed distally to the cavity, as demonstrated in figure 4.14. The optimal physics parameters determined in section 3.1.2 were utilized. The atomic de-excitation was turned on and the production threshold for each particle was set to 1 μm. The backscatter was calculated using equation 4.1.

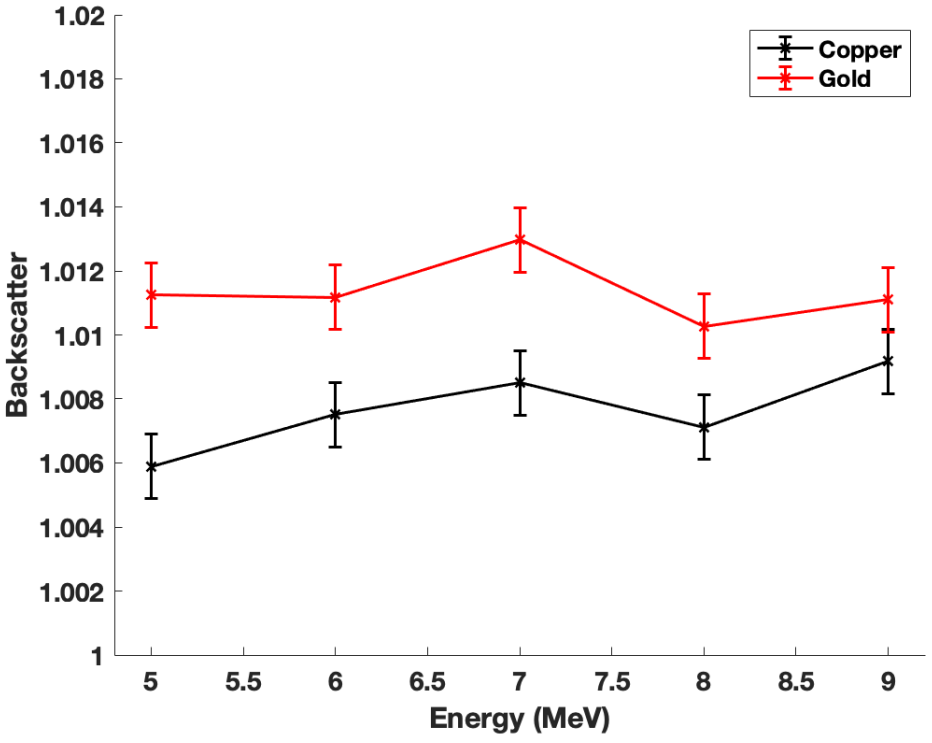

Figure 5.4: The backscatter due to the presence of the gold or copper collector.

Figure 5.4 shows the backscatter from the collector, simulated as both gold and copper separately, as a function of alpha energy. For the gold collector, the mean backscatter was calculated to be 1.1% and was observed to be energy independent given the uncertainty in the simulation results. The backscatter for the copper collector was observed to increase with increasing alpha energy. However, the maximum backscatter was found to be $< 1\%$. The parallel incidence of the alpha particle beam for these simulations leads to a low probability of backscattering. If the alpha particles strike a surface with an oblique angle, the backscatter typically increases due to the multiple Coulomb scattering of the particle deflecting its path. Therefore, the results shown in figure 5.4 cannot be directly substituted for the measurement setup utilized in this work.

5.1.2 COMSOL electric field lines simulations

The constructed PCB must have uniform electric field lines, at least in the vicinity of the collector and the guard. Presence of any fringe fields or regions of non-uniform electric fields can lead to a deviation of the cavity's actual volume from the nominal volume. Further, any sharp edges in the geometry may lead to electric field distortion. For the PCB EC, the clearance between the conducting regions such as the collector and the guard, as well as the clearance between the segmented guard, was selected to be 0.2 mm. It is important to demonstrate that this gap is sufficient for the definition of the active volume of the air cavity.

The COMSOL Multiphysics® simulation code was used to simulate the electric field lines inside the air gap between the PCB and the source substrate. A 3D model of the PCB was constructed and shown in figure 5.5. Only the region with the segmented guard and the collector was simulated since the air cavity is subtended by the collector and is defined by the gap between the collector and the guard. The source substrate was simulated to be a

cylinder made out of a generic conductor and was applied with a constant static electric potential such that the electric field strength inside the air gap remained 100 V/mm. The collector and the guard were also simulated to be conductors as well. The air gap between the source substrate and the PCB was arbitrarily selected to be 100 μm. The air between the collector and the guard had a physical density of 1.197 kg/m^3, relative permittivity of 1.0, and electric conductivity of 5.0E-015 S/m. The collector-guard insulator (CGI) was allowed to float during these simulations. A triangular "extra-fine" mesh was created with sides $< 5\mu m$ for high-resolution electric field simulations. A streamline plot was used to visualize the electric field lines in the geometry. The electric field lines near the CGI and near the edges of the segmented guard were of interest in this work. Two 2D slice profiles, shown as bolded black lines on figure 5.5, were extracted from the 3D simulation results.

Figure 5.6 shows the 2D profile of the electric field lines near the CGI. The electric field lines were observed to be uniform in the guard and the collector regions and were noted to diverge exactly halfway in the CGI gap. As found previously in section 4.1.2 for the D400 EC, the radius of the air cavity was calculated to be:

$$r_{\text{cavity}} = 0.5(r_{\text{collector}} + r_{\text{guard inner}}) \tag{5.1}$$

where $r_{\text{collector}}$ is the radius of the collector and $r_{\text{guard inner}}$ is the inner radius of the guard. The radius of the air cavity was calculated to be 2.10 mm, which is $\sim$80 μm larger than the air cavity subtended by the D400 EC.

The electric field lines between two segmented guards are shown in figure 5.7. The lead represents a 0.2 mm thick conducting region separating the segmented guards. The 0.2 mm clearance between the segmented guards and the lead is also shown. The field lines were observed to be uniform everywhere except near the edges of the geometrical

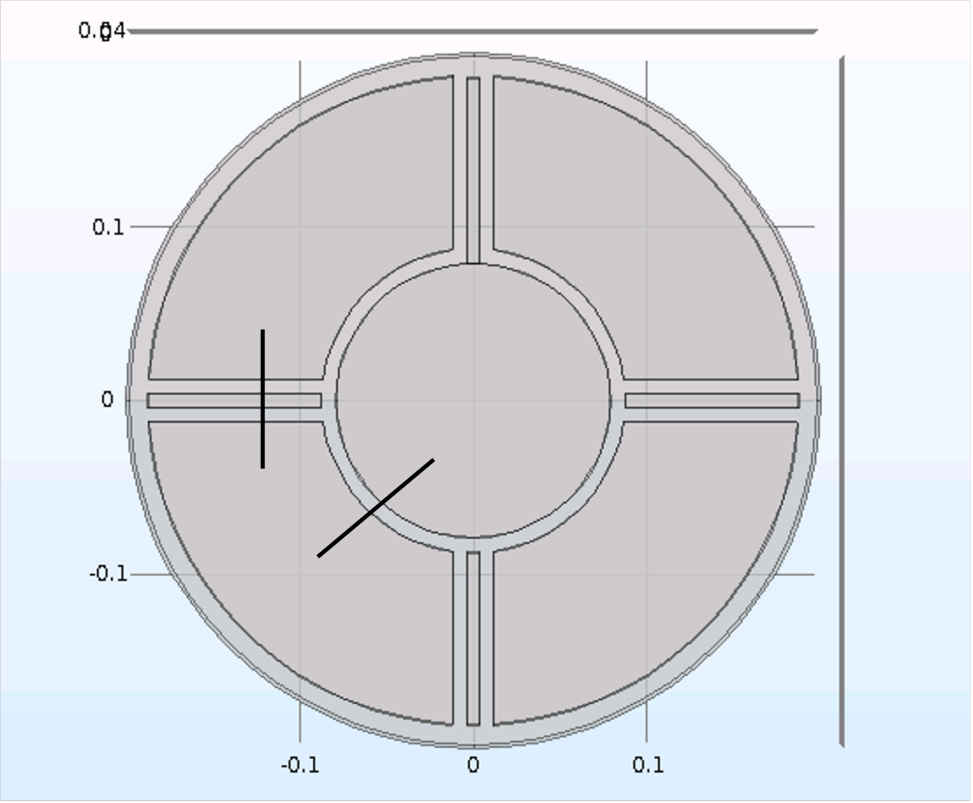

Figure 5.5: The schematic of the PCB EC simulated in COMSOL Multiphysics®. The black lines demonstrate the 2D slice profiles that were extracted from the 3D simulation results.

components. The individual segmented guard regions were found to be well seperated from each other with the field lines halfway in the clearance region terminating at the guard. It can be concluded that a 0.2 mm clearance between the guard segments is sufficient for well-defined guard regions.

5.1.3 Capacitance and parallelism measurements

5.1.3.1 Parallel alignment between the detector and the source

A parallel alignment between the PCB and the source substrate can be achieved using the segmented guard design. Figure 5.8 shows the coordinate system used for this purpose

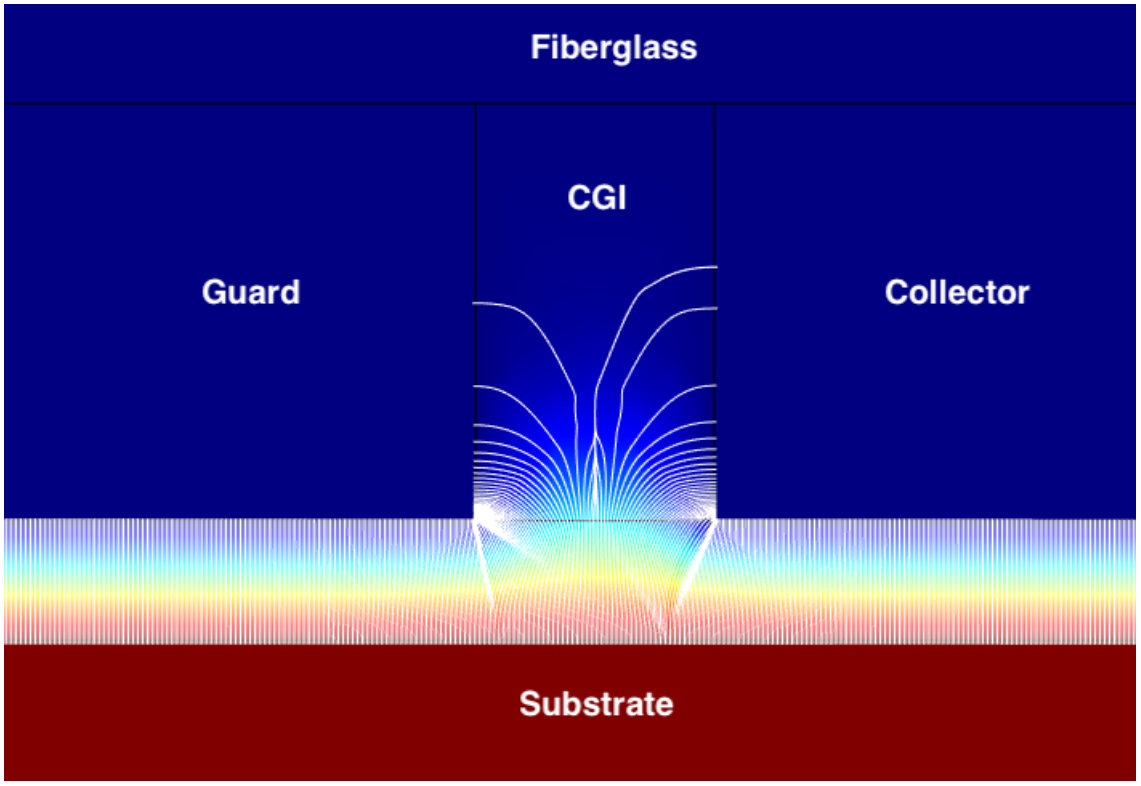

Figure 5.6: The electric field lines near the collector-guard insulator (CGI) for a 100 μm air gap.

and the connection of the segmented guards to their respective channels. The rotation about the x and y axes is represented by u and v, respectively. A parallel configuration can be achieved by minimizing the differential capacitance between the positive and negative terminals of a given channel. For example, a rotation along the x axis (denoted by u) will induce a capacitance imbalance between the positive and negative connections of channel 1. It is important that the x and y axes shown in figure 5.8 align with the x and y axes of the hexapod stage.

The differential capacitance across the opposing guards was measured using a commercial two-channel capacitance to digital convertor (CDC) shown in figure 5.9. The CDC has an internal temperature sensor to correct for the atmospheric changes over time. Due to the electronics of the CDC, differential capacitance can only be measured for a single channel at a time. Figure 5.10 shows the circuit used to measure differential capacitance for

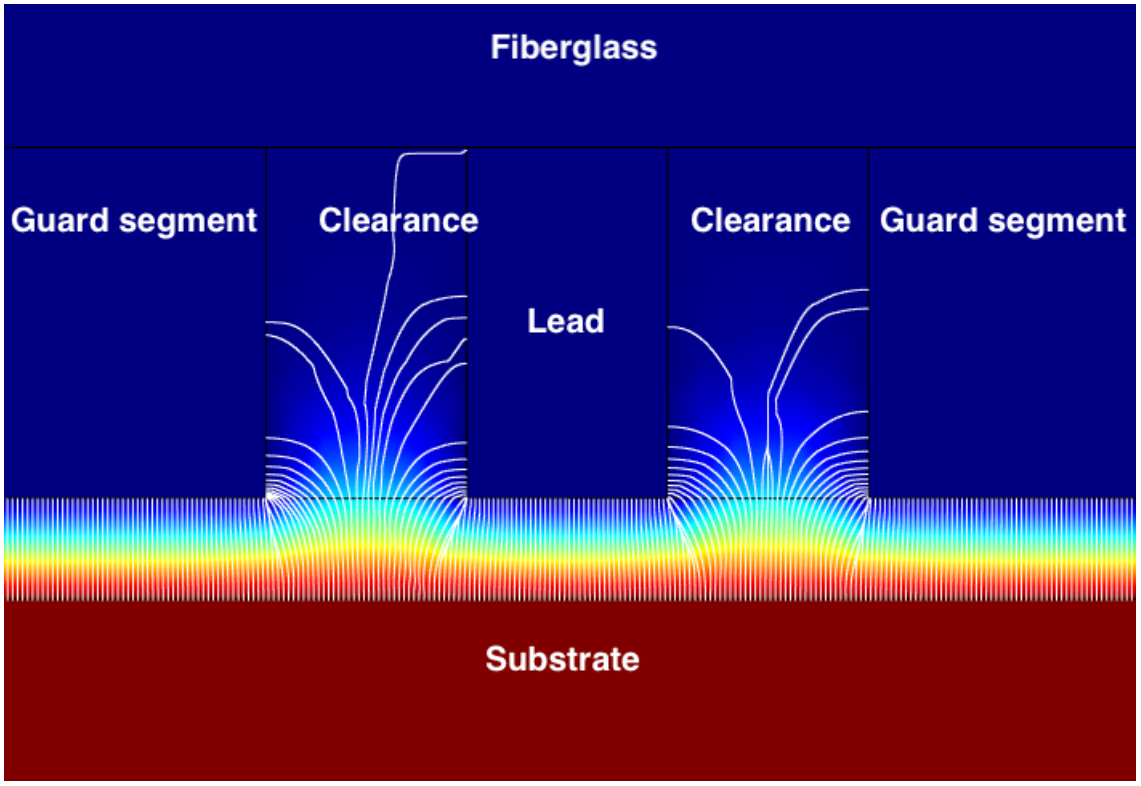

Figure 5.7: The electric field lines near the segmented guard edges for a 100 μm air gap.

each channel. An excitation voltage square-wave pulse train with a frequency of 32 kHz and height of 6.5 V was applied to the source substrate using the excitation channel. The difference in the capacitance induced by the voltage pulse between the positive and negative connection was measured by the CDC. For these measurements, a continuous pulse train was used and the differential capacitance was sampled with a rate of 90 Hz.

The CDC was placed inside a customized aluminum case with coaxial connections for each channel, as shown in figure 5.11. The excitation channel was connected to the source substrate and the guard connections are shown in figure 5.8. Therefore, differential capacitances for channel 1 and channel 2 were minimized by rotation along the x and y axes, respectively. After aligning the center of the PCB with the center of the source substrate using the centering part, the PCB was operated in segmented mode. The CDC software was turned on and the excitation pulses were allowed to be transmitted to the

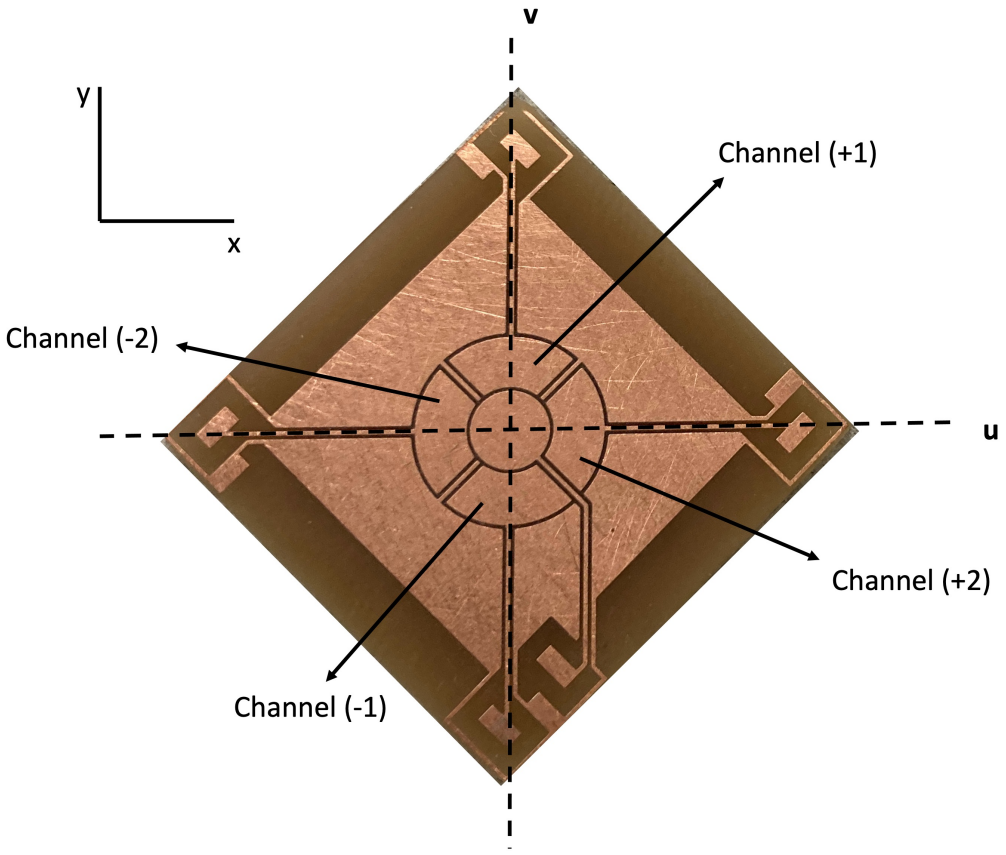

Figure 5.8: A schematic of the PCB segmented mode readout procedure is shown.

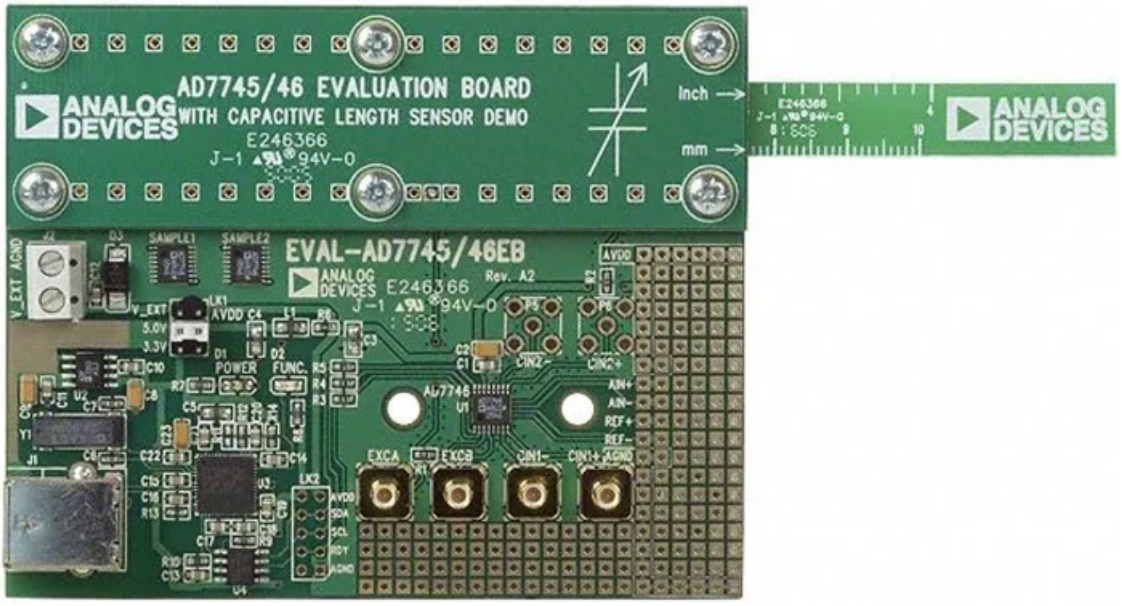

Figure 5.9: A picture of the capacitor to digital convertor (AD7746 Analog Devices) employed in this work.

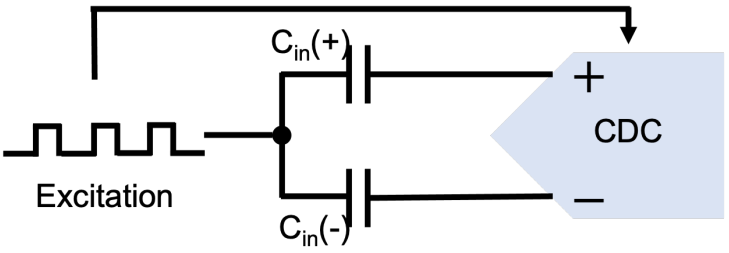

Figure 5.10: The circuit used to measure differential capacitance across the opposing guards.

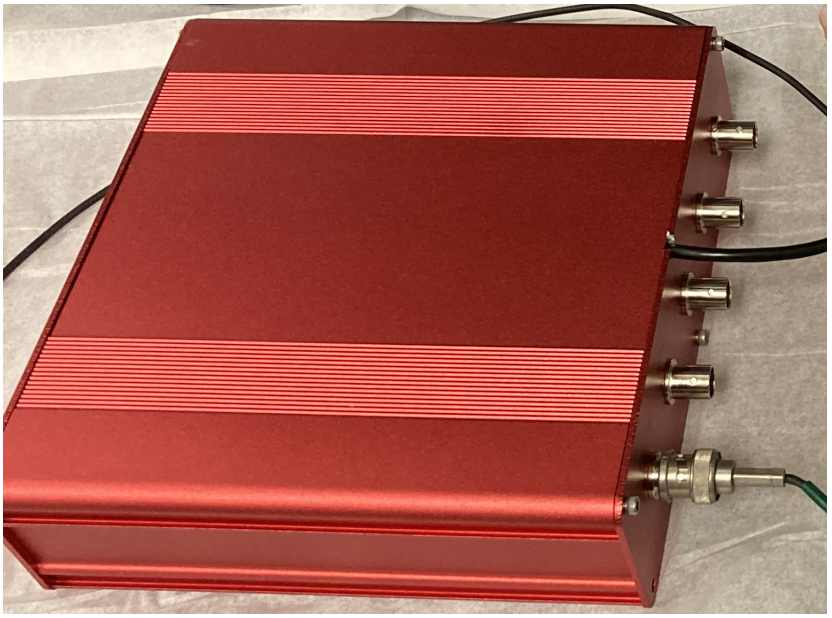

Figure 5.11: The aluminum case for the CDC board with the individual channels.

source substrate. Channel 1 was monitored first. The differential capacitance signal was allowed to stabilize over several minutes. Using the hexapod motion stage, a rotation about the x-axis was applied in both positive and negative direction and the capacitance readout signal was observed. The direction that led to a drop in differential capacitance was selected to be the rotational direction of interest. The source substrate was rotated in 0.1 deg increments until the differential capacitance was noted to rise again. When an increase in signal was noted, a 0.1 deg rotational step was applied in the opposite direction and the substrate was rotated in increments of 0.01 deg. By switching from 0.1 deg increments to smaller rotations, the differential capacitance was minimized with a larger

rotational accuracy. Once the minima was discovered, the input signal was switched from channel 1 to channel 2 and the procedure described above was repeated. This method was iterated at least twice to ensure that the differential capacitance was minimized along both directions. Figure 5.12 shows a screenshot of the differential capacitance decreasing with the rotational increments. Following the parallel alignment, the PCB guard channels were disconnected from the CDC and combined together to operate in the combined mode.

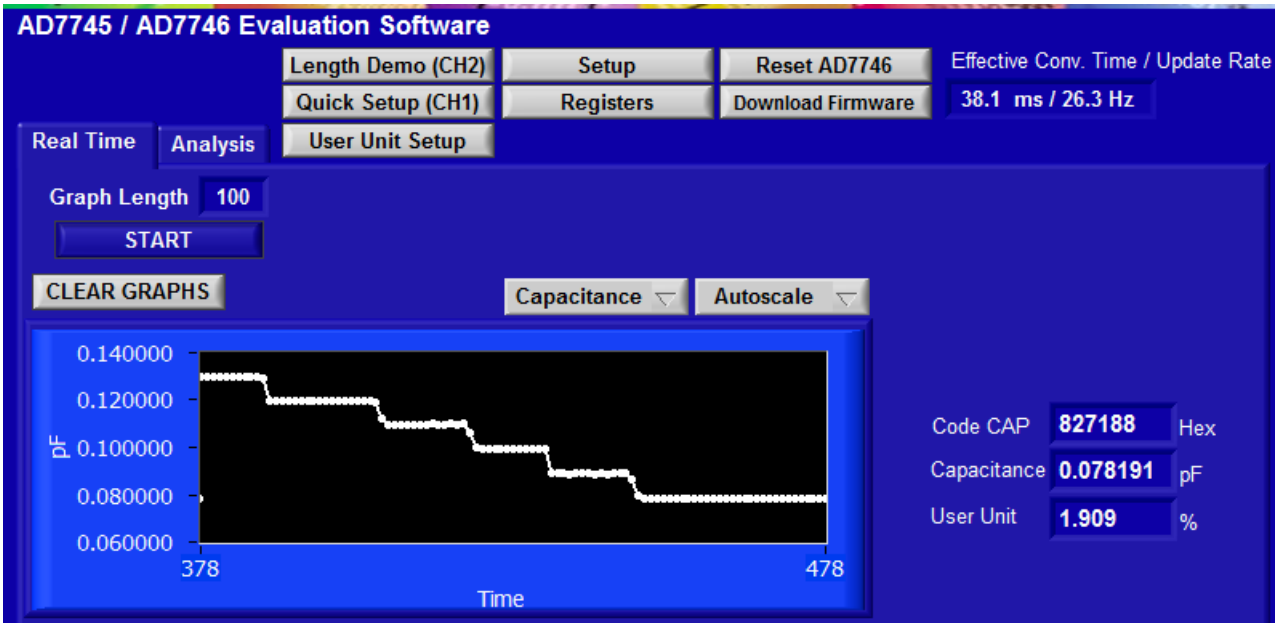

Figure 5.12: A screenshot of the CDC software displaying the minimization of the differential capacitance by rotating the source substrate.

5.1.3.2 Capacitance measurements

The diameter of the air cavity subtended by the PCB collector and the absolute air gap between the source substrate and the PCB EC was measured using the capacitance measurement methods outlined in section 4.1.3.2. The PCB was operated in the combined mode. A dummy source was utilized to measure the diameter of the cavity and the offset between the assumed air gap and the actual air gap using equation 4.6. A ΔV of 90 V bias was applied for each air gap. The induced charge was collected using a MAX 4000

electrometer in the threshold mode. The air gap was increased five times with 50 μm increments and charge was collected at each interval. Following this experiment, the offset in the air gap was applied as a translational shift using the hexapod stage and the measurements were repeated with the known air gaps ranging from 200 μm to 400 μm in 50 μm increments. Figure 5.13 shows the results from a single trial plotting $1/C$ against $l_{assumed}$. The initial air gap was assumed to be zero, therefore, l_{offset} was calculated to be the y-intercept of the curve. Figure 5.14 shows the capacitance measurements following the determination and application of the l_{offset} shift.

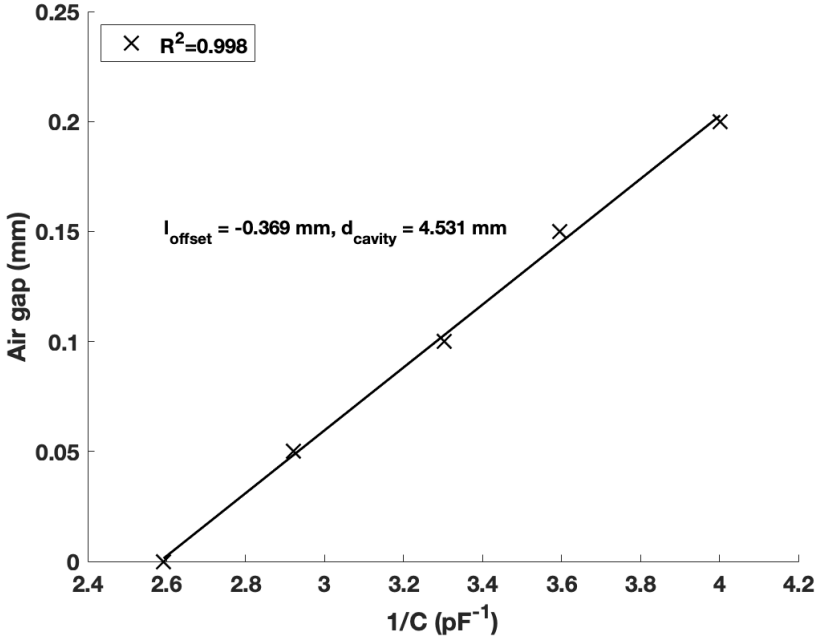

Figure 5.13: Determination of the absolute air gap and the cavity diameter using the capacitance method. Measurements with an arbitrary unknown initial air gap are shown.

Four trials were conducted to measure the diameter of the air cavity and to assess the variation in the measurements. During each trial, the source and detector assemblies were centered and aligned parallel to each other using the hexapod motion stage before acquiring capacitance measurements. Since capacitance measurements were acquired both before and after the determination of the l_{offset} shift, each trial yielded two measurements

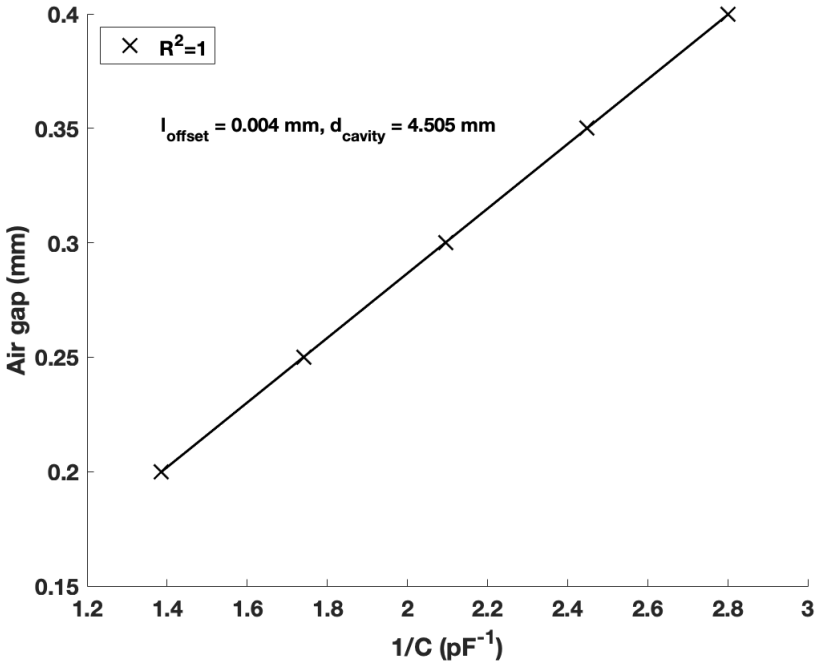

Figure 5.14: Confirmation of the absolute air gap and the cavity diameter using the capacitance method. Measurements with a l_{offset} shift applied are shown.

of the A_{eff}. Table 5.1 shows the results from the capacitance measurements using the dummy source. A variation of 0.40% was determined in the cavity diameter based on the multiple trial results. This variation was observed to be much smaller than the variation in the A_{eff} measurements of the D400 EC shown in table 4.3. A smaller variation in the PCB diameter measurements can be partially attributed to the higher accuracy of the parallel alignment method utilized by the PCB detector system. The nominal diameter of the cavity was calculated to be 4.20 mm, as previously determined in section 5.1.2. Therefore, the measurements shown in table 5.1 conclude that the actual diameter of the PCB cavity was 330 μm greater than the nominal diameter. The variation seen in the measured A_{eff} arise from any tilts in the detector or the source leading to a reduction of the cavity diameter.

The offset in the air gap was re-measured using the voltage increase method introduced in section 4.1.3.2 when a radioactive source was employed. For each measurement trial,

Table 5.1: Effective diameter of the air cavity determined from the capacitance measurements using a dummy source.

Trial	Cavity diameter (mm)
1	4.55/4.51
2	4.54/4.52
3	4.53/4.51
4	4.55/4.53
Avg.	4.53±0.40%

this contactless method was utilized to determine the initial air gap using a ΔV of 90 V using the ^{210}Po source described in 4.1.4.

5.2 Monte Carlo correction factors for ^{210}Po

The TOPAS Monte Carlo (MC) code was employed to calculate correction factors for the ^{210}Po source when using the PCB EC instead of the D400 EC. A modular physics list was used consisting of *G4RadioactiveDecay*, *G4Decay*, *G4HadronElasticPhysicsHP*, *G4HadronPhysicsQGSP_BIC_HP*, *G4IonElasticPhysics*, *G4IonQMDPhysics*, and *G4StoppingPhysics*. A modified *G4EMStandardOpt4* physics list was used for electromagnetic physics. The electromagnetic parameters for electrons were unchanged since the *G4EMStandardOpt4* physics list is considered to be highly accurate for light charged particle transport [93][100]. For alpha particles, the optimal electromagnetic physics parameters determined in section 3.1.2 were utilized.

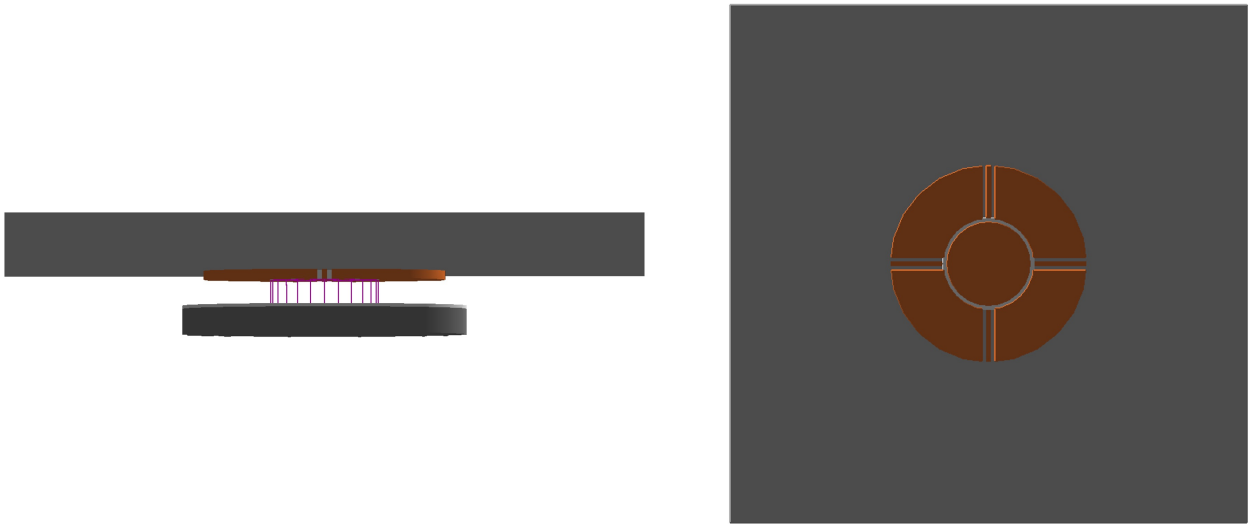

Figure 5.15: The graphics rendering of the PCB EC in TOPAS MC code. The left figure shows the XZ view of the PCB and the source substrate. The right figure shows the XY view of the PCB without the presence of the substrate.

Figure 5.15 shows an illustration of the simulated PCB EC in TOPAS MC code. Since the absorbed dose to air cavity was of interest, only the collector and the segmented guard were explicitly simulated. The diameter of the air cavity was selected as 4.53 mm based on the capacitance results discussed in section 5.1.3.2. It is important to note that the air

cavity diameter subtended by the PCB EC is larger than the D400 cavity by 491 μm. The segmented guard was simulated by creating a guard ring and subtracting the clearance regions using boolean solid geometry in GEANT4. The PCB was simulated to be copper with a thin gold layer. The GEANT4 internal materials $G4\_AIR$ and $G4\_WATER$ were selected to represent air and water. The mean excitation energies of air and water were 85.7 eV and 78 eV, respectively.

5.2.1 $\mathbf{k}_{point}$

The k_{point} correction factor was calculated for the PCB EC using equation 2.21. The ^{210}Po source was modeled as a circular planar source with uniform emission distribution and 3.2 mm diameter. The k_{point} correction was calculated independently for air gap ranging from 300-525 μm. The atomic de-excitation was turned on and the production thresholds were set to 1 μm for these simulations.

Figure 5.21 shows the point correction for the PCB EC. The mean correction was calculated to be 6.02% with a percent standard deviation of 0.62%. Similar to the k_{point} correction calculated for the D400 EC, the correction factor was found to increase with the air gap. However, the point correction was observed to be smaller for the PCB EC than the D400 EC by a mean value of 1.7%. The larger diameter of the PCB air cavity is less sensitive to the change in source diameter leading to a smaller correction factor.

5.2.2 Correction factors for the cylindrical shell method

The MC-calculated correction factors for the dosimetric formalism described in section 2.3.3 are calculated and reported in this section.

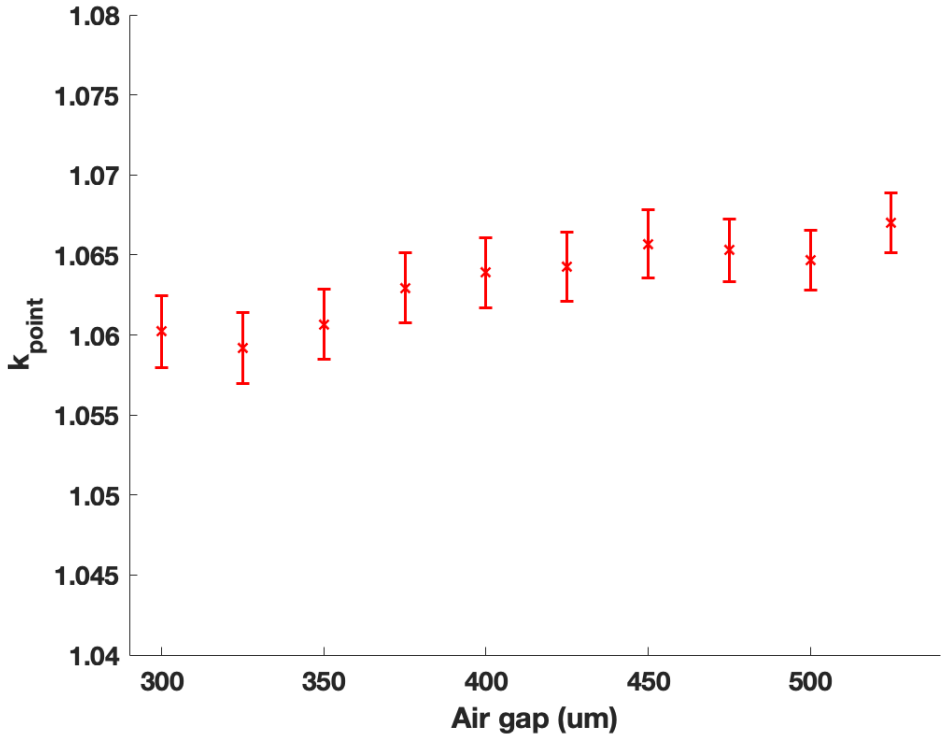

Figure 5.16: The k_{point} correction factor as a function of air gap for a ^{210}Po point source.

5.2.2.1 $\mathbf{k}_{backscatter}$

The backscatter correction factor was previously introduced in section 4.2.2.1 and was calculated using equation 4.11. Air gaps of 300-525 μm with increments of 25 μm were simulated independently. The production thresholds were set to 1 μm and the atomic de-excitation parameter was turned on. Figure 5.17 shows the results for the ^{210}Po source. The correction was observed to be greater for smaller air gaps than for larger air gaps. A mean correction of 8.10% was calculated with a maximum correction of 9.45%. The $k_{backscatter}$ correction magnitude for the PCB EC was observed to be slightly larger than the D400 backscatter correction. The D400 and PCB $k_{backscatter}$ values were within 1.5% of each other. Therefore, it can be concluded that the majority of the backscatter originates due to the source substrate.

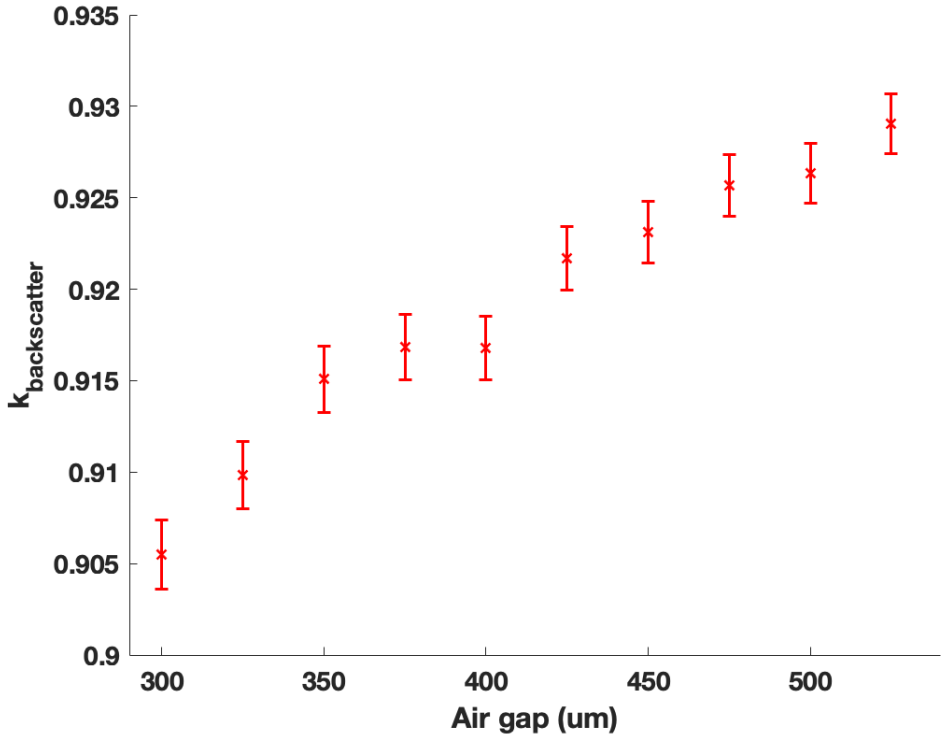

Figure 5.17: The backscatter correction factor for the PCB EC with a point ^{210}Po source.

As demonstrated by figures 5.4 and 5.17, the magnitude of the backscatter correction is largely dependent on the angular distribution of the alpha particles striking a given material rather than the material composition itself. Since the alpha particle source was simulated as an isotropically-emitting point source on the surface of the source substrate, the trajectory angle of the alpha particle inside the substrate has a wide distribution. For alpha particles traveling orthogonal to the substrate's surface, a large number of multiple Coulomb scattering events are required to deflect the trajectory of the particle back towards the air cavity. However, for the particles with oblique trajectories closer to the air cavity can be easily deflected by a small number of scattering events. Thus, the backscatter correction is dominated by alpha particles traversing close to the surface of the substrate.

5.2.2.2 $\mathbf{k}_{inv}\mathbf{k}_{cav}$

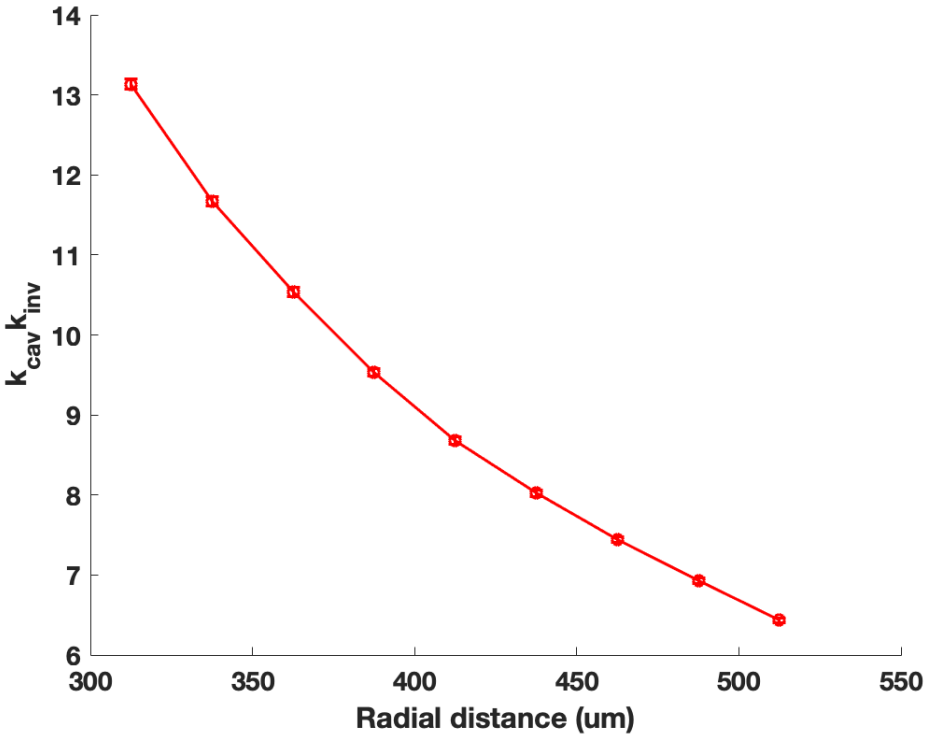

Figure 5.18: The $k_{inv}k_{cav}$ correction factor for the PCB EC with a point ^{210}Po source.

The $k_{inv}k_{cav}$ correction factor was previously introduced in section 4.2.2.2 and was calculated using equation 4.12. This correction factor was calculated using the parameters and geometry described in section 4.2.2.2 except with the radius of the cylindrical shells reflecting the radius of the PCB air cavity instead of the D400 air cavity. Figure 5.18 shows the $k_{inv}k_{cav}$ correction factor for a point ^{210}Po source. Due to the larger diameter of the PCB air cavity, relative to the D400 air cavity, the $k_{inv}k_{cav}$ correction factor was roughly 17% greater for the PCB EC. A sharp decline in the correction factor was observed with the increasing radial distance from the source. Using the analytical expression given in equation 2.23, the k_{inv} and k_{cav} correction factors were deconvolved and plotted in figure 5.19. It is worth noting that the calculation of the k_{inv} correction assumes a straight trajectory of the alpha particles with no significant deflection due to scattering events.

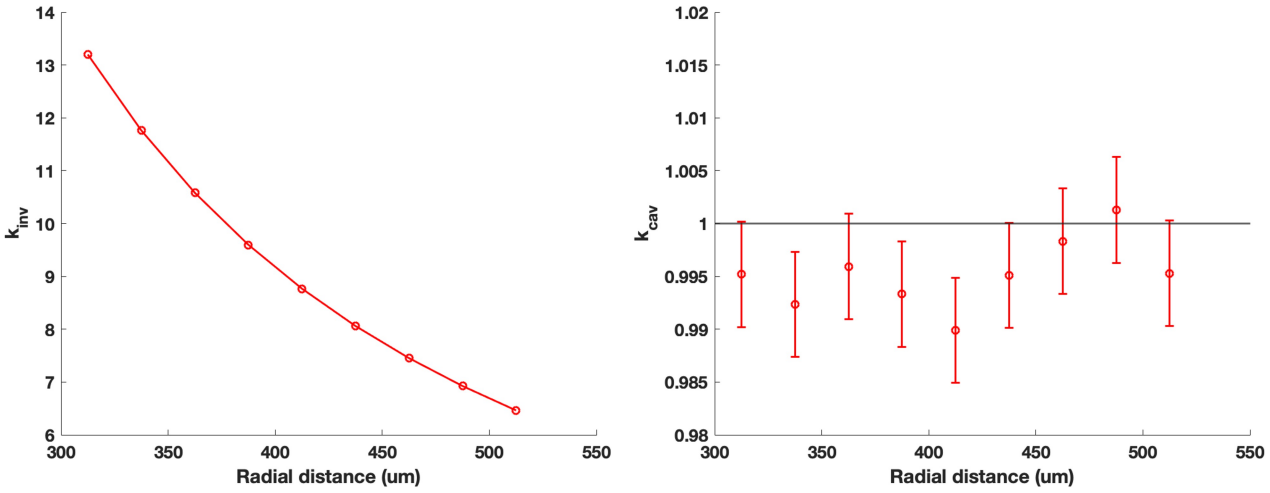

Figure 5.19: The k_{inv} correction (left), calculated using an analytical expression, and the k_{cav} correction factor (right) for the PCB EC with a point ^{210}Po source.

Similar to the D400 EC, the k_{cav} correction factor was found to be $< 1\%$ for the PCB EC.

The conversion from absorbed dose to air at an arbitrary radial distance to surface absorbed dose to water is independent of the employed detector and has been previously discussed in detail in section 4.2.2.3.

5.2.3 Correction factors for the extrapolation method

The MC-calculated correction factors for the extrapolation method dosimetric formalism described in section 2.3.4 were calculated and reported in this section. Both dosimetric formalism introduced in this work share a common k_{point} correction factor.

5.2.3.1 $k_{backscatter}$

The backscatter correction factor was calculated using MC simulations and equation 2.27. Air gaps of 300-525 μm were simulated with production thresholds set to 1 μm

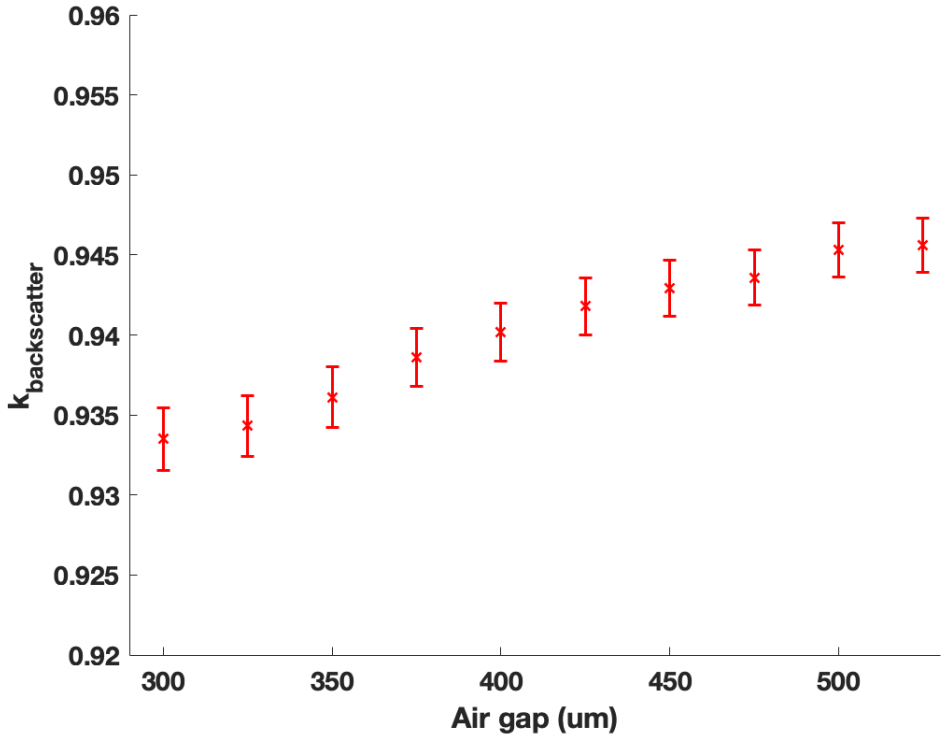

Figure 5.20: The backscatter correction factor for the PCB EC with a point ^{210}Po source.

and atomic de-excitation turned on. Figure 5.20 shows the $k_{backscatter}$ correction for the PCB EC. The mean correction was calculated to be 6.62% with a maximum correction of 9.97%. This correction was found to decrease with increasing air gap. Compared to the backscatter correction for the D400 EC, the PCB correction was found to be larger by 1% due to its metal-based electrode. Therefore, although the D400 EC was composed of water-equivalent materials, the $k_{backscatter}$ for the PCB and D400 ECs was similar to each other. This result corroborates our hypothesis that the dominant contributor to the overall backscatter is the source substrate rather than the detector.

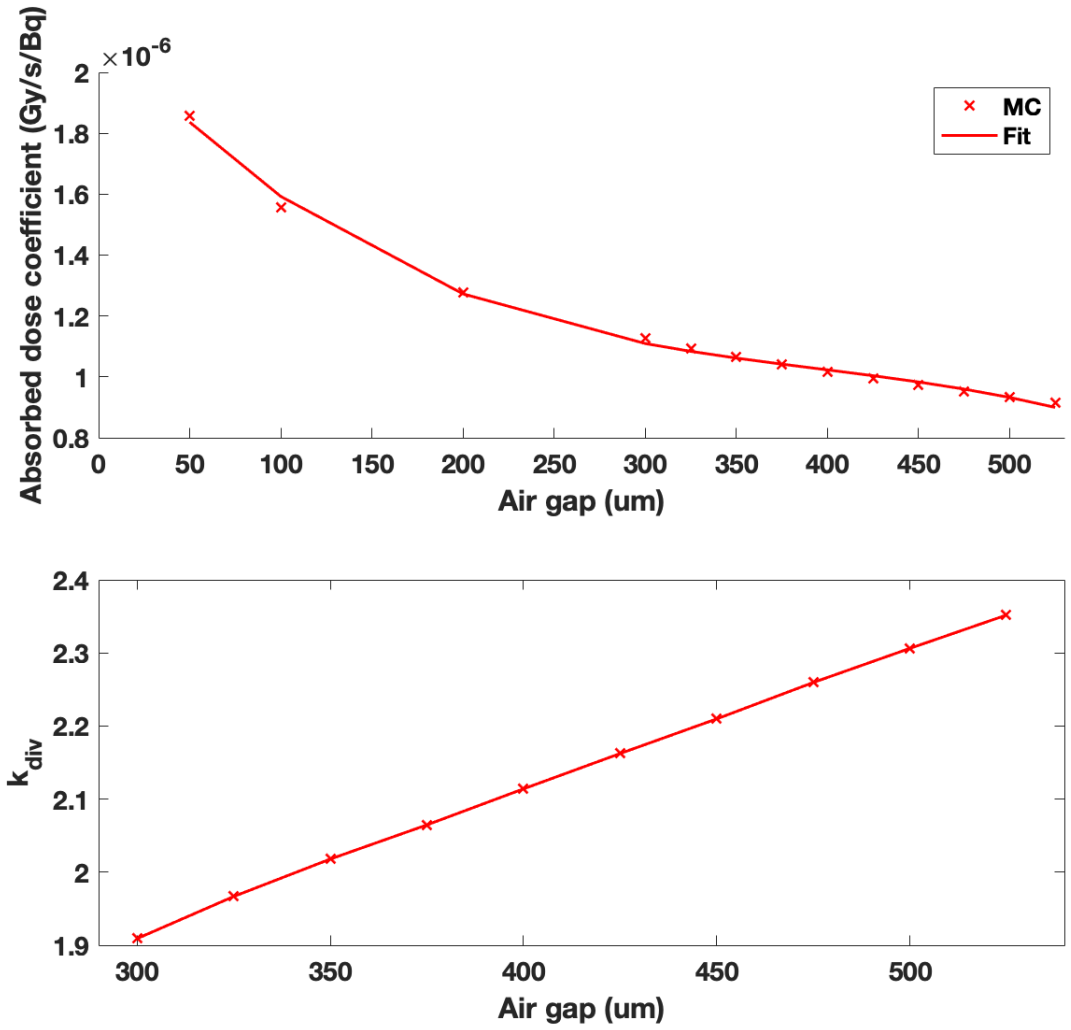

Figure 5.21: Top: absorbed dose to cavity plotted as a function of air gap with a 3rd order polynomial fit. Bottom: the divergence correction factor for 300-525 μm air gaps.

5.2.3.2 $\mathbf{k}_{div}$

The divergence correction was calculated using equation 2.28. Absorbed dose to cavity was scored for air gaps ranging from 50-525 μm with production thresholds set to 1 μm and atomic de-excitation turned on. Absorbed dose at air gaps $< 300\mu m$ were also simulated to accurately extrapolate the curve to a zero air gap. A 3rd order polynomial function was used to fit the dose versus air gap curve and the intercept was taken as the

$D_{cavity,point,water}(l \rightarrow 0)$ value. The divergence correction was then computed for air gaps in the 300-525 μm range.

The absorbed dose as a function of air gap with a polynomial fit is shown in figure 5.21. The k_{div} correction ranged from 91% to 235%. A linear relationship was found, with an R^2 of 0.98, between the divergence correction and the air gap. Similar to the D400 EC, the divergence correction for the PCB was the largest correction factor due to their construction similarities. The largest difference between the D400 EC k_{div} and PCB EC k_{div} was calculated to be 1.74%, which is due to the difference in the collector diameter of the two ECs.

5.3 Measurement of absorbed dose from a ^{210}Po source

The constructed primary standard was evaluated using a ^{210}Po source described in section 4.1.4. The measurements consisted of ionization current readings at various air gaps with an electrical bias applied to the source substrate. The measured absorbed dose to air cavity was directly compared with MC-calculated dose. Using the formalism provided in equation 2.20 and the Monte Carlo (MC)-based correction factors calculated in section 5.2, the absorbed dose to air was measured and then converted to absorbed dose to water at 1 μm radial distance from a point source. The surface absorbed dose to water was also determined using the formalism provided in equation 2.26 and correction factors calculated in section 5.2.

The ionization chamber (IC)-specific correction factors were calculated individually and applied to the measured ionization current. A more detailed discussion of these correction factors and their measurement can be found in section 4.3.

5.3.1 Ionization current measurements

The stability of the signal was investigated by acquiring ionization current measurements at an arbitrary air gap for a long period of time. The current was measured using a MAX4000 electrometer (Standard Imaging, Middleton, WI) at a rate of 1 Hz for 10 minutes. The current was observed to be fluctuating within 0.22% of the mean value, as shown in figure 5.22. The mean period of the oscillation was found to be 20 seconds. The signal stability for both the PCB and the D400 ECs was observed to be similar with slightly different oscillation periods. Acquiring multiple charge readings for 60 seconds is sufficient for good statistics.

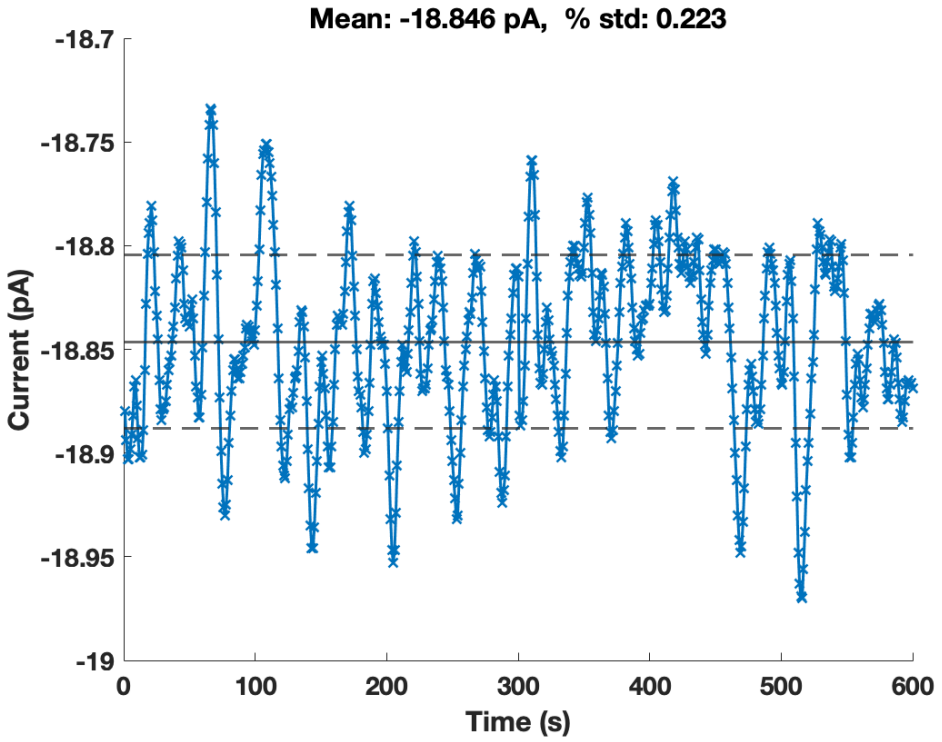

Figure 5.22: The stability of the PCB ionization current signal over time.

Various measurement trials were performed to measure the PCB ionization current from the ^{210}Po source. The measurement procedure for the PCB EC was identical to the procedure described in section 4.3.2 for the D400 EC except for the rotational alignment step. Independent measurements were acquired for each trial and the entire process was repeated each time. Following the lateral alignment of the source and the detector, the PCB was operated in segmented guard mode and the rotational alignment was performed by minimizing the differential capacitance across both guard channels. This procedure is described in great detail in section 5.1.3.1. The initial air gap between the source and the PCB EC was determined using the capacitance method described in section 4.1.3.2. A voltage change from -10 V to -100 V was applied to measure the charge induced by the capacitance. Following the initial air gap measurements, the recombination, polarity, and air density correction was calculated. For details related to the measurement procedure, the reader is referred to section 4.3.2 as the procedure was kept the same between the

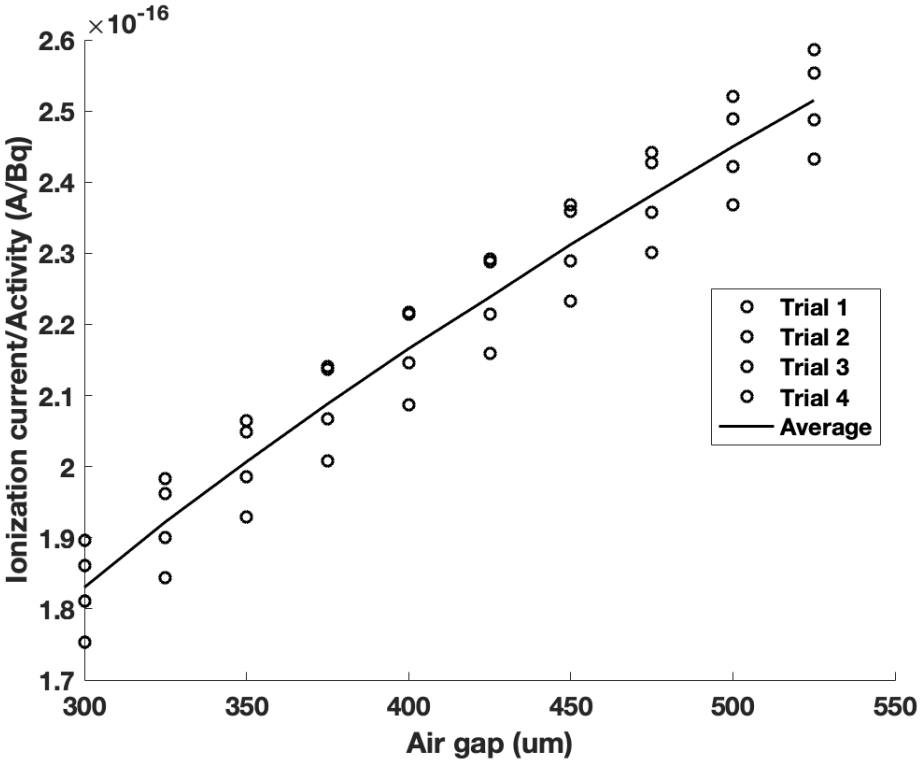

Figure 5.23: The ionization current, normalized by radioactivity, collected by the PCB EC at each air gap. The radioactivity values were decay corrected.

two detectors. Figure 5.23 displays the current readings for the four trials conducted in this study. Percent standard error in the range of 1.35-1.70% was found in the ionization current readings when results from all trials were considered. The current readings for the PCB EC were observed to be closer to each other than the current readings for the D400 EC when considering all measurement trials. The low standard error in the PCB current readings can be partially due to the more robust rotational alignment procedure employed for this detector than for the D400 EC.

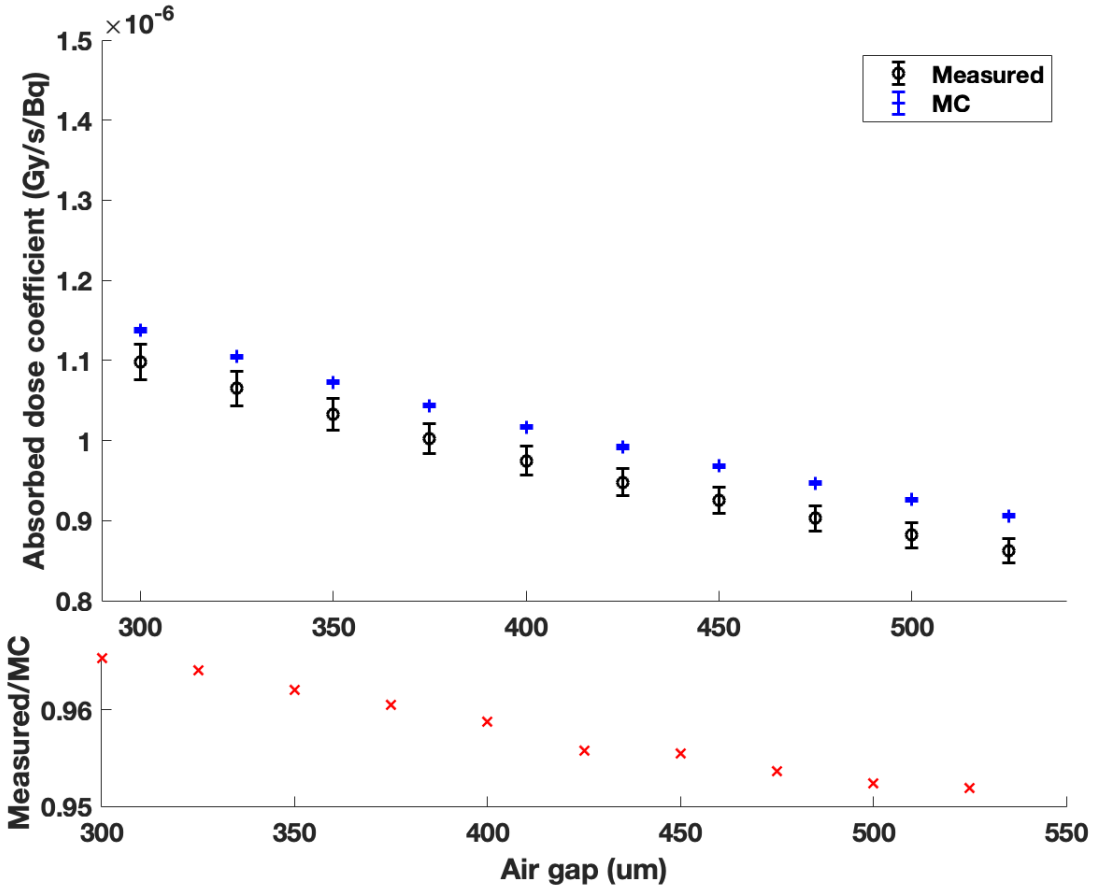

Figure 5.24: The measured and MC simulated absorbed dose to cavity as a function of air gaps in the 300-525 μm range.

5.3.2 Comparison of measured and MC absorbed dose to cavity

The accuracy of the MC-predicted absorbed dose to cavity, normalized by radioactivity, was assessed by comparing it with the measured absorbed dose. The measurement apparatus was simulated using parameters discussed in section 5.2 and the ^{210}Po source was modeled to match the measured source specifications. The measured absorbed dose to cavity was calculated using equation 4.20. Figure 5.24 displays the comparison between the MC-calculated and measured absorbed dose for the PCB EC. Mean and maximum deviations of 4.2% and 4.81% were calculated between the measured and MC data. This agreement was found to be worse than the agreement found between the measured and

MC data for the D400 absorbed dose to cavity. Nevertheless, the deviations between any datasets must be evaluated considering the uncertainty in the data.

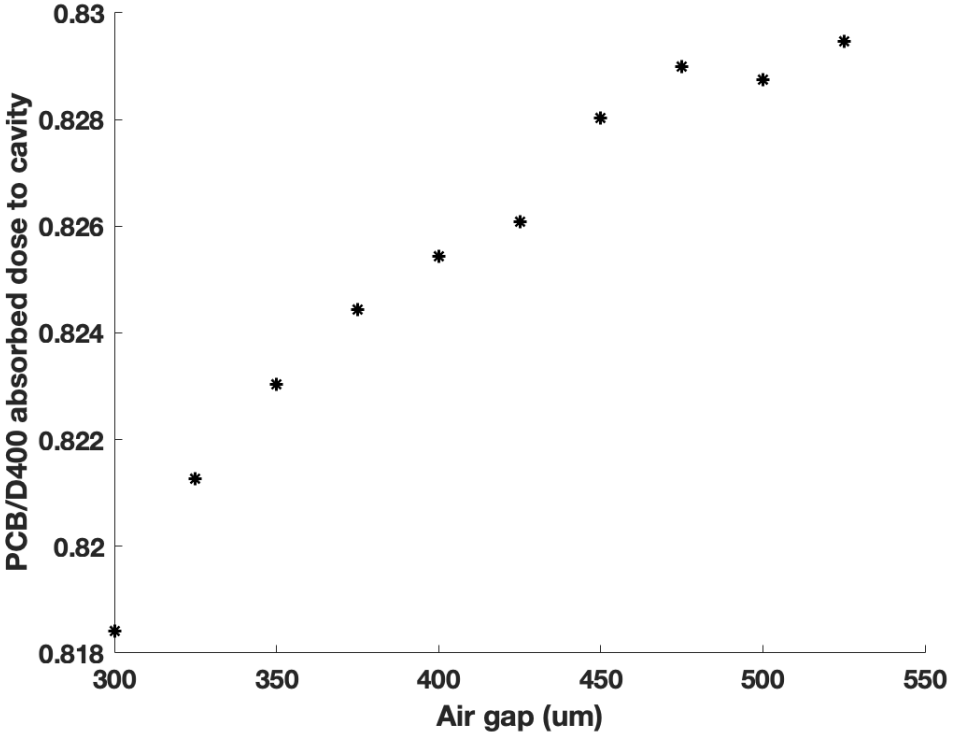

Figure 5.25: The measured PCB absorbed dose to cavity normalized by the measured D400 absorbed dose to cavity.

Figure 5.25 shows a comparison between the measured D400 and PCB absorbed dose to cavity. On average, the PCB absorbed dose was found to be 17.46 % lower than the D400 absorbed dose. Such a large difference in absorbed dose between the two detectors can be explained by the differences in their collector diameters. As the collector diameter increases, the mean track-length of the alpha particles traversing the air cavity also increases leading to a greater inverse-square fall off along the lateral directions. Consider the reduction in absorbed dose as a function of off-axis distance. This effect can be quantified by equation 2.23. At 300 μm and 525 μm air gaps, the PCB k_{inv} is 20% and 17.7%, respectively, greater than the D400 k_{inv}. Therefore, this difference manifests in the absorbed dose to cavity and leads to differences shown in figure 5.25.

5.3.2.1 Uncertainty budget

Table 5.2: Uncertainty budget for the absorbed dose measurement, acquired with the PCB EC, at a 300 μm air gap.

Component of uncertainty	Type A (%)	Type B (%))
Net current	0.13	
Current repeatability	1.70	
Air density correction		0.10
Recombination correction		0.10
Average energy per ion pair		0.20
Air collection volume		0.40
Radioactivity		1.00
Combined uncertainty (k=1)	2.04	
Combined uncertainty (k=2)	4.08	

Table 5.3: Uncertainty budget for the absorbed dose measurement, acquired with the PCB EC, at a 500 μm air gap.

Component of uncertainty	Type A (%)	Type B (%))
Net current	0.13	
Current repeatability	1.35	
Air density correction		0.10
Recombination correction		0.10
Average energy per ion pair		0.20
Air collection volume		0.40
Radioactivity		1.00
Combined uncertainty (k=1)	1.76	
Combined uncertainty (k=2)	3.52	

Tables 5.2 and 5.3 show the combined uncertainty in the measured absorbed dose to air cavity for the 300 μm and 500 μm air gaps. The Type A uncertainty in the PCB current reading was similar to the uncertainty found for the D400 EC. The standard error in the PCB current reading across all four measurement trials was found to be $< 2\%$, which is smaller than the error found for the D400 measurements. Since this uncertainty originates partially due to the positional and rotational errors, it can be concluded that the differential capacitance method to align the source and detector in a

parallel configuration was more repeatable and precise than the D400 rotational alignment method. Any offsets in the initial air gap possibly led to the current deviations between the measurement trials. Similar to the D400 uncertainty, the PCB combined uncertainty was found to be decreasing with increasing air gap. The combined uncertainty at k=1 ranged between 1.75-2.04%.

5.3.3 Absorbed dose measurements using the cylindrical shell method

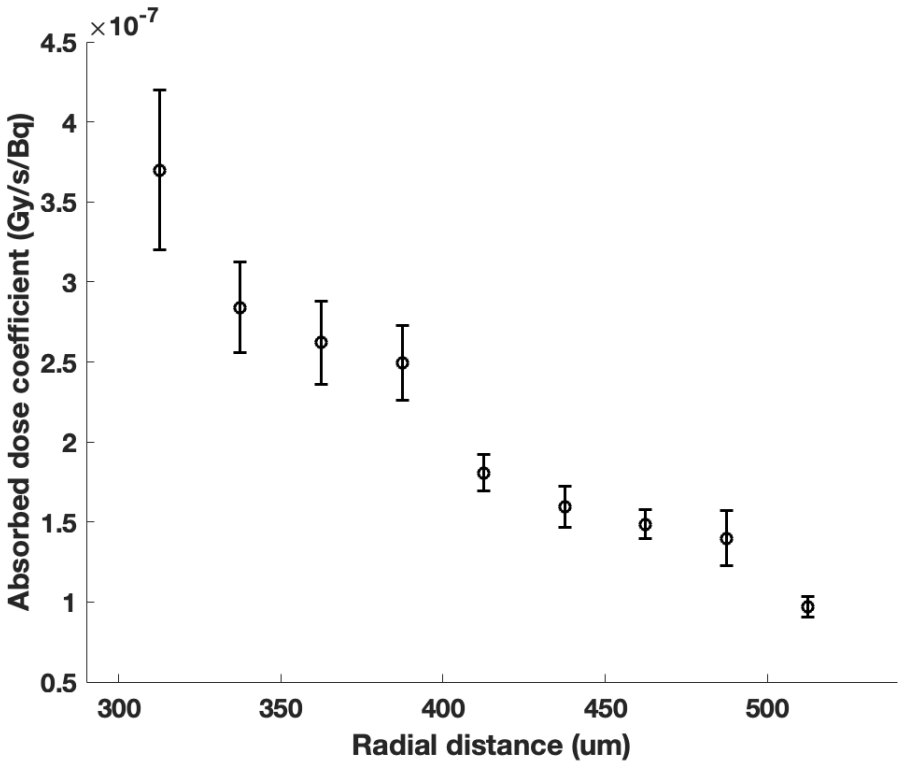

Figure 5.26: Measured absorbed dose to air as a function of radial distance from a point ^{210}Po source using the cylindrical shell method.

Using equation 2.20 reported in section 2.3.3, the absorbed dose to air at various radial distances from a point ^{210}Po was measured using the PCB EC and shown in figure 5.26. Similar to the absorbed dose to air measured using the D400 EC, the PCB absorbed

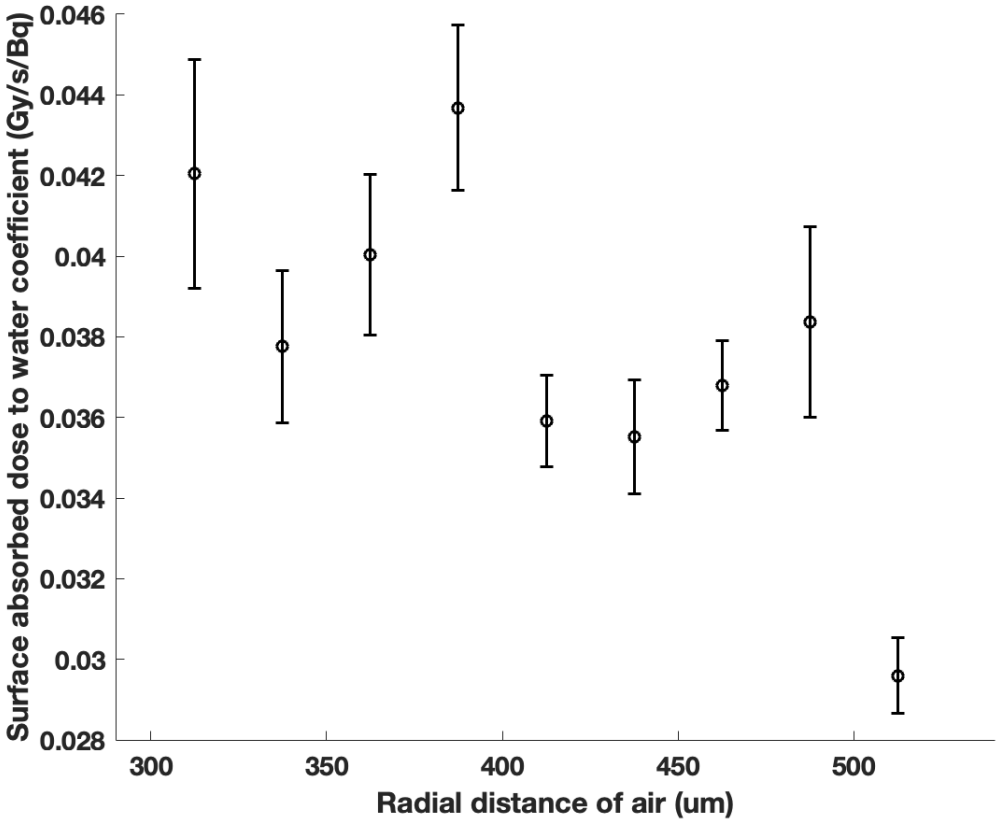

Figure 5.27: Surface absorbed dose to water measured at each radial distance from a point ^{210}Po source using the cylindrical shell method.

dose to air was found to decrease as a function of radial distance due to the inverse-square effect. Equation 4.13 was employed to convert this absorbed dose to air to surface absorbed dose to water. Figure 5.27 shows the calculated surface absorbed dose to water by converting absorbed dose to air at each radial distance. The mean surface dose to water was calculated to be 0.0377 Gy/s/Bq with a percent standard deviation of 10.88%. Figure 5.28 compares the D400 surface absorbed dose to water with PCB surface absorbed dose to water. Large differences were noted for absorbed dose measured using the two detectors. The high uncertainties associated with these measurements lead to large differences in absorbed dose to water between the detectors as well as between the individual air gaps.

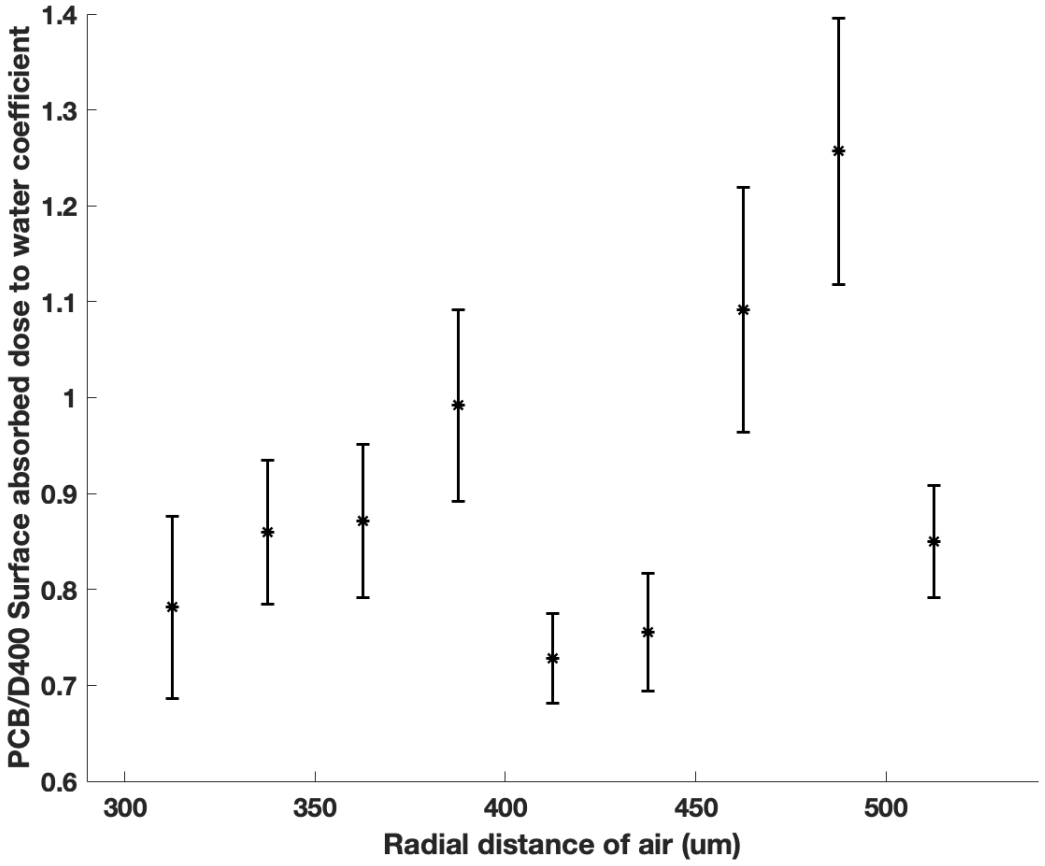

Figure 5.28: The PCB surface absorbed dose to water normalized by the D400 surface absorbed dose to water measured using the cylindrical shell method for a ^{210}Po source.

5.3.3.1 Uncertainty budget

The combined uncertainty for absorbed dose to air at a 312.5 μm radial distance from a point ^{210}Po source is shown in table 5.4. The largest component of uncertainty was the current repeatability uncertainty in the net ionization current readings calculated by the difference in the current readings at 300 μm and 325 μm air gaps. As discussed in section 4.3.4.1, the current difference method combines the uncertainty in current readings at each air gap leading to a much larger uncertainty in the ionization current across multiple trials. However, the standard error in the current repeatability for the PCB EC was observed to be much smaller than the repeatability for the D400 EC. This is due to the high

Table 5.4: Uncertainty budget for the absorbed dose to air measurement, using the PCB EC, at a 312.5 μm radial distance from a point source.

Component of uncertainty	Type A (%)	Type B (%))
Net current	0.20	
Current repeatability	6.65	
Air density correction		0.10
Recombination correction		0.10
Average energy per ion pair		0.20
Air collection volume		0.40
Radioactivity		1.00
k_{point} correction		0.20
$k_{backscatter}$ correction		0.20
k_{cav} correction		0.20
Combined uncertainty (k=1)	6.75	
Combined uncertainty (k=2)	13.50	

repeatability of the differential capacitance method to align the apparatus that was used for the PCB EC. Although the overall uncertainty at k=1 in the PCB absorbed dose to air was $< 7\%$, large differences in the mean surface absorbed dose to water were found leading to a prohibitively high uncertainty in the dose to water measurements.

5.3.4 Absorbed dose measurements using the extrapolation method

The dosimetric formalism for the extrapolation method of measuring surface absorbed dose to water was previously introduced in section 2.3.4 and can be calculated using equation 2.26. The ionization current at each air gap, corrected by the ion chamber-specific correction factors and MC-calculated correction factors, is shown in figure 5.29. A linear relationship was found between the corrected ionization curve and air gap with an R^2 of 1.00. The mean slope of the curve was calculated to be 1.11×10^{-18} A/Bq/μm. The surface absorbed dose to water was measured to be 2.3035×10^{-06} Gy/s/Bq. This value was noted to differ by 20.33 % when compared to the surface absorbed dose to water measured using the D400 chamber. This difference is due to the difference in the

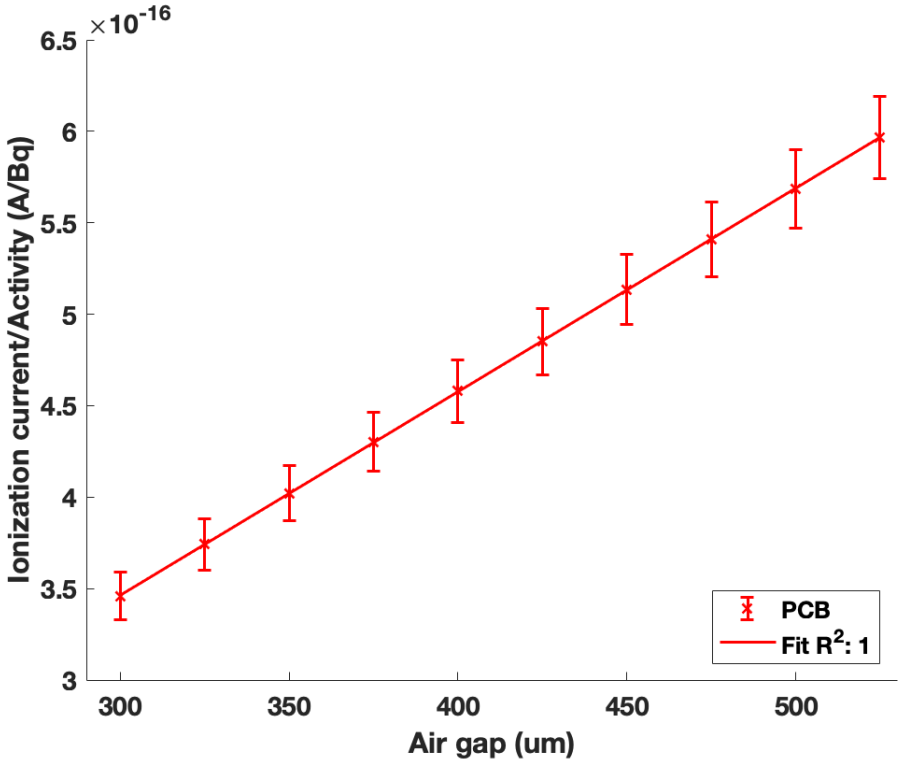

Figure 5.29: Corrected ionization current at each air gap for the ^{210}Po source.

collector diameter of the two detectors, which leads to different absorbed dose to air cavity between the two detectors. This effect was previously discussed in section 5.3.2 in more detail. The differences in the inverse-square fall off along the lateral direction between the two detectors can be removed by applying the ratio of k_{inv} calculated for the D400 EC to k_{inv} calculated for the D400 EC to the D400 surface absorbed dose to water. By doing so, the PCB and D400 surface absorbed dose to water agree within 5% of each other.

5.3.4.1 Uncertainty budget

The combined uncertainty in the surface absorbed dose to water using the extrapolation method is shown in table 5.5. The repeatability in the slope of the ionization current versus air gap curve was calculated to be 1.42% by considering the standard error in

Table 5.5: Uncertainty budget for the surface absorbed dose to water measured using the PCB EC.

Component of uncertainty	Type A (%)	Type B (%))
Net current	0.20	
Current slope repeatability	1.42	
Air density correction		0.10
Recombination correction		0.10
Average energy per ion pair		0.20
Air collection volume		0.40
Radioactivity		1.00
$(\frac{S_{col}}{\rho})$		2.45
k_{point} correction		0.20
$k_{backscatter}$ correction		0.20
k_{div} correction		1.79
Combined uncertainty (k=1)	3.55	
Combined uncertainty (k=2)	7.10	

the slope. The slope uncertainty for both detectors was found to be similar despite having large differences in uncertainty in the current measurements. Since the deviations in the ionization current were consistent for all air gaps between different measurement trials, the slope magnitude was found to be more repeatable. The surface absorbed dose to water uncertainty using the extrapolation method was found to be 3.55% at k=1. Therefore, when the detector dependence from the surface absorbed dose to water values was removed, the surface absorbed dose to water measured using the D400 and the PCB ECs agreed within 5%, which is within the k=2 uncertainty of the measured absorbed dose.

Chapter 6

Conclusions and future work

6.1 Main conclusions

6.1.1 Monte Carlo investigation of alpha particle transport

The GEANT4 alpha particle transport algorithm and the internal radioactive decay database were evaluated in the first part of this work. A Fano cavity test was utilized and various electromagnetic transport parameters such as $dRover$, final range, and $stepMax$ were varied until an agreement between the theoretical and calculated result was found for the Urban and the Wentzel-VI multiple Coulomb scattering (MCS) models. The internal GEANT4 radioactive decay data for various alpha-emitting radionuclides were compared to the decay data extracted from the MIRD and RADAR databases.

The default electromagnetic parameters were found to be unsuitable for both investigated MCS models if an agreement of $<1\%$ is desired between the theoretical and calculated results. Reducing the strength of the mass density gradient between the walls and the cavity resulted in a better agreement with the theory. Limiting the maximum step value to

$\leq 1\ \mu m$ resulted in an agreement of <0.3%, however, the simulation time with this change increased by 4400 % and 2595 % for the Urban and the Wentzel-VI models, respectively. Considering the computational efficiency and the accuracy results shown in this study, a *dRover* value of 0.1 and a final range of 1 μm were observed to be optimal and yielded an agreement of <0.3% between the theory and the calculation for both MCS models. With the optimal parameters, the computational time was calculated to be 550% and 319% longer, on average, than the default parameters for the Urban and the Wentzel-VI models, respectively.

Overall, good agreement was found between the GEANT4 internal radioactive decay data and the MIRD and RADAR databases for the investigated alpha-emitting radionuclides. The alpha peak energies were found to be within 0.6 keV of each other and the peak intensities were found to be within 1.5 % of each other. Any discrepancies observed in the intensity and total alpha energy released were found to be within 2 % of each other. Thus, the GEANT4 *G4RadioActiveDecay* class was found suitable for alpha particle dosimetry.

6.1.2 Construction and evaluation of a D400 planar windowless extrapolation chamber

A D400 extrapolation chamber (EC)-based standard for surface absorbed dose to water was constructed and evaluated using a pure alpha emitter. The surface flatness of the D400 EC was measured to be $< 20\mu m$ using interferometry. The radius of the air cavity was predicted using COMSOL simulations and confirmed using capacitance measurements. A method to rotationally align the EC with the source plate was devised using a hexapod motion stage. By employing a windowless EC setup with a thin film source, the attenuation of alpha particles was minimized and a contactless method was

proposed to determine the absolute air gap between the EC and the source substrate. The EC-specific correction factors, except k_{TP}, were found to be $< 0.5\%$ for all measurement trials while the MC-calculated correction factors were calculated to be much larger. The divergence correction was noted to be the highest correction factor due to the sharp fall-off of the absorbed dose as a function of air gap. Variations of up to 18.40 % in the surface absorbed dose to water were found when using the cylindrical shell dosimetric formalism. The dominant contributor to the overall uncertainty was the repeatability of the ionization current readings between different measurement trials. Using the extrapolation dosimetric formalism, the surface absorbed dose to water per radioactivity was measured to be 2.8913×10^{-6} Gy/s/Bq for a ^{210}Po source with a combined uncertainty of 3.59 % at k=1.

6.1.3 Construction and evaluation of a printed circuit board (PCB) extrapolation chamber

A PCB-based EC was constructed and employed for absorbed dose measurements leading to a more repeatable rotational alignment between the EC and the source substrate. The higher rotational alignment repeatability for the PCB EC, relative to the D400 EC, was reflected in the current repeatability uncertainty component. The current repeatability dropped from 3.29-2.19 % to 1.70-1.35 % for the same air gaps when switching from the D400 EC to the PCB EC. The rotational alignment for the PCB EC was performed using a differential capacitance method, which has previously been shown to be highly accurate and precise. However, lateral positional errors and errors in the determination of the initial air gap still manifest in both absorbed dose standards. The diameter of the PCB air cavity was measured to be 0.54 mm greater than the diameter of the D400 air cavity. The correction factors calculated for the PCB EC resembled closely to the

magnitudes calculated for the D400 EC. Despite the metal electrodes used for the PCB EC, the backscatter correction was found to be similar to the D400 EC. When employing the cylindrical shell dosimetric formalism, the variations in the surface absorbed dose were reported to be 10.88%. The surface absorbed dose to water from a ^{210}Po source was measured to be 2.3035×10^{-6} Gy/s/Bq with a combined uncertainty of 3.75% at k=1 using the extrapolation method. The uncertainty in the surface absorbed dose to water remained similar between the PCB EC and the D400 EC used in our previous study.

6.2 Future work

In the future, techniques to reduce the uncertainty in the initial air gap measurements must be explored. This can be potentially achieved by increasing the capacitance of the air cavity. Capacitance induced across the air gap can be increased by either increasing the collector radius or by taking the capacitance measurements at lower air gaps. Visual monitoring of the air gap must be incorporated in the apparatus to ensure that the source material doesn't contaminate the collector for smaller air gaps.

The comparison between the Monte Carlo-calculated absorbed dose to air and experimentally-measured absorbed dose can be improved by acquiring measurements at a larger range of air gaps. The extended comparison would allow Monte Carlo validation for depth dose regions distally to the plateau region. As the air gap increases, the applied voltage increases in order to maintain the electric field strength. Absorbed dose comparisons beyond a 10 mm air gap will require voltages over 1000 V, which may limit the maximum air gap utilized in measurements.

The constructed apparatus can be utilized for other clinically-relevant radionuclides, such as $^{225}Ac/^{223}Ra/^{227}Th/^{212}Pb/^{211}At$, absorbed dose measurements in the future. A local

supplier (NorthStar) of ^{225}Ac is currently available to the author and absorbed dose measurements for this source will be performed in the future. Additionally, the mixed particle emission from these sources can further characterize the absorbed dose standard. The dosimetric formalism needs to be revised to incorporate absorbed dose from both the beta and the alpha particle components. Since 1 Bq of the aforementioned radionuclides leads to multiple alpha emissions, an increase in signal-to-noise ratio (SNR) is expected for the same plated activity. The presence of a long decay chain for these sources further complicates the measurements and allows investigation of the impact of the radioactive daughter migration on absorbed dose.

Finally, the measured absorbed dose must be compared to commonly-utilized dose calculation platforms. This thesis validated the GEANT4 Monte Carlo code by comparing the calculated absorbed dose with the measured absorbed dose. This process must be performed for other platforms as well such as MCNP and TOPAS n-Bio. Such comparisons will foster confidence in the dose calculation techniques for alpha particles.

This thesis work has set the stage for measurement of the ratio of the absorbed dose to water to activity. This quantity can be a calibration value for a dose calibrator or a well chamber and could be used in the clinic to determine the absorbed dose to water.

Bibliography

[1] Saori Obayashi. Breakthrough alpha-ray treatment of cancer without external radiation. *EurekAlert!*, 2019.

[2] Nkemakonam C. Okoye, Jakob E. Baumeister, Firouzeh Najafi Khosroshahi, Heather M. Hennkens, and Silvia S. Jurisson. Chelators and metal complex stability for radiopharmaceutical applications. *Radiochimica Acta*, 107(9-11):1087–1120, 2019. doi: https://doi.org/10.1515/ract-2018-3090. URL `https://www.degruyter.com/view/journals/ract/107/9-11/article-p1087.xml`.

[3] Neeta Pandit-Taskar. Targeted radioimmunotherapy and theranostics with alpha emitters. *J Med Imaging Radiat Sci*, Aug 2019. ISSN 1876-7982 (Electronic); 1876-7982 (Linking). doi: 10.1016/j.jmir.2019.07.006.

[4] Clemens Kratochwil, Frank Bruchertseifer, Frederik L Giesel, Mirjam Weis, Frederik A Verburg, Felix Mottaghy, Klaus Kopka, Christos Apostolidis, Uwe Haberkorn, and Alfred Morgenstern. 225ac-psma-617 for psma-targeted alpha-radiation therapy of metastatic castration-resistant prostate cancer. *J Nucl Med*, 57 (12):1941–1944, Dec 2016. ISSN 1535-5667 (Electronic); 0161-5505 (Linking). doi: 10.2967/jnumed.116.178673.

[5] Vivek Subbiah, Pete M. Anderson, Kalevi Kairemo, Kenneth Hess, Winston W. Huh, Vinod Ravi, Najat C. Daw, Neeta Somaiah, Joseph A. Ludwig, Robert S.

Benjamin, Sant Chawla, David S. Hong, Funda Meric-Bernstam, Gregory Ravizzini, Eugenie Kleinerman, Homer Macapinlac, and Eric Rohren. Alpha particle radium 223 dichloride in high-risk osteosarcoma: A phase i dose escalation trial. *Clinical Cancer Research*, 25(13):3802–3810, 2019. ISSN 1078-0432. doi: 10.1158/1078-0432.CCR-18-3964. URL `https://clincancerres.aacrjournals.org/content/25/13/3802`.

[6] Cristina Müller, Christiaan Vermeulen, Ulli Köster, Karl Johnston, Andreas Türler, Roger Schibli, and Nicholas P. van der Meulen. Alpha-pet with terbium-149: evidence and perspectives for radiotheragnostics. *EJNMMI Radiopharmacy and Chemistry*, 1(1):5, 2016. doi: 10.1186/s41181-016-0008-2. URL `https://doi.org/10.1186/s41181-016-0008-2`.

[7] E.N. Dulov, E.V. Voronina, L.R. Tagirov, and M.M. Bikchantaev. *ALPHA SPECTROSCOPY*. PhD thesis, Kazan Federal University, 2013.

[8] Martin Berger, J Coursey, and M Zucker. ESTAR, PSTAR, and ASTAR: Computer Programs for Calculating Stopping-Power and Range Tables for Electrons, Protons, and Helium Ions (version 1.21), 1999.

[9] Bruno Melo Mendes, Paula Cristina Guimarães Antunes, Isabela Soares Lopes Branco, Eduardo do Nascimento, Baljeet Seniwal, Telma Cristina Ferreira Fonseca, and Helio Yoriyaz. Calculation of dose point kernel values for monoenergetic electrons and beta emitting radionuclides: Intercomparison of monte carlo codes. *Radiation Physics and Chemistry*, 181:109327, 2021.

[10] Abigail E Besemer, You Ming Yang, Joseph J Grudzinski, Lance T Hall, and Bryan P Bednarz. Development and validation of rapid: a patient-specific monte carlo three-dimensional internal dosimetry platform. *Cancer biotherapy & radiopharmaceuticals*, 33(4):155–165, 2018.

[11] Harald H. Rossi and Marco Zaider. Elements of microdosimetry. *Medical Physics*, 18 (6):1085–1092, 1991. doi: 10.1118/1.596616. URL https://aapm.onlinelibrary.wiley.com/doi/abs/10.1118/1.596616.

[12] I Billas, D Shipley, S Galer, G Bass, T Sander, A Fenwick, and V Smyth. Development of a primary standard for absorbed dose from unsealed radionuclide solutions. *Metrologia*, 53(6):1259, 2016.

[13] Ahtesham Ullah Khan and Larry A. DeWerd. Evaluation of the GEANT4 transport algorithm and radioactive decay data for alpha particle dosimetry. *Applied Radiation and Isotopes*, 176(April):109849, 2021. ISSN 09698043. doi: 10.1016/j.apradiso.2021.109849. URL https://doi.org/10.1016/j.apradiso.2021.109849.

[14] Michael G. Stabin and Lydia C.Q.P. Da Luz. Decay data for internal and external dose assessment. *Health Physics*, 83(4):471–475, 2002. ISSN 00179078. doi: 10.1097/00004032-200210000-00004.

[15] Jon B Hansen. Development of a convex windowless extrapolation chamber to measure surface dose rate from Ru-106/Rh-106 episcleral plaques. *ProQuest Dissertations and Theses*, page 248, 2018. URL https://ezproxy.library.wisc.edu/login?url=https://www.proquest.com/dissertations-theses/development-convex-windowless-extrapolation/docview/2040945824/se-2?accountid=465https://uwi-primoalma-prod.hosted.exlibrisgroup.com/openurl/WISC/wisc_services_page?

[16] Hans-Joachim Selbach, Hans-Michael Kramer, and WS Culberson. Realization of reference air-kerma rate for low-energy photon sources. *Metrologia*, 45(4):422, 2008.

[17] Archana Kaliyaraj Selva Kumar, Yifei Zhang, Danlei Li, and Richard G. Compton. A mini-review: How reliable is the drop casting technique? *Electrochemistry Communications*, 121(September):106867, 2020. ISSN 13882481. doi: 10.1016/j.elecom.2020.106867. URL https://doi.org/10.1016/j.elecom.2020.106867.

[18] Geoff Delaney, Susannah Jacob, Carolyn Featherstone, and Michael Barton. The role of radiotherapy in cancer treatment. *Cancer*, 104(6):1129–1137, 2005. doi: 10.1002/cncr.21324. URL https://onlinelibrary.wiley.com/doi/abs/10.1002/cncr.21324.

[19] Faiz M Khan and John P Gibbons. *Khan's the physics of radiation therapy*. Lippincott Williams & Wilkins, 2014.

[20] Lawrence E. Williams, Gerald L. DeNardo, and Ruby F. Meredith. Targeted radionuclide therapy. *Medical Physics*, 35(7Part1):3062–3068, 2008. doi: 10.1118/1.2938520. URL https://aapm.onlinelibrary.wiley.com/doi/abs/10.1118/1.2938520.

[21] Jean-Francois Chatal and Cornelis A Hoefnagel. Radionuclide therapy. *The Lancet*, 354(9182):931 – 935, 1999. ISSN 0140-6736. doi: https://doi.org/10.1016/S0140-6736(99)06002-X. URL http://www.sciencedirect.com/science/article/pii/S014067369906002X.

[22] Cornelis A. Hoefnagel. Radionuclide cancer therapy. *Annals of Nuclear Medicine*, 12(2):61–70, 1998. doi: 10.1007/BF03164831. URL https://doi.org/10.1007/BF03164831.

[23] Ashutosh Dash, F. F. (Russ) Knapp, and M. R. A. Pillai. Targeted radionuclide therapy - an overview. *Current Radiopharmaceuticals*, 6(3):152–180, 2013-09-01T00:00:00. URL https://www.ingentaconnect.com/content/ben/crp/2013/00000006/00000003/art00006.

[24] Phillip M Devlin. *Brachytherapy: applications and techniques*. Springer Publishing Company, 2015.

[25] National Research Council (US) and Medicine Institute of Medicine (US) Committee on State of the Science of Nuclear. Advancing nuclear medicine through innovation. 2007.

[26] Jamal Zweit. Radionuclides and carrier molecules for therapy. *Physics in Medicine and Biology*, 41(10):1905–1914, oct 1996. doi: 10.1088/0031-9155/41/10/004. URL https://doi.org/10.1088%2F0031-9155%2F41%2F10%2F004.

[27] Mark N Gaze. The current status of targeted radiotherapy in clinical practice. *Physics in Medicine and Biology*, 41(10):1895–1903, oct 1996. doi: 10.1088/0031-9155/41/10/003. URL https://doi.org/10.1088%2F0031-9155%2F41%2F10%2F003.

[28] T. E. Wheldon. Biological targeting of radionuclides. 66(782,suppl24):89–95, 1993. URL http://inis.iaea.org/search/search.aspx?orig_q=RN:24059186.

[29] Carolyn J Anderson and Jason S Lewis. Radiopharmaceuticals for targeted radiotherapy of cancer. *Expert Opinion on Therapeutic Patents*, 10(7):1057–1069, 07 2000. doi: 10.1517/13543776.10.7.1057. URL https://doi.org/10.1517/13543776.10.7.1057.

[30] Devrim Ersahin, Indukala Doddamane, and David Cheng. Targeted radionuclide therapy. *Cancers (Basel)*, 3(4):3838–3855, Oct 2011. ISSN 2072-6694 (Print); 2072-6694 (Electronic); 2072-6694 (Linking). doi: 10.3390/cancers3043838.

[31] Joseph A O Donoghue and Kirsten I Hopkins. *Biologically targeted radionuclide therapy*, pages 246–264. The British Institute of Radiology, 2020/08/16 2007. ISBN

0-905749-60-X. doi: doi:10.1259/9780905749839.chapter14. URL https://doi.org/10.1259/9780905749839.chapter14.

[32] Mine Araz, Gülseren Aras, and Özlem N. Küçük. The role of 18f–naf pet/ct in metastatic bone disease. *Journal of Bone Oncology*, 4(3):92 – 97, 2015. ISSN 2212-1374. doi: https://doi.org/10.1016/j.jbo.2015.08.002. URL http://www.sciencedirect.com/science/article/pii/S2212137415300099.

[33] David M Goldenberg. Targeted therapy of cancer with radiolabeled antibodies. *J Nucl Med*, 43(5):693–713, May 2002. ISSN 0161-5505 (Print); 0161-5505 (Linking).

[34] Misara Hamoudeh, Muhammad Anas Kamleh, Roudayna Diab, and Hatem Fessi. Radionuclides delivery systems for nuclear imaging and radiotherapy of cancer. *Advanced Drug Delivery Reviews*, 60(12):1329 – 1346, 2008. ISSN 0169-409X. doi: https://doi.org/10.1016/j.addr.2008.04.013. URL http://www.sciencedirect.com/science/article/pii/S0169409X08001166. Delivery Systems for the Targeted Radiotherapy of Cancer.

[35] Ashutosh Dash, Sudipta Chakraborty, Maroor Raghavan Ambikalmajan Pillai, and Furn F. (Russ) Knapp. Peptide receptor radionuclide therapy: An overview. *Cancer Biotherapy and Radiopharmaceuticals*, 30(2):47–71, 2020/08/16 2015. doi: 10.1089/cbr.2014.1741. URL https://doi.org/10.1089/cbr.2014.1741.

[36] Stavroula Sofou. Radionuclide carriers for targeting of cancer. *International journal of nanomedicine*, 3(2):181–199, 2008. doi: 10.2147/ijn.s2736. URL https://pubmed.ncbi.nlm.nih.gov/18686778.

[37] A. Aerts, N. R. E. N. Impens, M. Gijs, M. D'Huyvetter, H. Vanmarcke, B. Ponsard, T. Lahoutte, A. Luxen, and S. Baatout. Biological carrier molecules of radiopharmaceuticals for molecular cancer imaging and targeted cancer therapy. *Current Pharmaceutical Design*, 20(32):5218–5244, 2014-10-01T00:00:00. URL https://www.ingentaconnect.com/content/ben/cpd/2014/00000020/00000032/art00013.

[38] George Sgouros. Alpha-particles for targeted therapy. *Adv Drug Deliv Rev*, 60 (12):1402–1406, Sep 2008. ISSN 0169-409X (Print); 0169-409X (Linking). doi: 10.1016/j.addr.2008.04.007.

[39] Alejandro Bertolet, José Ramos-Méndez, Harald Paganetti, and Jan Schuemann. The relation between microdosimetry and induction of direct damage to dna by alpha particles. *Physics in Medicine & Biology*, 66(15):155016, 2021.

[40] George Sgouros, John C Roeske, Michael R McDevitt, Stig Palm, Barry J Allen, Darrell R Fisher, A Bertrand Brill, Hong Song, Roger W Howell, Gamal Akabani, SNM MIRD Committee, Wesley E Bolch, Ruby F Meredith, Barry W Wessels, and Pat B Zanzonico. Mird pamphlet no. 22 (abridged): radiobiology and dosimetry of alpha-particle emitters for targeted radionuclide therapy. *Journal of nuclear medicine : official publication, Society of Nuclear Medicine*, 51(2):311–328, 02 2010. doi: 10.2967/jnumed.108.058651. URL https://www.ncbi.nlm.nih.gov/pubmed/20080889.

[41] 4th Skelton, William P, Samantha W Dibenedetto, Shiyi S Pang, Kelsey Pan, Jacob L Barish, Adaeze Nwosu-Iheme, and Long Dang. A single-center retrospective analysis of the effect of radium-223 (xofigo) on pancytopenia in patients with metastatic castration-resistant prostate cancer. *Cureus*, 12(1):e6806–e6806, 01 2020. doi: 10.7759/cureus.6806. URL https://pubmed.ncbi.nlm.nih.gov/32140364.

[42] Håkan Andersson, Jörgen Elgqvist, György Horvath, Ragnar Hultborn, Lars Jacobsson, Holger Jensen, Börje Karlsson, Sture Lindegren, and Stig Palm. Astatine-211-labeled antibodies for treatment of disseminated ovarian cancer. *Clinical Cancer Research*, 9(10):3914s–3921s, 2003. ISSN 1078-0432. URL `https://clincancerres.aacrjournals.org/content/9/10/3914s`.

[43] Bryce JB Nelson, Jan D Andersson, and Frank Wuest. Targeted alpha therapy: progress in radionuclide production, radiochemistry, and applications. *Pharmaceutics*, 13(1):49, 2021.

[44] Urs B. Hagemann, Christine Ellingsen, Joachim Schuhmacher, Alexander Kristian, Anne Mobergslien, Véronique Cruciani, Katrine Wickstroem, Christoph A. Schatz, Christoph Kneip, Sven Golfier, Roger Smeets, Steinar Uran, Hartwig Hennekes, Jenny Karlsson, Roger M. Bjerke, Olav B. Ryan, Dominik Mumberg, Karl Ziegelbauer, and Alan S. Cuthbertson. Mesothelin-targeted thorium-227 conjugate (msln-ttc): Preclinical evaluation of a new targeted alpha therapy for mesothelin-positive cancers. *Clinical Cancer Research*, 25(15):4723–4734, 2019. ISSN 1078-0432. doi: 10.1158/1078-0432.CCR-18-3476. URL `https://clincancerres.aacrjournals.org/content/25/15/4723`.

[45] Stephen Tronchin, Jake C Forster, Kevin Hickson, and Eva Bezak. Dosimetry in targeted alpha therapy. A systematic review: current findings and what is needed. *Physics in Medicine & Biology*, 67(9):09TR01, may 2022. ISSN 0031-9155. doi: 10.1088/1361-6560/ac5fe0. URL `https://iopscience.iop.org/article/10.1088/1361-6560/ac5fe0`.

[46] J C Roeske and T G Stinchcomb. Dosimetric framework for therapeutic alpha-particle emitters. *J Nucl Med*, 38(12):1923–1929, Dec 1997. ISSN 0161-5505 (Print); 0161-5505 (Linking).

[47] Wesley E Bolch, Keith F Eckerman, George Sgouros, and Stephen R Thomas. Mird pamphlet no. 21: a generalized schema for radiopharmaceutical dosimetry–standardization of nomenclature. *J Nucl Med*, 50(3):477–484, Mar 2009. ISSN 0161-5505 (Print); 0161-5505 (Linking). doi: 10.2967/jnumed.108.056036.

[48] Gustavo A. Santa Cruz. Microdosimetry: Principles and applications. *Reports of Practical Oncology & Radiotherapy*, 21(2):135 – 139, 2016. ISSN 1507-1367. doi: https://doi.org/10.1016/j.rpor.2014.10.006. URL `http://www.sciencedirect.com/science/article/pii/S1507136714001710`. 7th Young BNCT meeting.

[49] J. Booz, L. Braby, J. Coyne, P. Kliauga, L. Lindborg, H-G. Menzel, and N. Parmentier. Report 36. *Journal of the International Commission on Radiation Units and Measurements*, os19(1):NP–NP, 04 2016. ISSN 1473-6691. doi: 10.1093/jicru/os19.1.Report36. URL `https://doi.org/10.1093/jicru/os19.1.Report36`.

[50] Yuni K Dewaraja, Eric C Frey, George Sgouros, A Bertrand Brill, Peter Roberson, Pat B Zanzonico, and Michael Ljungberg. Mird pamphlet no. 23: quantitative spect for patient-specific 3-dimensional dosimetry in internal radionuclide therapy. *J Nucl Med*, 53(8):1310–1325, Aug 2012. ISSN 1535-5667 (Electronic); 0161-5505 (Print); 0161-5505 (Linking). doi: 10.2967/jnumed.111.100123.

[51] Susan D. Kost, Yuni K. Dewaraja, Richard G. Abramson, and Michael G. Stabin. VIDA: A voxel-based dosimetry method for targeted radionuclide therapy using Geant4. *Cancer Biotherapy and Radiopharmaceuticals*, 30(1):16–26, 2015. ISSN 15578852. doi: 10.1089/cbr.2014.1713.

[52] I R Marsh, A E Besemer, and B Bednarz. Patient-Specific Alpha Particle Dosimetry Using Radiopharmaceutical Assessment Platform for Internal Dosimetry (RAPID). *International Journal of Radiation Oncology, Biology, Physics*, 105(1):E699, 9 2019.

ISSN 0360-3016. doi: 10.1016/j.ijrobp.2019.06.948. URL https://doi.org/10.1016/j.ijrobp.2019.06.948.

[53] Greta SP Mok and Yuni K Dewaraja. Recent advances in voxel-based targeted radionuclide therapy dosimetry. *Quantitative Imaging in Medicine and Surgery*, 11 (2):483, 2021.

[54] Wesley E Bolch, Lionel G Bouchet, James S Robertson, Barry W Wessels, Jeffry A Siegel, Roger W Howell, Alev K Erdi, Bulent Aydogan, Sylvain Costes, Evelyn E Watson, et al. Mird pamphlet no. 17: the dosimetry of nonuniform activity distributions—radionuclide s values at the voxel level. *Journal of Nuclear Medicine*, 40 (1):11S–36S, 1999.

[55] Stephen A Graves, Ryan T Flynn, and Daniel E Hyer. Dose point kernels for 2,174 radionuclides. *Medical physics*, 46(11):5284–5293, 2019.

[56] Ashok Tiwari, Stephen A Gravesa, and John Sunderland. The impact of tissue type and density on dose point kernels for patient-specific voxel-wise dosimetry: A monte carlo investigation. *Radiation research*, 193(6):531–542, 2020.

[57] Ahtesham Ullah Khan and Larry A DeWerd. A monte carlo investigation of dose point kernel scaling for α-emitting radionuclides. *Cancer Biotherapy & Radiopharmaceuticals*, 36(3):252–259, 2021.

[58] Wilfried Schneider, Thomas Bortfeld, and Wolfgang Schlegel. Correlation between ct numbers and tissue parameters needed for monte carlo simulations of clinical dose distributions. *Physics in Medicine & Biology*, 45(2):459, 2000.

[59] RR Kinsey, CL Dunford, JK Tuli, and TW Burrows. The nudat/pcnudat program for nuclear data. Technical report, Brookhaven National Lab., Upton, NY (United States), 1996.

[60] Franklin C Wong. Mird: radionuclide data and decay schemes. *Journal of Nuclear Medicine*, 50(12):2091–2091, 2009.

[61] Michael G Stabin and Lydia CQP da Luz. Decay data for internal and external dose assessment. *Health physics*, 83(4):471–475, 2002.

[62] Ernesto Amato, Lucrezia Auditore, Antonio Italiano, Daniele Pistone, Pedro Arce, Alfredo Campennì, and Sergio Baldari. Full monte carlo internal dosimetry in nuclear medicine by means of gamos. In *Journal of Physics: Conference Series*, volume 1561, page 012002. IOP Publishing, 2020.

[63] Panagiotis Papadimitroulas, William D Erwin, Vasiliki Iliadou, Theodora Kostou, George Loudos, and George C Kagadis. A personalized, monte carlo-based method for internal dosimetric evaluation of radiopharmaceuticals in children. *Medical physics*, 45(8):3939–3949, 2018.

[64] Pedro Pérez and Mauro Valente. Dosis: An integrated computational tool for patient-specific dosimetry in nuclear medicine by monte carlo and dose point kernel approaches. *Applied Radiation and Isotopes*, 150:135–140, 2019.

[65] F Botta, A Mairani, RF Hobbs, A Vergara Gil, M Pacilio, K Parodi, M Cremonesi, MA Coca Pérez, A Di Dia, M Ferrari, et al. Use of the fluka monte carlo code for 3d patient-specific dosimetry on pet-ct and spect-ct images. *Physics in Medicine & Biology*, 58(22):8099, 2013.

[66] S Chiavassa, Isabelle Aubineau-Lanièce, A Bitar, A Lisbona, J Barbet, D Franck, JR Jourdain, and M Bardiès. Validation of a personalized dosimetric evaluation tool (oedipe) for targeted radiotherapy based on the monte carlo mcnpx code. *Physics in Medicine & Biology*, 51(3):601, 2006.

[67] Domenico Finocchiaro, Jonathan I Gear, Federica Fioroni, Glenn D Flux, Iain Murray, Gastone Castellani, Annibale Versari, Mauro Iori, and Elisa Grassi. Uncertainty analysis of tumour absorbed dose calculations in molecular radiotherapy. *EJNMMI physics*, 7(1):1–16, 2020.

[68] A Bertolet, MA Cortés-Giraldo, and A Carabe-Fernandeza. An analytical microdosimetric model for radioimmunotherapeutic alpha emitters. *Radiation Research*, 194(4):403–410, 2020.

[69] Chen-Yu Huang, Susanna Guatelli, Bradley M Oborn, and Barry J Allen. Microdosimetry for targeted alpha therapy of cancer. *Computational and mathematical methods in medicine*, 2012, 2012.

[70] J Schuemann, AL McNamara, J Ramos-Méndez, J Perl, KD Held, H Paganetti, S Incerti, and B Faddegon. Topas-nbio: an extension to the topas simulation toolkit for cellular and sub-cellular radiobiology. *Radiation research*, 191(2):125–138, 2019.

[71] Joseph M DeCunha, Fernanda Villegas, Martin Vallières, Jose Torres, Sophie Camilleri-Broët, and Shirin A Enger. Patient-specific microdosimetry: a proof of concept. *Physics in Medicine & Biology*, 66(18):185011, 2021.

[72] PR Almond. Absorbed dose to water: Standards and traceability for radiation oncology. *Radioactivity and Radiochemistry*, 6(4):44–a, 1995.

[73] Brian E Zimmerman and Steven Judge. Traceability in nuclear medicine. *Metrologia*, 44(4):S127, 2007.

[74] Denis E. Bergeron, Karsten Kossert, Sean M. Collins, and Andrew J. Fenwick. Realization and dissemination of activity standards for medically important alpha-emitting radionuclides. *Applied Radiation and Isotopes*, 184(January):110161, 2022.

ISSN 18729800. doi: 10.1016/j.apradiso.2022.110161. URL https://doi.org/10.1016/j.apradiso.2022.110161.

[75] Norman V Klassen and Carl K Ross. Water calorimetry: the heat defect. *Journal of research of the National Institute of Standards and Technology*, 102(1):63, 1997.

[76] Carlos Eduardo deAlmeida, Ricardo Ochoa, Marilene Coelho de Lima, Mariano Gazineu David, Evandro Jesus Pires, José Guilherme Peixoto, Camila Salata, and Mario Antônio Bernal. A feasibility study of fricke dosimetry as an absorbed dose to water standard for 192ir hdr sources. *PLoS One*, 9(12):e115155, 2014.

[77] Jon B Hansen, Wesley S Culberson, and Larry A DeWerd. Windowless extrapolation chamber measurement of surface dose rate from a 90sr/90y ophthalmic applicator. *Radiation Measurements*, 108:34–40, 2018.

[78] JGP Peixoto and CEV de Almeida. Implementation of the brazilian primary standard for x-rays. Technical report, 2002.

[79] SM Mohammadi, H Tavakoli-Anbaran, and HZ Zeinali. Free-air ionization chamber, fac-ir-300, designed for medium energy x-ray dosimetry. *Journal of Instrumentation*, 12(01):T01008, 2017.

[80] RF Laitano and MP Toni. The primary exposure standard of enea for medium energy x-ray: characteristics and measurements procedures. Technical report, ENEA, 1983.

[81] Louis Harold Gray. An ionization method for the absolute measurement of γ-ray energy. *Proceedings of the Royal Society of London. Series A-Mathematical and Physical Sciences*, 156(889):578–596, 1936.

[82] LV Spencer and Frank H Attix. A theory of cavity ionization. *Radiation research*, 3(3):239–254, 1955.

[83] G Failla. The measurement of tissue dose in terms of the same unit for all ionizing radiations. *Radiology*, 29(2):202–215, 1937.

[84] P. Andreo, D. T. Burns, K. Hohlfeld, M. S. Huq, T. Kanai, F. Laitano, V. G. Smyth, and S. Vynckier. Absorbed Dose Determination in External Beam Radiotherapy An International Code of Practice for Dosimetry Based on Standards of Absorbed Dose to Water. *Technical Report Series No. 398*, 2006(June):229, 2001. URL http://www-pub.iaea.org/books/IAEABooks/5954/Absorbed-Dose-Determination-in-External-Beam-Radiotherapy-An-International-Code-

[85] John W Luetzelschwab, Christie Storey, Katrina Zraly, and David Dussinger. SELF ABSORPTION OF ALPHA AND BETA PARTICLES IN A FIBER-GLASS FILTER. *Health Physics*, 79(4):425–430, oct 2000. ISSN 0017-9078. doi: 10.1097/00004032-200010000-00012. URL http://journals.lww.com/00004032-200010000-00012.

[86] Kwang Ho Lee, Ji Yong Shin, and Eun Hee Kim. Measurement of activity distribution in an Am-241 disc source using peeled-off Gafchromic EBT3 films. *Applied Radiation and Isotopes*, 135(September 2017):192–200, 2018. ISSN 18729800. doi: 10.1016/j.apradiso.2018.01.037. URL https://doi.org/10.1016/j.apradiso.2018.01.037.

[87] Mark J. Rivard, Bert M. Coursey, Larry A. DeWerd, William F. Hanson, M. Saiful Huq, Geoffrey S. Ibbott, Michael G. Mitch, Ravinder Nath, and Jeffrey F. Williamson. Update of AAPM Task Group No. 43 Report: A revised AAPM protocol for brachytherapy dose calculations. *Medical Physics*, 31(3):633–674, feb 2004. ISSN 00942405. doi: 10.1118/1.1646040. URL http://doi.wiley.com/10.1118/1.1646040.

[88] R. E.P. Taylor and D. W.O. Rogers. An EGSnrc Monte Carlo-calculated database of TG-43 parameters. *Medical Physics*, 35(9):4228–4241, 2008. ISSN 00942405. doi: 10.1118/1.2965360.

[89] MJ Berger. Nist xcom: photon cross sections database. *http://www. nist. gov/pml/data/xcom/index. cfm*, 2010.

[90] Chen-Yu HUANG, Susanna GUATELLI, Bradley M. OBORN, and Barry J. ALLEN. Background Dose for Systemic Targeted Alpha Therapy. *Progress in Nuclear Science and Technology*, 2(0):187–190, 2011. ISSN 2185-4823. doi: 10.15669/pnst.2.187.

[91] S. Agostinelli, J. Allison, K. Amako, J. Apostolakis, H. Araujo, P. Arce, M. Asai, D. Axen, S. Banerjee, G. Barrand, F. Behner, L. Bellagamba, J. Boudreau, L. Broglia, A. Brunengo, H. Burkhardt, S. Chauvie, J. Chuma, R. Chytracek, G. Cooperman, G. Cosmo, P. Degtyarenko, A. Dell'Acqua, G. Depaola, D. Dietrich, R. Enami, A. Feliciello, C. Ferguson, H. Fesefeldt, G. Folger, F. Foppiano, A. Forti, S. Garelli, S. Giani, R. Giannitrapani, D. Gibin, J. J. Gomez Cadenas, I. Gonzalez, G. Gracia Abril, G. Greeniaus, W. Greiner, V. Grichine, A. Grossheim, S. Guatelli, P. Gumplinger, R. Hamatsu, K. Hashimoto, H. Hasui, A. Heikkinen, A. Howard, V. Ivanchenko, A. Johnson, F. W. Jones, J. Kallenbach, N. Kanaya, M. Kawabata, Y. Kawabata, M. Kawaguti, S. Kelner, P. Kent, A. Kimura, T. Kodama, R. Kokoulin, M. Kossov, H. Kurashige, E. Lamanna, T. Lampen, V. Lara, V. Lefebure, F. Lei, M. Liendl, W. Lockman, F. Longo, S. Magni, M. Maire, E. Medernach, K. Minamimoto, P. Mora de Freitas, Y. Morita, K. Murakami, M. Nagamatu, R. Nartallo, P. Nieminen, T. Nishimura, K. Ohtsubo, M. Okamura, S. O'Neale, Y. Oohata, K. Paech, J. Perl, A. Pfeiffer, M. G. Pia, F. Ranjard, A. Rybin, S. Sadilov, E. di Salvo, G. Santin, T. Sasaki, N. Savvas, Y. Sawada, S. Scherer, S. Sei, V. Sirotenko, D. Smith, N. Starkov, H. Stoecker, J. Sulkimo, M. Takahata,

S. Tanaka, E. Tcherniaev, E. Safai Tehrani, M. Tropeano, P. Truscott, H. Uno, L. Urban, P. Urban, M. Verderi, A. Walkden, W. Wander, H. Weber, J. P. Wellisch, T. Wenaus, D. C. Williams, D. Wright, T. Yamada, H. Yoshida, and D. Zschiesche. GEANT4 - A simulation toolkit. *Nuclear Instruments and Methods in Physics Research, Section A: Accelerators, Spectrometers, Detectors and Associated Equipment*, 506(3):250–303, 2003. ISSN 01689002. doi: 10.1016/S0168-9002(03)01368-8.

[92] M Elbast, A Saudo, D Franck, F Petitot, A Desbre, and Laboratoire De Radiotoxicologie Experimentale. Microdosimetry of alpha particles for simple and 3D voxelised geometries using MCNPX and GEANT4 Monte Carlo codes. 150(3):342–349, 2012.

[93] V. N. Ivanchenko, O. Kadri, M. Maire, and L. Urban. Geant4 models for simulation of multiple scattering. *Journal of Physics: Conference Series*, 219(1 PART 3), 2010. ISSN 17426596. doi: 10.1088/1742-6596/219/3/032045.

[94] Vladimir Ivanchenko, Alexander Bagulya, Samer Bakr, Marilena Bandieramonte, Denis Bernard, Marie-Claude Bordage, Jeremy Brown, Helmut Burkhardt, Paolo Dondero, Sabine Elles, Vladimir Grichine, Susanna Guatelli, Farah Hariri, Alexander Howard, Sebastien Incerti, Soon Yung Jun, Omrane Kadri, Ioanna Kyriakou, Michel Maire, Alfonso Mantero, Mihaly Novak, Daren Sawkey, Daren Sawkey, Igor Semeniouk, Anton Sokolov, and Laszlo Urban. Progress of Geant4 electromagnetic physics developments and applications. *EPJ Web of Conferences*, 214:02046, 2019. doi: 10.1051/epjconf/201921402046.

[95] Ugo Fano. Note on the Bragg-Gray Cavity Principle for Measuring Energy Dissipation. *Radiation Research*, 1(3):237, jun 1954. ISSN 00337587. doi: 10.2307/3570368. URL `https://www.jstor.org/stable/3570368?origin=crossref`.

[96] Ana Lourenço, Hugo Bouchard, Sebastian Galer, Gary Royle, and Hugo Palmans. The influence of nuclear interactions on ionization chamber perturbation factors in proton beams: FLUKA simulations supported by a Fano test. *Medical Physics*, 46 (2):885–891, 2019. ISSN 00942405. doi: 10.1002/mp.13281.

[97] J. Sempau and P. Andreo. Configuration of the electron transport algorithm of PENELOPE to simulate ion chambers. *Physics in Medicine and Biology*, 51(14): 3533–3548, 2006. ISSN 00319155. doi: 10.1088/0031-9155/51/14/017.

[98] Edmond Sterpin, Jefferson Sorriaux, Kevin Souris, Stefaan Vynckier, and Hugo Bouchard. A Fano cavity test for Monte Carlo proton transport algorithms. *Medical Physics*, 41(1):1–10, 2014. ISSN 00942405. doi: 10.1118/1.4835475.

[99] Anastasia Makarova, Bernard Gottschalk, and Wolfgang Sauerwein. Comparison of Geant4 multiple Coulomb scattering models with theory for radiotherapy protons. *Physics in medicine and biology*, 62(15):5959–5974, jul 2017. ISSN 1361-6560. doi: 10.1088/1361-6560/aa6ce3. URL `http://arxiv.org/abs/1204.4470http://www.ncbi.nlm.nih.gov/pubmed/28682790`.

[100] P. Arce, D. Bolst, M. C. Bordage, J. M.C. Brown, P. Cirrone, M. A. Cortés-Giraldo, D. Cutajar, G. Cuttone, L. Desorgher, P. Dondero, A. Dotti, B. Faddegon, C. Fedon, S. Guatelli, S. Incerti, V. Ivanchenko, D. Konstantinov, I. Kyriakou, G. Latyshev, A. Le, C. Mancini-Terracciano, M. Maire, A. Mantero, M. Novak, C. Omachi, L. Pandola, A. Perales, Y. Perrot, G. Petringa, J. M. Quesada, J. Ramos-Méndez, F. Romano, A. B. Rosenfeld, L. G. Sarmiento, D. Sakata, T. Sasaki, I. Sechopoulos, E. C. Simpson, T. Toshito, and D. H. Wright. Report on G4-Med, a Geant4 benchmarking system for medical physics applications developed by the Geant4 Medical Simulation Benchmarking Group. *Medical Physics*, 48(1):19–56, 2021. ISSN 00942405. doi: 10.1002/mp.14226.

[101] Jörg Wulff, Kilian-Simon Baumann, Nico Verbeek, Christian Bäumer, Beate Timmermann, and Klemens Zink. TOPAS/Geant4 configuration for ionization chamber calculations in proton beams. *Physics in Medicine & Biology*, 63(11): 115013, jun 2018. ISSN 1361-6560. doi: 10.1088/1361-6560/aac30e. URL https://iopscience.iop.org/article/10.1088/1361-6560/aac30e.

[102] S. Elles, V. N. Ivanchenko, M. Maire, and L. Urban. Geant4 and Fano cavity test: Where are we? *Journal of Physics: Conference Series*, 102(1):1–25, 2008. ISSN 17426596. doi: 10.1088/1742-6596/102/1/012009.

[103] E. Simiele and L. Dewerd. On the accuracy and efficiency of condensed history transport in magnetic fields in GEANT4. *Physics in Medicine and Biology*, 63(23):aaedc9, nov 2018. ISSN 13616560. doi: 10.1088/1361-6560/aaedc9. URL https://doi.org/10.1088/1361-6560/aaedc9https://doi.org/10.1088%2F1361-6560%2Faaedc9.

[104] Steffen Hauf, Markus Kuster, Matej Batič, Zane W. Bell, Dieter H.H. Hoffmann, Philipp M. Lang, Stephan Neff, Maria Grazia Pia, Georg Weidenspointner, and Andreas Zoglauer. Radioactive decays in Geant4. *IEEE Transactions on Nuclear Science*, 60(4):2966–2983, 2013. ISSN 00189499. doi: 10.1109/TNS.2013.2270894.

[105] F. C. Wong. MIRD: Radionuclide Data and Decay Schemes. *Journal of Nuclear Medicine*, 50(12):2091–2091, 2009. ISSN 0161-5505. doi: 10.2967/jnumed.109.069948.

[106] F. W. Spiers. The Influence of Energy Absorption and Electron Range on Dosage in Irradiated Bone. *The British Journal of Radiology*, 22(261):521–533, sep 1949. ISSN 0007-1285. doi: 10.1259/0007-1285-22-261-521. URL http://www.birpublications.org/doi/10.1259/0007-1285-22-261-521.

[107] L. V. Spencer and F. H. Attix. A Theory of Cavity Ionization. *Radiation Research*, 3(3):239–254, 1955. URL https://www.jstor.org/stable/3570326.

[108] W. M. Yao, C. Amsler, D. Asner, R. M. Bamett, J. Beringer, P. R. Burchat, Cd Carone, C. Caso, O. Dahl, G. D'ambrosio, A. Dcgouvca, M. Doscr, S. Eidelman, J. L. Feng, T. Ghcrghctta, M. Goodman, C. Grab, D. E. Groom, A. Gurtu, K. Hagiwara, K. G. Hayes, J. J. Hernandez-Rey, K. Hikasa, H. Jawahcry, C. Kolda, Y. Kwon, M. L. Mangano, A. V. Manohar, A. Masoni, R. Miqucl, K. Monig, H. Murayama, K. Nakamura, S. Navas, K. A. Olive, L. Rape, C. Patrignani, A. Picpkc, G. Punzi, G. Raffclt, J. G. Smith, M. Tanabashi, J. Tcrning, N. A. Tornqvist, T. G. Trippc, P. Vogcl, T. Watari, C. G. Wohl, R. L. Workman, M. Schmitt, and Particle Data Group. Review of particle physics. *Journal of Physics G: Nuclear and Particle Physics*, 33(1), July 2006. ISSN 0954-3899. doi: 10.1088/0954-3899/33/1/001.

[109] T. Pfuhl, F. Horst, C. Schuy, and U. Weber. Dose build-up effects induced by delta electrons and target fragments in proton Bragg curves—measurements and simulations. *Physics in Medicine & Biology*, 63(17):175002, aug 2018. ISSN 1361-6560. doi: 10.1088/1361-6560/aad8fc. URL https://iopscience.iop.org/article/10.1088/1361-6560/aad8fc.

[110] L E Porter and Hong Lin. Methods of calculating the Barkas-effect correction to Bethe–Bloch stopping power. *Journal of Applied Physics*, 67(11):6613–6620, jun 1990. ISSN 0021-8979. doi: 10.1063/1.345094. URL https://doi.org/10.1063/1.345094.

[111] Steven P. Ahlen. Theoretical and experimental aspects of the energy loss of relativistic heavily ionizing particles. *Rev. Mod. Phys.*, 52:121–173, Jan 1980. doi: 10.1103/RevModPhys.52.121. URL https://link.aps.org/doi/10.1103/RevModPhys.52.121.

[112] M. J. Berger, M. Inokuti, H. H. Andersen, H. Bichsel, D. Powers, S . M. Seltzer, D . Thwaites, and D. E. Watt. *ICRU Report 49*, volume os25. 1993. ISBN 0913394610. doi: 10.1093/jicru/os25.2.Report49. URL https://academic.oup.com/jicru/article/2923918/Report.

[113] M E Brandan, E Fantuzzi, V Gregoire, R W Howell, and H G Paretzke. *Report 90*, volume 14. 2014. ISBN 2065187892365. doi: 10.1093/jicru/ndw043.

[114] Kai Siegbahn. *Alpha-, beta-and gamma-ray spectroscopy*. Elsevier, 2012. ISBN 0444596992.

[115] Jon B. Hansen, Wesley S. Culberson, and Larry A. DeWerd. Surface dose rate from a flat 106Ru/106Rh episcleral plaque measured with a planar windowless extrapolation chamber and un-laminated EBT3 film. *Radiation Measurements*, 121 (December 2018):18–25, 2019. ISSN 13504487. doi: 10.1016/j.radmeas.2018.12.002. URL https://doi.org/10.1016/j.radmeas.2018.12.002.

[116] C. G. Soares. Calibration of ophthalmic applicators at nist: A revised approach. *Medical Physics*, 18(4):787–793, 1991. doi: https://doi.org/10.1118/1.596632. URL https://aapm.onlinelibrary.wiley.com/doi/abs/10.1118/1.596632.

[117] Barry N. Taylor and Chris E. Kuyatt. Guidelines for Evaluating and Expressing the Uncertainty of NIST Measurement Results T Technical Note 1297. *National Institute for Standards and Technology, Gaithersburg, MD*, page D.1.1.2, 1994. URL http://physics.nist.gov/TN1297.

[118] Z BAY, P A NEWMAN, and H H SELIGER. Absolute measurement of W for Po 210 alpha particles in air, nitrogen, and carbon dioxide. *Radiation research*, 14(5):551–65, may 1961. ISSN 0033-7587. URL http://www.ncbi.nlm.nih.gov/pubmed/13688088.

[119] William P. Jesse. The Ionization by Polonium Alpha Particles in Air and the Average Energy to Make an Ion Pair. *Radiation Research*, 13(1):1, jul 1960. ISSN 00337587. doi: 10.2307/3570868. URL https://www.jstor.org/stable/3570868?origin=crossref.

[120] J. Perl, J. Shin, J. Schümann, B. Faddegon, and H. Paganetti. TOPAS: An innovative proton Monte Carlo platform for research and clinical applications. *Medical Physics*, 39(11):6818–6837, 2012. ISSN 00942405. doi: 10.1118/1.4758060.

[121] U. Giesen and J. Beck. New measurements of W-values for protons and alpha particles. *Radiation Protection Dosimetry*, 161(1-4):23–26, 2014. ISSN 17423406. doi: 10.1093/rpd/nct282.

[122] Tatsuaki Kanai, M Sudo, Naruhiro Matsufuji, and Y Futami. Initial recombination in a parallel-plate ionization chamber exposed to heavy ions. *Physics in medicine and biology*, 43(12):3549–58, dec 1998. ISSN 0031-9155. doi: 10.1088/0031-9155/43/12/012. URL http://www.ncbi.nlm.nih.gov/pubmed/9869031.

[123] S. Rossomme, A. Delor, S. Lorentini, M. Vidal, S. Brons, O. Jkel, G. A.P. Cirrone, S. Vynckier, and H. Palmans. Three-voltage linear method to determine ion recombination in proton and light-ion beams. *Physics in Medicine and Biology*, 65(4), 2020. ISSN 13616560. doi: 10.1088/1361-6560/ab3779.

[124] S. Rossomme, J. Horn, S. Brons, O. Jäkel, A. Mairani, M. Ciocca, V. Floquet, F. Romano, D. Rodriguez Garcia, S. Vynckier, and H. Palmans. Ion recombination correction factor in scanned light-ion beams for absolute dose measurement using plane-parallel ionisation chambers. *Physics in Medicine & Biology*, 62(13):5365–5382, jun 2017. ISSN 0031-9155. doi: 10.1088/1361-6560/aa730f. URL https://iopscience.iop.org/article/10.1088/1361-6560/aa730f.

[125] S. Rossomme, J. Hopfgartner, N. D. Lee, A. Delor, R. A. S. Thomas, F. Romano, A. Fukumura, S. Vynckier, and H. Palmans. Ion recombination correction in carbon ion beams. *Medical Physics*, 43(7):4198–4208, jun 2016. ISSN 00942405. doi: 10.1118/1.4953637. URL http://doi.wiley.com/10.1118/1.4953637.

[126] François DeBlois, Corey Zankowski, and Ervin B. Podgorsak. Saturation current and collection efficiency for ionization chambers in pulsed beams. *Medical Physics*, 27(5):1146–1155, may 2000. ISSN 00942405. doi: 10.1118/1.598992. URL http://doi.wiley.com/10.1118/1.598992.

[127] George Jaffé. Zur Theorie der Ionisation in Kolonnen. *Annalen der Physik*, 347 (12):303–344, 1913. doi: https://doi.org/10.1002/andp.19133471205. URL https://onlinelibrary.wiley.com/doi/abs/10.1002/andp.19133471205.

[128] J. W. Boag and T. Wilson. The saturation curve at high ionization intensity. *British Journal of Applied Physics*, 3(7):222–229, 1952. ISSN 05083443. doi: 10.1088/0508-3443/3/7/305.

[129] R E Greene, R S Pressly, and F N Case. A review of alpha radiation source preparation methods and applications. *Oak Ridge Report ORNL-4819*, 1972.

[130] E Holm. Source Preparations for Alpha and Beta Measurements. *Ris0 National Laboratory, Denmark, and Lund University, Sweden*, (January):1–17, 2001.

[131] M. T. Crespo. A review of electrodeposition methods for the preparation of alpha-radiation sources. *Applied Radiation and Isotopes*, 70(1):210–215, 2012. ISSN 09698043. doi: 10.1016/j.apradiso.2011.09.010. URL http://dx.doi.org/10.1016/j.apradiso.2011.09.010.

[132] D. S. Urch. Chapter 5. Radiochemistry. *Annual Reports Section "A" (Inorganic Chemistry)*, 76:247, 1979. ISSN 0260-1818. doi: 10.1039/ic9797600247. URL http://xlink.rsc.org/?DOI=ic9797600247.

[133] T. M. Semkow, A. J. Khan, D. K. Haines, and A. Bari. Rapid alpha spectroscopy of evaporated liquid residues for emergency response. *Health Physics*, 96(4):432–441, 2009. ISSN 00179078. doi: 10.1097/01.HP.0000336981.92713.a0.

[134] Azam Niroomand-Rad, Sou-Tung Chiu-Tsao, Michael P. Grams, David F. Lewis, Christopher G. Soares, Leo J. Van Battum, Indra J. Das, Samuel Trichter, Michael W. Kissick, Guerda Massillon-JL, Paola E. Alvarez, and Maria F. Chan. Report of AAPM Task Group 235 Radiochromic Film Dosimetry: An Update to TG-55. *Medical Physics*, 47(12):5986–6025, dec 2020. ISSN 0094-2405. doi: 10.1002/mp.14497. URL https://onlinelibrary.wiley.com/doi/10.1002/mp.14497.

[135] Bhaskar Mukherjee, Yaser H. Gholami, Uday Bhonsle, Reinhard Hentschel, and Joseph Khachan. A unique alpha dosimetry technique using Gafchromic EBT3® film and feasibility study for an activity calibrator for alpha-emitting radiopharmaceuticals. *British Journal of Radiology*, 88(1056), 2015. ISSN 00071285. doi: 10.1259/bjr.20150035.